

# Decoration of Cube-Like Ceria Crystals by Well-Dispersed Au Nanoparticles: Surface Influence.

Małgorzata A. Małecka<sup>1\*</sup>, Krzysztof Matus<sup>2</sup>, Piotr Woźniak<sup>1</sup>

<sup>1</sup>*Institute of Low Temperature and Structure Research, Polish Academy of Sciences,  
P.O. Box 1410, 50-950 Wrocław 2, Poland*

<sup>2</sup>*Department of Engineering Materials and Biomaterials, Silesian University of Technology,  
ul. Konarskiego 18a, 44-100 Gliwice, Poland*

## ABSTRACT

In this paper, the run of the decorating process of the active support, like CeO<sub>2</sub>, by the gold nanoparticles via deposition-precipitation method has been studied. Two types of the Au/CeO<sub>2</sub> systems with different mean particle size (but the same morphology) of the support have been investigated. It was noted that the decoration process proceeds easily only for large crystals with average size about 67 nm. Three hypotheses were tested in order to explain unsuccessful initial Au nanoparticles decoration of the cube-like CeO<sub>2</sub> crystals with average size about 14 nm as a support. The tests have shown that the ratio of the molar content of the chloroauric acid to the total surface area of the support ( $M_{Au}/S_{CeO_2}$ ) has a significant impact on the decorating process of CeO<sub>2</sub> by nano-Au. If the above ratio is too small, the thin layer of gold instead of the Au nanoparticles is formed on the support surface. In this paper, the calculations of the real surface area (from TEM/HRTEM data) were used to adjust the optimum the  $M_{Au}/S_{CeO_2}$  to obtain the Au/CeO<sub>2</sub> system with the desired properties.

\*corresponding author:

Dr. Hab. Małgorzata Alicja Małecka

P.O. Box 1410, 50-950 Wrocław, Poland,

Tel: (4871) 3954150, Fax (4871) 441029, e-mail: [M.Malecka@intibs.pl](mailto:M.Malecka@intibs.pl)

[doi.org/10.1002/slct.202000098](https://doi.org/10.1002/slct.202000098)

## INTRODUCTION

Nanocrystalline gold is a marvellous discovery in the catalysis. Catalysts based on the highly dispersed gold show high activity in many reactions, like CO oxidation, <sup>[1;2]</sup> WGS reaction, <sup>[3;4]</sup> complete benzene oxidation, <sup>[5;6]</sup> selective hydrogenation of 1,3-butadiene, <sup>[7-9]</sup> hydrogenation of crotonaldehyde, <sup>[10;11]</sup> cyclohexane oxidation <sup>[12-14]</sup> and reduction of NO by CO. <sup>[15]</sup> The decoration and keeping the high dispersion of the active phase play a key role in designing of the catalyst. Another important factor that should be taken into consideration is the characteristic of the support. Besides the passive supports, like SiO<sub>2</sub> or Al<sub>2</sub>O<sub>3</sub>, the active catalytic supports (like CeO<sub>2</sub>), which not only stabilize the active phase dispersion but also take part in the catalytic act, could be used. <sup>[16]</sup> The pure and doped ceria materials are active supports that are often used in catalysis. Ceria-supported metal catalysts (Me/CeO<sub>2</sub> systems), like Au/CeO<sub>2</sub>, <sup>[1;3;4;6;17]</sup> Pd/CeO<sub>2</sub>, <sup>[18]</sup> Ag/CeO<sub>2</sub> <sup>[19]</sup> and Ru/CeO<sub>2</sub>, <sup>[20]</sup> exhibit catalytic activity in processes such as the CO oxidation, <sup>[1;17;19]</sup> WGS reaction, <sup>[3;4]</sup> complete benzene oxidation <sup>[6]</sup> and the dehydrogenation of ammonia borane. <sup>[20]</sup>

The next important parameter for catalyst characterization is the size of the active phase nanoparticles distributed on the support surface. <sup>[21-23]</sup> The highest catalytic activity was observed for nanoparticles of gold with a size of circa 3 nm. <sup>[22;23]</sup> For Au particles having a size below this value, the catalytic activity significantly decreases. It is probably due to the impeded adsorption of CO molecule on the very small Au nanoparticle. <sup>[23]</sup> Similarly, the activity of nano-gold decreases with particle size augmentation to finally become inactive material, a symbol of immutability and permanence as a bulk gold.

The crystallization process of nanocrystalline metals on the support surface can proceed according to the one of three mechanisms – Volmer-Weber (VW), Frank-van der Merve (FM) and Stranski-Krastanov (SK) model. <sup>[24]</sup> In the first of them (Volmer-Weber), the nucleation of islands is favoured over extended growth at the layer edges. The stages in the VW growth mechanism include: nucleation of discrete islands, island growth, island impingement and coalescence. <sup>[24]</sup> The second one (Frank-van der Merve) is the most common growth model, also known as “layer-by-layer” growth. In the FM model a layer of atoms is started and completed before another layer starts to grow. <sup>[24]</sup> The last one (Stranski-Krastanov) is the combination of the two above mechanisms, where growth is initiated as a layer-by-layer mode but shifts to an island mode. <sup>[24]</sup> The two-stage Stranski-Krastanov mechanism starts with epitaxial growth of 3 – 7 % lattice mismatch material (larger lattice – in our case CeO<sub>2</sub>,  $a = 0.5411$  nm) on the crystalline substrate (smaller lattice – in our case Au,

$a = 0.407$  nm). The formation of the epitaxy layers will reach supercritical layers, where these layers will have less strain from the substrate layer, followed by the start of the relaxation process. This relaxation results in an island like epitaxy formation in the second stage. <sup>[25]</sup>

In this work, the influence of surface area of the ceria (support) on the crystallization process of gold nanoparticles on the support surface has been presented. The flow of Au nanoparticles crystallization on ceria surface, during the deposition-precipitation synthesis, <sup>[26]</sup> was deeply investigated with particular emphasis on the size of the CeO<sub>2</sub> crystals. The samples were detailedly subjected by SEM, TEM, EDX and FTIR methods.

## RESULTS AND DISCUSSION

During the study of Au/CeO<sub>2</sub> systems with controllable support morphology, the strange problems with the decorating of ceria surface by the gold nanoparticles were noted. In the case of large cubes of ceria ( $d_{av} = 67$  nm) as a support, the nanoparticles of gold (Fig.1A) were supported on ceria surface in a very uniform way. But in the case of small cube-like ceria crystals ( $d_{av} = 14$  nm), nanocrystalline gold supported on ceria surface was not detected. In a few places, on TEM and HRTEM images, the presence of the large (~10 nm), oval crystals of gold lying down next to the support has been detected (Fig.1B). Additionally, for better illustration of the presence of gold, the HAADF-STEM with EDX measurement was performed (see Fig.S1, Supporting Information) for the untreated sample Au/CeO<sub>2</sub> (small cube-like). The analysis of the HAADF images simultaneously with EDX data show that the large crystals of Au are visible in the sample but their presence is rather occasional. The above cases were sporadic (hard to find on TEM images). Fig.1 presents the TEM images of as prepared samples Au/CeO<sub>2</sub> (large cube-like) and Au/CeO<sub>2</sub> (small cube-like), where the lack of the Au nanoparticles in the Au/CeO<sub>2</sub> (small cube-like) sample is pointed out. Simultaneously, the global gold concentration (measured by the SEM-EDX method) in all samples is similar (see Fig.1).

The previous study of Bezkravnyy et. al. <sup>[28]</sup> as well as Ha et al. <sup>[29]</sup> show that the cerium oxide with a cube-like morphology is a good support for the nanocrystalline gold. However, in the study presented in, <sup>[28]</sup> only large cube-like CeO<sub>2</sub> crystals were taken into consideration. In the present work, we have been taken to answer the following question – Why the gold nanoparticles are invisible in Au/CeO<sub>2</sub> (small cube-like) sample?

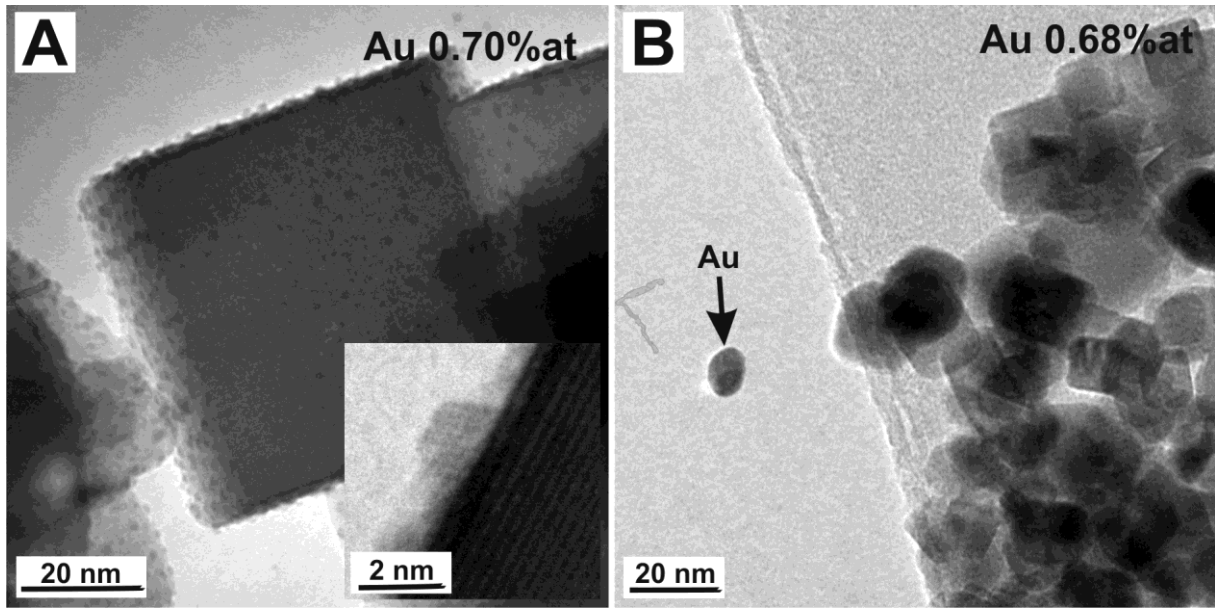


Fig.1. TEM images of as prepared samples (A) Au/CeO<sub>2</sub> (large cube-like) (with HRTEM image - inset), (B) Au/CeO<sub>2</sub> (small cube-like). The values of the average Au concentration from SEM-EDX method were added.

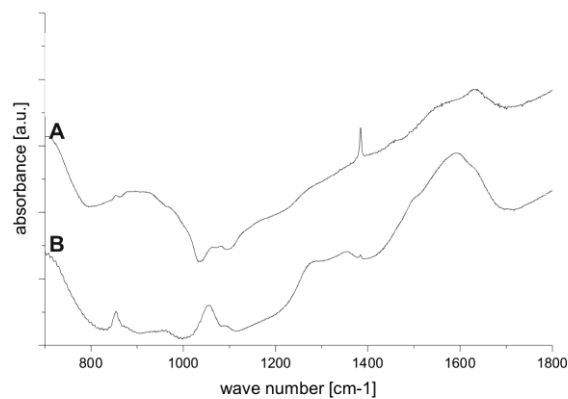


Fig.2. FTIR spectra of the as prepared supports (A) CeO<sub>2</sub> (large cube-like), (B) CeO<sub>2</sub> (small cube-like).

In Fig.2, the FTIR spectra of the investigated CeO<sub>2</sub> supports are shown. It could be noticed that the surface characteristics of the crystallites in each of the two samples are different. In all investigated samples, the characteristic, very sharp, strong band at 1384 cm<sup>-1</sup>, which could be assigned to the NO<sub>3</sub><sup>-</sup> stretching vibrations in KNO<sub>3</sub>,<sup>[30]</sup> was clearly visible. The presence of the KNO<sub>3</sub> in the as prepared (not preheated) oxide's samples has been widely discussed in our previous papers.<sup>[31;32]</sup> This is due to the use of Ce(NO<sub>3</sub>)\*6H<sub>2</sub>O as a cerium source, followed by chemical reaction occurring during the grinding and pressing of a nitrate

containing sample with KBr (preparation of samples for FTIR measurement). The surfaces  $\text{NO}_3^-$  groups could be removed from samples by the heat treatment at the 550 °C under the oxidizing conditions. <sup>[31]</sup> However, the ceria samples investigated in this work were not subjected to any heat treatment before decoration by the Au nanoparticles, so nitrate groups could be present on the support surface. Interestingly, the FTIR spectra recorded for the cube-like samples (large and small) significantly differ from each other. These differences cannot be related to the presence of the unwanted dopant, because the reaction mixtures used for synthesis of both supports were identical in the chemical composition, but differed only in the quantitative composition of the reagents. The difference between the FTIR spectra recorded for both cube-like samples were in the amount and types of surface carbonates. <sup>[33]</sup> The first hypothesis, which could be a response for previously asked question, is: the difference in surface characteristic between the  $\text{CeO}_2$  (large cube-like) and  $\text{CeO}_2$  (small cube-like) supports could be responsible for a failed decorating process in the case of the  $\text{Au/CeO}_2$  (small cube-like) sample. First, the effect of the difference in  $\text{NO}_3^-$  groups content on the decoration process was examined. For this purpose, the support ( $\text{CeO}_2$  (small cube-like)) was heated at 550 °C in static air by 3 h to remove nitrate residues. <sup>[31]</sup> The temperature treated ceria (called  $\text{CeO}_2$  (small cube-like\_550)) was decorated by gold in the same way as the untreated one. As shown in Fig.3, the result of decoration was the same as for untreated support - no nanocrystalline gold was visible on ceria surface. Based on the above result, it was found that the presence of  $\text{NO}_3^-$  groups on the ceria surface has no effect on the decorating process.

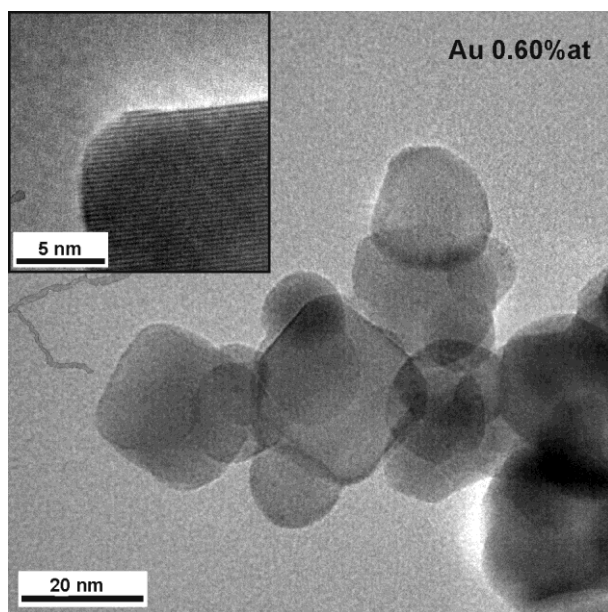


Fig.3. TEM image of as prepared  $\text{Au/CeO}_2$  (small cube-like\_550) (with HRTEM image - inset). The value of the average Au concentration from SEM-EDX method was added.

However, the literature review suggested another solution to this problem. In the paper, [34] the Pt/Al<sub>2</sub>O<sub>3</sub> systems were tested, where one of the most important factor, responsible for the decoration of the alumina surface by the platinum nanoparticles, was the curvature of the support surface. Adibi et al [34] noted that the initial Pt particle size distributions and their time evolution during sintering are different on the cones and the flat areas of the alumina. In our case, the CeO<sub>2</sub> (large cube-like) plays a role of “the large flat surface” and the sample CeO<sub>2</sub> (small cube-like) could correspond to “a strongly curved surface”, as is visible in Fig.1.

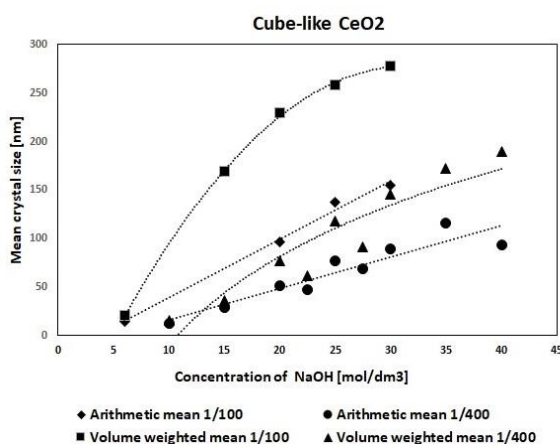


Fig.4. Mean crystal size calculated for various samples.

To resolve this issue, the series of the CeO<sub>2</sub> (cube-like) syntheses were performed by the hydrothermal method using the various conditions. Two basic variables of the reaction conditions have been chosen: (1) the molar ratio of Ce-source to base [Ce(NO<sub>3</sub>)<sub>3</sub>\*6H<sub>2</sub>O/NaOH] and (2) the molar concentration of NaOH in the reaction mixture [mol/dm<sup>3</sup>]. The obtained results of mean crystal size for two series of samples (Ce(NO<sub>3</sub>)<sub>3</sub>\*6H<sub>2</sub>O/NaOH = 1/400 and 1/100 with different concentration of NaOH ~ 5 < C<sub>m</sub> < 40) are presented in Fig.4. It is clearly seen that the molar concentration of NaOH in the reaction mixture is extremely important factor for the controllable synthesis of the cube-like ceria crystals. According to earlier data presented by Bezkrönyi et. al., [27] increasing the NaOH concentration leads to increasing the mean crystal size of the cubic ceria crystals. The great role, in the CeO<sub>2</sub> crystal growth process, plays also the molar ratio of Ce-source to base. For the 1/400 ratio, the particles of CeO<sub>2</sub> were significantly smaller than for the 1/100 one, but simultaneously the mean crystal size distributions calculated for the molar ratio Ce(NO<sub>3</sub>)<sub>3</sub>\*6H<sub>2</sub>O/NaOH of 1/400 were much narrower than for the 1/100 one (see Fig.S2 in

Supporting Information). This is clearly seen in the mutual relationship between arithmetic mean and volume weighted mean, which are diverged in the case of broad or bimodal crystal size distributions but convergent for the narrow ones. <sup>[35]</sup> The crystal size distributions for investigated series of samples have been posted in Fig.S3 (Supporting Information).

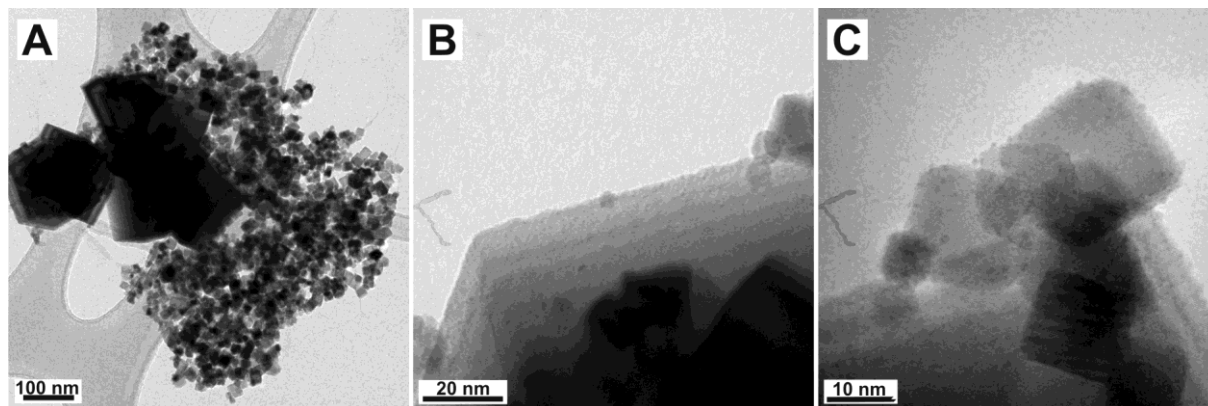


Fig.5. TEM images of CeO<sub>2</sub> (extra-large + small cube-like) (A) general view, detailed views from extra-large particle of ceria (B) and small particles of ceria (C).

To explain, if either the groups present on the support surface of both CeO<sub>2</sub> (large cube-like) and CeO<sub>2</sub> (small cube-like) or curvature of their surface are responsible for differences in decoration of oxide surface by the nanoparticles of gold, the deposition test on a mixed CeO<sub>2</sub> system (extra-large + small cube-like) was performed. As a support with bimodal crystal size distribution, the mixture of the two samples (CeO<sub>2</sub> (extra-large cube-like) and CeO<sub>2</sub> (small cube-like) with mean size 148 nm and 14 nm (mass ratio = 1:1), respectively) was prepared. Next, the decorating process by the deposition-precipitation method <sup>[26]</sup> was performed. In Fig.5, the TEM images of Au/CeO<sub>2</sub> (extra-large + small cube-like) sample are presented. It turned out that gold nanoparticles were present on the surface of both the extra-large as well as small crystals of cube-like ceria (Fig.5B and Fig.5C). This proves that neither differences in the presence of functional groups (carbonates observed by FTIR), nor the curvature of the surface of cube-like ceria crystallites (Fig.1) are responsible for the decoration process of ceria crystals by the gold (noble metal) nanoparticles, as it could be suggested by the literature. <sup>[34;36]</sup>

From the beginning, the puzzle to solve was the invisibility of gold nanoparticles in Au/CeO<sub>2</sub> (small cube-like) sample, while the global concentration of Au in all three samples (measured by the SEM-EDX method) was almost identical (see Fig.1). The amount of “free” (unsupported) gold crystals (Fig.1A, marked by arrow), visible on TEM images, was definitely too small in Au/CeO<sub>2</sub> (small cube-like) sample compared to the nanocrystalline

gold supported on the CeO<sub>2</sub> (extra-large cube-like). It was decided to calcine the Au/CeO<sub>2</sub> (small cube-like) sample at the 400 °C for 3 h in the hydrogen flow. In Fig.6, the TEM and HRTEM images of Au/CeO<sub>2</sub> (small cube-like) sample after heat treatment are shown. It turned out that after heat treatment at elevated temperature, the Au nanoparticles ( $d_{av} = \sim 3.7$  nm) were appearing on the surface of CeO<sub>2</sub> (small cube-like) crystals. The above observation suggests that the gold has been permanently present on CeO<sub>2</sub> (small cube-like) surface. Another explanation of that observation could be the dispersion of large Au crystallites present in the Au/CeO<sub>2</sub> (small cube-like) sample, but the HAADF-EDX results indicate that they are still present in the sample after heat treatment at 400 °C (Fig.S4, Supporting Information).

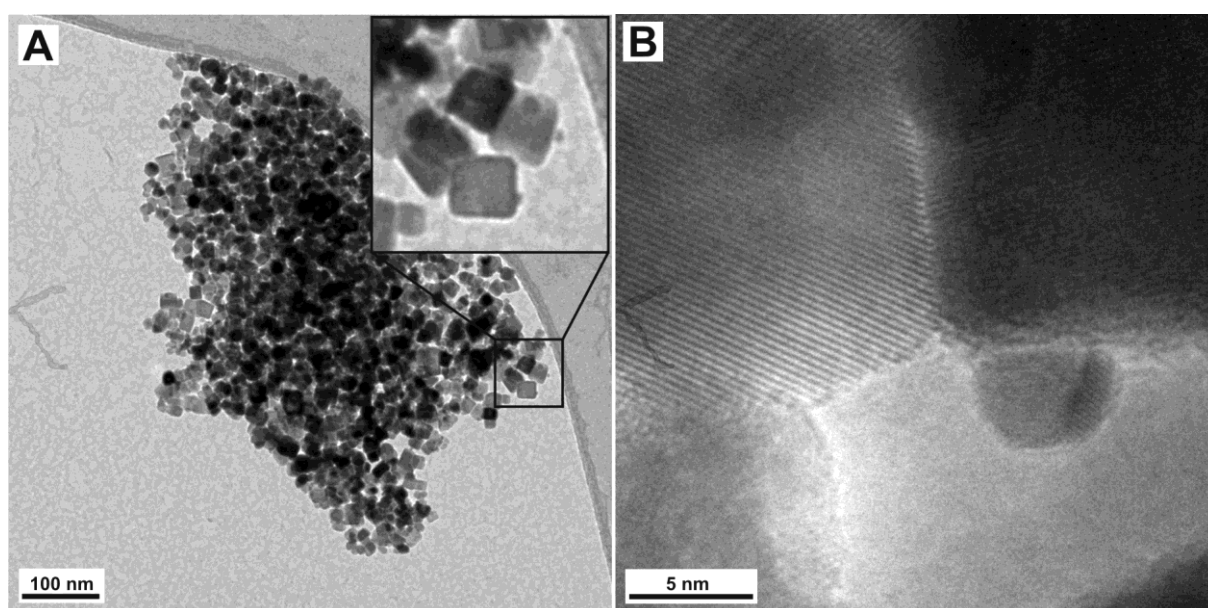


Fig.6. (A) TEM and (B) HRTEM images of Au/CeO<sub>2</sub> (small cube-like) sample after heat treatment at 400 °C in H<sub>2</sub> flow.

To confirm this hypothesis, the Au/CeO<sub>2</sub> (small cube-like), Au/CeO<sub>2</sub> (extra-large cube-like) and Au/CeO<sub>2</sub> (small cube-like heated at 400 °C) samples were detailedly investigated by the TEM-EDX technique. The presence of gold on the small cube-like ceria surface was confirmed by the performed measurements and it was noticed that the gold is present on the CeO<sub>2</sub> (small cube-like) support surface as a very thin film rather than very small nanoparticles. The Fig.7 shows TEM and HRTEM images with the small area TEM-EDX analysis, where the weak peak characteristic for Au is visible on EDX curve but the nanoparticles of gold have not been seen on the ceria surface. The combination of HRTEM and TEM-EDX results suggest that in the case of the Au/CeO<sub>2</sub> (small cube-like) sample, gold



was supported on the CeO<sub>2</sub> surface as a very thin film or ultra-small clusters, which during the heat treatment were sintered. [37] Visible in Fig.7B layer (or maybe better – frill) on the cubic ceria surface is thin carbon layer formed as a result of contamination of carbon during the measurement (in the microscope). Moreover, as seen in Fig.7B and Fig.S5, it is impossible to observe (under the conditions of the measurement) the postulated, in this work, a very thin film or ultra-small clusters of gold on ceria surface.

Additionally, the TEM-EDX results obtained for the Au/CeO<sub>2</sub> (extra-large cube-like) and Au/CeO<sub>2</sub> (small cube-like heated at 400 °C) samples were in good agreement with TEM images and confirmed the presence of well-defined nanoparticles of gold on the surfaces of the supports (see Fig.S6 and Fig.S7 in Supporting Information).

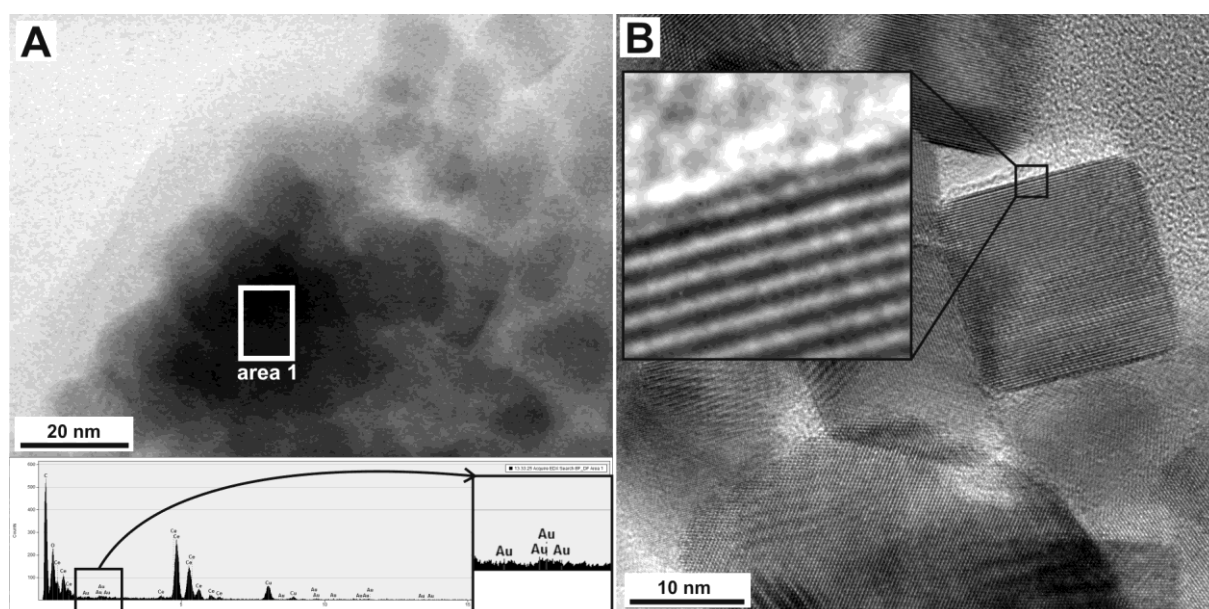


Fig.7. (A) TEM-EDX data and (B) HRTEM image of Au/CeO<sub>2</sub> (small cube-like) sample.

The HRTEM and TEM-EDX data from Au/CeO<sub>2</sub> (small cube-like) and Au/CeO<sub>2</sub> (small cube-like heated) samples prompted us to consider the mechanism of the decoration process by the deposition-precipitation method. [26] The formation of Au nanoparticles, as the “blank synthesis”, was performed according to, [26] except for the addition of ceria support. As a product, the large, misshapen particles of gold (see Fig.S8) were observed in TEM images. Above result can suggest that nanoparticles of gold, observed on the ceria surface (Fig.1), were formed directly on the support surface. Arguably, the molecules of the chloroauric acid (HAuCl<sub>4</sub>) have been adsorbed on the ceria surface and then were reduced to obtain the nanocrystalline gold particles. Literature provides the description of three mechanisms of growth of heterostructures on the support surface - Volmer-Weber (VW), Frank-van der

Merve (FM) and Stranski-Krastanov (SK).<sup>[24]</sup> One of the most important parameter that has to be taken into consideration during the study of the crystal growth of highly dispersed phase on the support surface is the total specific surface area of the support. According to the Stranski-Krastanov model of crystal growth, the amount of adsorbed material (e.g. metal precursor) is critical to the appearance of particles on the surface of the support. If the amount of adsorbed material is too low, no nanoparticles will be visible on the surface of the support and it will be present in the form of a thin layer.<sup>[38]</sup> In our case, the amount of chloroauric acid (calculated per unit area of the support) was ~10 times larger for the Au/CeO<sub>2</sub> (extra-large cube-like) sample than for Au/CeO<sub>2</sub> (small cube-like) one (Table 1). We believe that, such a difference in coverage by the gold of the ceria surface must have consequences in the final product.

To confirm the hypothesis about the main role of support surface area in decoration process, two more samples were prepared. The new samples were synthesized at the same conditions like Au/CeO<sub>2</sub> (small cube-like) one, but with doubly or quadruply decreased mass of CeO<sub>2</sub>. The samples were called Au/CeO<sub>2</sub> (small cube-like)<sub>0.5</sub> and Au/CeO<sub>2</sub> (small cube-like)<sub>0.25</sub>, respectively. The calculated values of the amount of chloroauric acid per unit area of the support for the new samples were comparable with CeO<sub>2</sub> (large cube-like) and CeO<sub>2</sub> (extra-large + small cube-like) ones (see Table 1 and Fig.S9 with paragraph “determination of the surface area of the support” in Supporting Information). The TEM images obtained for two new samples are presented in Fig.8. The analysis of the received images clearly shows that the nanoparticles of gold could be formed on the CeO<sub>2</sub> (small cube-like) surface if the global surface area is small enough. As shown in Fig.8A, halving the amount of the total surface area of the CeO<sub>2</sub> (small cube-like) support caused formation of the very small ( $d_{av} = \sim 1$  nm) gold nanoparticles rarely distributed on the CeO<sub>2</sub> crystals. The amount of HAuCl<sub>4</sub> per unit area of the support of CeO<sub>2</sub> (small cube-like)<sub>0.5</sub> is two times bigger than for CeO<sub>2</sub> (small cube-like) and is similar in magnitude to CeO<sub>2</sub> (extra-large + small cube-like). Subsequent reduction of the support amount in the decoration process (till  $\frac{1}{4}$  of initial value) lead to formation of the Au nanoparticles two times larger ( $d_{av} = \sim 2$  nm), evenly and rather evenly supported on the ceria surface (Fig.8B). The amount of HAuCl<sub>4</sub> per unit area of CeO<sub>2</sub> (small cube-like)<sub>0.25</sub> is four times larger than for CeO<sub>2</sub> (small cube-like) sample. According to our observations, too small ratio of the molar content of chloroauric acid to the total support surface area (in our case less than ~3.8, see Table 1.), is not conducive to formation of the gold nanoparticles, but in such conditions, the thin layer of gold is formed on the support surface. It appears that, the similar situation was described in<sup>[34]</sup> for the Pt/Al<sub>2</sub>O<sub>3</sub> systems, but

the obtained data have been interpreted differently. However, the decrease of the total support surface area by reducing its quantity or the increase of the molar content of  $\text{HAuCl}_4$  in the decorating process, lead to formation of the gold nanoparticles supported on the ceria surface. Such observation is in good agreement with the crystallization process of nanocrystalline metals on the support surface called Stranski-Krastanov (SK) model, <sup>[24]</sup> where growth is initiated as a layer-by-layer mode but shifts to an island mode. The similar observation was made for  $\text{Au/CeO}_2$  system <sup>[26]</sup> where under oxidative conditions, beside the gold nanoparticles on the ceria nanocubes, the extended atom layers at the metal-support interface were observed by the aberration-corrected electron microscopy. The data contained in the above paper can be very useful in the design process of the  $\text{Au/CeO}_2$  catalysts, where the size of the Au nanocrystallites supported on the support <sup>[22;23]</sup> plays an extremely important role. Estimation of the amount of chloroauric acid molecules per  $1 \text{ nm}^2$  of the support (in this case cube-like  $\text{CeO}_2$ ) will allow for proper adjustment of the size of gold particles deposited on the support using the deposition-precipitation method. <sup>[26]</sup> The use of an experimental data carrier (TEM - crystallite size distributions) for the calculation of the specific surface area slightly improves the accuracy of matching in relation to those carried out for average values (Table S1, Supporting Information).

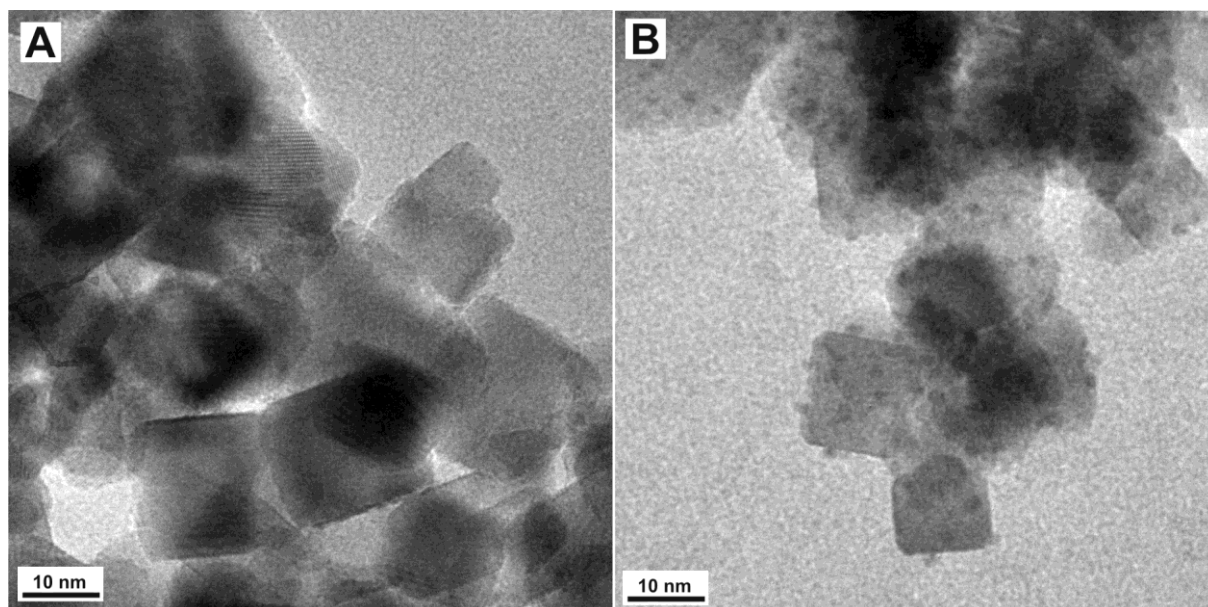


Fig.8. HRTEM image of (A)  $\text{Au/CeO}_2$  (small cube-like)\_0.5 and (B)  $\text{Au/CeO}_2$  (small cube-like)\_0.25 samples.

Table 1. Surface area of the support and ratio of surface of gold per unit area of the support

Sample	CeO <sub>2</sub> extra-large cube-like	CeO <sub>2</sub> small cube-like	CeO <sub>2</sub> extra-large + small cube-like	CeO <sub>2</sub> small cube-like_0.5	CeO <sub>2</sub> small cube-like_0.25	CeO <sub>2</sub> large cube-like
Arithmetic mean particle size of ceria [nm]	148	14	14 + 148	14	14	67
Calculated surface area per 0.05g (or 0.025g* or 0.0125g**) of ceria [nm <sup>2</sup> ]	3.1E+17	3.4E+18	1.8E+18	1.7E+18*	8.4E+17**	6.7E+17
Calculated surface area of ceria [g\cm <sup>2</sup> ]	6	68	36	68	68	13
Number of HAuCl <sub>4</sub> molecules per unit support area [nm <sup>-2</sup> ]	22.60	2.10	3.84	4.20	8.39	10.54

## CONCLUSIONS

In conclusion, the deposition-precipitation method <sup>[26]</sup> is appropriate for decoration of the ceria surface by the gold nanoparticles regardless of the support morphology. It was noted that the run of the decorating process of the ceria surface by the gold nanoparticles was very sensitive to the ratio of the total support surface area to the molar content of the chloroauric acid in the reaction mixture. When the amount of the HAuCl<sub>4</sub> molecules per 1 nm<sup>2</sup> of the CeO<sub>2</sub> was ~2 that, on TEM images, no Au nanoparticles supported on the ceria surface were observed, but gold was present in the Au/CeO<sub>2</sub> systems as a thin layer or small, thin islands. Doubling the above factor caused the appearance of the small nanoparticles of gold ( $d_{av} = 1$  nm) on the surface of ceria crystals. However, four times increase of the amount of the HAuCl<sub>4</sub> per 1 nm<sup>2</sup> of the support surface lead to increasing of the mean size of the Au nanoparticles ( $d_{av} = 3$  nm) supported on the ceria surface. The above results suggest that the run of the decorating process by the deposition-precipitation method is in good agreement with the Stranski-Krastanov (SK) model. The HAuCl<sub>4</sub> molecules have been adsorbed on the CeO<sub>2</sub> surface and then were reduced to metallic Au by the products of urea decomposition. Then, according to the Stranski-Krastanov mechanism, depending on the amount of the chloroauric acid per 1 nm<sup>2</sup> of the ceria surface, the two kinds of the Au/CeO<sub>2</sub> systems could be obtained. First, where the gold is present in the sample as a thin film or second, where the Au nanoparticles are located on the ceria surface. The results shown in this work may contribute to the improvement of the catalyst design process, where the active phase is the highly dispersed nanosized gold.

## SUPPORTING INFORMATION SUMMARY

The complete Experimental Section, HAADF, HRTEM, STEM-EDX data, mean crystal calculations and surface area calculations data can be obtained from the Supporting Information.

## ACKNOWLEDGMENTS

The author thanks Prof. Leszek Kępiński for inestimable help with discussion of experimental results and unshakable belief in author's capacity, Mrs. Zofia Mazurkiewicz for valuable help with preparation of the samples and Dr. Maciej Ptak for FTIR measurements. This work was supported by the National Science Centre (Grant No. UMO-2016/21/D/ST5/01640).

## CONFLICT OF INTEREST

The author declare no conflict of interest.

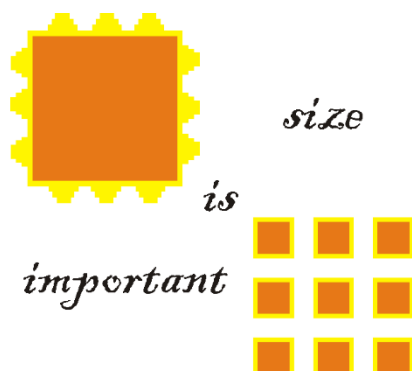
**KEY WORDS:** catalysis; ceria; gold; nanoparticles; TEM

## REFERENCES

- [1] M. A. Centeno, T. R. Reina, S. Ivanova, O. H. Laguna, J. A. Odriozola, *Catalysts* **2016**, *6*, 158.
- [2] O. H. Laguna, A. Pérez, M. A. Centeno, J. A. Odriozola, *Appl. Catal. B* **2015**, *176–177*, 385–395.
- [3] D. Andreeva, I. Ivanov, J. W. Sobczak, W. Lisowski, P. Petrova, M. V. Abrashev, L. Ilieva, *Current Topics in Catalysis* **2008**, *7*, 33-41.
- [4] D. Andreeva, I. Ivanova, L. Ilieva, J. W. Sobczak, G. Avdeev, T. Tabakova, *Appl. Catal. A* **2007**, *333*, 153–160.
- [5] L. Ilieva, P. Petrova, L. F. Liotta, J. W. Sobczak, W. Lisowski, Z. Kaszkur, G. Munteanu, T. Tabakova, *Catalysts* **2016**, *6*, 99.
- [6] D. Andreeva, P. Petrova, J. W. Sobczak, L. Ilieva, M. Abrashev, *Appl. Catal. B* **2006**, *67*, 237–245.
- [7] A. Hugon, L. Delannoy, C. Louis, *Gold Bull.* **2008**, *41*, 127-138.
- [8] X. Zhang, H. Shi, B. Q. Xu *Angew. Chem., Int. Ed.* **2005**, *44*, 7132-7135.
- [9] X. Zhang, H. Shi, B. Q. Xu, *Catal. Today* **2007**, *122*, 330-337.
- [10] J. E. Bailie, G. J. Hutchings, *Chem. Commun.* **1999**, *21*, 2151-2152.
- [11] R. Zanella, C. Louis, S. Giorgio, R. Touroude, *J. Catal.* **2004**, *223*, 328–339.
- [12] R. Zhao, D. Ji, G. Lv, G. Qian, L. Yan, X. Wang, J. Suo, *Chem. Commun.* **2004**, *7*, 904-905.
- [13] G. Lu, R. Zhao, G. Qian, Y. Qi, X. Wang, J. Suo, *Catal. Lett.* **2004**, *97*, 115-118.

- [14] G. Lu, D. Ji, G. Qian, Y. Qi, X. Wang, J. Suo, *Appl. Catal. A* **2005**, *280*, 175-180.
- [15] L. Ilieva, G. Pantaleo, J. W. Sobczak, I. Ivanov, A. M. Venezia, D. Andreeva, *Appl. Catal. B* **2007**, *76*, 107–114.
- [16] M. Yang, J. Liu, S. Lee, B. Zugic, J. Huang, L. F. Allard, M. Flytzani-Stephanopoulos, *J. Am. Chem. Soc.* **2015**, *137*, 3470–3473.
- [17] X. Wanga, B. Chena, G. Chen, X. Sun, *RSC Adv.* **2016**, *6*, 87978–87987.
- [18] C. Mira, J. J. Calvino, J. A. Pérez-Omil, J. M. Rodríguez-Izquierdo, S. Bernal, *Catal. Tod.* **2012**, *180*, 174–183.
- [19] S. Chang, M. Li, Q. Hua, L. Zhang, Y. Ma, B. Ye, W. Huang, *J. Catal.* **2012**, *293*, 195–204.
- [20] R. Wang, Y. Wang, M. Ren, G. Sun, D. Gao, Y. R. C. Chong, X. Li, G. Chen, *Int. J. Hydrogen Energy* **2017**, *42*, 6757-6764.
- [21] J. Wang, H. Tan, S. Yu, K. Zhou, *ACS Catal.* **2015**, *5*, 2873–2881.
- [22] M. Valden, X. Lai, D. W. Goodman, *Science* **1998**, *281*, 1647-1650.
- [23] M. Chen, D. W. Goodman, *Chem.Soc.Rev.* **2008**, *37*, 1860–1870.
- [24] S. L. Brantley, J. D. Kubicki, A. F. White, *Kinetics of Water-Rock Interaction*, Springer, New York, **2008**, p. 259.
- [25] Z. Othaman, L. K. Boo, S. Sakrani, R. Muhammad, *J. Fiz. UTM.* **2008**, *3*, 78-83.
- [26] Y. Lin, Z. Wu, J. Wen, K. Ding, X. Yang, K. R. Poeppelmeier, L. D. Marks, *NanoLett.* **2015**, *15*, 5375–5381.
- [27] O. S. Bezkrivnyi, R. Lisiecki, L. Kępiński, *Cryst. Res. Technol.* **2016**, *51*, 554-560.
- [28] O. Bezkrivnyi, P. Kraszkiewicz, I. Krivtsov, J. Quesada, S. Ordóñez, L. Kepinski, *Catal. Commun.* **2019**, *131*, 105798.
- [29] H. Ha, S. Yoon, K. An, H.Y. Kim, *ACS Catal.* **2018**, *8*, 11491–11501.
- [30] W. Bues, *Z. Phys. Chem.* **1957**, *NF 10*, 1–23.
- [31] M. A. Małecka, L. Kępiński, W. Miśta, *Appl. Catal. B* **2007**, *74*, 290–298.
- [32] M. A. Małecka, *ChemistrySelect* **2019**, *4*, 316 –320.
- [33] C. Binet, M. Daturi, J. C. Lavalley, *Catal. Tod.* **1999**, *50*, 207-225.
- [34] P. T. Z. Adibi, T. Pingel, E. Olsson, H. Grönbeck, C. Langhammer, *J. Phys. Chem. C* **2016**, *120*, 14918–14925.
- [35] R. J. Matyi, L. H. Schwartz, J. B. Butt, *Catal. Rev. Sci. Eng.* **1987**, *29*, 41-99.
- [36] K. A. Ledwa, M. Pawlyta, L. Kępiński, *Appl. Catal. B.* **2018**, *230*, 135–144.
- [37] K. Nakaso, M. Shimada, K. Okuyama, K. Deppert, *Aerosol Sci.* **2002**, *33*, 1061–1074.
- [38] Y. Zhou, Y. Li, W. Shen, *Chem. Asian. J.* **2016**, *11*, 1470-1488.

## Entry for the Table of Contents



As it known, the nanocrystalline gold is a marvelous discovery in the catalysis, and the run of the decorating process of the ceria surface by the gold nanoparticles is very important parameter for the description of the catalyst ( $\text{Au/CeO}_2$ ). It was noted that the run of the decorating process of the ceria surface by the gold nanoparticles was very sensitive to the total support surface area.

# Supplementary materials for

**Decoration of Cube-Like Ceria Crystals by Well-Dispersed Au Nanoparticles: Surface Influence.**

**Małgorzata A. Małecka<sup>1\*</sup>, Krzysztof Matus<sup>2</sup>, Piotr Woźniak<sup>1</sup>**

*<sup>1</sup>Institute of Low Temperature and Structure Research, Polish Academy of Sciences,*

*P.O. Box 1410, 50-950 Wrocław 2, Poland*

*<sup>2</sup>Department of Engineering Materials and Biomaterials, Silesian University of Technology,  
ul. Konarskiego 18a, 44-100 Gliwice, Poland*



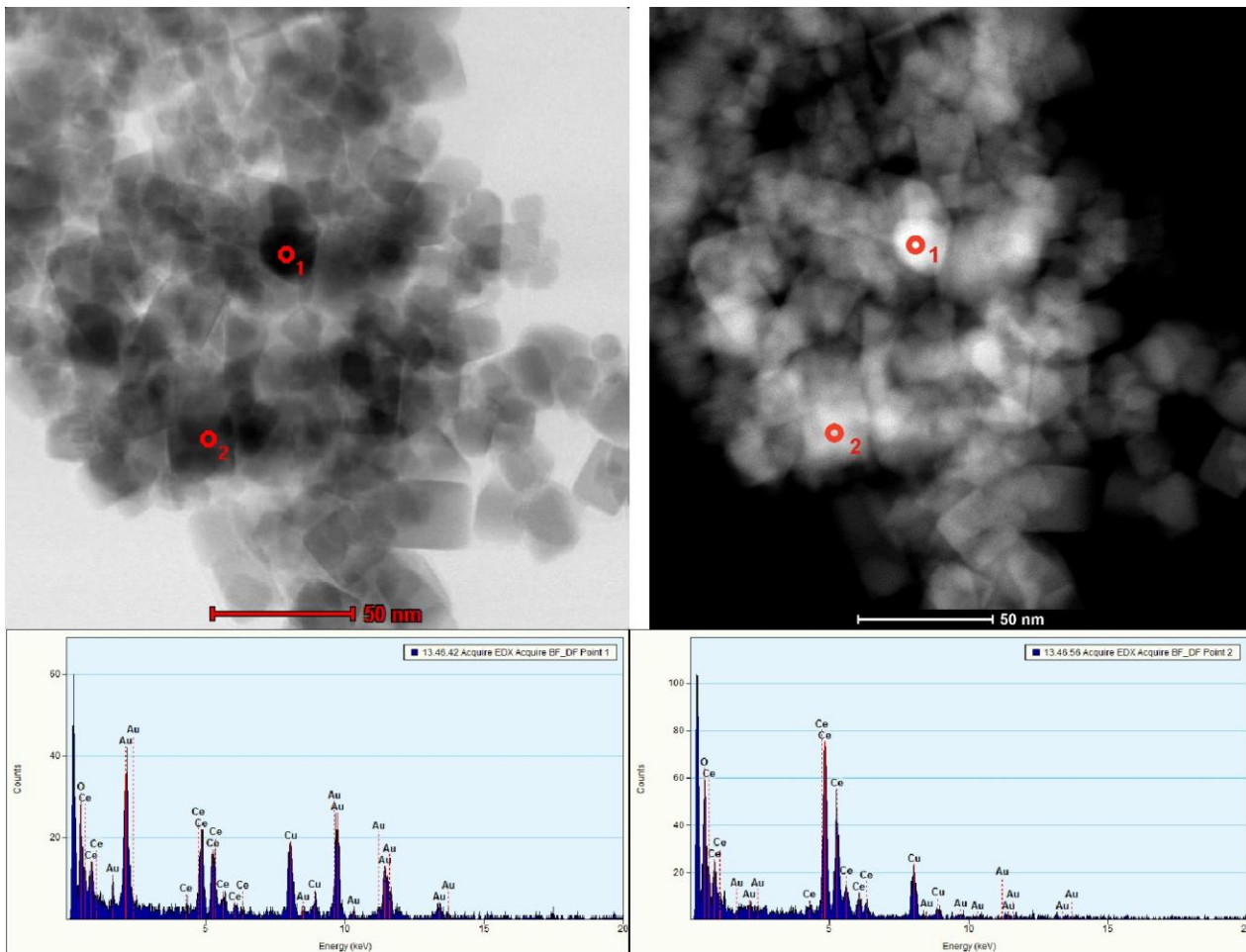


Fig.S1. TEM and HAADF images with EDX spectrum of Au/CeO<sub>2</sub> (small cube). Point 1 – large Au particle, point 2 – small cube of ceria decorated by Au (invisible).

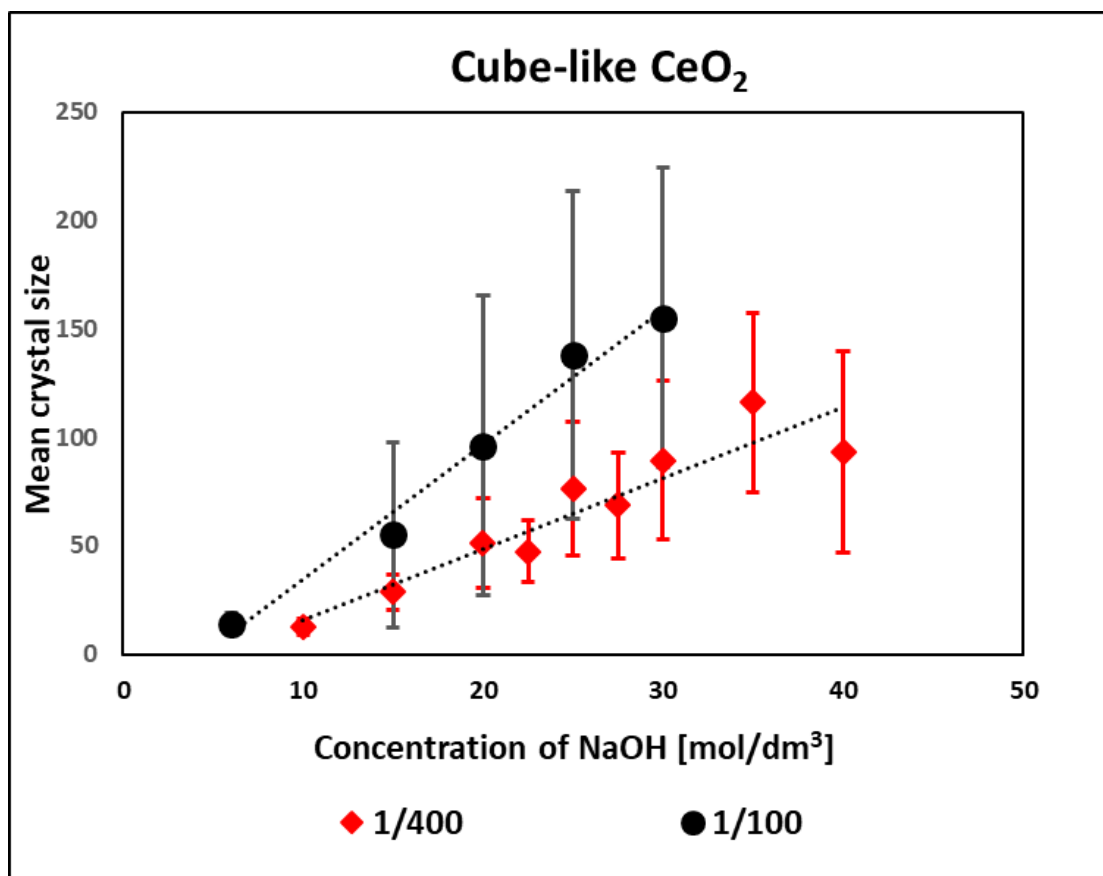


Fig.S2. Mean crystal size of CeO<sub>2</sub> cube-like particles

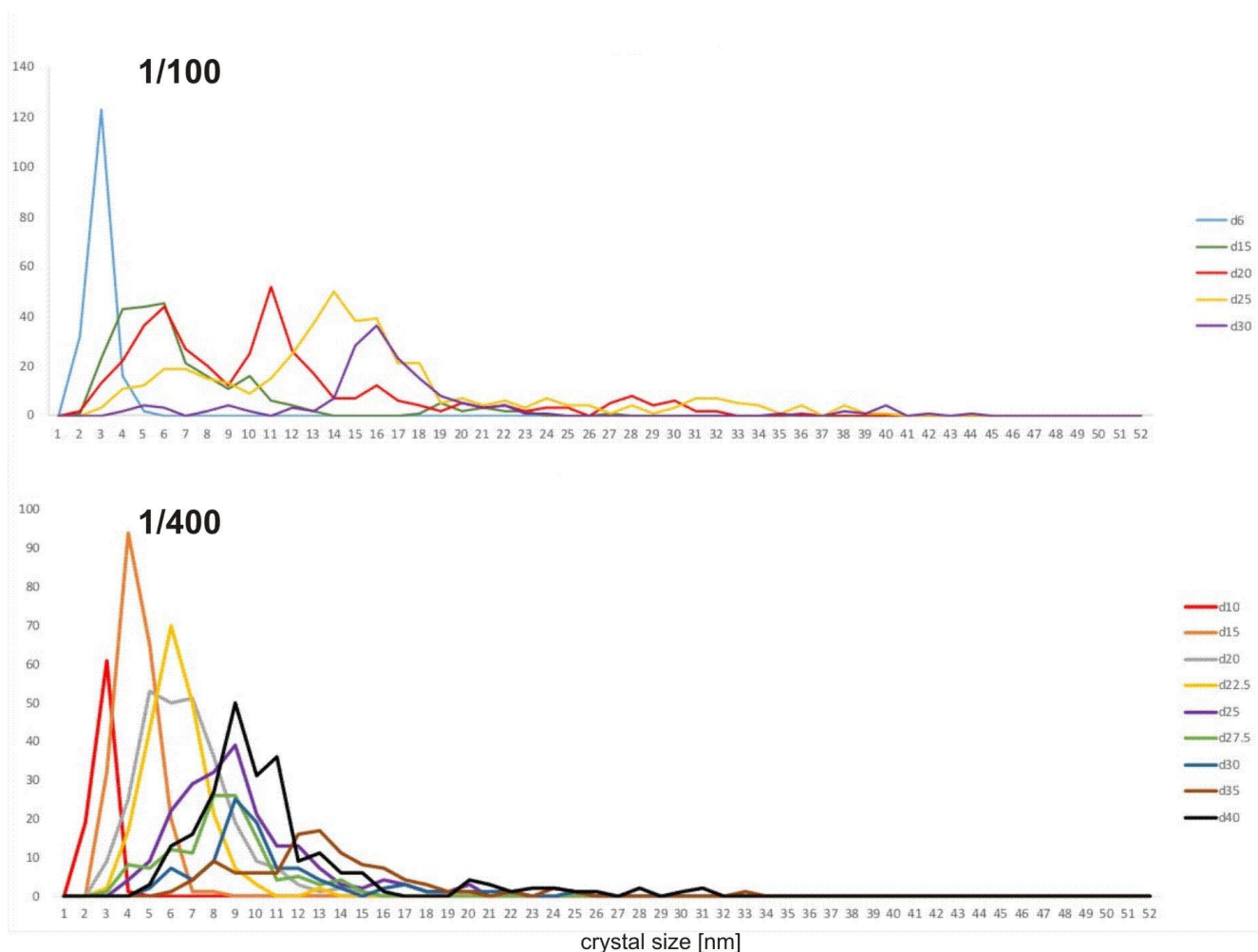


Fig.S3. The crystal size distribution of the CeO<sub>2</sub> cube-like crystals calculated for various Ce/NaOH (1/100 and 1/400) ratios and NaOH concentrations (d).

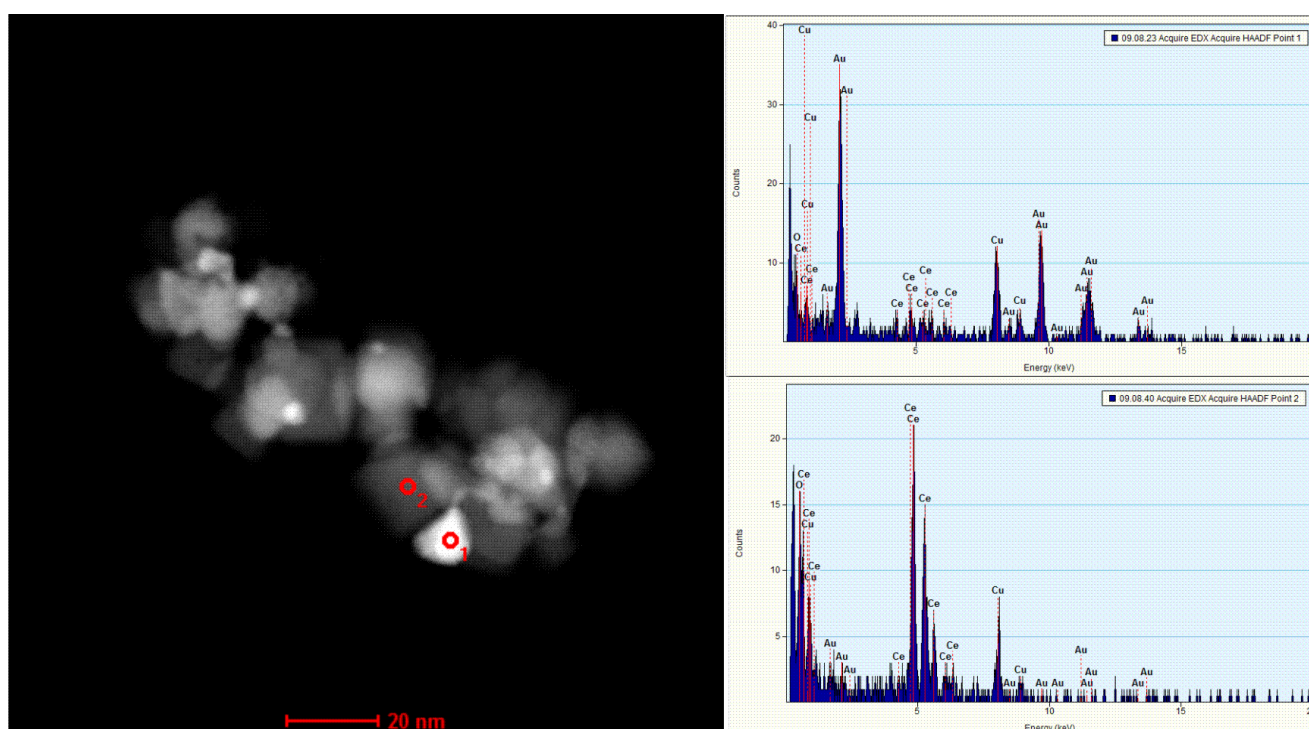


Fig.S4. HAADF image with EDX spectrum of Au/CeO<sub>2</sub> (small cube) after heat treatment at 400 °C in H<sub>2</sub> flow. Point 1 – large Au particle, point 2 – small cube of ceria decorated by nanocrystalline Au.

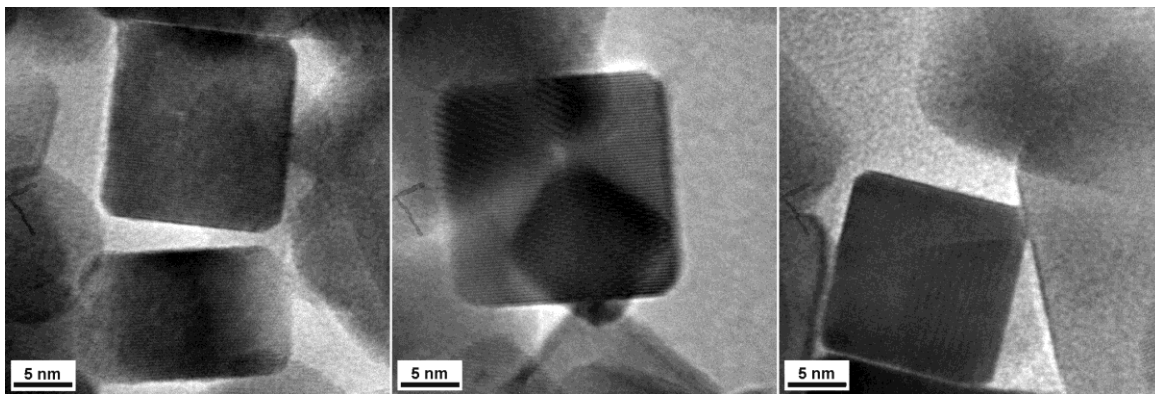


Fig.S5. HRTEM images of Au/CeO<sub>2</sub> (small cube-like) sample – single nanocubes

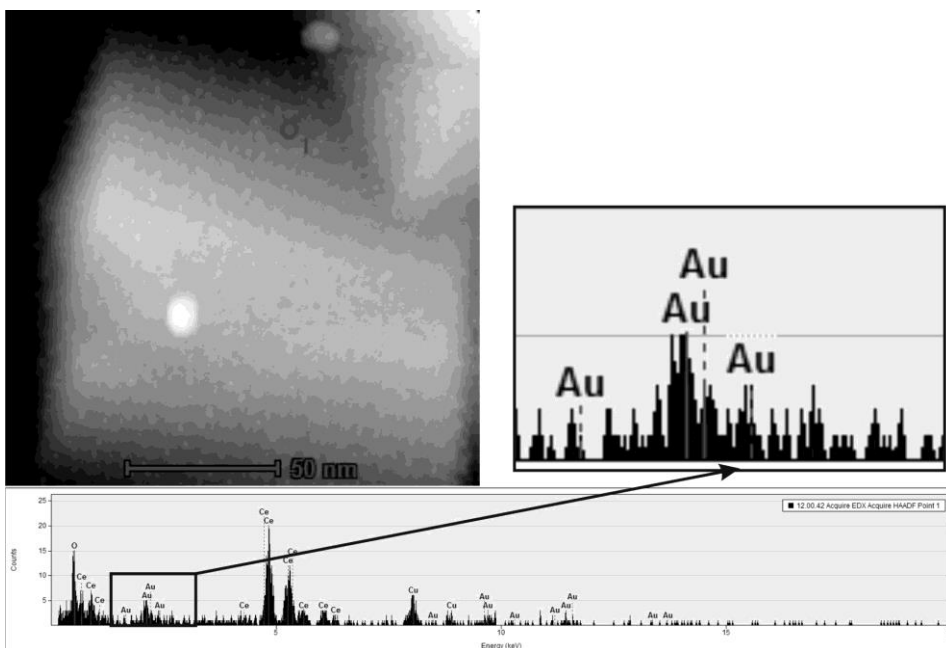


Fig.S6. HAADF image with EDX spectrum of Au/CeO<sub>2</sub> (extra-large cube-like) sample.

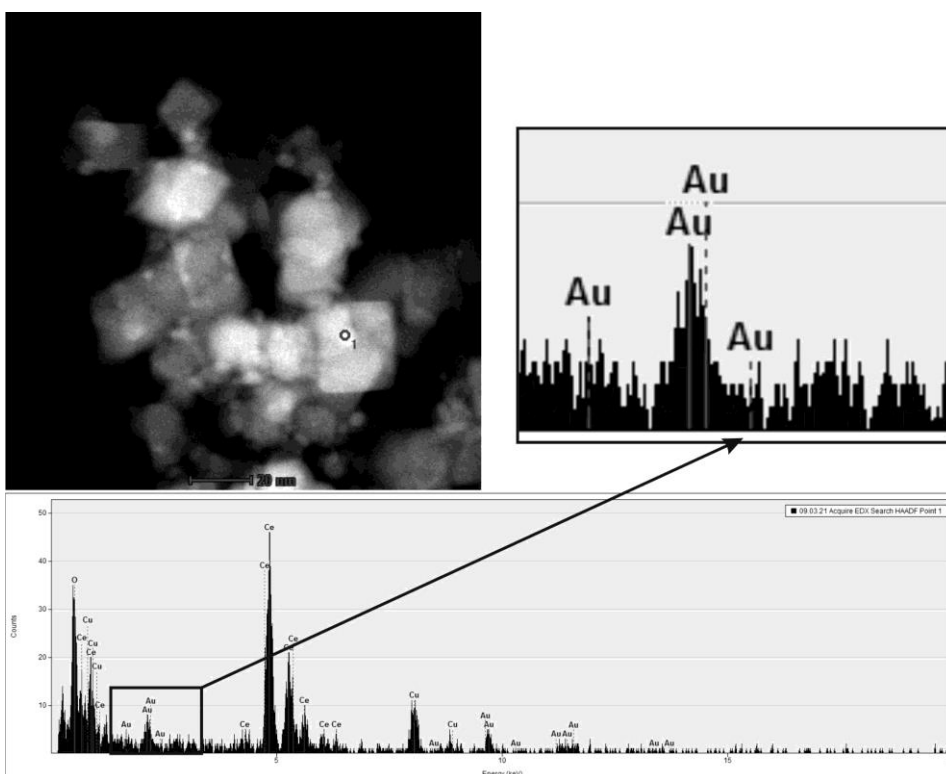


Fig.S7. HAADF image with EDX spectrum of Au/CeO<sub>2</sub> (small cube-like) sample after heat treatment at 400 °C in hydrogen flow.

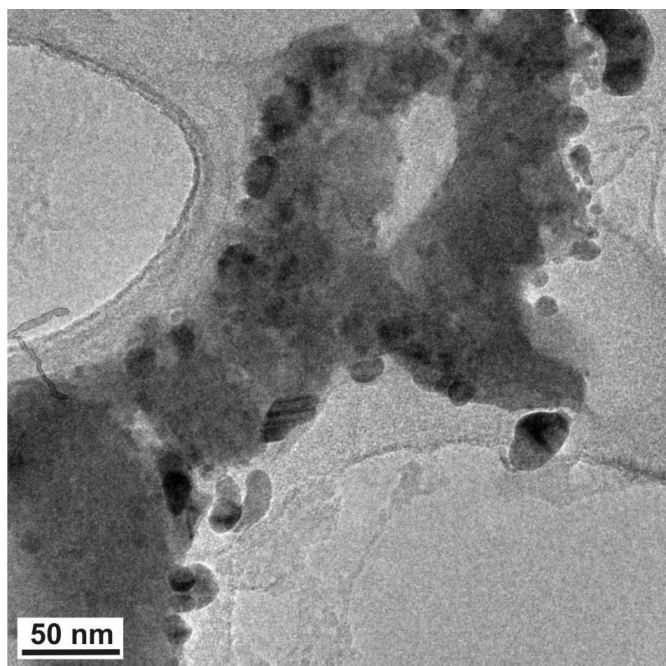


Fig.S8. TEM image of unsupported Au sample prepared by precipitation-deposition method.

### CALCULATIONS - Determination of the surface area of the support

Determination of the surface area of the support was performed on the basis of empirical distributions of sizes of particles (Fig.S9.). The lognormal curves were calculated to obtain the theoretical distribution of particle sizes, followed by determination of frequencies per each category of particle size ( from 1 to 30, 140 or 500 (according to a sample) with step 1). For each category of size, the number of particles was calculated based on the cerium oxide density data and volumes of particles. The restrictive condition was the total mass of 0.05 g for CeO<sub>2</sub> (extra-large cube-like), CeO<sub>2</sub> (large cube-like), CeO<sub>2</sub> (small cube-like) samples, 0,025 g for CeO<sub>2</sub> (small cube-like)<sub>0.5</sub> sample and 0,0125g for CeO<sub>2</sub> (small cube-like)<sub>0.25</sub> sample. The surface area for each category of particles size was calculated by multiplying frequency values per number of particles. Total surface area of the sample was obtained by summation of all as calculated categories.

Table S1. Surface area of the support calculated from mean particle size and from empirical distributions of particle size.

Sample	CeO <sub>2</sub> small cube-like	CeO <sub>2</sub> large cube-like
Arithmetic mean particle size of ceria [nm] / type of size distribution	14 / narrow size distribution	67 / broad size distribution
Calculated surface area per 0.05g of ceria [nm <sup>2</sup> ] from empirical distributions of particle size	3.4E+18	6.7E+17
Calculated surface area per 0.05g of ceria [nm <sup>2</sup> ] from mean particle size.	3.4E+18	8.8E+17

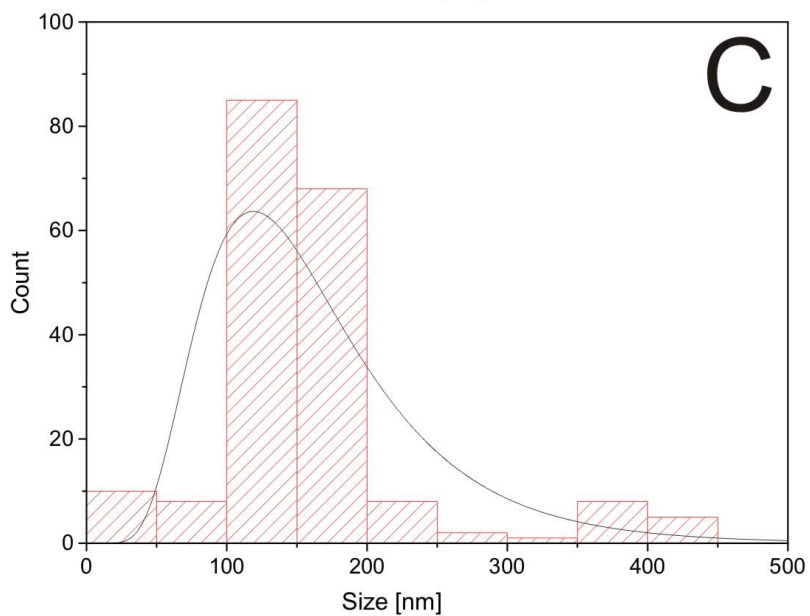
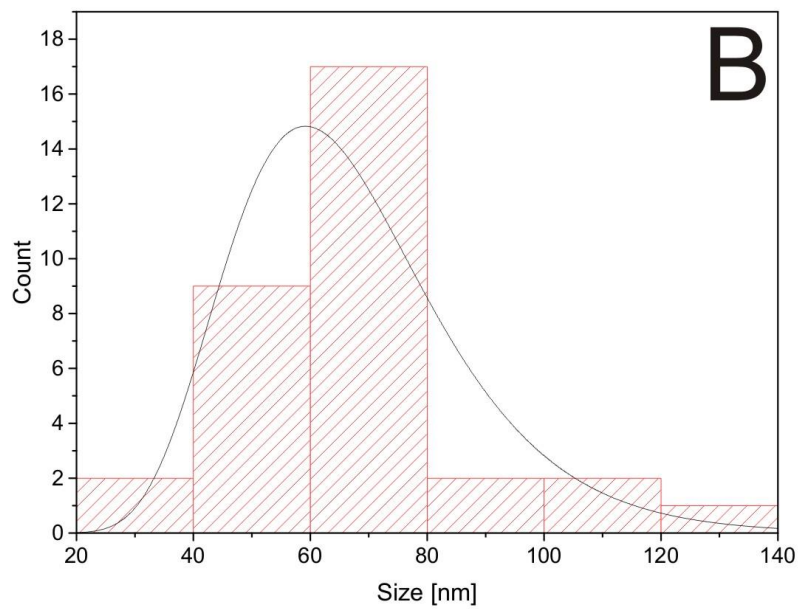
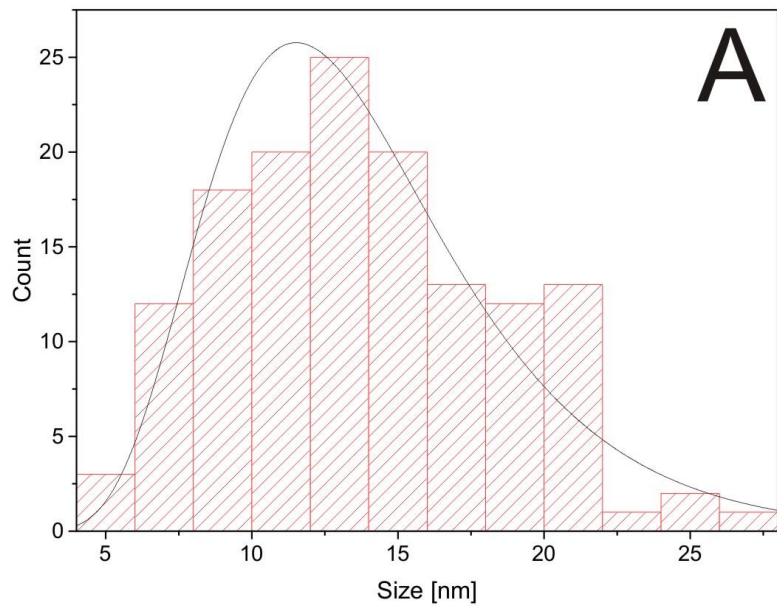


Fig. S9. Empirical distributions of size of particles for A) CeO<sub>2</sub> (small cube-like), B) CeO<sub>2</sub> (large cube-like), C) CeO<sub>2</sub> (extra-large cube-like) samples.

## EXPERIMENTAL SECTION

The cube-like nanocrystals of pure ceria were prepared by the hydrothermal technique <sup>[1;2]</sup>. The  $\text{Ce}(\text{NO}_3)_3 \cdot 6\text{H}_2\text{O}$  was first dissolved in distilled water. Next, the obtained solution was mixed with the appropriate amount of aqueous solution of NaOH (for cubic-like crystals – small <sup>[1]</sup> and large <sup>[2]</sup>), and then stirred for 60 min with magnetic stirrer. The final solution was then transferred to stainless steel Teflon-lined autoclave equipped with a microwave heating and treated at 220 °C for 3 h under autogenous pressure, to obtain cubic nanocrystals.

The Au/CeO<sub>2</sub> samples were prepared by the deposition-precipitation method <sup>[3]</sup>. Then, obtained product was dried at 70 °C. The solid product was heated at 400 °C in hydrogen flow by 3 h.

The phase composition and structural parameters of the crystalline phases present in the samples were determined by XRD (X'Pert PRO PANalytical powder diffractometer, CuK $\alpha$  radiation) with a FullProf program <sup>[4]</sup> used for the display and analysis of the diffractograms. The morphology and microstructure were investigated by TEM (Cs-corrected S/TEM Titan 80-300 FEI operating at 300 kV and Philips CM-20 SuperTwin operating at 160 kV). HRTEM images and SAED patterns were analysed with a DigitalMicrograph program. Local composition of the samples at a nanometer scale was studied by STEM-EDX technique using the Cs-corrected S/TEM Titan 80-300 FEI microscope equipped with EDAX EDX. The global, chemical composition and topography of the samples were checked with a FE-SEM microscope (FEI NovaNanoSEM 230) equipped with an EDX analyser (EDAX Genesis XM4). All SEM-EDX measurements were performed for samples included in the carbon resin tablets (PolyFast), from the same area (260  $\mu\text{m}$  x 330  $\mu\text{m}$ ). FT-IR spectra were acquired with Bio-Rad 575C spectrometer from the specimens prepared as KBr pallets.

### Reference to Experimental Section

- [1] O. Mendiuk, L. Kępiński, *Ceram. Int.* 2014, 40 14833-14843.
- [2] O. S. Bezkrovnyi, R. Lisiecki, L. Kępiński, *Cryst. Res. Technol.* 2016, 51 554-560.
- [3] Y. Lin, Z. Wu, J. Wen, K. Ding, X. Yang, K.R. Poeppelmeier, L.D. Marks, *NanoLett.* 2015, 15 5375–5381.
- [4] J. Rodríguez-Carvajal, *Physica B* 1993, 192 55–69.

## ARTICLE

# Confinement of nano-gold in 3D hierarchically structured gadolinium-doped ceria mesocrystal: synergistic effect of chemical composition and structural hierarchy in CO and propane oxidation.

Received 00th January 20xx,  
Accepted 00th January 20xx

DOI: doi.org/10.1039/D2CY01214F

Piotr Woźniak<sup>\*a</sup>, Małgorzata A. Małecka<sup>a</sup>, Piotr Kraszkiewicz<sup>a</sup>, Włodzimierz Miśta<sup>a</sup>, Oleksii Bezkravnyi<sup>a</sup>, Lidia Chinchilla<sup>b</sup>, Susana Trasobares<sup>b</sup>

The article presents knowledge-driven design of multifunctional hierarchically structured gold on ceria catalyst for environmental applications. Variety of configurations of gold-decorated ceria has been obtained by precise control of the surface coverage parameter in the deposition-precipitation procedure. Activity of hierarchical catalysts in CO and propane oxidation was compared with non-hierarchical gold-decorated nanocubes and nanoparticles. Synoptic description of structural hierarchy and surface properties of the material probed by variety of techniques (TEM, HRTEM, STEM-XED, SEM, ET, SI-EELS, ATR-FTIR, H<sub>2</sub>-TPR, CO-TPR, TPD-MS, N<sub>2</sub> physisorption, NAP-XPS) has been presented to identify underlying phenomena controlling the catalytic activity and indicate structure-reactivity dependencies. Several merits of materials architecture such as (1) surface area and porosity, (2) mutual arrangement of support crystallites, (3) nanoparticles confinement, (4) optimal size of nano-gold, (5) increased metal-support contact has been identified and discussed to explain the observed effect of enhanced catalytic activity. Due to extensive porosity induced by structural hierarchy and nano-gold confinement exceptional surface reducibility has been observed, and CO oxidation temperature has been shifted to ambient regime ( $T_{50} = 18^\circ\text{C}$ ) as compared to gold-decorated nanocubes ( $T_{50}=85^\circ\text{C}$ ). Also, hierarchical catalyst shows substantial propane oxidation facilitation ( $T_{50}=370^\circ\text{C}$ ) when compared to gold-decorated non-hierarchical catalysts ( $T_{50} = 480^\circ\text{C}$ ). Synergistic effect of structural hierarchy and support doping for propane oxidation enhancement has been demonstrated. Also, the effect of dopant-dependent catalyst architecture differences on gold nanoparticles stability has been discussed. The knowledge of materials architecture is necessary for the precise design of optimal multifunctional hierarchical catalyst.

## 1. Introduction

Supported gold nanoparticles has been an object of intensive research due to exceptional catalytic activity in technologically and environmentally important reactions.<sup>1</sup> Since the discovery of high activity of nano-gold in CO oxidation and acetylene hydrochlorination,<sup>2</sup> nowadays more research efforts are devoted to utilizing its potential in various organic reactions or in materials science.<sup>3,4</sup> Properties of heterogeneous gold catalysts has been summarized in many excellent reviews concerning structure and surface chemistry,<sup>5,6</sup> role of the support,<sup>7</sup> type of catalyzed reaction.<sup>8</sup> Also, many suggestions concerning optimization of supported gold catalysts to enhance activity, selectivity and stability in an established reactions has been provided, like adjusting Au nanoparticle size,<sup>9–11</sup> engineering metal-support interaction,<sup>12,13</sup>

shape modification of nanostructured support,<sup>14</sup> doping.<sup>15</sup> Very interesting emergent field relates to gold catalyst supported on hierarchically structured materials.<sup>16–19</sup> However, somewhat limited systematic research has been devoted to this topic, especially controlling catalytic properties as a function of multi-level catalyst architecture and surface chemical properties of this advanced systems.<sup>20</sup>

Various types of materials hierarchy have been signaled in the literature, like morphological, structural, compositional, porous hierarchy.<sup>21</sup> While morphological hierarchy describes materials having units with defined morphology spanning across different numbers of structure levels (e.g. multi-shell hollow spheres),<sup>16</sup> structural hierarchy relates to repetitive combination of units forming superstructures composed of mutually ordered nanoparticles (mesocrystals)<sup>22</sup> or materials with distinguished levels of structural units forming complex structures<sup>23</sup> (e.g. hollow nano-cone constructed ceria,<sup>24</sup> ceria nanobundles,<sup>25</sup> 3D flowerlike ceria).<sup>26</sup> Compositional hierarchy refers to spatial distribution of various building units differed by composition (e.g. core-shell mesoporous nanospheres,<sup>27</sup> hollow@mesoporous yolk-shell structure),<sup>28</sup> and porous hierarchy concerns distribution of multimodal pores within material (e.g. micro-macroporous zeolites).<sup>29</sup> Ensemble of

<sup>a</sup> Institute of Low Temperature and Structure Research, Polish Academy of Sciences, P.O. Box 1410, 50-950 Wrocław 2, Poland. E-mail: p.wozniak@intibs.pl

<sup>b</sup> Departamento de Ciencia de los Materiales e Ing. Metalúrgica y Química Inorgánica, Universidad de Cádiz, Campus Universitario de Puerto Real, 11510, Cádiz - España

†Electronic Supplementary Information (ESI) available: [details of any supplementary information available should be included here]. See DOI: 10.1039/x0xx00000x

nanoparticles that form higher-order hierarchical structure may possess unique properties that differs from individual nanoparticles and corresponding bulk samples, which may contribute to catalytic performance.<sup>30</sup> This is due to facilitated mass transfer, increased active sites availability as well as collective behavior of particles ensemble leading to emergent phenomena.<sup>23,31</sup>

Gold-decorated hierarchical materials may show further beneficial properties due to additional interfaces between metal and oxide inducing multiple interactions,<sup>20</sup> or increased sintering resistance due to metal nanoparticles confinement.<sup>32</sup> Theoretical modelling has shown that kinetics-controlled oxidation proceeds on exterior hierarchical nanostructures and diffusion-controlled regime in internal nanostructures.<sup>33</sup> Thus, embedding gold nanoparticles either on the exterior surface of hierarchical support or inside the material may show different catalytic behavior depending on system architecture. Also, pore morphology of the hierarchical support may influence metal nanoparticles size, shape,<sup>34</sup> and accessibility of active sites by reagents.<sup>33</sup> This, in turn, may have an impact on catalytic properties. Moreover, investigating the influence of mutual arrangement of support crystallites forming hierarchical structure on the catalytic activity may shed light into structure-activity relationship of this complex systems. Hierarchical materials translate advantages of nanomaterials properties to macroscale due to capability of easier technological manipulation with simultaneous preservation of nano-size-arising properties.<sup>35</sup> Much knowledge-driven design approaches have been taken for fabrication of hierarchical catalysts.<sup>36</sup>

Cerium oxide having large oxygen release/uptake capabilities due to easily  $\text{Ce}^{4+}/\text{Ce}^{3+}$  ion reducibility and defect accumulation potential has been used as oxygen storage component of three-way catalysts.<sup>37</sup> Each low-index crystallographic face of  $\text{CeO}_2$  exposes different number of coordination vacancies and has various O-vacancy formation energy, hence, the oxidation activity is highly dependent on ceria surface chemistry following the order  $\{110\} > \{100\} > \{111\}$ .<sup>38</sup> Studies of Au embedded on "active" catalyst support materials show enhanced CO oxidation activity as opposed to "inert" supports ( $\text{SiO}_2$ ,  $\text{Al}_2\text{O}_3$  or  $\text{MgO}$ ), which is caused by increased oxygen supply to the metal catalyst in the former case.<sup>39</sup> Moreover, due to the dependence of oxygen vacancy concentration on size of the ceria particles, the oxygen uptake/release may be enhanced by knowledgeable nanometer level design of shape and size of the particles.<sup>40–42</sup> Hence, cerium oxide is a promising material serving as the active support for metal catalysts, and is prone for rational architecture design and introduction of hierarchy.

Design of hierarchical catalyst at the meso-macro scale may be combined with defect engineering by introduction of dopants into ceria matrix.<sup>43,44</sup> Out of all lanthanides Sm and Gd possess the highest ionic conductivity within ceria structure which is ascribed to optimized ionic radii mismatch and subsequent structural distortions.<sup>45</sup> Incorporation of lanthanide  $\text{Ln}^{3+}$  ions create extrinsic oxygen vacancies modifying oxygen stoichiometry  $\text{Ce}_{1-x}\text{Ln}_x\text{O}_{2-x/2}$  that increases oxygen carrying capacity.<sup>46,47</sup> Hence, evaluating the influence of dopant microstructural changes on catalytic activity

while controlling the material mesoscale architecture at the same time is promising research area worth to pursue.

Automotive exhaust gases containing unburned hydrocarbons, carbon monoxide, nitrogen and sulfur oxides are major pollutants that are formed due to incomplete fuel combustion in oxygen-deficient regions of engines.<sup>48</sup> Environmental air pollution study by Fukusaki et al. revealed that alkanes constitute the highest proportion (~30%) of vehicle-related pollutants, and short-chain hydrocarbons like propane and isopentane are the main volatile organic compounds species in gasoline vehicles exhausts.<sup>49</sup> The elimination of toxic CO and environmentally harmful short-chain alkanes like propane are important for human health protection and for achieving environmental sustainability. Incomplete combustion of alkanes may lead to the formation of greenhouse gas byproducts, hence total combustion of VOCs is of major importance in environmental protection. Studies on supported gold catalysts indicate that different active sites/oxygen activation mechanism participate in CO and alkanes oxidation.<sup>50</sup> Due to that optimization of catalysts performance may include dealing with competing factors. Hence controlling architecture attributes and surface chemistry of complex hierarchical materials is crucial for improving the operation of multifunctional catalysts in automotive exhaust gases treatment.

The objective of this work was to inspect the role of multi-level structural hierarchy of catalyst on propane and CO oxidation activity. While majority of recent research focus on metal-decorated 0D and 1D nanostructures, this research concentrate on knowledge-driven 3D hierarchical mesocrystal catalyst design and study the influence of its architecture attributes: (i) size, morphology and composition of the catalyst support nanoparticles (ii) mutual arrangement of support crystallites, (iii) porosity, (iv) size and distribution of catalyst metal nanoparticles within hierarchical material, (v) surface properties, on the catalytic activity. Also, stability of Au nanoparticles catalyst embedded within hierarchical support was investigated. The knowledgeable combination of this structural merits allows to design real working catalyst for environmental protection.

## 2. Method

### 2.1. Materials and synthesis

The hierarchically structured catalyst support composed of nanoparticles (HSNPs) was produced in a two-step process via shape-selective hydrothermal synthesis of the mixed  $\text{Ce}_{1-x}\text{Gd}_x(\text{HCOO})_3$  ( $x=0; 0.1$ ) formate star-shaped particles followed by oxidative thermolysis leading to production of mixed  $\text{Ce}_{1-x}\text{Gd}_x\text{O}_{2-x/2}$  ( $x=0; 0.1$ ) oxide particles. The synthetic steps were described in detail in our previous work.<sup>51</sup>

The mixed oxide  $\text{Ce}_{1-x}\text{Gd}_x\text{O}_{2-x/2}$  ( $x=0; 0.1$ ) nanocubes (cubes) were prepared by hydrothermal technique.<sup>52</sup> The mixture of  $\text{Ce}(\text{NO}_3)_3 \cdot 6\text{H}_2\text{O}$  and  $\text{Gd}(\text{NO}_3)_3 \cdot 6\text{H}_2\text{O}$ , with suitable Ce:Gd ratio, were dissolved in distilled water. Next, the obtained solution was mixed with NaOH followed by stirring for 60 min with magnetic stirrer. The final solution was transferred to stainless steel Teflon-lined autoclave equipped with a microwave heating and treated at 220°C for 3h under autogenous pressure. The size of ceria nanocubes may



be precisely controlled by variation of NaOH and ceria precursor amounts,<sup>53</sup> and parameters for synthesis of particles with desired size < 20 nm has been selected ( $C_{\text{NaOH}} = 10 \text{ M}$ , the molar ratio of Ce-source to base = 1/400).

The mixed oxide  $\text{Ce}_{1-x}\text{Gd}_x\text{O}_{2-x/2}$  ( $x=0; 0.1$ ) nanoparticles (NPs) were synthesized by microemulsion (water-in-oil) method.<sup>54</sup> The powder sample was dried and then preheated in static air at 550 °C for 3 h to get rid of surface nitrate residues.<sup>55</sup>

Deposition-precipitation method was used to embed gold nanoparticles on the catalyst support.<sup>56</sup> Briefly, the mixture (suspension) of  $\text{HAuCl}_4$ ,  $(\text{NH}_2)_2\text{CO}$ ,  $\text{H}_2\text{O}$  and the catalyst support having predefined morphology (HSNPs, cubes or NPs) were stirred and kept at 80 °C in a silicone oil bath for 1.5 h. The mass ratio of  $\text{HAuCl}_4$  to catalyst support was carefully adjusted for gold morphology manipulation as described in our previous work.<sup>53</sup> One modification was applied to this procedure, namely for determination of the total surface area of hierarchically structured support, the  $S_{\text{BET}}$  specific surface area (determined from  $\text{N}_2$  physisorption) was used, instead of calculated surface area determined from TEM/HRTEM data. Also, the molar content of the chloroauric acid to the total surface area of the support ( $M_{\text{Au}}/S_{\text{CeO}_2}$ ) was remodified into the surface coverage parameter (SC) that was calculated according to the following formula:

$$SC [nm^{-2}] = \frac{n \times N_A \times 10^{-18}}{S_{\text{BET}} \times m}$$

where SC [elementary entities/nm<sup>2</sup>] – surface coverage parameter,  $n$  [mol] – moles of  $\text{HAuCl}_4$ ,  $S_{\text{BET}}$  [m<sup>2</sup>/g] – surface area of the catalyst support,  $m$  [g] – mass of the catalyst support,  $N_A$  – Avogadro constant.

Then, the obtained product was washed with water and methanol followed by drying at 70 °C for 24h. The change of color of hierarchical catalysts from yellow to black was observed. Next, the solid product was heated at 300 °C in static air by 3 h.

## 2.2. Characterization methods

For structure analysis, powder X-ray diffractograms (PXRD) were recorded on PANalytical X'Pert Pro X-ray diffractometer. FullProf program was used for the display and data analysis.<sup>57</sup> To estimate size of ceria and gold crystallites, Scherrer formula was applied to four main PXRD maxima ((111), (200), (220), (311)) of  $\text{CeO}_2$  and (111) maximum of Au.

Materials were subjected to detailed microscopic studies to get insight into their architecture in terms of morphology of building units at various levels of hierarchical organization. Transmission Electron Microscope (TEM) images and high resolution (HRTEM) images in bright-field (BF) and dark-field (DF) modes were collected via the use of Philips CM-20 SuperTwin as well as double aberration corrected FEI Titan<sup>3</sup> Themis 60-300 microscopes at the accelerating voltage of 160 kV and 200 kV, respectively. The particle size distribution plots were generated from TEM images analysis by measuring the diameter (AuNPs, ceria NPs) or side (ceria cubes) of 150-300 individual particles from TEM-transparent regions of the

samples (surface and sub-surface). The collected data were subjected to Analysis of Variance (ANOVA) statistical test with the use of OriginPro. To get insight into textural characteristics, Selected Area Electron Diffraction (SAED) patterns were collected and analyzed in DigitalMicrograph. Scanning electron microscope images were collected on FEI Nova NanoSEM 230 equipped with ETD and TLD detectors.

Electron Tomography was performed to gain insight into 3D structure of materials.

EDS spectrometer (EDAX PegasusXM4) was used for elemental analysis. Global concentration measurements were performed on samples placed in carbon resin and pressed at 180 °C in 250 bar to obtain a flat surface. Signals from three randomly selected areas of ca. 150  $\mu\text{m} \times 100 \mu\text{m}$  were collected to assure satisfactory statistical averaging. Selected area (ca. 2  $\mu\text{m} \times 2 \mu\text{m}$ ) concentration measurements of the individual hierarchically structured particles not subjected to pressure were performed. Line SEM-EDX profiles were acquired for selected hierarchical materials.

For gold distribution imaging Scanning Transmission Electron Microscope- X-ray Energy Dispersion Spectroscopy (STEM-XEDS) analysis was performed using the high efficient Super-X EDS system, integrated by 4 window-less SDD detectors symmetrically arranged around the sample and the objective lens pole pieces at the FEI Titan<sup>3</sup> Themis 60-300 microscope operated at 200 kV. The acquisition of XEDS maps was conducted using an electron probe less than 0.5 nm, beam current of 200 pA, convergence angle of 19 mrad and 20 keV of range. Each chemical map was collected as a series of frames, where an area of about 512 x 512 pixels was scanned approximately 100 times, employing spatially drift-compensation tool, with a dwell time per pixel of 30  $\mu\text{s}$ , taking approximately 15 minutes per spectral image dataset. The elemental maps of cerium and gold were generated using the family of the Ce-L $\alpha$  and Au-L $\alpha$  lines.

Cerium oxidation state analysis was performed by Spectrum Imaging-Electron Energy Loss Spectroscopy (SI-EELS) technique employing an electron-beam source at 80 kV, the spectrometer was set to 0.25 eV/channel for dispersion, dual-EELS mode, using a convergence angle of 19 mrad and a collection semi-angle of 49 mrad, and operated with relative low beam current ( $\approx 30 \text{ pA}$ ). Under those experimental conditions a high energy resolution of 0.9 eV was obtained at the zero-loss peak (ZLP) and that ZLP signal allow us aligned all EELS spectra.

Attenuated total reflectance Fourier transform infrared (ATR-FTIR) spectra in the range of 500-4000  $\text{cm}^{-1}$  were collected using a Nicolet iS50 spectrometer equipped with a diamond ATR (attenuated total reflection) accessory. The ATR correction was used to process spectra analysis.

The  $\text{N}_2$  adsorption-desorption isotherms were collected at -196 °C on ASAP 2020 Micromeritics. The specific surface area ( $S_{\text{BET}}$ ) of the nanomaterials was assessed by applying the Brunauer, Emmet, and Teller equation to as collected isotherms. Prior to measurement the samples were outgassed under vacuum at 200 °C for 4h to remove gas contaminants and moisture adsorbed on the materials surface.

The  $\text{H}_2$  temperature programmed reduction tests ( $\text{H}_2$ -TPR) were performed on Autochem II 2920 (Micromeritics, USA) equipped with

TCD detector. 50 mg of sample was placed in quartz reactor and flushed with helium for 15 minutes followed by reduction measurements in the 30 cm<sup>3</sup>/min flow of 5% H<sub>2</sub>/Ar<sub>2</sub> in the temperature range of -50°C – 900°C and 10°C/min temperature increase.

Temperature-programmed reduction (CO-TPR) measurements employing CO as a reductant were conducted using the same experimental setup than that employed for CO oxidation test. The composition of evolved gases was measured by OmniStar QMS-200 Pfeiffer Vacuum mass spectrometer. The total flow rate of the feed gas (5% CO in He) was 30 mL/min. The temperature was increased from -50°C up to 900°C at 10°C/min under the reactive atmosphere. Prior to every run, the catalysts were pretreated in situ at 500°C under flow of 5% O<sub>2</sub>/He for 30 min, and then, the catalysts were cooled down to -50°C in the gas flow and purged under inert gas.

Temperature-programmed desorption (TPD-MS) in helium of bare CeO<sub>2</sub> hierarchically structured support (HSNPs) calcined in air at 300°C was conducted using the same experimental setup than that employed in CO-TPR with MS gas detection. The total flow rate of the He was 30 mL/min. The temperature was increased from room temperature up to 1000°C at 10°C/min.

Near-ambient pressure X-ray photoelectron spectroscopy (NAP-XPS) measurements were performed using the laboratory NAP-XPS system (SPECS Surface Nano Analysis GmbH, Germany), equipped with a monochromated Al K $\alpha$  X-ray source of high intensity, a multichannel electron energy analyzer (Specs Phoibos 150) coupled with a differentially pumped electrostatic pre-lens system. Before measurements, the powder Ru/CeO<sub>2</sub> sample was pressed into a fine 5x5 mm<sup>2</sup> tungsten mesh using a hydraulic press at a pressure of 10 kPa and spot-welded to the sample holder. The NAP-XPS spectra were acquired during calcination in 1 mbar of O<sub>2</sub> at 300°C, and in 1 mbar of CO at RT, 100 and 200°C. The samples, being exposed to gasses, were heated in the NAP cell through contact with the hot stage heated from the rear (vacuum) side by high-energy electron irradiation. The sample temperature was controlled using K-type (chromel-alumel) thermocouple spot-welded to the tungsten mesh. The heating process was manually controlled, keeping the temperature ramp at about 1–2 °C/s. All spectra were collected at the analyzer pass energy of 20 eV.

### 3.3. Catalytic tests

The catalytic activity of the samples was assessed in CO and propane oxidation. In CO oxidation test, 50 mg of the catalyst (fine, unfractionated powder) was placed in a quartz microreactor (U-type microreactor, H = 18 cm, D = 9 mm, D (active zone)  $\approx$  6 mm) and installed in a commercial apparatus (Autochem II 2920, Micromeritics). The feed gas consisted of 1% CO, 5% O<sub>2</sub> and 94% He with a total flow rate of 50 ml/min with 3°C/min temperature increase between -50°C - 300°C. The composition of gases was measured by OmniStar QMS-200 Pfeiffer Vacuum mass spectrometer that was calibrated by gas mixtures of known composition and purity (CO 4.7; O<sub>2</sub> 5.0; He 5.0).

In propane oxidation test, 50 mg of sample was placed in fixed-bed flow reactor (quartz U-shaped tube, 4 mm inner diameter)

followed by installation in programmable furnace. The stepwise propane conversion measurements were performed in the temperature range of 20°C - 540°C in the gas flow (mixture 2500 ppm C<sub>3</sub>H<sub>8</sub> in the air (10% O<sub>2</sub> in N<sub>2</sub>), 100 cm<sup>3</sup>/min) followed by gas chromatography analysis (Perkin-Elmer ARNEL Clarus 500 equipped with Elite Plot-Q chromatographic column and a flame ionization detector). Conversion at each temperature point was recorded when steady-state conversion was reached in terms of peak area differences less than 1% between consecutive readings. The propane conversion was calculated using the following formula:

$$K = \frac{A_{RT} - A_T}{A_{RT}} * 100\%$$

when K- conversion [%], A<sub>RT</sub> – area of the peak at room temperature, A<sub>T</sub> – area of the peak at selected temperature.

## 3. Results and discussion

### 3.1. Catalyst architecture

#### 3.1.1. Nano-gold decoration of hierarchical particles

Shape-selective solvothermal synthesis followed by thermolytic decomposition of cerium formate produces cerium oxide catalyst supports that are characterized by three distinct levels of hierarchical structure (Fig.1.A). First level is composed of nano-sized ceria particles. At the second hierarchy level, the nanoparticles are arranged into porous rod-shaped arms. Then, such mesocrystalline units are arranged into star-shaped particles on the third organizational tier. Such hierarchical organization creates a material with high specific surface area (S<sub>BET</sub> = 144 m<sup>2</sup>/g, cf. Section 3.1.3), which is relatively high for the family of nanosized cerium oxide materials and fairly large for mesoporous ceria.<sup>58–60</sup> The addition of 10% Gd<sup>3+</sup> leads to the formation of mixed oxide gadolinium-doped ceria (GDC-10%) hierarchical support with preserved star-shaped morphology and increased specific surface area (S<sub>BET</sub> = 158 m<sup>2</sup>/g). Detailed description of physicochemical properties of as synthesized active catalyst support along with its CO oxidation efficiency and soot combustion performance may be found in our previous work.<sup>23</sup>

The deposition-precipitation method proved to be effective in applying gold to a hierarchical Ce<sub>1-x</sub>Gd<sub>x</sub>O<sub>2-x/2</sub> (x=0; 0.1) catalyst support. Microscopic images in Fig.1.B show the presence of gold in the material that was also confirmed by EDAX mapping. Differences in intensity contrast may suggest the presence of gold agglomerates inside the hierarchical support, as areas with similar contrast intensity in the HAADF image have a variety of signal intensities in the corresponding Au EDAX map. This suggests that gold particles are distributed between the interior of the hierarchical material and the exterior surface of the star-shaped support. SEM-EDS mapping of the entire particle at lower magnifications indicates the lack of gold segregation throughout the star-shaped particle on a global scale (Fig.1.C).

Due to the two-dimensional nature of transmission imaging, it is not possible to explicitly distinguish whether the gold particles are embedded inside the hierarchical support or on the outer surface of

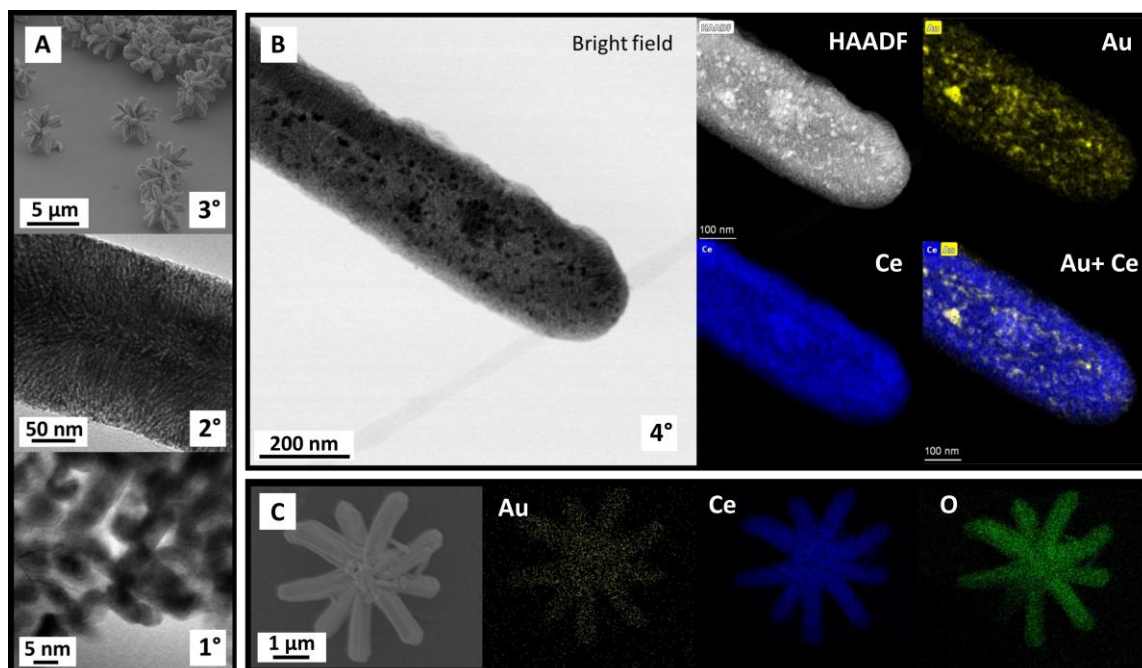


Fig 1. Hierarchical architecture of Au/CeO<sub>2</sub> catalyst: A) TEM images showing three levels of hierarchical organization of CeO<sub>2</sub> support; B) TEM Bright-Filed image of selected arm of Au/CeO<sub>2</sub> catalyst with corresponding HAADF image and XEDS maps of Au and Ce elemental distribution; C) SEM image of star-shaped Au/CeO<sub>2</sub> catalyst with corresponding SEM-EDS elemental maps of Au, Ce, and O.

the arm, or it is a combination of both possibilities. To get this knowledge, Electron Tomography along with volume reconstruction of the selected arm of Au<sub>5</sub>/CeO<sub>2</sub> star-shaped particle was performed (see animation in ESI). Longitudinal and transverse slices extracted from the reconstructed volume at various depths, visible on Fig 2.A and B respectively, show the location of gold particles along the porous channels proving its presence deep inside hierarchical support.

The nanosized nature of gold is confirmed by high-resolution STEM imaging (Fig. 2.C and D) showing high population of Au particles (from 2 to 6 nm) in the near-surface region of the arm. Freeze-frames from ET (Fig. 2.E-F) paused at different angles show that the high intensity contrast zones, indicating the position of gold, change their shape with the change of recording angle. This is shown in a series of images (from 70° to 122°, inlets in Fig.2.E-F), where a single high-intensity spot is broken down into three smaller ones with an elongated shape as the angle changes progress. This again confirms that AuNPs are deposited along the pores inside hierarchical support.

### 3.1.2. Engineering 4th hierarchy level

The effect of the decoration of cerium oxide by AuNPs in deposition-precipitation procedure has been proven to be responsive to the ratio of the total number of chloroauric acid molecules to the total surface area of the ceria support ( $M_{Au}/S_{CeO_2}$ ).<sup>53</sup> Herein, this ratio is referred to as the surface coverage parameter (SC), which denotes the number of molecules to the specific surface area of the support. Altering SC parameter value in deposition of gold onto the hierarchical ceria-based supports turned out to lead to the formation

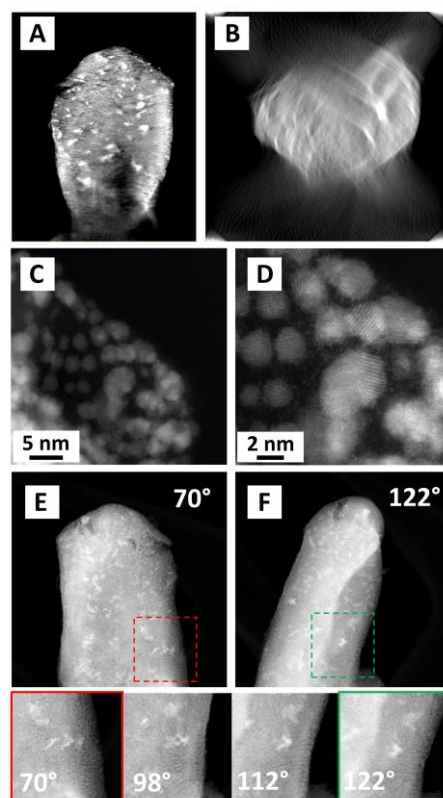


Fig. 2 Confinement of AuNPs within CeO<sub>2</sub> hierarchically structured catalyst. A) Longitudinal slice of ET volume reconstruction; B) Transverse slice of ET volume reconstruction; C-D) HR-STEM images of AuNPs in near-surface region; D); E-F) HAADF images collected at various angles (selected images presented on the bottom).

of systems with diverse architectures, which is shown in Fig. 3. The nomenclature convention  $Au_x$  ( $x = 0.5; 2; 5; 8$ ) has been adopted for samples containing different gold loadings where  $x$  denotes the value of the surface coverage parameter.

As shown in Fig. 3.A, sample with low gold loading ( $SC = 0.5$ ) has extensive regions with increased contrast that are larger than the contrast visible on a gold-free support (Fig. 1.A, middle panel showing 2° level of hierarchical structure). This indirectly indicates the presence of gold inside the material, but its morphological form has not been identified due to lack of electron transparency in the thicker areas of the sample. No AuNPs were observed both on the surface of the arms as well as within pores of the material. However, the gold presence inside the support was confirmed by SEM-EDS selected-region elemental analysis that indicates Au-2.7 wt% in  $CeO_2$  system and Au-2.9 wt% in GDC-10% one (See Fig. S1. in ESI). Increasing SC value to 2 leads to formation of AuNPs inside the material (Fig. 3.B). Their presence is visible as Moiré patterns on round-shaped higher contrast regions indicating that nano-sized gold particles are embedded within the hierarchically structured support. However, for this SC value no Au particles were observed on the support exterior surface. Increasing gold loading ( $SC = 5$ ) induces additional formation of gold nanoparticles on the exterior surface of the hierarchical catalyst support (Fig. 3.C). Well-dispersed gold nanoparticles of uniform size are visible on the arms of star-shaped particles. Large value of surface coverage parameter ( $SC = 8$ ) causes gold overloading because metal agglomerates are observed on the particles exterior

surface (Fig. 3.D). This sample was excluded from further analysis due to presence of significant amount of AuNPs in gold agglomerates and thus reduced gold-support contact for large amount of AuNPs.

The global scale differences in the architecture of variously gold-loaded GDC-10% HSNPs are shown in Fig. 4.A and 4.B. For  $Au_2/GDC-10\%$  HSNPs no gold particles are observed on the outer surface of the arms (Fig. 4.A), oppositely to  $Au_5/GDC-10\%$  HSNPs (Fig. 4.B) for which plenty of gold is visible. At the same time, linear EDAX scans indicate the presence of gold in both systems, which implicates its presence inside the hierarchical structure even in the lower gold-loaded sample. Also, this suggests an increased sorption properties of ceria hierarchically structured supports and facilitated growth of gold particles within confined spaces of material pores in the first instance.

PXRD patterns confirm phase purity of all  $Au/Ce_{1-x}Gd_xO_{2-x/2}$  ( $x = 0; 0.1$ ) HSNPs systems (Fig. 4.C.) Location of 2 $\theta$  diffraction maxima and their relative intensities correspond to  $CeO_2$  fluorite structure ((111) = 28.5491°; (200) = 33.0766°; (220) = 47.4886°; (311) = 56.3265°, ref. 00-004-0593). The addition of  $Gd^{3+}$  dopant boosts peak broadening, which indicates a decrease in size of oxide crystals.<sup>61</sup> Only one, the most intense  $Au(111) = 38.1^\circ$ , diffraction maximum was observed in all the samples due to the nanosized nature of gold particles. For  $Au_{0.5}/HSNPs$ , slight elevation of the peak above the background corresponding to  $Au(111)$  maximum was observed, indicating peak broadening to a large extent, and thus formation of very small gold

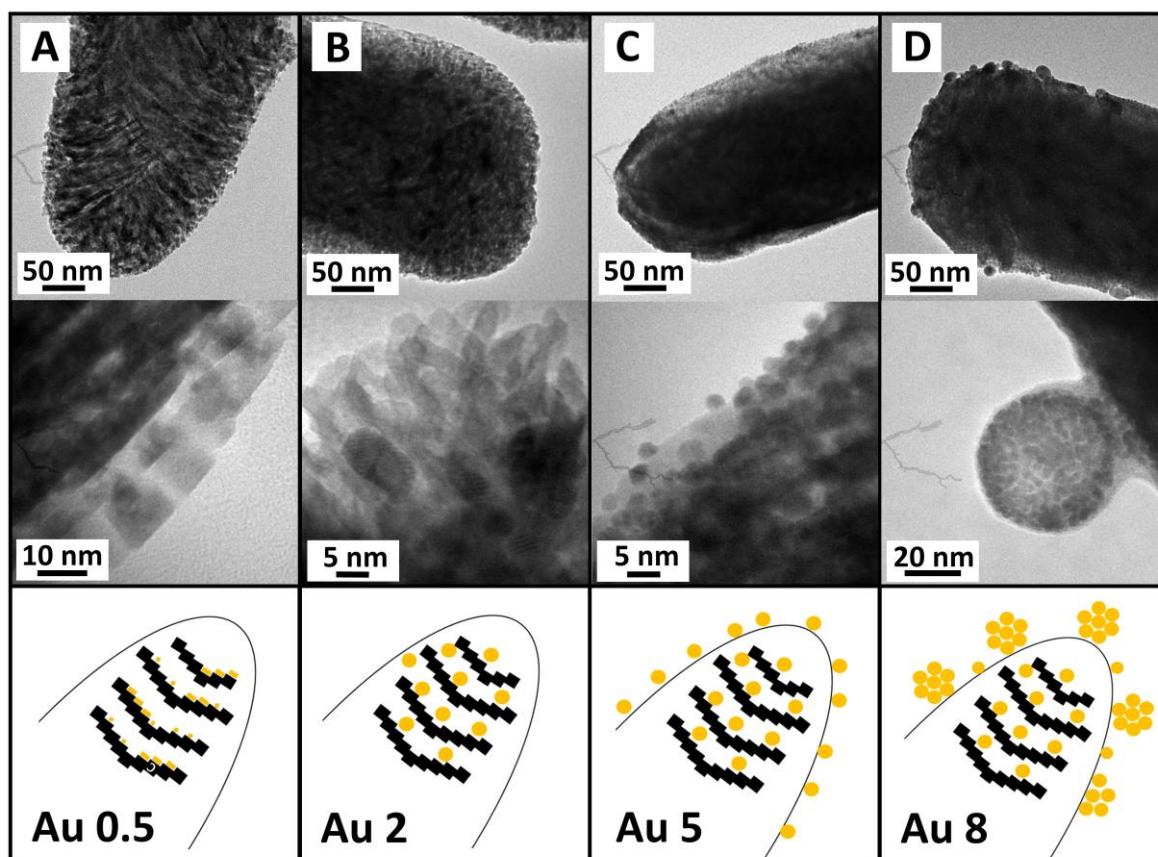


Fig. 3 TEM images of  $Au/CeO_2$  catalyst showing the influence of the surface coverage parameter (SC) value on 4<sup>th</sup> level architecture form: A)  $SC=0.5$ ; B)  $SC=2$ ; C)  $SC=5$ ; D)  $SC=8$ . (See description in text).

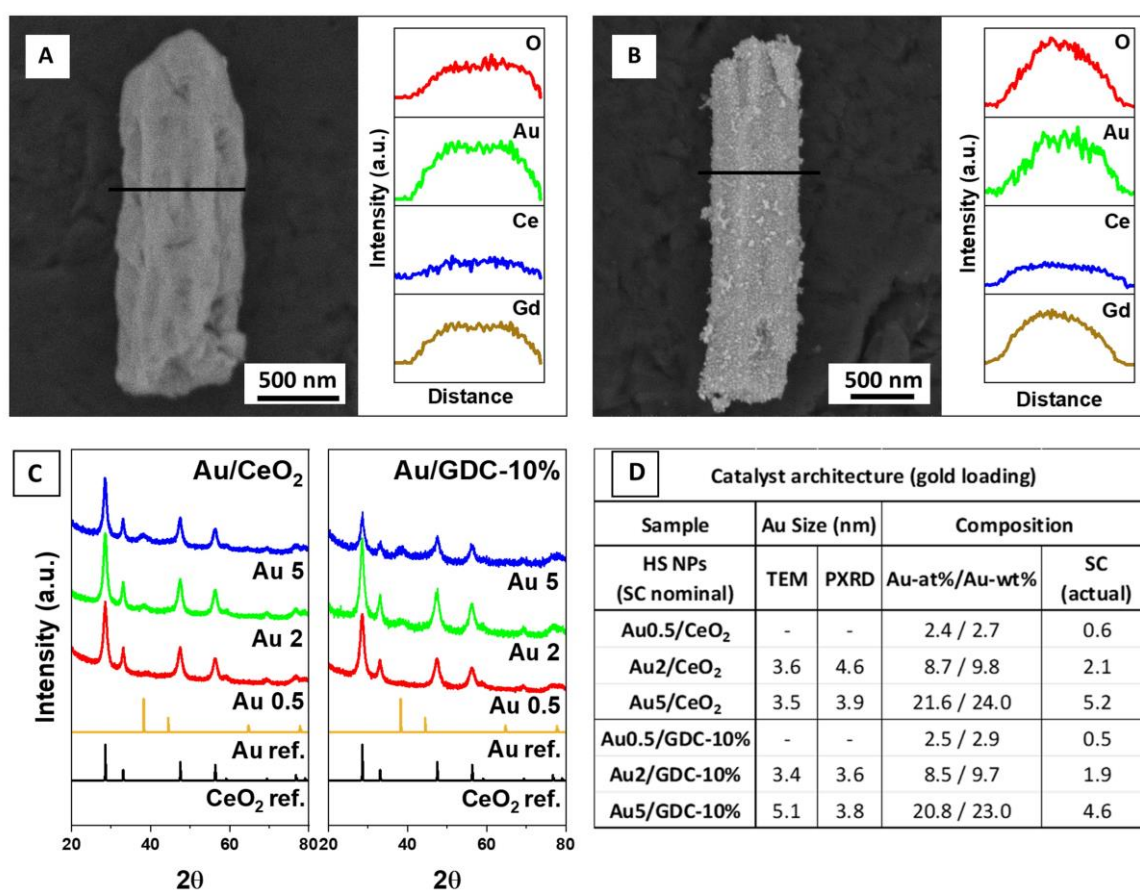


Fig. 4 Architecture of catalyst at 4<sup>th</sup> level of hierarchical organization. A) SEM-EDX line profiles of Au2/GDC-10% HSNPs arm; B) SEM-EDX line profiles of Au5/GDC-10% HSNPs arm; C) PXRD of Au/Ce<sub>1-x</sub>Gd<sub>x</sub>O<sub>2-x/2</sub> (x=0; 0.1) HSNPs; D) Size and composition summary. Arithmetic mean of 150-300 AuNPs (TEM) and size value determined by Scherrer formula (PXRD). Atomic percent of gold (Au at%) in Au/GDC-10% (from SEM-EDX measurement - %at of Au, Ce and Gd) calculated as  $(\text{Au} \times 100)/(\text{Au} + \text{Ce} + \text{Gd})$ . Weight percent of gold (Au-wt%) in GDC-10% (from SEM-EDX measurement - %at of Au, Ce and Gd) calculated as  $(\text{Au} \times M_{\text{Au}} \times 100)/(\text{Au} \times M_{\text{Au}} + \text{Ce}_{1-x}\text{Gd}_x\text{O}_{2-x/2} \times M_{\text{Ce}_{1-x}\text{Gd}_x\text{O}_{2-x/2}})$ , where x=0 or 1). Due to inflated at% O in EDX measurements, the amount of oxygen was calculated from the stoichiometric formula. SC- surface coverage parameter value.

species. The maximum is clearly visible for Au2 and Au5 systems. This allowed to use Scherrer formula to estimate the size of gold particles and the results confirm their nano-sized nature (Fig. 4.D). Comparison of average AuNPs size determined from PXRD and microscopic data indicates convergence of results showing size falling into 3- 5 nm range in all tested systems.

For better comparison of AuNPs size determined from PXRD and TEM, the length number arithmetic mean (obtained from TEM data) has been recalculated into the volume-weighted mean (Fig. S2.A in ESI).<sup>61</sup> Comparison of the results shows similarity in Au2/CeO<sub>2</sub> HSNPs sample. For the remaining samples, a slightly higher value of volume-weighted mean over the mean size obtained from PXRD is observed, which may indicate an underestimation of the number of small AuNPs present inside the material when calculating size from TEM data. Example of such sub-nanometer AuNP is presented in Fig. S2.B and C in ESI. In the literature, particles below 5 nm show exceptional activity in room temperature CO oxidation while larger-sized AuNPs exhibit activity loss.<sup>5</sup> This proves that the deposition-precipitation

method allows to decorate hierarchically structured catalyst support by finely dispersed gold nanoparticles having optimal size for potential high catalytic activity.

Composition probed by EDAX indicates a similar gold loading for Au/CeO<sub>2</sub> and Au/GDC-10% catalysts that ranges from 2,7-2.9 Au-wt% for Au0.5 systems up to 24.0-23.0 Au-wt% for Au5 ones (Fig. 4D). This indicates that due to extensive surface area the hierarchical particles possess high capacity to assimilate large amount of active metal. Especially, the value of Au-9.8 wt% for Au2/CeO<sub>2</sub> implicate again the high sorption potential of hierarchically structured particles, considering that all gold has been absorbed inside the particles. For model catalyst composed of Au2/CeO<sub>2</sub> nanocubes (gold loading value  $M_{\text{Au}}/S_{\text{CeO}_2}=2$ ) no distinct AuNPs are observed on ceria,<sup>53</sup> in contrast with hierarchical ceria support with roughly similar gold loading (SC=2). This confirms that confined space in hierarchical support allow to form gold particles for relatively low SC value. Also, reduction of Au2/GDC-10% in H<sub>2</sub> flow did not yield AuNPs on the exterior surface of support (Fig. S3 in ESI), which diverges from our

previous result on powdered nanocube catalyst. This may suggest that no gold layer is formed on the exterior surface of hierarchical support when small SC value is used in gold deposition. Alternatively, H<sub>2</sub> may induce relocation of sub-nano gold clusters into the interior of the material.

The empirical values of surface coverage parameter determined from EDAX shows the convergence with the nominal ones (Fig. 4.D), which confirms the effectiveness of the nanoparticle's deposition approach taken and the possibility of intentional design of materials with varied architectures.

N<sub>2</sub> physisorption study allowed to examine pore architecture of hierarchical materials. As shown in Fig. 5.A, isotherms of CeO<sub>2</sub> and GDC-10% hierarchical supports have the shape between type IV and type II, which indicates presence of meso- and macropores.<sup>62</sup> As has been studied in our previous work, the presence of large cavities connected by thin slits may be inferred from hysteresis loop features and TEM images inspection.<sup>51</sup> However, the addition of Gd<sup>3+</sup> dopant into CeO<sub>2</sub> HSNPs slightly modifies pore characteristics by lowering the participation of pores with larger sizes in the pore distribution (Fig. 5.B). The reduced proportion of pores larger than 5 nm is visible for GDC-10% HSNPs and the pore size maximum shifts to lower values.

The phantom maximum around 4 nm may be ascribed to tensile strength effect that is a technique artifact<sup>63</sup>. TEM images inspection indicates the pore size in range of 1.3 nm - 4.5 nm for CeO<sub>2</sub> HSNPs and 0.7 nm - 2.3 nm for GDC-10% HSNP (see left panel in Fig. 5C and 5D).

The N<sub>2</sub> adsorption-desorption isotherms of gold-decorated materials preserve similar shape as undecorated supports (Fig. 5.A), which proves stability of architecture after gold deposition process. Despite a noticeable reduction of S<sub>BET</sub> by 19% for Au5/CeO<sub>2</sub> HSNPs and 23% for Au5/GDC-10% HSNPs, the Au-decorated catalyst supports preserve high specific surface area, 117 m<sup>2</sup>/g, and 122 m<sup>2</sup>/g, respectively.

Incorporation of Gd<sup>3+</sup> into ceria crystallites has been shown to modulate architecture of the hierarchical support that, in turn, influences 4<sup>th</sup> level of the hierarchical structure. As shown in Fig. 5.C, AuNPs are deposited along the channels inside the hierarchical support and their average size is 3.5 nm, as visible on attached size distribution plot. A comparison of the sizes of AuNPs inside the CeO<sub>2</sub> HSNPs system (Fig. 5.C) and on the outer surface of the arms (see Fig. 3.C) shows similarity of sizes that indicates a uniform spread of AuNPs throughout the Au5/CeO<sub>2</sub> hierarchical support. This effect is

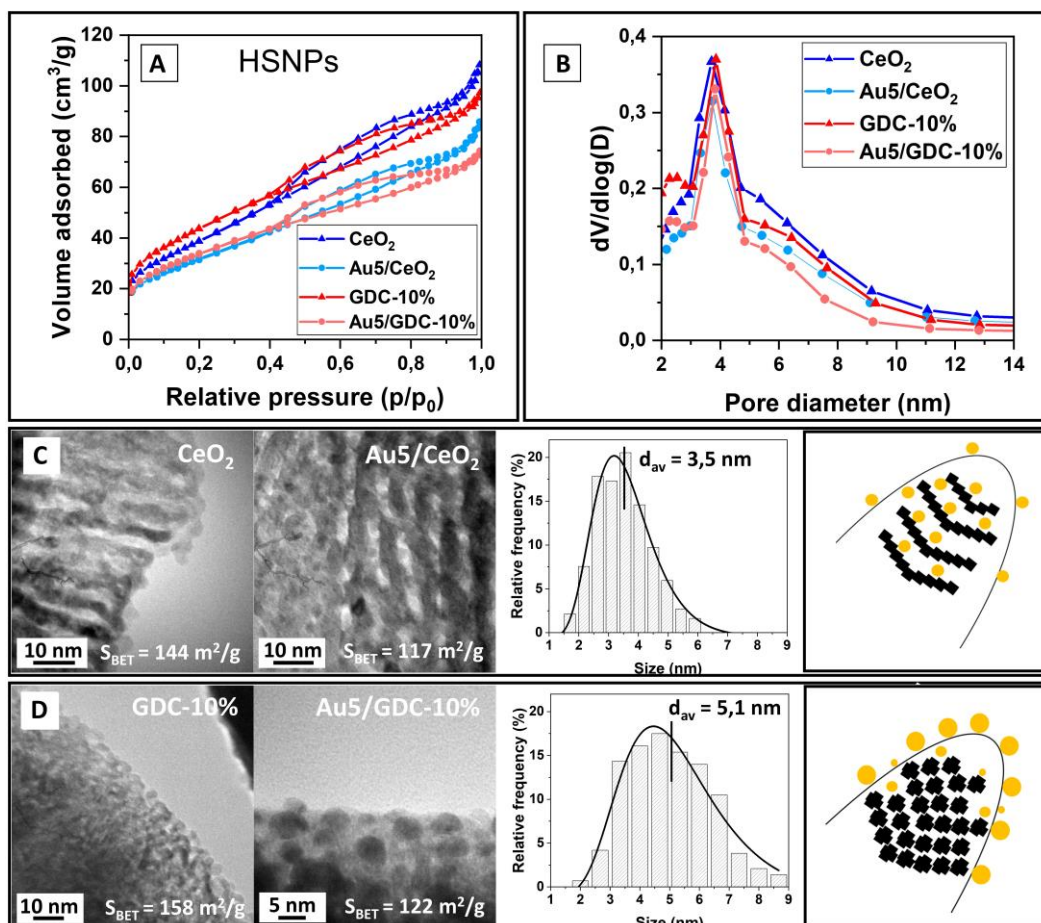


Fig. 5 A) Adsorption-desorption isotherms and B) pore size distribution of undecorated/gold-decorated CeO<sub>2</sub> HSNPs and GDC-10% HSNPs systems; C) TEM images of CeO<sub>2</sub> HSNPs (left) and Au5/CeO<sub>2</sub> HSNPs (right) along with AuNPs size distribution and schematic representation of catalyst architecture. D) TEM images of GDC-10% HSNPs (left) and Au5/GDC-10% HSNPs (right) along with AuNPs size distribution and schematic representation of catalyst architecture. Size distribution plots created from Au particles detected in surface and sub-surface regions of hierarchical materials (see representative TEM images in Fig. S4.A and B in ESI).

visible on TEM images presented in Fig. S4.A in ESI. On the contrary, in systems containing  $Gd^{3+}$  ions, gold particles are mainly observed on the outer surface of the material (Fig. S4.B in ESI) and with an average size of 5.1 nm, as shown in Fig 5.D. Their size distribution is also more broaden, that indicates growth of larger particles on the exterior surface of the hierarchical support.

Thorough analysis of HRTEM images shows the exposition of (111)/(100) crystal planes on the exterior surface of  $CeO_2$  HSNPs (Fig. S5 in ESI) and the dominance in exposition of (100) surface planes for GDC-10% HSNPs (Fig. S6 in ESI). The exterior surface of  $CeO_2$  HSNPs support is more faceted as opposed to exposition of smoother surfaces on GDC-10% support. This translates into the difference in the size and the number of particles on the outer surface, because in the first case they are anchored between the crystallites, and in the second case, their growth on smooth (100) surfaces is not spatially limited

### 3.1.3. Architecture of reference materials

To investigate of how the architecture of hierarchical systems affects catalytic performance, in particular the arrangement of support nanoparticles into higher order structure, the activity of star-shaped hierarchically structured support (HSNPs) was compared with two reference materials, ceria nanocubes synthesized by hydrothermal method (cubes) and microemulsion-derived ceria nanoparticles (NPs). Fig. 6.A shows the size distribution of ceria nanoparticles as well as the morphology of all three types of catalytic supports studied. The average size of  $CeO_2$  NPs ( $6.8 \pm 1.6$  nm) decreases when doped by  $Gd^{3+}$  forming GDC-10% NPs ( $5.1 \pm 1.6$  nm). A comparison of these results with the size of nanoparticles in hierarchical systems indicates an almost identical particle size distribution, both in  $CeO_2$  HSNPs ( $5.1 \pm 1.4$  nm) and GDC-10% HSNPs ( $3.2 \pm 1.1$  nm). For  $CeO_2$  NPs, the exposition of all main ceria planes, (111), (110), (100), has been detected (Fig. 6.D.b), and planes are randomly oriented in all directions. On the contrary, the preferential orientation of crystallites within hierarchical materials has been observed in SAED pattern (Fig. 6.D.g), which show distinct maxima instead of fully developed diffraction circles. Thorough analysis of HRTEM images indicates that (100) planes are exposed dominantly inside the hierarchical support along the pores (Fig. 6.D.h).

The second reference material, ceria nanocubes, is treated in the literature as a model system due to the exposure of almost exclusively (100) crystallographic planes (Fig. 6.D.e). Interestingly, no size change was observed after doping since the average size of the particles is  $17.8 \pm 4.6$  nm for  $CeO_2$  cubes and  $18.0 \pm 4.8$  nm for GDC-10% cubes (Fig. 6.A).

PXRD confirms phase purity of all samples and shows diffraction line broadening for NPs and HSNPs systems (Fig.6.C). The average size of nanoparticles obtained from PXRD stays in line with size values determined from TEM (Fig. 6.B). For a better comparison of crystal size determined from both methods, the length number arithmetic mean (obtained from TEM data) has been recalculated into volume-weighted mean size (Fig. A7.A in ESI).<sup>61</sup> Comparison of

the mean size values shows similarity in NPs sample. However, discrepancy is observed for cubes and HSNPs. For cubes, larger values of volume-weighted mean as compared to size values obtained from PXRD indicates the presence of some proportion of small ceria crystallites with non-cubic morphology (Fig. S7.B and C in ESI). Per contra, reversed effect observed for HSNPs may suggest the formation of slightly larger crystallites in some regions of hierarchical catalyst sample.

Zhou and Huebner have shown that the concentration of oxygen vacancies was two orders of magnitude larger for 4 nm  $CeO_2$  crystallites as compared to 60 nm crystals, and the rapid growth of this concentration was observed for particles with sizes below 20 nm.<sup>64</sup> Oxygen vacancy concentration increase to some optimum level, in turn, is associated with catalytic activity enhancement for various reactions.<sup>65–67</sup> All materials investigated in this study meet the criterion of nanoparticles size below 20 nm indicated by the literature, hence comparing reactivity of systems having similar size of building units but different architecture (Fig.6.D) will provide insight into the role it plays in catalytic reactivity.

The composition of all  $Gd^{3+}$ -doped materials is close to the nominal 10% dopant value (Fig. 6.B). Also, the specific surface area of  $CeO_2$  HSNPs is almost twice as large ( $S_{BET}=144$  m<sup>2</sup>/g) as  $CeO_2$  NPs ( $S_{BET}=75$  m<sup>2</sup>/g) and five times larger than  $CeO_2$  cubes ( $S_{BET}=29$  m<sup>2</sup>/g). The surface area drop for powdered samples can be attributed to the lack of organization of ceria nanoparticles into higher-order architecture and the tendency to agglomeration. The introduction of  $Gd^{3+}$  into ceria results in increase of the surface area for all systems. The significant increase observed for GDC-10% HSNPs (Fig. 6.B) indicates preservation of hierarchical architecture.

The applied gold deposition procedure is effective only to cubes and HSNPs. For these two systems, AuNPs are visible on the surface of the materials when SC = 5 (Fig. 6.D.f and 6.D.i). Large gold precipitates of 5-30 nm are observed next to ceria particles in Au/ $CeO_2$  NPs and Au/GDC-10% NPs (Fig. 6.D.c), which implies that the method of gold deposition used is ineffective when ceria NPs synthesized by microemulsion method is used as support.

PXRD confirm the presence of gold in all samples (Fig. 7.A). Line broadening of Au(111) =  $38.1^\circ$  maximum is observed for HSNPs and cube catalysts. Comparison of the particle mean size estimated by TEM and PXRD (Fig. 7.B) indicates convergence of results ( $d_{av} \leq 5$  nm for HSNPs and cubes). Also, for these systems, the empirical value of surface coverage (calculation based on SEM-EDX composition results) is close to the nominal value of 5. On the contrary, PXRD of the gold-decorated microemulsion-derived NPs show a distinct narrow maximum, indicating formation of large AuNPs ( $d_{av} = 24.4$  nm for Au5/ $CeO_2$  HSNPs and  $d_{av} = 11.2$  for Au5/GDC-10% HSNPs.) Also, the empirical surface coverage, differs significantly from the nominal value of 5 (Fig. 7.B). This indicates that precise control of gold deposition on irregularly shaped ceria nanoparticles is more difficult than on shaped-engineered nanoparticles or hierarchical supports.

To test the interaction effect of the support morphology and the presence of dopant in ceria on the AuNPs size, the gold nanoparticles size data (obtained from TEM) were submitted to two-way ANOVA

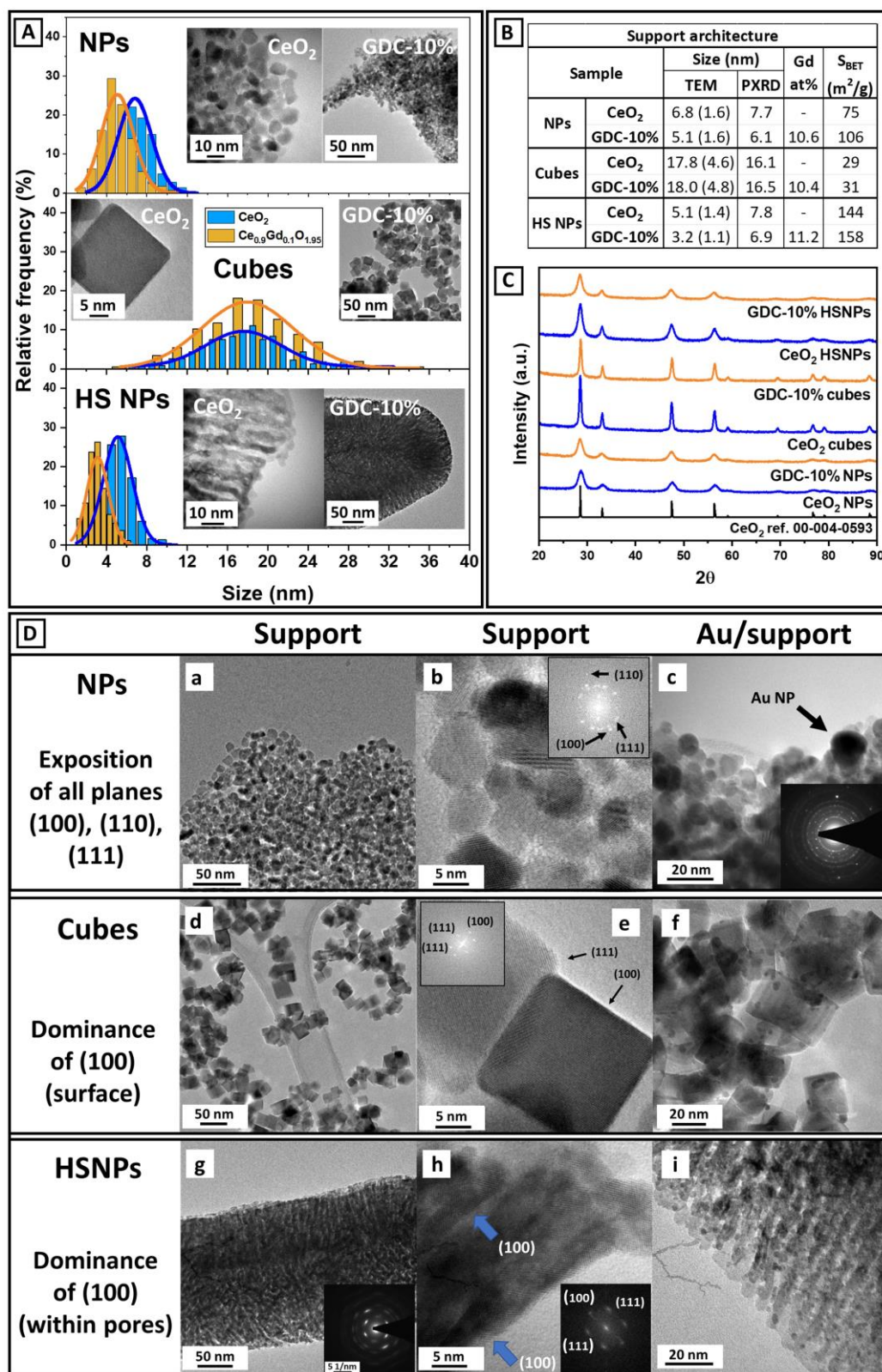


Fig. 6. Architecture of Au/CeO<sub>2</sub> and Au/GDC-10% catalysts differing by morphology: nanoparticles (NPs), nanocubes (cubes), hierarchically structured nanoparticles (HSNPs); A) Size distribution of support crystallites (determined from TEM as length number arithmetic mean); B) Summary of size (standard deviation in brackets), composition and the specific surface area; C) XRD patterns of supports; D) TEM (a, c, d, f, g, i), HRTEM (b, e, h), digital diffraction pattern (inset in b, e, h), SAED (inset in c, g). Analysis shows the exposition of (100), (110) and (111) crystal planes in NPs (a-c), dominance of (100) planes on cubes (d-f) and dominant exposition of (100) planes inside HSNPs support (g-i)



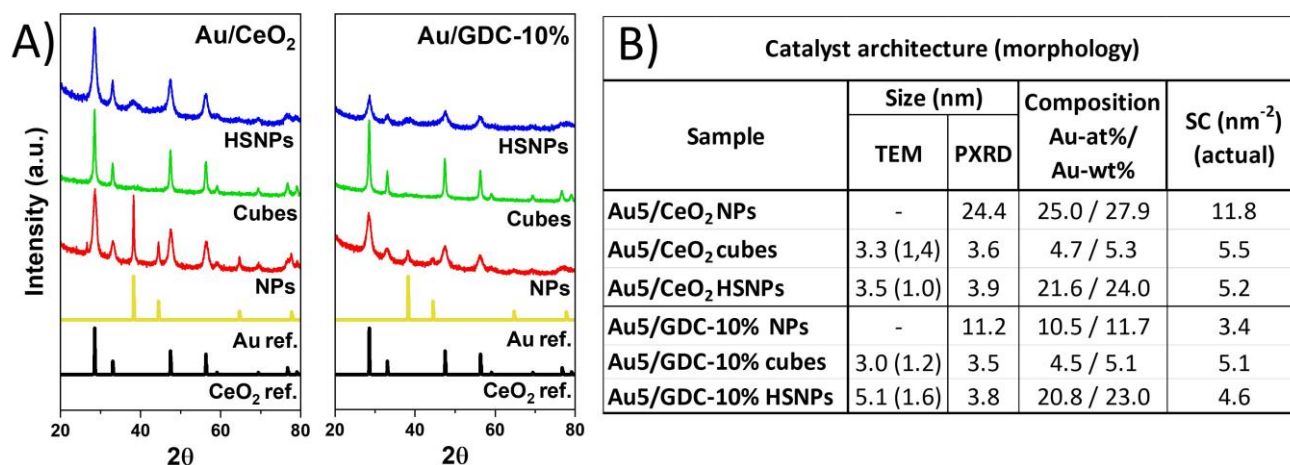


Fig. 7 Architecture of catalysts. A) PXRD of samples differing by morphology; B) size (standard deviation in parentheses) and composition summary; mean AuNPs size calculated as length number arithmetic mean (TEM) and determined from Scherrer formula (PXRD); concentration of gold (Au at%) in Gd-doped ceria catalysts (from SEM-EDX measurement - %at of Au, Ce and Gd) calculated as  $(\text{Au} \times 100) / (\text{Au} + \text{Ce} + \text{Gd})$ . Weight percent of gold (Au-wt%) in Gd-doped ceria catalysts (from SEM-EDX measurement - %at of Au, Ce and Gd) calculated as  $(\text{Au} \times M_{\text{Au}} \times 100) / (\text{Au} \times M_{\text{Au}} + \text{Ce}_{1-x}\text{Gd}_x\text{O}_{2-x/2} \times M_{\text{Ce}_{1-x}\text{Gd}_x\text{O}_{2-x/2}})$ , where  $x=0$  or  $1$ ). Due to inflated at% O in EDX measurements, the amount of oxygen was calculated from the stoichiometric formula. SC – surface coverage parameter.

with two levels of the presence of dopant (undoped Au5/CeO<sub>2</sub> and doped Au5/GDC-10%) and two levels of morphology (cubes and the HSNPs). Because of the lognormal nature of the AuNPs size distribution all data were logarithmically transformed and met normality requirements (see details in Fig. S8 in ESI). Interaction between the dopant presence and morphology was significant,  $F(1,1237) = 163.76$ ,  $p < .001$ . Tukey HSD post-hoc analysis has shown that there is no significant difference between size of AuNPs deposited on Au5/CeO<sub>2</sub> cubes and Au5/GDC-10% cubes ( $p > .001$ ). Oppositely, there is size difference between Au5/CeO<sub>2</sub> HSNPs and Au5/GDC-10% HSNPs ( $p < 0.001$ ). Also, while there is no difference in the AuNPs size between undoped cubes and the undoped hierarchically structured particles ( $p > .001$ ), there is a statistically significant difference in the AuNPs size between Au5/GDC-10% cubes and Au5/GDC-10% HSNPs ( $p < 0.001$ ). Hence, the architecture differences of the GDC-10% hierarchical support induced by doping influences the size of gold nanoparticles when deposited on the hierarchical catalyst support.

### 3.2. Chemical characterization

#### 3.2.1. H<sub>2</sub>-TPR

H<sub>2</sub>-TPR tests were conducted for gold-decorated ceria-based catalysts with various support morphologies (NPs, cubes, HSNPs) and various degrees of gold content (SC = 0.5, 2 or 5). Comparison of reducibility of highly gold-loaded samples differing by morphology is shown in Fig. 8.A. An increase of peak area ascribed to the surface reduction is observed for the Au5/CeO<sub>2</sub> HSNPs system, which suggest that ordering of the support nanoparticles into a hierarchical structure improves the redox properties of catalyst. Whereas Au5/CeO<sub>2</sub> cubes and Au5\*/CeO<sub>2</sub> NPs show similar surface-to-bulk reduction ratio, 34%/66% and 40%/60% respectively, this trend is reversed for Au5/CeO<sub>2</sub> HSNPs showing 64%/34% surface-to-bulk

reducibility. This is due to the maximization of the Au-support interfacial contact and thus the increased exposure of the interfacial active sites, critical factor in catalytic activity enhancement.<sup>12,68–71</sup>

Also, the number of reduction maxima in Au5/CeO<sub>2</sub> HSNPs catalyst (three surface peaks) is higher than in Au5/CeO<sub>2</sub> cubes (two surface peaks) and simultaneously lower than in Au5\*/CeO<sub>2</sub> NPs (four surface peaks). In Au5\*/CeO<sub>2</sub> NPs system the number of various kinds of reducing sites is maximized due to contact with all types of crystallographic planes, as opposed to Au5/CeO<sub>2</sub> cubes, for which (100) planes are exposed in dominance. In the literature, the occurrence of several H<sub>2</sub>-TPR reduction peaks for gold-decorated ceria(100) surface is related to morphology of gold nanoclusters, and higher number of peaks has been observed for multilayer gold islands.<sup>72</sup>

Fig. 8.B shows H<sub>2</sub>-TPR of hierarchically structured ceria catalysts with low gold content (SC = 0.5). The surface reduction is increased when compared to Au5/cubes, however, there is no reduction maximum at -5°C which is observed in the high gold-containing hierarchical samples. Also, the area of maximum near 40°C is substantially reduced, so the surface reduction of Au0.5/CeO<sub>2</sub> HSNPs and Au0.5/GDC-10% HSNPs is decreased by 7%-13% as compared to their high gold-loaded (SC = 5) counterparts (Table 1). This may indicate the presence of not fully grown Au particles inside the pores. Nevertheless, the increased H<sub>2</sub>-TPR surface reducibility, when compared to Au5/CeO<sub>2</sub> cubes, may be the synergistic effect of high surface area of HSNPs and gold confinement (in the form of either clusters or islands) in the pores of hierarchically structured supports that increases metal-support contact. This interpretation is also supported by the fact that Au5/CeO<sub>2</sub> cubes system contains two-times higher amount of gold than Au0.5/CeO<sub>2</sub> HSNPs one, 5.3 Au-wt% and 2.7 Au-wt%, respectively.

On the contrary, the clearly marked presence of the low-temperature reduction maxima at -5°C and ~40°C in Au<sub>2</sub> and Au<sub>5</sub>

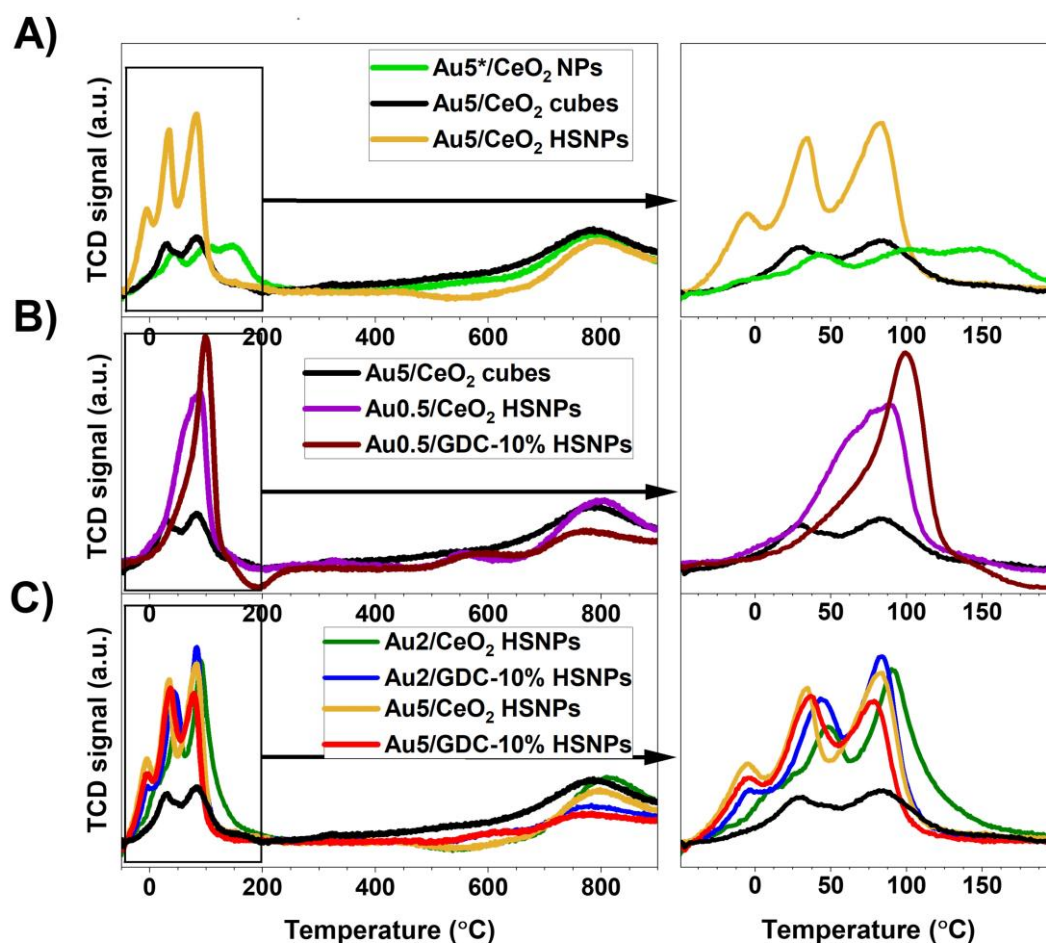


Fig. 8. H<sub>2</sub>-TPR of catalysts differing by: A) support morphology, B) presence of dopant in low gold-loaded HSNPs catalyst in which no AuNPs morphology was detected, C) gold loading and dopant presence in HSNPs catalyst for which fully developed AuNPs were detected. For comparison purposes curve for Au<sub>5</sub>/CeO<sub>2</sub> cubes (black) has been shown in each panel. Au<sub>5</sub>\* refers to gold-decorated CeO<sub>2</sub> NPs sample that was derived from additional synthesis for H<sub>2</sub>-TPR measurement; nominal value of surface coverage parameter (5) deviates from empirical one (SC = 14; Au-at% = 29.4, S<sub>BET</sub> = 75 m<sup>2</sup>/g, A<sub>u, size(TEM)</sub> = 3 nm - 60 nm) due to difficulty to control deposition of gold on powdered nanoceria (see Section 3.1.3).

Table 1 H<sub>2</sub> consumption calculated from H<sub>2</sub>-TPR data.

Sample	Catalyst (Au/Ce <sub>1-x</sub> Gd <sub>x</sub> O <sub>y</sub> )			Support (Ce <sub>1-x</sub> Gd <sub>x</sub> O <sub>y</sub> )	Support active phase (CeO <sub>2</sub> )		
	Total (mmol/g)	Surface* (% total)	Bulk** (% total)	Total (mmol/g)	Total (mmol/g)	Surface* (mmol/g)	Bulk** (mmol/g)
Au <sub>5</sub> / CeO <sub>2</sub> cubes	1.02	34	66	1.08	1.08	0.36	0.72
Au <sub>5</sub> * / CeO <sub>2</sub> NPs	0.91	40	60	1.18	1.18	0.47	0.71
Au <sub>0.5</sub> / CeO <sub>2</sub> HSNPs	1.21	51	49	1.24	1.24	0.64	0.61
Au <sub>0.5</sub> / GDC-10% HSNPs	0.98	58	42	1.01	1.11	0.65	0.46
Au <sub>2</sub> / CeO <sub>2</sub> HDNPs	1.13	60	40	1.25	1.25	0.75	0.51
Au <sub>2</sub> / GDC-10% HSNPs	1.01	65	35	1.11	1.23	0.80	0.42
Au <sub>5</sub> / CeO <sub>2</sub> HSNPs	1.07	64	36	1.40	1.40	0.72	0.50
Au <sub>5</sub> / GDC-10% HSNPs	0.89	67	33	1.15	1.27	0.85	0.41

\* Calculated in range -40°C - 500°C; range 150°C - 250°C excluded from integration in Au<sub>0.5</sub>/GDC-10% HSNPs sample due to negative consumption values.

\*\* Calculated in range 500°C - 900°C; range 460°C - 630°C excluded from integration for Au<sub>2</sub>/CeO<sub>2</sub> HSNPs and Au<sub>5</sub>/CeO<sub>2</sub> HSNPs samples due to negative consumption values that originates from hydrogen desorption from the sample into the gas stream.<sup>73</sup>

systems (Fig. 8.C), for which the presence of fully grown AuNPs was observed, indicates presence of the additional reduction path with low activation energy. The surface reduction extent is about twice as high as compared to Au5/CeO<sub>2</sub> cubes (Table 1). Regardless of over twofold gold loading differences between Au2 and Au5 systems, they show rather similar reduction course and extent, indicating that AuNPs confinement inside the pores of the hierarchical materials is a dominant factor in reducibility enhancement over increasing Au-support contact on the exterior surface of the support. However, there is systematic surface reducibility enhancement when Gd-dopant is introduced along with gold loading increase, and Au5/GDC-10% catalyst shows the highest surface to bulk reducibility (67%/33%), which indicates the synergetic effect of this factors on catalyst reducibility.

H<sub>2</sub> consumption calculated per mere CeO<sub>2</sub> allows to assess the impact of dopant and the presence of AuNPs on the reduction properties contributed by the support active phase. All hierarchical systems show a twofold increase in hydrogen consumption as compared to CeO<sub>2</sub> cubes. Closer inspection shows that increasing the amount of gold systematically increases the reducing capacity of doped and non-doped systems, which may be related to increasing the number of active gold-support contact sites. Concurrently, a comparison of systems with the same amount of gold but differing in the presence of dopant in support indicates a decrease in total H<sub>2</sub> consumption for doped samples. This may be related to the

formation of extrinsic oxygen vacancies in the materials bulk.<sup>74</sup> This is evidenced by separation of the total H<sub>2</sub> consumption of the active CeO<sub>2</sub> phase into the surface and bulk contributions, which shows decrease in bulk reduction and concurrent increase in surface reduction as compared to undoped hierarchical samples (see Table 1). However, for Gd-doped HSNPs samples the absolute value of surface reduction is twice the value of bulk reduction indicating the facilitation of reducibility by matrix doping.

### 3.2.2. CO-TPR

CO-TPR was measured to better understand the contribution of the surface reducibility as compared to reducibility probed by H<sub>2</sub>-TPR that has greater bulk penetration potential. Fig. 9.A compares reducibility of HSNPs supports to the model CeO<sub>2</sub> cubes. All samples are characterized by occurrence of four maxima that corresponds to various reducible species in the material. CeO<sub>2</sub> HSNPs show onset of CO<sub>2</sub> release at ~150°C, which is slightly lower than values reported in the literature for pristine CeO<sub>2</sub> (~200°C).<sup>75</sup> Gd-doping shifts the onset reduction temperature to ~200°C. Surprisingly, the onset reduction temperature for CeO<sub>2</sub> cubes starts near 0°C that may be linked to occurrence of highly reactive oxygen species present either on defected sites of cubes (corners and edges, see Fig. S12 in ESI) or nano-oval particles present in the sample (see Fig. S7 in ESI).

Division into three regions of reduction (surface, subsurface, and

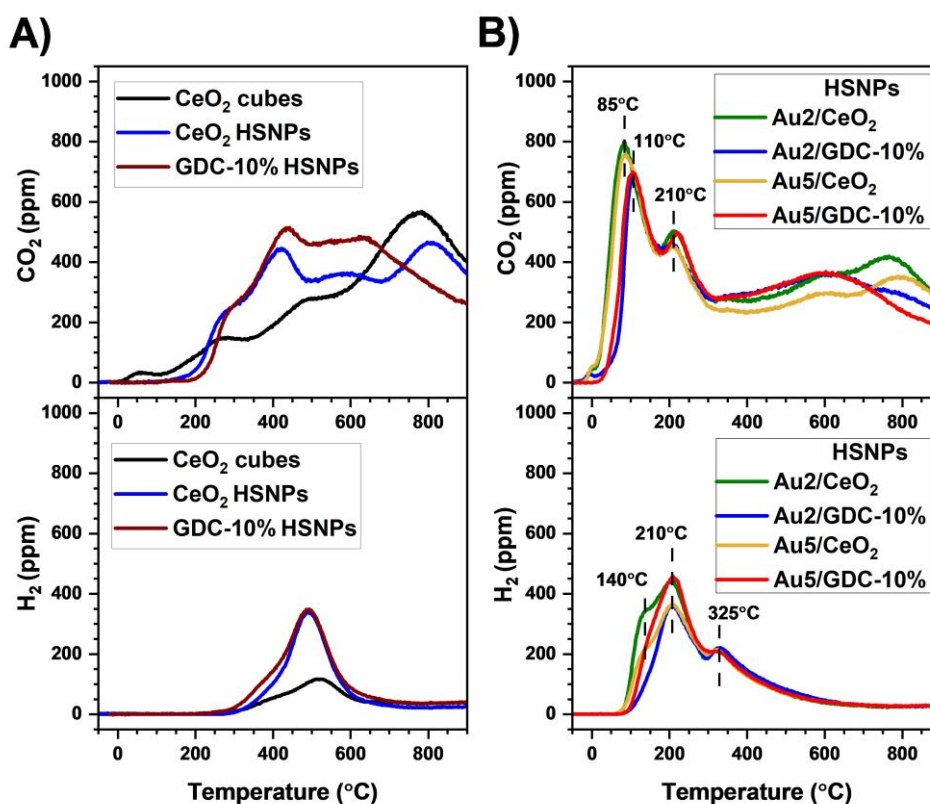


Fig. 9.A Temperature dependences of the CO<sub>2</sub> (top) and H<sub>2</sub> (down) evolution during CO-TPR for (A) CeO<sub>2</sub> and GDC-10% supports differing by morphology (cubes, HSNPs); (B) Au/CeO<sub>2</sub> and Au/GDC-10% HSNPs catalysts differing by gold loading (SC = 2 or 5).

bulk) has been made based on CeO<sub>2</sub> cubes plot analysis and literature considerations. As HRTEM result have shown, the dominance of (100) ceria planes are observed for both, cubes and HSNPs (see Section 3.1.3), hence the low-temperature maximum at ~260°C, that occurs at the same temperature for all three samples, has been ascribed to the surface reduction of oxygen at this crystal planes. This process reaches stabilization above ~260°C that is followed by onset of subsurface reduction maximum at 350°C that coincides with onset of H<sub>2</sub> release at ~300°C. First principles calculations have shown that the uptake of small amounts of hydrogen by ceria is thermodynamically spontaneous below 665 K with the formation of HCe<sub>4</sub>O<sub>8</sub>.<sup>76</sup> Also, hydroxyls near the surface help to stabilize oxygen vacancy clusters at Ce(111) surface.<sup>77</sup> Hence, due to coincidence of maximum of H<sub>2</sub> and CO<sub>2</sub> evolution at ~480°C has been ascribed to the process of reduction from the subsurface regions of ceria. This is followed by bulk reduction at 810°C.

Evolution of CO<sub>2</sub> in hierarchical supports shows increased maximum at ~260°C that indicates intensified surface reduction taking place at CeO<sub>2</sub>(100) planes. However, the cumulative surface oxygen consumption in all catalyst supports studied is similar up to 330°C (Fig. S13 in ESI) that indicates a similar amount of active oxygen availability in cubes and HSNPs, despite the greater specific surface area of hierarchical supports. Nevertheless, the subsurface reduction of HSNPs samples is increased and shifted to lower temperatures, 420°C and 435°C for CeO<sub>2</sub> HSNPs and GDC-10% HSNPs, respectively. Since the position of hydrogen ejection maxima is not changed but intensified for HSNPs, the effect of intensification of subsurface reduction is ascribed to augmented exposition of surface due to the arrangement of crystallites in hierarchical structure.

CO-TPR profile of GDC-10% HSNPs support shows two major differences as compared to its undoped counterpart. There is a shift of bulk reduction towards lower temperatures, from 810°C to 630°C, proving that doping ceria matrix facilitates migration of bulk oxygen. Also, slightly delayed surface oxygen consumption is observed that is indication of possible dopant segregation on the crystallites surface.

Fig. 9.B shows CO-TPR for gold decorated HSNPs systems. A shift of surface and subsurface reduction to temperatures far below 300°C is observed. Surface reduction maxima for gold-decorated CeO<sub>2</sub> HSNPs occurs at 85°C and for gold-decorated GDC-10% HSNPs at 110°C. This indicates an inhibitory effect of the dopant presence on the surface reducibility.

Interestingly, there is no distinct division into the surface and subsurface reduction as a function of temperature since hydrogen desorption maxima coincide with low-temperature maxima of CO<sub>2</sub> formation. As visible in Fig. 9.B, surface reduction of gold decorated CeO<sub>2</sub> HSNPs reaches maximum in 85°C that coincides with onset of H<sub>2</sub> release at the same temperature followed maximum of H<sub>2</sub> release at 140°C. This may be associated with the simultaneous activation of surface and subsurface oxygen at the regions around the gold-support interface. Curiously, this effect is less pronounced for gold decorated GDC-10% HSNPs (no explicit presence of H<sub>2</sub> ejection maximum at 140°C), which indicates that the number of hydroxyl groups at Au-Gd-doped support interface is slightly diminished.

A shift of hydrogen ejection from 520°C for non-Au-decorated systems to 325°C for gold-decorated ones proves strong influence of AuNPs on the support redox properties. Also, differences in peak intensity of H<sub>2</sub> release at 210°C are not consistently related to either the presence of Gd<sup>3+</sup> or the Au loading, so other underlying factors are causing the observed effect.

### 3.2.3. NAP-XPS

NAP-XPS spectra were collected to characterize the dynamic operation of catalysts under reducing and oxidating atmospheres. The chemical state of Au5/CeO<sub>2</sub> HSNPs and Au5/GDC-10% HSNPs exposed to CO was recorded for temperatures corresponding to two main reduction maxima, visible in CO-TPR profiles (Fig. 9.B), namely 100°C and 200°C, as well as in the room temperature of 27°C that corresponds to the beginning of surface reduction process. Also, the spectra were recorded in oxidizing O<sub>2</sub> gas in 300°C that corresponds to the temperature in which depletion of surface/subsurface reduction is observed (Fig. 9.B). Since XPS is surface-sensitive technique, probing into ca. 10 atomic layers,<sup>78</sup> only samples containing AuNPs visible on the surface of star-shaped particle arms were chosen for examination. All collected profiles are presented in Fig. 10.

The reduction degree of ceria support (Ce<sup>3+</sup>/Ce ratio) has been calculated by the fitting procedure described in Skála et al. and has been presented in Fig. 10 as percentage values.<sup>79</sup> Briefly, three doublets assigned to Ce<sup>4+</sup> and two doublets assigned to Ce<sup>3+</sup>, were used for fitting the Ce 3d spectra. Ce<sup>3+</sup>/Ce ratio was calculated as the ratio of Ce<sup>3+</sup>-related peaks areas to the total area of all Ce-related doublets. As seen in Figure 12.A and B (left panels), the Ce 3d region of Au5/CeO<sub>2</sub> HSNPs and Au5/GDC-10% HSNPs samples exposed to 1 mbar O<sub>2</sub> at 573 K can be well-fitted by three doublets assigned to Ce<sup>4+</sup> only, indicating complete ceria oxidation. It was impossible to obtain reasonable Ce 3d spectra after decreasing the temperature of both samples to room temperature in the presence of oxygen. But it is reasonable to assume that such a decrease should not affect the chemical state of ceria in them. In fact, analysis by EELS-SI in several areas (See Fig. S14 in ESI) show the presence of only Ce<sup>4+</sup> oxidation state in the surface, near-surface and bulk regions of the arm of CeO<sub>2</sub> and GDC-10% HSNPs. The presence of Ce<sup>3+</sup> was detected only after electron beam irradiation over previously analyzed areas as shown in Figure S14, note that the reduction occurs locally on the surface of the arm, maintaining the Ce<sup>4+</sup> oxidation state in the core of the particle. The measurement was made on samples exposed to air and without initial CO reduction before loading to the microscope. Discussion of the dopant influence on ceria oxidation state has been described in our previous paper.<sup>51</sup>

The exposition of both Au5/CeO<sub>2</sub> and Au5/GDC-10% samples to 1mbar CO at elevated temperatures (≥100°C) results in partial reduction of ceria. Wherein the doping of ceria support by Gd slightly decreases its reducibility. The Ce<sup>3+</sup>/Ce percentage in Au5/CeO<sub>2</sub> and Au5/GDC-10% samples exposed to 1 mbar CO at 200°C was 10% and 5%, respectively. In the literature, doping Au/CeO<sub>2</sub> with Eu decreases

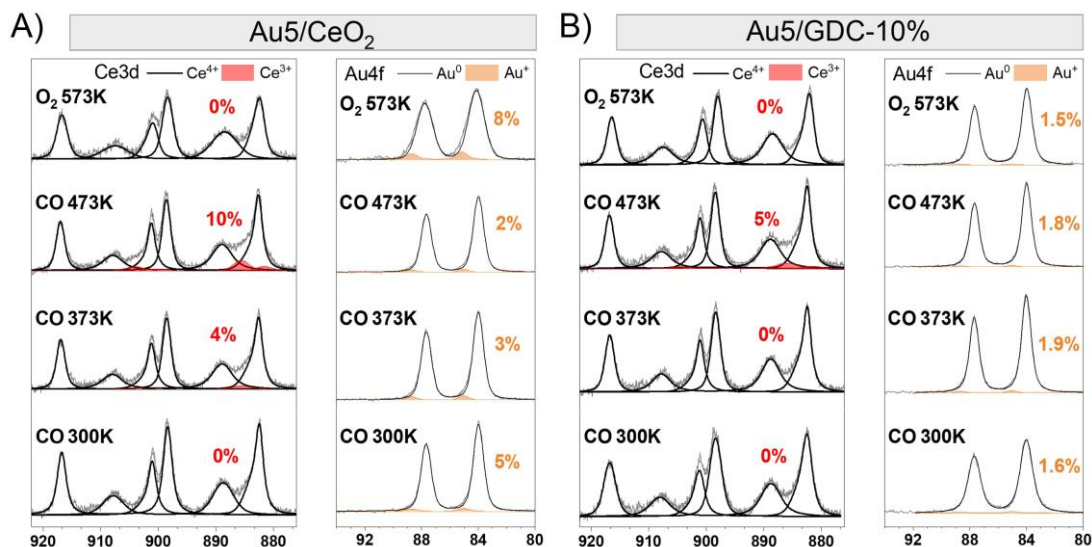


Fig. 10. NAP-XPS of A) Au5/CeO<sub>2</sub> HSNPs; B) Au5/GDC-10% HSN

the reducibility of ceria support in real working conditions which stays in line with our results.<sup>80</sup>

The Au 4f regions of spectra for both samples are shown in Fig. 10.A and B (right panels). All Au 4f spectra are well fitted only by Au<sup>0</sup> and Au<sup>+</sup> doublets and no other oxidation forms of gold are observed. Predominance of Au<sup>0</sup> is observed for both samples in all tested conditions indicating the presence of metallic AuNPs on the support surface. Detailed analysis of Au 4f region recorded for Au5/CeO<sub>2</sub> sample exposed to 1mbar CO at 27°C shows some minimal amount of Au<sup>+</sup> (5%) that is reduced with the temperature increase (2% Au<sup>+</sup> at 200°C). Oppositely, no such reduction effect is observed for Au5/GDC-10% sample exposed to 1 mbar CO, for which there is 1.6% of Au<sup>+</sup> at 27°C and 1.8% of Au<sup>+</sup> at 200°C. So, the exposition of Au-decorated systems to CO results in a slight reduction of gold to the metallic state only for undoped Au5/CeO<sub>2</sub> sample. Also, exposing both samples to O<sub>2</sub> at 300°C leads to restoration of the oxidized form of gold for CeO<sub>2</sub> HSNPs (8% Au<sup>+</sup>), while no such effect is observed for Au5/GDC-10% HSNPs (1.5% Au<sup>+</sup>). This indicates larger extent of dynamical behavior of gold when deposited on CeO<sub>2</sub> support and, reversely, greater stabilization of AuNPs on Gd<sup>3+</sup>-doped ceria.

All Gd 3d spectra recorded for Au5/GDC-10% could be well fitted by only Gd<sup>3+</sup>-related doublet centered at 1186.6-1218.6 eV, as presented in Fig. S15.A in ESI.<sup>81</sup> Moreover, Gd/Ce ratio in all studied conditions was the same: 0.17-0.19 (see S15.B in ESI). This may indicate possible segregation of dopant on the surface of hierarchically structured particles arms since the global SEM-EDX measurements indicate Ge<sup>3+</sup> amount close to 10% (cf. Fig. 6.B).

### 3.3. Catalytic activity

All materials with different architecture were subjected to catalytic tests. In order to determine possible heat or mass transfer effects, and thus determine whether kinetic regime condition for intrinsic catalyst properties comparison has been satisfied, two diagnostic test has been conducted. Firstly, the degree of propane conversion

stays the same for various reactor loads of CeO<sub>2</sub> HSNPs that were tested in different flow rates while the space velocity was kept constant (Fig. S16.A and B in ESI). This proves negligible intrareactor and interphase effects for hierarchical catalyst supports. Secondly, TOF values for Au/CeO<sub>2</sub> HSNPs and Au/GDC-10% HSNPs with different loadings of Au stays the same under similar reaction conditions in propane oxidation, which proves no heat and mass transfer limitations for gold hierarchical catalysts (Fig. S16. C in ESI). For comparative purposes all the samples were tested in similar reaction conditions.

To evaluate performance of a given catalyst turnover frequency (TOF) was determined at low conversions (<15%). In this study, the TOF, defined as the rate of propane consumption per number of active sites, was calculated in two ways depending on assumptions about the nature of the active site on the catalyst. Firstly, specific reaction rate was normalized to the mole number of Au contained in the mass of the active catalyst phase (Au/Ce<sub>1-x</sub>O<sub>2-y</sub>).<sup>82</sup> As this approach assumes that each gold atom is an active site, it is suitable for systems in which the particles are highly dispersed and have a narrow size distribution. Due to the fact that systems tested in this study are characterized by high degree of complexity (gold deposited on active support, high gold loading, relatively broad Au NPs size distribution, varied localization of Au NPs within hierarchical system) a different approach has been taken to describe hierarchical gold catalysts. In the new approach the gold atoms at the Au/ceria interface has been taken as active sites and the number of Au atoms in the ring around gold nanoparticles (modeled as a half-sphere) has been quantified based on histograms generated from TEM data (see description in Fig. S17 in ESI). This approach is rationalized by DFT-confirmed experimental observation that the oxidation of Au-bound CO occurs at the Au-CeO<sub>2</sub> interface.<sup>83</sup> Also, chemisorption study revealed that despite the lower accessibility of the metal surface in embedded Au@CeO<sub>2</sub> systems, the increased activity may be ascribed to the larger extent to metal-support interaction.<sup>84</sup> Such approach allows to determine the number of active sites more accurately than

just taking the average particle size, especially for the polydispersed or the non-uniformly distributed wide size range systems.

### 3.3.1. Propane oxidation: role of architecture

Propane conversion for non-decorated catalyst supports shows superiority of hierarchical systems over cubic and NPs ones (Fig. S18 in ESI). CO oxidation rates normalized by BET specific surface follows the order  $\text{CeO}_2$  HSNPs >  $\text{CeO}_2$  cubes >  $\text{CeO}_2$  NPs with rates  $r_{330^\circ\text{C}} = 15.1 \times 10^6 > 8.0 \times 10^6 > 1.4 \times 10^6 \text{ mol m}^{-2} \text{ h}^{-1}$ , respectively. The similar trend is observed for GDC-10% supports. However, a reduced value of the reaction rate for GDC-10% systems proves the inhibitory effect of dopant on the intrinsic activity of ceria-based supports. The influence of the size of support particles on the oxidation process is visible, since bulk  $\text{CeO}_2$  shows almost no activity in tested temperature regimes reaching 4% conversion at  $540^\circ\text{C}$ . Also, additional propane conversion process at  $180^\circ\text{C} - 400^\circ\text{C}$  is observed for  $\text{CeO}_2$  HSNPs, whose presumable origin has been previously discussed.<sup>51</sup>

Fig. 11. A and B show propane oxidation performance of gold-decorated systems differing in morphology. Since various gold loadings modifies the hierarchical catalyst activity differently (cf. section 3.3.2), high gold loaded samples ( $\text{SC} = 5$ ) were chosen for propane oxidation tests. Decoration of ceria supports by AuNPs greatly influences propane oxidation, especially in hierarchical systems in which the temperature of half-conversion is reduced to  $T_{50} = 420^\circ\text{C}$  for Au5/ $\text{CeO}_2$  HSNPs and to  $T_{50} = 370^\circ\text{C}$  for Au5/GDC-10% HSNPs. This translates into reduction of  $T_{50}$  by nearly  $100^\circ\text{C}$  for the gold-decorated Au5/GDC-10% HSNPs when compared to the non-decorated hierarchical system of  $\text{CeO}_2$  HSNPs and  $165^\circ\text{C}$  of  $T_{50}$  reduction when compared to the non-hierarchical  $\text{CeO}_2$  NPs.

The specific rate values for Au5/ $\text{CeO}_2$  cubes and Au5/GDC-10% cubes indicate their slightly enhanced catalytic performance over hierarchical systems (see Table 2). This trend is also observed in TOF (calculated for atomically dispersed Au atoms; see  $\text{TOF}_{[a]}$  in Table 2). However, taking into consideration TOF calculated for Au NP interphase-exposed atoms (see  $\text{TOF}_{[b]}$  in Table 2), the hierarchical systems shows two times higher oxidation performance over cubic ones. While the first metric ( $\text{TOF}_{[a]}$ ) shows that cubic gold catalyst has greater catalytic performance when mass of the Au active phase in catalyst is taken as critical factor in catalyst design, the second metric ( $\text{TOF}_{[b]}$ ) shows superiority of hierarchical systems over cubic due to maximized Au/support interface contact.

The effect of gold confinement in increasing catalytic activity is visible when Au2/ $\text{CeO}_2$  HSNPs and Au5/ $\text{CeO}_2$  cubes are compared. Both systems have similar Au NP size,  $r_{\text{av,TEM}} = 3.6 \text{ nm}$  and  $3.3 \text{ nm}$ , and they show similar specific rates,  $r_{300^\circ\text{C}} = 0.77 \times 10^{-2}$  and  $0.76 \times 10^{-2} \text{ mol}_{\text{CO}} \text{ g}_{\text{Au}}^{-1} \text{ h}^{-1}$ , respectively. However, Au2/ $\text{CeO}_2$  HSNPs have lower activation energy ( $E_a = 49 \text{ kJ/mol}$ ) when compared to Au5/ $\text{CeO}_2$  cubes ( $E_a = 57 \text{ kJ/mol}$ ). Also,  $\text{TOF}_{[b]}$  values are higher for hierarchical catalyst ( $\text{TOF}_{300^\circ\text{C}} = 0.43 \times 10^{-2} \text{ s}^{-1}$ ) when compared to cubes ( $\text{TOF}_{300^\circ\text{C}} = 0.26 \times 10^{-2} \text{ s}^{-1}$ ).

For Au5/ $\text{CeO}_2$  NPs and Au5/GDC-10% NPs the low values of specific rates is indicative of lower performance of powdered

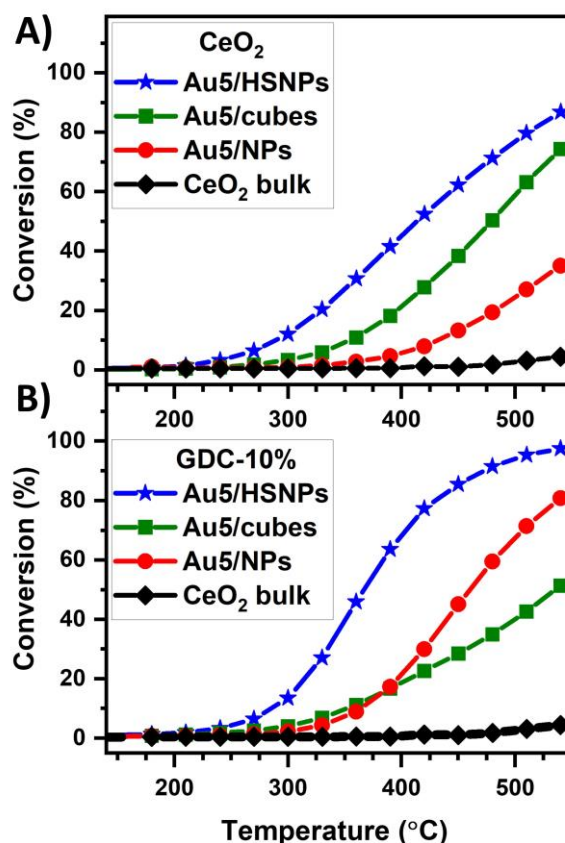


Fig. 11. Propane conversion plots of samples differing by support morphology, nanoparticles (NPs), nanocubes (cubes), hierarchically structured particles (HSNPs); A) Au5/ $\text{CeO}_2$  catalysts; B) Au5/GDC-10% catalysts

mixtures characterized by loose Au/ceria contact. Lower catalytic performance may be linked as well to formation of large AuNPs with a mean size of  $24.4 \text{ nm}$ . Also, considering the course of the conversion curves, some faster loss of performance is observed for powdered catalysts (cubes and NPs), which may be caused by sintering.<sup>85</sup> Despite the fair specific rate and  $\text{TOF}_{[a]}$  and  $\text{TOF}_{[b]}$  values for Au5/GDC-10% cubes (see Table 2), this catalyst shows the lowest  $T_{50} = 540^\circ\text{C}$ , which may be linked to sintering of particles at high temperatures as TEM images inspection suggest (see Fig. S21.D in ESI). Whereas such facilitated intergrowth of Gd-doped particles leads to formation of additional porosity within hierarchical systems,<sup>51</sup> it results in loss of surface availability for non-hierarchically organized powdered nanomaterial.

Propane oxidation profiles for solely hierarchically structured systems, presented in Fig. S19 in ESI, shows the occurrence of specific activation threshold, since the conversion curves follows the same track up to  $300^\circ\text{C}$  for  $\text{CeO}_2$  HSNPs, Au5/ $\text{CeO}_2$  HSNPs and Au5/GDC-10% HSNPs samples. The addition of catalytic promoters would perhaps allow this activation threshold to be lowered.<sup>86</sup>

### 3.3.2. Propane oxidation: role of gold loading

Fig. 12.A shows propane conversion profiles for  $\text{CeO}_2$  hierarchical systems with different gold loadings, and for comparative purposes

**Table 2** Kinetic data for propane oxidation

Catalyst	$r_{300^\circ\text{C}} \times 10^2$ ( $\text{mol}_{\text{CO}} \text{g}_{\text{Au}}^{-1} \text{h}^{-1}$ )	$E_a$ ( $\text{kJ/mol}$ )	$\text{TOF}_{300^\circ\text{C}} \times 10^2$ [a] ( $\text{s}^{-1}$ )	$\text{TOF}_{300^\circ\text{C}} \times 10^2$ [b] ( $\text{s}^{-1}$ )	Reference
Au0.5/CeO <sub>2</sub> HSNPs	1.07	63	2.18	-	This work
Au2/CeO <sub>2</sub> HSNPs	0.77	49	0.43	0.49	This work
Au5/CeO <sub>2</sub> HSNPs	0.61	55	0.14	0.43	This work
Au5/CeO <sub>2</sub> cubes	0.76	57	0.78	0.26	This work
Au5/CeO <sub>2</sub> NPs	0.04	65	0.01	-	This work
Au0.5/GDC-10% HSNPs	1.13	52	2.14	-	This work
Au2/GDC-10% HSNPs	1.85	49	1.05	1.18	This work
Au5/GDC-10% HSNPs	0.72	51	0.17	1.11	This work
Au5/GDC-10% cubes	0.96	47	1.04	0.61	This work
Au5/GDC-10% NPs	0.24	61	0.11	-	This work
Literature reference	Architecture description				
1%-Au/CeO <sub>2</sub>	1.47	Au (5 nm) / nano-CeO <sub>2</sub> (NP; 23 nm)			[87]
8.2wt%-Au/CeO <sub>2</sub>	1.10	Au (4.3 nm)/(hierarchical/nano)-CeO <sub>2</sub> (tubes; 10.6 nm)			[88]
10.8wt%-Au/GDC-10%	0.89	Au (3.8 nm)/(hierarchical/nano)-CeO <sub>2</sub> (tubes; 8.1 nm)			[88]

Comparative data to known systems has been presented in Literature reference part of the table (calculated for 300°C). In architecture description the morphology (NP- nanoparticles, cubes, hierarchical systems) as well as the mean size of gold and ceria particles has been given in brackets. Specific rate ( $r$ ) refers to the moles of the CO molecules converted per gram of gold per hour.<sup>1</sup>

[a] – TOF normalized to number of gold atoms calculated according to Ledwa et al.<sup>82</sup>

[b] – TOF normalized to the number of Au/CeO<sub>2</sub> interface gold atoms (see description in Section 3.3); for Au0.5/HSNPs and Au5/NPs systems no TEM data for Au NPs size distribution precluded quantification of the number of interface active sites.

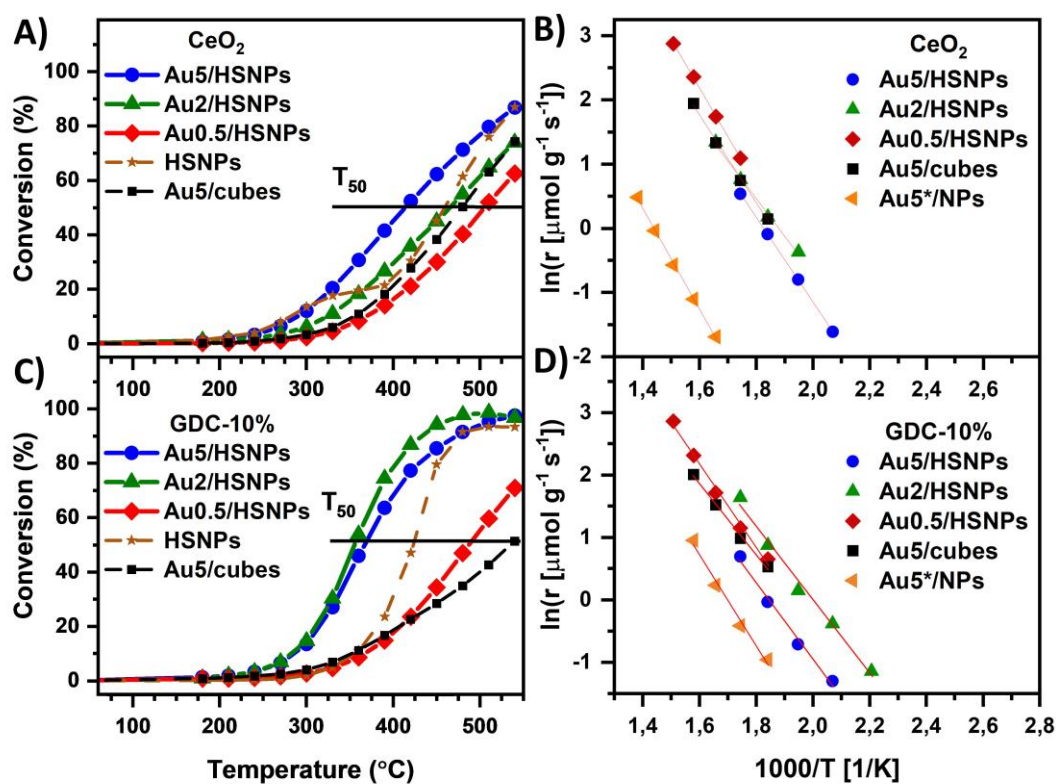


Fig. 12. Propane conversion plots of samples differing by gold loading (Au  $x$ , where  $x$  denotes surface coverage parameter value) and corresponding Arrhenius plots for low conversions (<15%) with additional data for catalysts differing in architecture. A-B) Au  $x$ /CeO<sub>2</sub> HSNPs; C-D) Au  $x$ /GDC-10% HSNPs.

conversion for Au5/CeO<sub>2</sub> cubes as well as no gold containing CeO<sub>2</sub> HSNPs were also presented. Increasing gold loading systematically reduces the temperature of 10% conversion from T<sub>10</sub> = 370°C for Au0.5/CeO<sub>2</sub> HSNPs to T<sub>10</sub> = 290°C for Au5/CeO<sub>2</sub> HSNPs. This suggests that increasing Au content improves catalytic properties in terms of reaching the lowest conversion temperatures. However, comparison of specific rates shows reversed order of catalyst intrinsic activity following the sequence Au0.5/CeO<sub>2</sub> HSNPs > Au0.5/CeO<sub>2</sub> HSNPs > Au0.5/CeO<sub>2</sub> HSNPs (Table 2). Since the chosen metric (specific rate) was normalized to mass of Au active phase, it favors systems with low gold loadings. The low-temperature CO chemisorption can be an alternative effective approach for quantifying gold active surface area that would enable to characterize the studied materials more accurately.<sup>89</sup> Nevertheless, inspection of activation energy trends shows that hierarchical systems with intermediate gold loadings with gold particles confined within ceria pores, namely Au2/CeO<sub>2</sub> HSNPs and Au2/GDC-10% HSNPs, have the lowest activation energy values (E<sub>a</sub> = 49 kJ/mol), indicating their highest catalytic performance. Comparison of TOF<sub>[b]</sub> values of this systems with cubic ones shows twofold increased activity of Au/HSNPs catalysts (see Table 2).

Interestingly, gold decoration kills the occurrence of the low temperature mechanism of propane oxidation observed for undecorated CeO<sub>2</sub> HSNPs (Fig. 12.A). Also, since all catalysts were tested in similar reaction conditions, comparison of T<sub>50</sub> for variously gold loaded samples shows that for the low gold loaded Au0.5 catalysts T<sub>50</sub> is shifted below the one for non-gold-decorated catalytic supports (Fig. 12.A and B). There is a specific threshold of gold content in hierarchical systems beyond which high-temperature propane oxidation outperforms the non-decorated catalyst supports. For Au/CeO<sub>2</sub> HSNPs this value lies between SC = 2 and 5, and for Au/GDC-10% ones between SC = 0.5 and 2. This indicates that the specified size of the AuNPs must be achieved to accentuate the catalytic properties of the system.

The effect of Gd-doping on activity enhancement is visible when Au2/CeO<sub>2</sub> HSNPs catalyst is compared to Au2/GDC-10% one for which activation energy is similar (E<sub>a</sub> = 49 kJ/mol). However, the specific rate and TOF<sub>[b]</sub> values are more than twofold higher for Au2/GDC-10% (Table x). Also, for this sample conversion is enhanced in higher temperature regimes (300°C-450°C) when compared to Au5/CeO<sub>2</sub> HSNPs, which indicates the mutual effect of AuNPs and Gd dopant presence on propane oxidation enhancement.

Also, the light-off curve of Au5/GDC-10% cubes coincide with the non-decorated GDC-10% HSNPs support one, which indicates that the presence of gold nanoparticles on the ceria surface does not necessary lead to lowering propane oxidation temperature. Hence, confinement of gold particles inside the material seems to play critical role in catalytic performance facilitation. A slight flattening of the light-off curve for Au5/GDC-10% HSNPs when compared to Au2/GDC-10% HSNPs sample indicates the occurrence of internal diffusion limitation<sup>90</sup> This may be caused by growth of particles during reaction in high temperature regimes (see Section 3.3.4).

### 3.3.3. CO oxidation: role of architecture and gold loading

CO oxidation tests were carried out on samples in which presence of AuNPs was detected in microscopic investigation, namely systems for which SC = 2 or 5. This choice was made on the basis of literature premises indicating that gold particles having size below 5 nm show good activity for CO oxidation<sup>5</sup> as well as the observation that insufficient amount of gold loading in hierarchical systems (SC = 0.5) influences propane oxidation ambiguously showing fair specific rate values along with relatively high apparent activation energy (Section 3.3.2.).

The results of catalytic CO oxidation tests are shown in Fig. 13.A. All the gold-decorated hierarchically structured samples shift CO oxidation into lower temperatures (T<sub>50</sub>=15°C - 48°C) as compared to model Au5/CeO<sub>2</sub> cubes (T<sub>50</sub>=85°C). TOF<sub>[b]</sub> values at 25°C for hierarchical catalysts, Au2/CeO<sub>2</sub> HSNPs and Au5/CeO<sub>2</sub> HSNPs, are higher than for non-hierarchical Au5/CeO<sub>2</sub> cubes, 0.78 × 10<sup>2</sup> s<sup>-1</sup>, 0.93 × 10<sup>2</sup> s<sup>-1</sup> and 0.54 × 10<sup>2</sup> s<sup>-1</sup>, respectively. This effect may be linked to the confinement of AuNPs inside the pores of hierarchical support and thus increased metal-support contact. The highest temperature shift was observed for Au2/GDC-10% HSNPs (T<sub>50</sub>=15°C) followed by Au5/CeO<sub>2</sub> (T<sub>50</sub>=18°C), Au2/CeO<sub>2</sub> (T<sub>50</sub>=32°C) and Au5/GDC-10% HSNPs (T<sub>50</sub>=48°C), which is also reflected in the order of TOF values (see Table 3 and Fig. S20.A in ESI). Various influence of gold loading on TOF values may indicate that CO oxidation on this system is structure-sensitive reaction.<sup>91,92</sup>

Fig. 13.B shows the AuNPs size distribution plots. Each plot reflects the distribution of AuNPs in TEM-transparent regions of the sample, as they were constructed by taking 150-300 AuNPs detected on surface and subsurface regions of hierarchically structured supports. Thus, for lower gold-loaded samples (SC = 2) the plots reflect the dominant size of particles that growth was confined by the pore geometry of the support. Contrarily, for high gold-loaded samples (SC = 5), the plots reflect the dominant size of nanoparticle which growth was mainly not constrained by the pores within support. Such non-constrained increase in size of nano-gold is observed for Au5/GDC-10% system, which is related to the specific architecture of the support described in Section 3.1.2.

In the literature, the catalytic activity of AuNPs deposited on TiO<sub>2</sub>(100) exhibit volcano-like size dependence with particles of 2.5-3.5 nm showing the highest activity.<sup>93</sup> Also, Ta et al. have shown that gold nanoparticles of 2-4 nm size deposited on rod-shaped CeO<sub>2</sub> are highly active and distinctively stable under realistic conditions.<sup>94</sup> Also, metal to non-metal transition occurs for AuNPs having size <4 nm that coincides with onset of CO oxidation activity.<sup>95</sup> Moreover, the melting point of 2 nm Au clusters is ~573K and increases for larger nanoparticles.<sup>85</sup> Even though the size of AuNPs plays a greater role in the oxidation of CO on reducing than non-reducing oxides,<sup>99</sup> the metal-support interaction tuning is most impactful for metal nanoparticles smaller than 4 nm.<sup>12</sup> Due to those reasons the range of



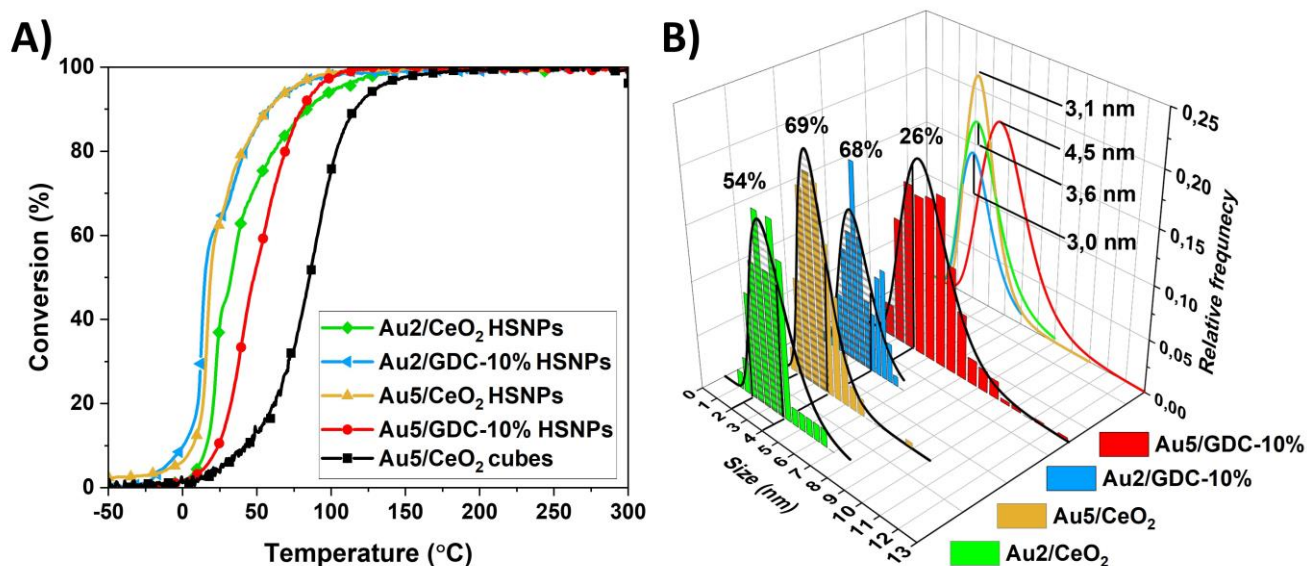


Fig. 13. A) CO conversion plot of hierarchically structured catalysts; B) Size distribution plots of AuNPs detected in surface/sub-surface region of hierarchically structured catalysts (see description in text). Comparative Au5/CeO<sub>2</sub> cubes from ref. <sup>96</sup>

**Table 3** Kinetic data for CO oxidation

Catalyst	$r_{25^\circ\text{C}}$ ( $\text{mol}_{\text{CO}} \text{gAu}^{-1} \text{h}^{-1}$ )	$E_a$ ( $\text{kJ/mol}$ )	$\text{TOF}_{10^\circ\text{C}} \times 10^2$ [a] ( $\text{s}^{-1}$ )	$\text{TOF}_{10^\circ\text{C}} \times 10^2$ [b] ( $\text{s}^{-1}$ )	Reference
Au2/CeO <sub>2</sub> HSNPs	0.10	88	0.68	0.78	This work
Au5/CeO <sub>2</sub> HSNPs	0.07	31	0.30	0.93	This work
Au2/GDC-10% HSNPs	0.16	35	2.87	3.24	This work
Au5/GDC-10% HSNPs	0.01	58	0.09	0.56	This work
Au5/CeO <sub>2</sub> cubes <sup>#</sup>	0.04	37	1.62	0.54	This work
Literature reference		Architecture description			
5.7wt%-Au/CeO <sub>2</sub>	0.05	Au (3.7 nm; range 1-7 nm) / nano-CeO <sub>2</sub> (NP)			[ <sup>97</sup> ]
1wt%-Au/CeO <sub>2</sub>	0.04	Au (range 4-19 nm) / nano-CeO <sub>2</sub> (NP.; 14 nm)			[ <sup>98</sup> ]
10at%-Au/CeO <sub>2</sub>	0.33	nano-Au / nano-CeO <sub>2</sub> (NP; 5 nm); co-precipitation			[ <sup>99</sup> ]
0.47%-Au/CeO <sub>2</sub>	0.0 <sup>#</sup>	Au (3.1 nm) / nano-CeO <sub>2</sub> (cubes; 20nm)			[ <sup>100</sup> ]
1.1at%-Au/CeO <sub>2</sub>	0.15	Au (bimodal <1nm and 3-6 nm) / nano-CeO <sub>2</sub> (cubes)			[ <sup>101</sup> ]
1.3wt%-Au/CeO <sub>2</sub>	0.08	Au (20 nm) / nano-CeO <sub>2</sub> (NP.; 15 nm)			[ <sup>102</sup> ]
9.3wt%-Au/CeO <sub>2</sub>	0.07	Au (<20 nm) / (hierarchical/nano)-CeO <sub>2</sub> (hollow nanospheres)			[ <sup>103</sup> ]
4.2wt%-Au/CeO <sub>2</sub>	0.13	Au (<20 nm) / (hierarchical/nano)-CeO <sub>2</sub> (hollow nanospheres)			[ <sup>103</sup> ]
1.8wt%-Au/CeO <sub>2</sub>	0.11	Au (<20 nm) / (hierarchical/nano)-CeO <sub>2</sub> (hollow nanospheres)			[ <sup>103</sup> ]
0.98wt%-Au/CeO <sub>2</sub>	0.20	Au(7.4 nm)/nano-CeO <sub>2</sub> (8.9 nm); anion adsorption			[ <sup>104</sup> ]

Comparative data to known systems has been presented in Literature reference part of the table (calculated for 25°C). In architecture description the morphology (NP- nanoparticles, cubes, hierarchical systems) as well as the mean size of gold and ceria particles has been given in brackets. Specific rate ( $r$ ) refers to the moles of the CO molecules converted per gram of gold per hour.<sup>1</sup>

<sup>#</sup> Data from ref. <sup>96</sup>

<sup>##</sup> no conversion below 90°C

[a] – TOF normalized to number of gold atoms calculated according to Ledwa et al. <sup>82</sup>

[b] – TOF normalized to the number of Au/CeO<sub>2</sub> interface gold atoms (see description in Section 3.3); for Au0.5/HSNPs and Au5/NPs systems no TEM data for Au NPs size distribution precluded quantification of the number of interface active sites.

2-4 nm has been selected as the optimal size for catalytic activity inspection. As visible on Fig. 13.B, the proportion of Au particles falling within the region of as defined optimal size correlates well

with the sequence of TOF<sub>[b]</sub> values (Table 3) and light-off curves presented in Fig. 13.A.

The CO oxidation performance of Au<sub>2</sub>/GDC-10% HSNPs is better than Au<sub>2</sub>/CeO<sub>2</sub> HSNPs sample, which reflects the proportion of optimum sized AuNPs having 68% and 54%, respectively. Increasing the gold loading in Au<sub>2</sub>/CeO<sub>2</sub> HSNPs induces growth of Au nanoparticles that fill the pores and deposit on the external surface of the hierarchical support macroparticle in the amount that corresponds to 69% of optimally sized NPs, which runs parallel to shift of TOF from  $0.78 \times 10^{-2} \text{ s}^{-1}$  to  $0.93 \times 10^{-2} \text{ s}^{-1}$ .

Oppositely, overgrowth of AuNPs in Au<sub>5</sub>/GDC-10% HSNPs for which only 26% of optimally sized Au nanoparticles occurs on the surface/subsurface regions of the support decreases CO oxidation performance, moves the half-conversion into higher temperatures and reduces TOF to  $0.56 \times 10^{-2} \text{ s}^{-1}$ . Only for this sample the modal size value of 4.5 nm falls outside the range of optimally sized active nanoparticles. The activity of this catalyst is comparable to Au<sub>5</sub>/CeO<sub>2</sub> cubes when TOF<sub>[b]</sub> for both systems are compared (see Table 3). However, activation energy for Au<sub>5</sub>/CeO<sub>2</sub> cubes is lower than for Au<sub>5</sub>/GDC-10% HSNPs, 37 kJ/mol and 58 kJ/mol, respectively. For nanocubes the modal value of Au NPs size is 2.6 nm and the proportion of particles with optimal size constitute 59% (Fig. S21.E in ESI). This suggest that optimally-sized gold nanoparticles play an important role in catalytic activity. Also, maximization of Au/surface contact for optimally-sized Au NPs are deposited within catalyst in dominance translates into higher CO oxidation activity. This is visible in Au<sub>2</sub>/GDC-10% HSNPs and Au<sub>5</sub>/CeO<sub>2</sub> HSNPs samples, for which activation energy is the lowest among tested catalysts, as well as TOF<sub>[b]</sub> values are the highest.

Reduction of catalysts in the flow of H<sub>2</sub> shifts CO oxidation temperatures into lower values with the highest shift registered for Au<sub>5</sub>/GDC-10% HSNPs (Fig. S22 in ESI) and T<sub>10</sub> far below -30°C. The lowest half-conversion temperature is observed for Au<sub>5</sub>/CeO<sub>2</sub> HSNPs sample (T<sub>50</sub> = 3°C). Due to possible surface reconstruction,<sup>105</sup> the shape of CO oxidation curves deviates from classical S-type indicating the occurrence of at least two modes of oxidation. The low-temperature mode has classical S-shape. However, for each sample some saturation of the process occurs in the temperatures from -5 °C to 25°C, depending on catalyst, and CO oxidation shifts to second mode (see Fig. S22.B in ESI).

### 3.3.4 Nano-gold stability in catalytic tests

Fig. 14. shows the AuNPs size distributions generated from TEM data for catalysts before and after CO and propane oxidation. For both Au<sub>5</sub>/CeO<sub>2</sub> HSNPs and Au<sub>5</sub>/GDC-10% HSNPs catalysts a systematic shift of modal value is observed when the final temperature of reaction increases. However, for Gd-doped sample the shift is larger. While initially small AuNPs deposited on the CeO<sub>2</sub> HSNPs (modal size value 3.1 nm) grows to 4.2 nm after propane oxidation (Fig. 14.A and 14.C), the growth proceeds from 4.5 nm to 7.5 nm for GDC-10% catalysts (Fig. 14.D and 14.F). The initial Au size difference between undoped and Gd-doped freshly synthesized catalysts is caused by differences in architecture that was discussed in the section 3.1.2. Similar trend is observed for samples evaluated after CO oxidation, however, due to lower reaction temperature (up to 300°C) the growth in size is slightly lower (see Fig. 14.B and 14.E).

For both catalysts there is a systematic reduction in the proportion of particles with optimal size of 2-4 nm, however, this reduction is smaller for Au<sub>5</sub>/CeO<sub>2</sub> HSNPs system. While for Au<sub>5</sub>/CeO<sub>2</sub> HSNPs the proportion decreases from 69% to 29% after propane oxidation, this proportion falls from 26% to 1% for Au<sub>5</sub>/GDC-10% HSNPs. This is due to the shift of the whole size distribution into larger values. Examination of AuNPs growth on model gold-decorated cubic samples shows the similar growing behavior (see Fig. S21.E in ESI), namely the shift of the whole size distribution into larger values. The modal value shifts from 2.6 nm to 5.1 nm for Au<sub>5</sub>/CeO<sub>2</sub> cubes after propane oxidation, and similar trend is observed for Au<sub>5</sub>/GDC-10% cubes, from 2.5 nm to 5.3 nm. Unique in this respect is Au<sub>5</sub>/CeO<sub>2</sub> HSNPs system, for which the shift of the entire size distribution is not observed, but the distribution is anchored in low size values (< 2 nm). TEM images corresponding to each distribution plot (Fig. 14) show that for CeO<sub>2</sub> HSNPs sample AuNPs are confined within pores even after propane oxidation (Fig. 14.C; confined particles marked by arrows). This proves sintering resistance of the hierarchical catalyst at elevated temperatures (540°C).

Similar anchoring effect is observed for Au<sub>5</sub>/GDC-10% HSNPs after CO oxidation (conducted up to 300°C) indicating confinement of AuNPs. However, after propane oxidation (conducted up to 540°C) the shift of the whole size distribution is visible (Fig. 14.F). This may be linked to collective intergrowth of GDC-10% nanoparticles, which causes formation of additional porosity in hierarchical support.<sup>51</sup> For gold-decorated system this process forces AuNPs out of the interior of the hierarchical material and leads to the growth of the AuNPs on the exterior surface of star-shaped support. Also, due to the formation of larger pores AuNPs grow into larger sizes and effect of nano-gold confinement is not observed. Also, due to lack of confinement of AuNPs on model cubic sample there is a shift of the whole distribution plots into higher size values (Fig. S21 in ESI).

To confirm this observation, two-way ANOVA has been conducted on AuNPs size data obtained from TEM images for the samples after propane oxidation, and two levels of presence of dopant (undoped Au<sub>5</sub>/CeO<sub>2</sub> and doped Au<sub>5</sub>/GDC-10%) and two levels of morphology (cubes and HSNPs) have been tested. Because of the lognormal nature of AuNPs size distribution all data were logarithmically transformed and met normality requirements (see details in Fig. S23 in ESI). The interaction between the dopant presence and morphology was significant,  $F(1,1307)=272.89$ ,  $p < .001$ . Tukey HSD post-hoc analysis has shown that there is no significant difference between the size of AuNPs embedded in Au<sub>5</sub>/CeO<sub>2</sub> cubes and Au<sub>5</sub>/GDC-10% cubes ( $p > .001$ ). Oppositely, there is significant difference in AuNPs size embedded in Au<sub>5</sub>/CeO<sub>2</sub> HSNPs and Au<sub>5</sub>/GDC-10% HSNPs ( $p < .001$ ). Comparison of mode values in size distribution of 4.2 nm for Au<sub>5</sub>/CeO<sub>2</sub> HSNPs and 7.5 nm for Au<sub>5</sub>/GDC-10% HSNPs proves the rapid growth of particles within doped system. Interestingly, there is significant difference between AuNPs size on the undoped Au<sub>5</sub>/CeO<sub>2</sub> cubes and the undoped Au<sub>5</sub>/CeO<sub>2</sub> hierarchically structured particles ( $p < .001$ ) with mode values in size distribution having 4.2 nm and 5.1 nm, respectively.

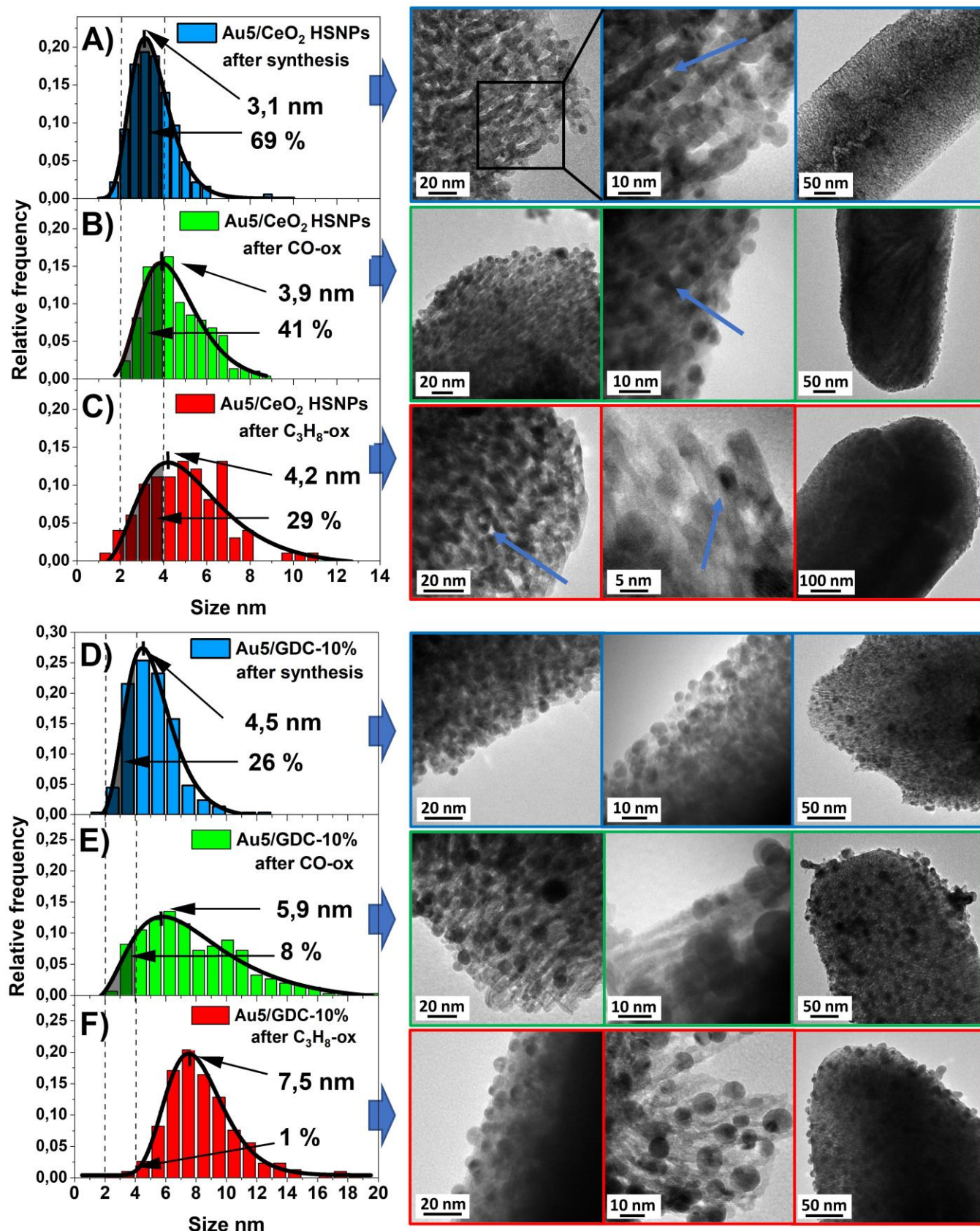


Fig. 14. Size distribution plots of AuNPs before and after of CO or propane oxidation with corresponding representative TEM images; confined gold nanoparticles marked by arrows. A) Au5/CeO<sub>2</sub> HSNPs after synthesis; B) Au5/CeO<sub>2</sub> HSNPs after CO-ox; C) Au5/CeO<sub>2</sub> HSNPs after propane-ox; D) Au5/GDC-10% HSNPs after synthesis E) Au5/GDC-10% HSNPs after CO-ox; F) Au5/GDC-10% HSNPs after propane-ox.

This proves confinement of nano-gold within CeO<sub>2</sub> hierarchically structured support. Significant difference between AuNPs size on the Gd-doped cubes and the Gd-doped hierarchically structured particles ( $p < .001$ ) proves, again, the rapid growth of particles that may be caused by support intergrowth commented earlier.

## 4. Discussion

**The pertinence of surface coverage parameter.** The deposition-precipitation is an effective method for the knowledgeable decoration of the hierarchically structured catalyst support by nano-gold leading to formation of variety of architectures (cf. Fig. 3). Gold deposition is controlled by selecting the appropriate value of the surface coverage parameter (SC) based on knowledge of the specific surface area of the catalyst support. This parameter has been identified as an important factor controlling a form of gold on the model ceria nanocubes, since thin islands/layer of gold form for low values of surface coverage ( $M_{Au}/S_{CeO_2} = 2$ ), and exceeding some threshold value leads to the growth of nanoparticles according to the Stranski-Krastanov (SK) model, as the most likely scenario.<sup>53</sup> In this study, the use of the small value of SC = 2 leads to the formation of AuNPs that deposit along the pores inside the hierarchical support (cf. Fig 2, Fig. 5, ET in ESI). Accelerated diffusion of metal precursor into the crystal mesopores may be responsible for the formation of nano-gold particles in the interior of hierarchical support at first when relatively low SC values are used.<sup>34</sup> Due to the confinement of AuNPs within hierarchical support the metal-support contact is increased, which is discussed in the literature as the deciding factor facilitating catalytic activity.<sup>84,106</sup>

At the same time, this approach is not effective for precise gold decoration of the non-hierarchically structured ceria support that is composed of loosely arranged nanoparticles, leading to the formation of large gold crystals (5-30 nm) next to the ceria nanosized particles (cf. Fig 6.D.c), and the gold loadings in terms of SC values deviates strongly from the nominal ones (cf. Fig 7.B). This indicates that the organization of the ceria nanoparticles into a hierarchical structure allows for easier manipulation of the material in terms of its further processing in metal deposition while retaining nanosized properties of the support at the same time.<sup>107</sup>

Variety of effective gold deposition methods have been presented in the literature,<sup>108</sup> and the deposition-precipitation procedure with the use of HAuCl<sub>4</sub> as gold precursor significantly improves propane oxidation activity of ceria-based catalysts when compared to other gold precursors such as AuBr<sub>3</sub> and AuI.<sup>87</sup> An advantage of this method lies in the ability to control the chemical form of the hydroxychloro gold (III) complexes  $[Au(OH)_xCl_{4-x}]^-$  by means of pH variation and the ability to adjust pH value to the isoelectric point of the support. Thanks to this, gold complexes deposit on the support while avoiding the formation of molecular aggregates in solution.<sup>108</sup> However, when the precursor amount exceeds support capacity for gold loading, which for the systems investigated in this study has a relatively high value (SC = 8), some

gold agglomerates form on the exterior surface of hierarchical support (cf. Fig. 3.D), which leads to decrease in metal-support contact. Due to large capacity for metal loading hierarchical systems have promising use in electrocatalysis.<sup>109</sup>

**The influence of Gd doping on the structural hierarchy of the gold decorated catalyst.** The 4<sup>th</sup> level of hierarchical structure of the studied systems is comprised of metal nanoparticles intentionally dispersed in various regions of the support hierarchical microparticle, either inside or inside/the exterior surface. The distribution and size of AuNPs are dependent not only on the surface coverage parameter value used in deposition-precipitation procedure, but also on the architecture of the support (pore size and geometry) that may be modulated by doping. In the literature, doping of ceria hierarchical systems has several beneficial effects, such as the hindrance of growth of support particles,<sup>110</sup> formation of additional pores due to collective intergrowth of support particles,<sup>51</sup> or increased activity and stability of catalytic support in catalytic oxidation.<sup>51,111</sup>

In this study, deposition of AuNPs on hierarchical supports leads to the formation of systems with various metal nanoparticles distributions depending on the dopant presence within ceria. For undoped CeO<sub>2</sub> HSNPs gold nanoparticles are dispersed relatively evenly throughout the interior and exterior surface of the support particles. The narrow size distribution of AuNPs ( $d_{av} = 3.5 \pm 1.0$  nm) is owned to sufficient pore sizes of the support (~1-4 nm) for AuNPs growth (cf. Fig 5.C). In contrast, for Gd-doped HSNPs systems - for which pores are smaller (~1-2 nm) - formation of larger AuNPs ( $d_{av} = 5.1 \pm 1.6$  nm) on the exterior surface of hierarchical support has been observed (cf. Fig. 5.D). Interestingly, doping model ceria nanocubes by 10% Gd has not influenced the size of AuNPs, since no difference in the dominant size values was observed in comparisons between undoped and doped systems (Fig. S21.E in ESI). This result is contrary to study by Sudarsanam et al. that revealed promotional role of dopants (Fe<sup>3+</sup>, La<sup>3+</sup> and Zr<sup>4+</sup>) for obtaining smaller AuNPs on doped cerium oxide.<sup>104</sup>

The distinctive AuNPs growth for HSNPs may be rationalized by difference in the architecture between two hierarchical supports. From the one hand, similar decrease of the surface area after gold deposition (~20%) and comparable gold content in both Au5/GDC-10% HSNPs and Au5/CeO<sub>2</sub> HSNPs systems (~23-24 wt%) indicates comparable gold loading. As TEM and PXRD results suggest, subnanometer gold clusters form within both hierarchical systems (cf. Fig. S2 in ESI). Besides the larger total surface area of Gd-doped hierarchically structured catalyst support (158 m<sup>2</sup>/g), the available internal space for the growth of optimal-sized gold nanoparticles is reduced as compared to undoped one (144 m<sup>2</sup>/g). Larger pores of CeO<sub>2</sub> HSNPs allow more unrestrained growth of AuNPs inside hierarchical structure. From the other hand, considering the low melting temperature of Au clusters,<sup>85</sup> smaller pores in Gd-doped system may aid gold migration and coalescence on the not spatially-restrained exterior surface of microparticles. Thermally induced

diffusion of atomically dispersed Au outward to the surface has been observed by Allard et al.<sup>112</sup>

Also, the difference in texture of the exterior surface of HSNPs may explain observed effect of AuNPs size differences, since the growth of Au on CeO<sub>2</sub> HSNPs proceeds on crystallites exposing (111)/(100) planes as opposed to smooth (100) planes on GDC-10% HSNPs. Wang et al. showed that the strength of gold-ceria interaction follows the order (110) > (111) > (100), and weakened interaction on (100) surface is caused by formation of oxygen vacancies in the subsurface region.<sup>113</sup> A significant amount of (111) planes exposed in CeO<sub>2</sub> HSNPs support may stabilize AuNPs due to anchoring of nanoparticles on oxygen vacancies.<sup>114</sup> This, again, confirms that difference in architecture influences form of gold in catalyst. Hence, inadequate selection of the value of the surface coverage parameter without considering the nature of porosity within hierarchical catalyst support leads to production of material that is characterized by occurrence of a significant fraction of particles with sizes that do not fall within the desired values of the catalytic optimum for specified reaction (like size < 5 nm for CO oxidation).

**The surface properties of catalysts.** Thorough chemical properties inspection provided several interesting observations. Firstly, the results of H<sub>2</sub>-TPR, CO-TPR and NAP-XPS measurements are apparently contradictory, since H<sub>2</sub>-TPR indicates an improvement of surface reducibility over bulk one when catalyst is doped with 10% Gd<sup>3+</sup> (see Table 1), while CO-TPR and NAP-XPS show a slight decline of surface reducibility for Gd-doped catalysts. Moreover, calculation of surface-to-bulk reducibility ratio based on CO-TPR data, but applying the same approach as applied to H<sub>2</sub>-TPR data, indicates that doping does not significantly change this proportion (cf. Fig. S13.B in ESI). As CO-TPR and XPS are surface sensitive techniques, it may be concluded that doping ceria matrix slightly lowers surface reducibility of catalysts. Simultaneously, the H<sub>2</sub>-TPR study allows to evaluate sub-surface reducibility due to the higher penetration potential of small hydrogen molecules, and the results prove that doping of ceria matrix facilitates capability of oxygen migration in sub-surface and bulk regions of ceria particles. This translates into facilitated catalytic activity of Gd-doped gold catalysts, like in propane oxidation tests (cf. Fig. 11), despite slightly reduced surface reducibility of the support. Hence, it is postulated that catalytic activity enhancement of Gd-doped systems stems from facilitated supply of oxygen from sub-surface/bulk regions to the catalyst surface. As shown in the literature, doping of CeO<sub>2</sub> with diverse types of trivalent (Ga<sup>3+</sup>) or tetravalent (Zr<sup>4+</sup>) cations has been chosen as an important factor in improving the lattice oxygen mobility.<sup>115,116</sup>

Secondly, over twofold increase of the gold loading within ceria hierarchical supports, from SC = 2 to SC = 5, does not significantly change the H<sub>2</sub>-TPR (Fig. 8.C) and CO-TPR reducibility profiles, qualitatively and quantitatively (Fig. 9.B). Closer inspection of H<sub>2</sub>-TPR results shows that the amount of active oxygen decreases along with the increase of gold loading (total H<sub>2</sub> consumption is 1.21 mmol/g for Au0.5/CeO<sub>2</sub> and 1.07 mmol/g for Au5/CeO<sub>2</sub>), which may be caused by lowering accessibility of the metal active phase due to blocking the pores by nanoparticles within pores. Similar effect was observed

by Cargnello et al., however, despite lower metal accessibility the catalytic activity was enhanced that may be ascribed to increased metal-support interaction.<sup>84</sup> Nevertheless, total H<sub>2</sub> consumption reaches 1.09 mmol/g for the no gold-containing star-shaped catalyst support,<sup>23</sup> which indicates that decoration of support by gold, actually increases the amount of active oxygen that may be linked to increasing CeO<sub>2</sub> oxygen mobility at the Au-support contact by weakening Ce-O bond.<sup>70</sup>

NAP-XPS study has shown that gold nanoparticles deposited on CeO<sub>2</sub> HSNPs undergo more dynamical changes under various atmospheres as compared to Gd-doped support. In the literature, small contact angle between Au nanoparticle and CeO<sub>2</sub> support (39°), indicating more strong metal-support interaction, is increased to 127° when Au is deposited on Gd<sub>2</sub>O<sub>3</sub>, which indicates weak metal support interaction.<sup>117</sup> Interestingly, the higher rigidity of Au on Gd-doped sample does not translate into sintering-resistance, since statistical analysis has shown that AuNPs grow similarly on (100) surface of model Au5/CeO<sub>2</sub> cubes and Au5/GDC-10% cubes (cf. Fig S21).

Also, dopant surface segregation in Gd-doped hierarchical support is not excluded, since composition measurements by various techniques gives slightly different values, 11.6% (SEM-EDS, global concentration) and 17.8% (NAP-XPS, surface concentration). Also, the comparison of the mean size of crystallites in GDC-10% HSNPs determined in TEM and PXRD suggests that hierarchical support is composed of smaller nanoparticles at the edges of the arms (4.1 nm, volume-weighted mean from TEM) and possibly with larger crystals inside the material (6.9 nm from PXRD). Due to larger surface-to-volume ratio in smaller nanoparticles, exposure of dopant excess may be observed in the outer regions of the stars-shaped particle arms.

The literature on the subject studying gold model catalysts enumerates many factors affecting activity.<sup>5</sup> For this reason, the total activity of the real working catalyst may be contributed by many mechanisms, and reaction may proceed along many paths.<sup>96,118</sup> Also, reaction mechanisms vary depending on oxidation reaction.<sup>7</sup> Comparison of CO oxidation performance between Au/ceria-based catalysts studied in this work with benchmark Pt/Al<sub>2</sub>O<sub>3</sub> shows superiority of gold systems. Specific rate of commercial 5wt%-Pt/Al<sub>2</sub>O<sub>3</sub> catalyst is one order of magnitude lower than for 5.3wt%-Au/CeO<sub>2</sub> cubes studied here, having  $r_{25^\circ\text{C}} = 0.006 \text{ mol}_{\text{CO}} \text{ g}_{\text{Pt}}^{-1} \text{ h}^{-1}$  and  $r_{25^\circ\text{C}} = 0.04 \text{ mol}_{\text{CO}} \text{ g}_{\text{Au}}^{-1} \text{ h}^{-1}$ , respectively.<sup>119</sup> Hierarchical gold systems show even higher specific rate values (see Table 3). However, propane oxidation at 300°C for Pt/Al<sub>2</sub>O<sub>3</sub> is one order of magnitude higher (TOF<sub>300°C</sub> = ~0.05 s<sup>-1</sup>) than gold-based catalysts.<sup>120</sup> Alloying Au NPs may be a way to increase activity of studied systems

In the following parts, the influence of catalyst architecture and gold loading on CO and propane oxidation will be discussed.

**The role of catalyst architecture and surface chemistry in CO oxidation.** Due to the adopted synthetic approach a hierarchical catalyst support having three defined structural levels was produced, and material is composed of ceria nanoparticles exposing predominantly (100) crystal planes (1<sup>st</sup> level of hierarchical

organization), which are arranged in an ordered manner forming mesocrystal that is characterized by expanded pore system (2<sup>nd</sup> level of hierarchical organization). Morphology-controlled study by Li et al. have shown that ceria nanoparticles with well-defined crystal planes show higher catalytic activity over irregularly shaped nanoparticles.<sup>121</sup> Also, the CO oxidation activity of non-gold-decorated star-shaped hierarchical support is enhanced due to mutual organization of ceria crystallites that introduces porosity which, in turn, facilitates mass transfer.<sup>23</sup>

It is believed that CO oxidation proceeds through Mars-van Krevelen mechanism on Au/CeO<sub>2</sub>,<sup>122,123</sup> and the final catalytic activity, especially in real catalytic system, is a combination of several factors such as activation of oxygen (either by molecular oxygen, or atomic oxygen, or surface hydroxyls), efficiency of oxygen replenishment on active catalytic support, and degree of CO chemisorption on gold nanoparticles.<sup>5,124</sup> Guo et al. have shown that metallic gold, either as nanoparticles or clusters, plays much more critical role in low-temperature CO oxidation than cationic gold species.<sup>125</sup> In this study, hierarchical support having small pores facilitates formation of sufficiently small gold nanoparticles inside the porous structure. Due to that the metal-support contact is increased. Enhancement of CO oxidation performance for gold-decorated HSNPs as compared to gold-decorated cubes is ascribed to confinement of nano-gold particles within porous support (see Fig. 13 and TOF<sub>[b]</sub> in Table 3). However, overgrowth of gold nanoparticles on Au5/GDC-10% causes slight decline in intrinsic activity. Hence, simultaneous formation of optimal-sized AuNPs as well as the increased extent of metal-support contact improves catalytic activity of hierarchical catalysts.<sup>84</sup>

Since the size of the pores in the studied hierarchical systems is favorable for formation of ultrasmall gold nanoparticles [Fig. S2.C in ESI], the question about the influence of support architecture on the electronic state of nano-gold and its role in catalytic oxidation is of significant importance. The onset average size of Au NP for the shift from "molecular-like" to "metallic" properties is 1.7 nm (cluster composed of 147 gold atoms) and cross-over region lies between 150-250 atoms.<sup>126,127</sup> Bond pointed out that fractional positive or negative charges characteristic for gold clusters being in non-metallic state may account enhanced catalytic activity.<sup>124</sup> Also, gold clusters can oxidize CO via activation of O<sub>2</sub> by electron transfer.<sup>128</sup> From the other hand, Qian et al. point out that low-coordinated Au atoms on Au nanoparticles with bulk Au-like electronic structure are active site in low-temperature CO oxidation.<sup>129</sup> Also, Chen et al. have demonstrated that the catalytic activity is contributed by the size-dependent different reaction pathways.<sup>97</sup> For Au/CeO<sub>2</sub> with Au particles of 3.7 ± 0.9 nm CO oxidation is contributed by reaction pathway of CO adsorbed on Au nanoparticle as well as by reaction pathways of carbonate, bicarbonate and formate facilitated decomposition. For Au NPs of 1.7 ± 0.6 nm the oxidation is contributed by adsorbed CO and other species act as spectators and even likely block active sites.

Taking this into account it is not excluded that the presence of small clusters inside hierarchical support may be responsible for activity enhancement when compared to non-hierarchical cubes.

However, the exact proportion of small gold clusters within systems is not known. XPS being the surface-sensitive technique is not able to indicate the gold state inside hierarchical supports. Nevertheless, taking into account that Au NP are formed after exceeding a certain threshold of gold content,<sup>53</sup> and this condition is met for both Au2 and Au5 systems tested in CO oxidation, moreover presence of Au nanoparticles is confirmed by TEM, it is assumed in this study that histograms reflects size distribution of gold inside support having pores sufficiently large for NP growth with size range of 2-4 nm that reflects cross-over region between non-metallic and bulk metallic state.

Surface chemical characterization indicates the advantages of hierarchically structured materials. H<sub>2</sub>-TPR study has shown that Au/HSNPs have the highest amount of active oxygen over powdered cubes and NPs. This is linked to exposition of the mutually ordered and highly active CeO<sub>2</sub>(100) planes within hierarchical catalyst (TEM study) and increased surface area (BET). Also, Au/CeO<sub>2</sub> HSNPs have a slightly higher amount of active oxygen over Gd catalyst in reducing conditions (CO-TPR). However, this technique does not provide information about dynamical aspect of catalyst function in real conditions, in which O<sub>2</sub> replenishing is important. Hence, NAP-XPS was employed, and the results show that the extent of active surface oxygen in Gd-doped HSNPs is slightly lowered, however, the effectivity in oxygen replenishment is as effective as on CeO<sub>2</sub> HSNPs catalyst (cf. Fig. 10).

A mechanism involving hydroxyls has been proposed as playing a significant role in enhancing CO oxidation.<sup>5</sup> Gold presence on the metal oxide support (Au/Fe<sub>2</sub>O<sub>3</sub>) has been proven to enhance formation of hydroxyl groups as compared to bare support,<sup>5</sup> which is also observed in Au/CeO<sub>2</sub> catalysts studied here. CO-TPR results have shown that higher number of hydrogen was present in Au2/CeO<sub>2</sub> HSNPs and Au5/GDC-10% HSNPs catalysts, that in turn, showed the lowest CO oxidation activity among studied samples. Davó-Quñonero et al. have shown that the presence of OH groups on ceria may hinder CO adsorption due to less basicity of OH groups that hamper reaction with acidic CO as well due to lower concentration of available O sites.<sup>130</sup> On the contrary, Au2/GDC-10% HSNPs and Au5/CeO<sub>2</sub> HSNPs catalysts show the highest activity in CO oxidation with the similar course of reaction (cf. Fig. 13.A), however, this samples differ in the considerable extent in the amount of surface oxygen available for reaction (Fig. 9.B and S13.A in ESI). Hence, the mere amount of active oxygen contained in the catalyst (as well as its oxygen replenishment potential), does not play decisive role in activity enhancement, but an additional factor influencing activation of oxygen in real operating conditions must play critical role.

In this study the order of T<sub>50</sub> in CO oxidation follows the order of gold nanoparticles population magnitude with as chosen optimal size of 2-4 nm. According to the literature the nanoparticles of gold with a size of about 3 nm show the highest activity in the low temperature catalytic reactions.<sup>93,131</sup> Also, the number of AuNPs having certain size may be a factor that modulates catalytic activity, since adsorption energy of CO on metal nanoparticles (as tested on unsupported Pd<sub>n</sub> clusters) is a size-dependent property, and shows the lowest values for effective particle diameter of 1-2 nm.<sup>132</sup> Thus,

designing material with optimal particles size distribution and keeping this distribution stable is an important challenge in real catalyst development. Here, the size of nanoparticles is controlled by the surface coverage parameter and the dopant-dependent support architecture. The optimally sized AuNPs are confined within the pores of the same sizes. This increases metal-support interaction that may be responsible for lowering CO oxidation activity when compared to Au5/CeO<sub>2</sub> cubes catalyst exposing similar CeO<sub>2</sub>(100) planes.

Comparison of CO oxidation performance to known catalysts described in the literature for which conversion at 25°C was reported shows general similarity in the order of magnitude of specific rate values. Comparison to systems containing gold in polyform state, having relatively broad Au size distributions, shows superiority of CeO<sub>2</sub> hierarchical systems over powdered Au/nano-CeO<sub>2</sub> catalysts. (see ref.<sup>97,98</sup> in Table 3) However, some powdered systems shows relatively high specific rate (ref. <sup>99,104</sup> in Table 3) that may be caused by different synthetic methods used to prepare catalysts. Specific rate value for comparative catalyst (Au5/CeO<sub>2</sub> cubes) is within the literature range for gold-decorated cubes (Table 3). The advantage of this study is that the systems were synthesized using the same procedure and were tested under the same conditions, which enable rigorous comparisons between catalysts. Interestingly, comparison of Au2/CeO<sub>2</sub> HSNPs system to hierarchical catalyst having similar gold loading, Au/(hierarchical/nano)-CeO<sub>2</sub> (hollow nanospheres), shows slightly elevated specific rate for star-shaped catalyst. Nevertheless, Gond et al. have shown a converted U-shape dependence of specific rate as a function of gold loading,<sup>103</sup> so testing CO oxidation activity of star-shaped catalysts with Au loading <10% would be worth to study.

**The role of catalyst architecture and gold loading in propane oxidation.** Hierarchical catalysts have shown increased propane oxidation performance over nonpowdered cubes and NPs (cf. Fig. 11). This effect may stem from increased surface area due to mutual regular arrangement of ceria nanoparticles forming hierarchical structure. Ali et al. have indicated that large surface area and small crystallite size are the key factors in complete propane oxidation.<sup>87</sup> Also, Solsona et al. have shown, the main properties determining propane oxidation activity seem to be the surface area and the number of bulk/sub-surface defects.<sup>133</sup>

The studied hierarchical materials may take on high amount of gold (even 24 wt%) due to large surface area. Whereas in many systems high gold loading decrease oxidation activity, i.e. Cu-10% deposited on CeO<sub>2</sub> (octahedra) showed lower CO oxidation activity than Cu-4% counterpart,<sup>134</sup> here increasing gold up to 23wt% (Au5/CeO<sub>2</sub> HSNPs) keeps propane oxidation performance at relatively similar level (see TOF<sub>[a]</sub> in Table 2). However, lower gold loadings (Au-2.7wt% in Au0.5/HSNPs) seems to have ambiguous impact on propane oxidation performance. Due to low value of surface coverage parameter (SC = 0.5) it is likely that small Au clusters are formed inside hierarchical support and gold is in highly dispersed form. Hence, TOF<sub>[a]</sub> and specific rate metrics are higher when compared to other systems. The fraction of low-coordinated Au

atoms on gold particles and clusters may be the active sites that enhances catalytic performance. It is possible that significant fraction of such gold entities show no-metallic properties due to small size. From the other hand, Au0.5/HSNPs systems show one of the highest activation energies for propane oxidation. As Chen et al. have shown, there are more reaction pathways for larger Au particles,<sup>97</sup> which may explain lowering activation energy for higher gold loaded systems, and relatively high values for low gold-loaded ones.

Blick et al. have demonstrated that gold in the form of 2D-rafts has caused lowering of methane oxidation activity by blocking methane coupling reactions that occur on oxygen vacancies, and the presence of 3D particles of gold, having size of 5-10 nm, were necessary to invoke Au/MgO activity.<sup>135</sup> Taking this into consideration, the reduced propane oxidation activity in Au0.5/CeO<sub>2</sub> HSNPs and Au0.5/GDC-10% HSNPs, being lower than no gold-containing supports, seems to be caused by blocking support active sites by clusters/layers of gold. Hence, the appropriate selection of SC value leading to production of nanoparticles in hierarchical system is crucial to improve the propane oxidation activity.

As shown in the literature, the mechanism of propane oxidation on ceria-supported Au catalyst involves activation of C-H and C-C bonds by Au<sup>+1</sup> and Au<sup>+3</sup> ionic forms of gold with subsequent formation of radicals that may be attacked by free electron present on reduced ceria.<sup>87</sup> On the contrary, Wang et al. have shown that metallic species are beneficial for activation of C-H bond during propane oxidation and the high concentration of metallic Pt particles on the Nb<sub>2</sub>O<sub>5</sub> catalyst support is responsible for higher propane oxidation activity over Pt/CeO<sub>2</sub> catalyst in which oxidized forms of Pt were detected.<sup>136</sup> This study has shown no presence of Au<sup>3+</sup> and scarce amount of Au<sup>+</sup> with dominance of metallic gold that leaves an open question about the dominant propane oxidation reaction path on Au/ceria, especially if the form of gold inside the material has been not detected. Nevertheless, considering H<sub>2</sub>-TPR and TEM results it is inferred that metallic AuNPs are formed inside the hierarchical support and presence of AuNPs is crucial for propane oxidation activity facilitation.

Comparison of propane oxidation performance to known gold on ceria catalysts shows the same order of magnitude of specific rate at 300°C but the exact values are slightly lower (see Table 2). Au2/GDC-10% HSNPs system shows the highest performance among the studied systems that surpass the non-hierarchical and hierarchical gold catalysts described in the literature.

Whereas on Au/CeO<sub>2</sub> HSNPs, gold nanoparticles grow inside due to well-fitted pores to adopt optimal size, for Au/GDC-10% HSNPs there is over-growth of AuNPs on the exterior surface of hierarchical support. This may be linked to exposition of mainly (100) on which gold species may move easier than on more varied (100)/(111) surface of Au/CeO<sub>2</sub> HSNPs. CeO<sub>2</sub>(111) planes may stabilize AuNPs due to anchoring of nanoparticles on oxygen vacancies.<sup>114</sup>

The problem of large amount of Au, disadvantage from economical point of view, may be resolved by using smaller amount of hierarchical catalyst in industrial use. As H<sub>2</sub>-TPR results have shown, 2.2-fold mass decrease of Au2/CeO<sub>2</sub> HSNPs would equalize absolute surface reduction values to Au5/cubes.

**Structural merits of the hierarchical architecture that improve catalytic oxidation.** Several correlations between catalytic activity and structural merits of the architecture of hierarchical catalysts has been identified such as: (1) high specific surface area, (2) metal nanoparticles confinement, (3) metal nanoparticles size and metal-support interaction, (4) hierarchical catalyst stability.<sup>137</sup> They will be discussed in this order.

Firstly, the arrangement of the ceria nanoparticles into a hierarchical structure produces support with high specific surface area that increases intrinsic activity in propane oxidation when compared to non-hierarchical supports (cubes, NPs). This is probably due to facilitated transfer of reagents to the surface-active sites.<sup>23</sup> This trend is retained also for gold-decorated systems when hierarchical Au/HSNPs are compared with non-hierarchical Au/NPs. Au/cubes have slightly higher intrinsic activity that may be linked to differences in gold embedding, being either on extended flat surfaces or on rather composite arrangement of nanoparticles).

Secondly, confinement of AuNPs inside the hierarchical support boosts intrinsic activity when compared to gold-decorated nanocubes in which nanoparticles are deposited on the surface (cf. Fig 6.D.f). This effect is due to increased metal-support interaction in hierarchical system,<sup>138</sup> but cannot be explained solely by this factor. Additional decoration of the exterior surface of the star-shaped hierarchical particles (through increasing gold loading) does not substantially improve CO oxidation activity (cf. Table 3), even though the number of metal-support active sites are increased. Hence, the presence of optimally-sized AuNPs inside the pores of hierarchical support plays a crucial role in reducing CO oxidation temperature. Decreasing gold loading in hierarchical catalysts into the level of Au5/cubes is worth to evaluate to check if catalytically active form of gold (in CO oxidation) will grow inside hierarchical support, especially when industrial application demands low Au loadings.

Thirdly, the size of nanoparticles confined within pores of hierarchical supports falls within range of catalytic activity for CO and propane oxidation (< 5 nm). Many studies have shown that catalytic activity is a size-dependent process, and the optimum size of metal nanoparticles depends on the type of catalytic reaction.<sup>139</sup> Whereas optimum size of AuNPs for CO oxidation deposited on TiO<sub>2</sub> is 3.5 nm,<sup>93</sup> the optimum size for aerobic oxidation of alcohols on Au/CeO<sub>2</sub> is 6.9 nm. Also, propene epoxidation was more effective when catalyzed by Au clusters (1-2 nm) than Au nanoparticles (>2nm).<sup>140</sup> Reduction of 4-nitrophenol increases while increasing the diameter of Au nanoparticles in the range 10-58 nm.<sup>141</sup> Hierarchical support has a potential for embedding size-selected metal particles, either confined within pores or on the exterior surface of particles, tailored for specific reaction.

Fourthly, CeO<sub>2</sub> HSNPs prevent AuNPs growth during oxidation reaction due to pore confinement and stability of architecture in higher temperatures (cf. Fig. 14). The tendency for sintering of nano-Au is caused by reducing melting temperature of gold linked to quantum-size effects (i.e., 600 K for Au particles with diameter of 2 nm).<sup>6,85</sup> Masoud et al. have shown that AuNPs grow upon thermal treatment irrespective of the support character, being either

reducible (TiO<sub>2</sub>) or non-reducible (SiO<sub>2</sub>, Al<sub>2</sub>O<sub>3</sub>), however, the growth of gold nanoparticles deposited on reducible TiO<sub>2</sub> oxide is more pronounced and proceeds through Ostwald ripening as most likely growing mechanism.<sup>142</sup>

Typical lifetime of industrial catalysts for low temperature water gas shift reaction reaches 2-4 years.<sup>143</sup> Several factors contribute to catalyst stability such as resistance to poisoning and fouling, lack of thermal degradation and sintering, resistance to vapor formation or solid-solid reactions. Loss of stability of Au/ceria systems has been reported in the literature and possible factors that influences activity decline has been identified as: Au NPs growth, over-reduction of ceria, poisoning by carbon-related species.<sup>144</sup> Au/ceria system is generally of not heightened stability, and Au/zeolite is a promising more stable candidate for CO and VOC oxidation.<sup>120</sup> However, in this study the influence of hierarchical architecture on stability of gold nanoparticles was tested, and it was shown that confinement of gold nanoparticles within hierarchical support allows to preserve significant fraction of small gold nanoparticles that play an important role in low-temperature CO oxidation. To further increase active phase stability alloying of Au nanoparticles is a possible strategy.<sup>143</sup> Also, addition of catalytic promoters may suppress gold migration within pores of hierarchical support. From the other hand doping ceria support is a strategy to increase stability of hierarchical catalyst support.<sup>51</sup>

As Lu et al. confirms, gold sintering emerges at CO treated Au/CeO<sub>2</sub>(111), thus its stability is intimately connected with reactivity.<sup>145</sup> In this research, TEM investigation followed by statistical testing shows that growth of AuNPs in oxidation reactions depends on the architecture of the catalyst support. For cubes having flat surface the AuNPs growth after oxidation reaction is not affected by the presence of dopant in ceria matrix. However, the growth of AuNPs is faster on Gd-doped hierarchical support. This may be rationalized by observation that architecture of Gd-doped sample changes with the temperature.<sup>51</sup> The reduced sintering resistance of AuNPs on Gd-doped hierarchically structured catalyst may be caused by the collective intergrowth of support nanoparticles that forces out AuNPs from the pores of the material. Confinement of metal particles is advantageous only when the porous material is stable under reaction conditions.<sup>137</sup> Depositing nano-gold on the preheated GDC-10% HSNPs support, on which architecture changes have already taken place, followed by catalytic testing would examine this hypothesis.

Also, smaller pores within GDC-10% HSNPs induce formation of subnanometer Au clusters that possess decreased melting temperature, that in turn facilitates migration and growth of AuNPs on the surface of the support microparticle. Thus, the architecture of the support influences the properties of metal particles, which should be taken into consideration during the design of hierarchical catalysts.

Alternatively, faster growth of AuNPs on GDC-10% HSNPs may be caused by lowering metal-support interaction, which is pronounced due to large exposure of Gd dopant on the surface of small support nanoparticles ( $d_{av} = 3.2$  nm (TEM); 6.9 nm (PXRD)). Hu and Li have shown that sintering kinetics exhibit volcano dependence on metal-



support binding energy.<sup>146</sup> Perhaps changes of surface characteristics is sufficient for changing mechanism of growth from Ostwald ripening to particle migration in hierarchical systems composed of small support particles. Further in situ study is necessary to confirm this hypothesis. Also, investigating the materials in several catalytic cycles to check whether the gold confinement will maintain the stability of the material, or it will clog the pores and thus lower the catalytic performance is direction worth to pursue.

To sum up, the catalytic activity of complex hierarchical materials decorated with gold varies depending on the type of reaction and material characteristics. The acquired knowledge allows for knowledgeable design of multifunctional material and adapting its form to specific needs. Decoration of hierarchical supports with less expensive metals or creation of mixed-metal systems would allow to further exploit the potential of hierarchical catalysts.

## Conclusions

In this contribution, knowledge-driven design of highly active working catalyst substantially enhancing CO and propane oxidation owing to hierarchical architecture has been presented.

The findings are summarized below:

1. Shape-selective synthesis followed by wet chemical gold deposition produces hierarchical catalyst having Au and ceria particles in size below 5 nm. Exposition of active (100) ceria crystal planes and extensive porosity of mesocrystal support as well as nano-gold confinement increases metal-support contact. Due to that exceptional increase in H<sub>2</sub>-TPR surface reducibility is observed.
2. Adjustment of the surface coverage parameter in gold deposition procedure allows to knowledgeably design hierarchical catalyst with various gold forms (layer/cluster, nanoparticle, or particle agglomerates) localized in different parts of hierarchical support. Due to high specific surface area such support is capable for taking high metal loadings that is restricted on powdered non-hierarchical systems.
3. Increasing gold loading does not necessary lead to catalytic oxidation enhancement. Pore geometry and size may restrict the growth of optimal-sized AuNPs leading to activity decline. Thus, the knowledge of the materials porosity is necessary for optimal catalyst design.
4. Gd doping facilitates propane oxidation for both non-hierarchical and hierarchical gold catalysts, showing two-fold TOF increase. Also, the Gd-doped hierarchical gold catalyst shows four-fold TOF increase over the undoped non-hierarchical one, proving the synergistic effect of doping and structural hierarchy in propane oxidation.
5. Hierarchical gold catalysts (Au<sub>5</sub>/CeO<sub>2</sub>) reduces CO oxidation to ambient temperature (T<sub>50</sub>=18°C) as compared to non-hierarchical gold-decorated

Au<sub>5</sub>/CeO<sub>2</sub> nanocubes (T<sub>50</sub> = 85°C). This effect is caused by the confinement of AuNPs within pores of hierarchical support. Analysis of interdependence between catalyst architecture, AuNPs size, and gold loading indicates that presence of optimally-sized Au NPs leads to enhancement of CO oxidation. Trade-off between gold size and maximization of Au/interface contact within hierarchical support is crucial in catalytic performance facilitation.

6. Stability of AuNPs is increased by confinement of particles within the hierarchical structure when compared to gold-decorated ceria nanocubes in which AuNPs are present only at the surface.
7. Several structural merits of the architecture of hierarchical catalyst are linked to catalytic oxidation enhancement: (1) high specific surface area, (2) mutual arrangement of support crystallites (3) metal nanoparticles confinement, (4) optimal size of metal nanoparticles, (5) maximalization of metal-support contact.

## Author Contributions

Piotr Woźniak: Conceptualization, Funding acquisition, Project administration, Methodology, Investigation, Formal analysis, Visualization, Writing - original draft, Writing - review & editing. Małgorzata A. Małecka: Conceptualization, Supervision, Writing - review & editing. Piotr Kraszkwicz: Investigation, Formal analysis, Writing - review & editing. Włodzimierz Miśta: Investigation, Formal analysis. Oleksii Bezkrovnyi: Investigation, Formal analysis. Lidia Chinchilla: Investigation, Formal analysis. Susana Trasobares: Investigation, Formal analysis.

## Conflicts of interest

There are no conflicts to declare.

## Acknowledgements

The research leading to these results has received funding from the European Union Horizon 2020 research and innovation programme under grant agreement No. 823717-ESTEEM3. The authors thank Mrs. Ewa Bukowska, Dr Maciej Ptak and Dr Misha Vorokhta for XRD, ATR-FTIR and NAP-XPS measurements, respectively.

## Notes and references

- 1 G. C. Bond, C. Louis and D. T. Thompson, *Catalysis by Gold, Catalytic Science Series*, 2006, vol. 6.
- 2 A. S. Alshammari, *Catalysts*, 2019, 9.
- 3 A. S. K. Hashmi, *Chem Rev*, 2007, 107, 3180–3211.
- 4 C. M. Hendrich, K. Sekine, T. Koshikawa, K. Tanaka and A. S. K. Hashmi, *Chem Rev*, 2021, 121, 9113–9163.
- 5 R. Meyer, C. Lemire, S. K. Shaikhtudinov and H.-J. Freund, *Surface Chemistry of Catalysis by Gold\**, .

- 6 J. Gong, *Chem Rev*, 2012, **112**, 2987–3054.
- 7 M. Sankar, Q. He, R. v. Engel, M. A. Sainna, A. J. Logsdail, A. Roldan, D. J. Willock, N. Agarwal, C. J. Kiely and G. J. Hutchings, *Chem Rev*, 2020, **120**, 3890–3938.
- 8 T. Takei, T. Akita, I. Nakamura, T. Fujitani, M. Okumura, K. Okazaki, J. Huang, T. Ishida and M. Haruta, in *Advances in Catalysis*, Academic Press Inc., 2012, vol. 55, pp. 1–126.
- 9 J. T. Miller, A. J. Kropf, Y. Zha, J. R. Regalbuto, L. Delannoy, C. Louis, E. Bus and J. A. van Bokhoven, *J Catal*, 2006, **240**, 222–234.
- 10 Z. Kónya, V. F. Puentes, I. Kiricsi, J. Zhu, J. W. Ager, M. K. Ko, H. Frei, P. Alivisatos and G. A. Somorjai, *Chemistry of Materials*, 2003, **15**, 1242–1248.
- 11 S. Cao, F. F. Tao, Y. Tang, Y. Li and J. Yu, *Chem Soc Rev*, 2016, **45**, 4747–4765.
- 12 T. W. van Deelen, C. Hernández Mejía and K. P. de Jong, *Nat Catal*, 2019, **2**, 955–970.
- 13 E. S. Lokteva and E. v. Golubina, *Pure and Applied Chemistry*, 2019, **91**, 609–631.
- 14 A. Trovarelli and J. Llorca, *ACS Catal*, 2017, **7**, 4716–4735.
- 15 T. Tabakova, D. Dimitrov, M. Manzoli, F. Vindigni, P. Petrova, L. Ilieva, R. Zanella and K. Ivanov, *Catal Commun*, 2013, **35**, 51–58.
- 16 P. Xu, R. Yu, H. Ren, L. Zong, J. Chen and X. Xing, *Chem Sci*, 2014, **5**, 4221–4226.
- 17 Z. Zhang, H. Shi, Q. Wu, X. Bu, Y. Yang and J. Zhang, *Mater Lett*, 2019, **242**, 20–23.
- 18 Y. Zhang, Y. Xu, Y. Zhou, S. Xiang, X. Sheng, Q. Wang and C. Zhang, *New Journal of Chemistry*, 2015, **39**, 9372–9379.
- 19 J. Zhang, Y. Jin, C. Li, Y. Shen, L. Han, Z. Hu, X. Di and Z. Liu, *Appl Catal B*, 2009, **91**, 11–20.
- 20 Z. Ma and S. Dai, *ACS Catal*, 2011, **1**, 805–818.
- 21 L.-H. Chen, Y. Li and B.-L. Su, *PERSPECTIVES MATERIALS SCIENCE Special Topic: Hierarchically Porous Materials Hierarchy in materials for maximized efficiency*, 2020.
- 22 L. Zhou and P. O'Brien, *Journal of Physical Chemistry Letters*, 2012, **3**, 620–628.
- 23 P. Woźniak, W. Miśta and M. A. Małecka, *CrystEngComm*, 2020, **22**, 5914–5930.
- 24 J. Zhang, H. Yang, S. Wang, W. Liu, X. Liu, J. Guo and Y. Yang, *CrystEngComm*, 2014, **16**, 8777–8785.
- 25 R. Rao, M. Yang, C. Li, H. Dong, S. Fang and A. Zhang, *J Mater Chem A Mater*, 2015, **3**, 782–788.
- 26 W. Liu, L. Feng, C. Zhang, H. Yang, J. Guo, X. Liu, X. Zhang and Y. Yang, *J Mater Chem A Mater*, 2013, **1**, 6942–6948.
- 27 G. Zhang, Y. Ma, F. Liu, Z. Tong, J. Sha, W. Zhao, M. Liu and Y. Zheng, *Front Chem*, DOI:10.3389/fchem.2021.671220.
- 28 L. Liu, W. He, Z. Fang, Z. Yang, K. Guo and Z. Wang, *Ind Eng Chem Res*, 2020, **59**, 19938–19951.
- 29 A. G. Machoke, A. M. Beltrán, A. Inayat, B. Winter, T. Weissenberger, N. Kruse, R. Güttel, E. Spiecker and W. Schwieger, *Advanced Materials*, 2015, **27**, 1066–1070.
- 30 Z. Nie, A. Petukhova and E. Kumacheva, *Nat Nanotechnol*, 2010, **5**, 15–25.
- 31 M. G. Ma and H. Cölfen, *Curr Opin Colloid Interface Sci*, 2014, **19**, 56–65.
- 32 K. Ariga, M. Nishikawa, T. Mori, J. Takeya, L. K. Shrestha and J. P. Hill, *Sci Technol Adv Mater*, 2019, **20**, 51–95.
- 33 M. Halhouli, J. Kieninger, O. Yurchenko and G. Urban, *ChemCatChem*, 2017, **9**, 354–364.
- 34 D. Xu, H. Lv and B. Liu, *Front Chem*, 2018, **6**.
- 35 *Exploring the Significance of Structural Hierarchy in Material Systems—A review Ning Pan Nanomaterials in the Environment, Agriculture & Technology (NEAT) Biological System Engineering*, .
- 36 M. O. Coppens, T. Weissenberger, Q. Zhang and G. Ye, *Adv Mater Interfaces*, 2021, **8**.
- 37 D. R. Mullins, *Surf Sci Rep*, 2015, **70**, 42–85.
- 38 J. Paier, C. Penschke and J. Sauer, *Chem Rev*, 2013, **113**, 3949–3985.
- 39 M. M. Schubert, S. Hackenberg, A. C. van Veen, M. Muhler, V. Plzak and J. J. Behm, *J Catal*, 2001, **197**, 113–122.
- 40 N. J. Lawrence, J. R. Brewer, L. Wang, T. S. Wu, J. Wells-Kingsbury, M. M. Ihrig, G. Wang, Y. L. Soo, W. N. Mei and C. L. Cheung, *Nano Lett*, 2011, **11**, 2666–2671.
- 41 A. Trovarelli and J. Llorca, *ACS Catal*, 2017, **7**, 4716–4735.
- 42 Y. Xu, S. S. Mofarah, R. Mehmood, C. Cazorla, P. Koshy and C. C. Sorrell, *Mater Horiz*, 2021, **8**, 102–123.
- 43 H. J. Kim, M. G. Jang, D. Shin and J. W. Han, *ChemCatChem*, 2020, **12**, 11–26.
- 44 K. Polychronopoulou, A. A. Alkhoori, A. M. Efstathiou, M. A. Jaoude, C. M. Damaskinos, M. A. Baker, A. Almutawa, D. H. Anjum, M. A. Vasiliades, A. Belabbes, L. F. Vega, A. F. Zedan and S. J. Hinder, *ACS Appl Mater Interfaces*, 2021, **13**, 22391–22415.
- 45 M. Coduri, S. Checchia, M. Longhi, D. Ceresoli and M. Scavini, *Front Chem*, 2018, **6**, 1–23.
- 46 R. Schmitt, A. Nenning, O. Kraynis, R. Korobko, A. I. Frenkel, I. Lubomirsky, S. M. Haile and J. L. M. Rupp, *Chem Soc Rev*, 2020, **49**, 554–592.
- 47 S. Bhavsar, N. Isenberg, A. More and G. Veser, *Appl Energy*, 2016, **168**, 236–247.
- 48 N. K. Soliman, *Journal of Materials Research and Technology*, 2019, **8**, 2395–2407.
- 49 Y. Fukusaki, M. Umehara, Y. Kousa, Y. Inomata and S. Nakai, *Atmosphere (Basel)*, DOI:10.3390/atmos12101322.
- 50 B. E. Solsona, T. Garcia, C. Jones, S. H. Taylor, A. F. Carley and G. J. Hutchings, *Appl Catal A Gen*, 2006, **312**, 67–76.
- 51 P. Woźniak, M. A. Małecka, L. Chinchilla and S. Trasobares, *Mater Res Bull*, DOI:10.1016/j.materresbull.2022.111816.
- 52 Z. Wu, M. Li, J. Howe, H. M. Meyer and S. H. Overbury, *Langmuir*, 2010, **26**, 16595–16606.
- 53 M. A. Małecka, K. Matus and P. Woźniak, *ChemistrySelect*, 2020, **5**, 2871–2877.
- 54 M. A. Małecka and L. Kępiński, *J Alloys Compd*, 2007, **430**, 282–291.
- 55 M. A. Małecka, L. Kępiński and W. Miśta, *Appl Catal B*, 2007, **74**, 290–298.

- 56 R. Zanella, S. Giorgio, C. R. Henry and C. Louis, *Journal of Physical Chemistry B*, 2002, **106**, 7634–7642.
- 57 J. Rodríguez-Carvajal, *PHYSICA Recent advances in magnetic structure determination neutron powder diffraction*, 1993, vol. 192.
- 58 Q. Wang, K. L. Yeung and M. A. Bañares, *Catal Today*, 2020, **356**, 141–154.
- 59 S. Liang, E. Broitman, Y. Wang, A. Cao and G. Veser, *J Mater Sci*, 2011, **46**, 2928–2937.
- 60 E. Özkan, A. Hofmann, M. Votsmeier, W. Wang, X. Huang, C. Kübel, F. Badaczewski, K. Turke, S. Werner and B. M. Smarsly, *Langmuir*, 2021, **37**, 2563–2574.
- 61 R. J. Matyi, L. H. Schwartz and J. B. Butt, *Catalysis Reviews*, 1987, **29**, 41–99.
- 62 J. Sing, K. S. W., Everett, D. H., Haul R. A. W., Moscou, L., Pierotti, R. A., Rouquerol and T. Siemieniowska, *Pure & Appl. Chem.*, 1985, **57**, 603–619.
- 63 J. C. Groen, L. A. A. Peffer and J. Pérez-Ramírez, *Microporous and Mesoporous Materials*, 2003, **60**, 1–17.
- 64 X. D. Zhou and W. Huebner, *Appl Phys Lett*, 2001, **79**, 3512–3514.
- 65 H. H. Liu, Y. Wang, A. P. Jia, S. Y. Wang, M. F. Luo and J. Q. Lu, *Appl Surf Sci*, 2014, **314**, 725–734.
- 66 G. B. della Mea, L. P. Matte, A. S. Thill, F. O. Lobato, E. v. Benvenuto, L. T. Arenas, A. Jürgensen, R. Hergenröder, F. Poletto and F. Bernardi, *Appl Surf Sci*, 2017, **422**, 1102–1112.
- 67 M. Yang, G. Shen, Q. Wang, K. Deng, M. Liu, Y. Chen, Y. Gong and Z. Wang, *Roles of Oxygen Vacancies of CeO<sub>2</sub> and Mn-doped CeO<sub>2</sub> with the same morphology in Benzene Catalytic Oxidation*, 2021.
- 68 M. Cargnello, V. V. T. Doan-Nguyen, T. R. Gordon, R. E. Diaz, E. A. Stach, R. J. Gorte, P. Fornasiero and C. B. Murray, *Science (1979)*, 2013, **341**, 771–773.
- 69 A. Goguet, R. Burch, Y. Chen, C. Hardacre, P. Hu, R. W. Joyner, F. C. Meunier, B. S. Mun, D. Thompsett and D. Tibiletti, *Journal of Physical Chemistry C*, 2007, **111**, 16927–16933.
- 70 A. Longo, L. F. Liotta, G. Pantaleo, F. Giannici, A. M. Venezia and A. Martorana, *Journal of Physical Chemistry C*, 2012, **116**, 2960–2966.
- 71 Tana, F. Wang, H. Li and W. Shen, in *Catalysis Today*, Elsevier B.V., 2011, vol. 175, pp. 541–545.
- 72 J. Wang, H. Tan, S. Yu and K. Zhou, *ACS Catal*, 2015, **5**, 2873–2881.
- 73 L. A. Bruce, M. Hoang, A. E. Hughes and T. W. Turney, *Surface area control during the synthesis and reduction of high area ceria catalyst supports*, 1996.
- 74 S. Bernal, G. Blanco, G. Cifredo, J. A. Pérez-Omil, J. M. Pintado and J. M. Rodríguez-Izquierdo, *J Alloys Compd*, 1997, **250**, 449–454.
- 75 A. I. Boronin, E. M. Slavinskaya, A. Figueroba, A. I. Stadnichenko, T. Y. Kardash, O. A. Stonkus, E. A. Fedorova, V. v. Muravev, V. A. Svetlichnyi, A. Bruix and K. M. Neyman, *Appl Catal B*, , DOI:10.1016/j.apcatb.2021.119931.
- 76 K. Sohlberg, S. T. Pantelides and S. J. Pennycook, *J Am Chem Soc*, 2001, **123**, 6609–6611.
- 77 X. P. Wu and X. Q. Gong, *Phys Rev Lett*, , DOI:10.1103/PhysRevLett.116.086102.
- 78 M. Kjærøvik, M. Ramstedt, K. Schwibbert, P. M. Dietrich and W. E. S. Unger, *Front Chem*, , DOI:10.3389/fchem.2021.666161.
- 79 T. Skála, F. Šutara, K. C. Prince and V. Matolín, *J Electron Spectros Relat Phenomena*, 2009, **169**, 20–25.
- 80 O. S. Bezkravnyy, D. Blaumeiser, M. Vorokhta, P. Kraszkiewicz, M. Pawlyta, T. Bauer, J. Libuda and L. Kepinski, *Journal of Physical Chemistry C*, 2020, **124**, 5647–5656.
- 81 X. Ren, L. Liu, Y. Li, Q. Dai, M. Zhang and X. Jing, *J Mater Chem B*, 2014, **2**, 5541–5549.
- 82 K. A. Ledwa, L. Kępiński, M. Ptak and R. Szukiewicz, *Appl Catal B*, , DOI:10.1016/j.apcatb.2020.119090.
- 83 H. Ha, S. Yoon, K. An and H. Y. Kim, *ACS Catal*, 2018, **8**, 11491–11501.
- 84 M. Cargnello, C. Gentilini, T. Montini, E. Fonda, S. Mehraeen, M. Chi, M. Herrera-Collado, N. D. Browning, S. Polizzi, L. Pasquato and P. Fornasiero, *Chemistry of Materials*, 2010, **22**, 4335–4345.
- 85 P. Buffat and J.-P. Borel, *Size effect on the melting temperature of gold particles*, 1976, vol. 13.
- 86 F. S. Al-Sultan, S. N. Basahel and K. Narasimharao, *Fuel*, 2018, **233**, 796–804.
- 87 A. M. Ali, M. A. Daous, A. Arafat, A. A. Alzahrani, Y. Alhamed, A. Tuerdimaimaiti and L. A. Petrov, *J Nanomater*, , DOI:10.1155/2015/901439.
- 88 P. Woźniak, P. Kraszkiewicz and M. A. Małecka, *CrystEngComm*, , DOI:10.1039/d2ce00827k.
- 89 F. Menegazzo, M. Manzoli, A. Chiorino, F. Boccuzzi, T. Tabakova, M. Signoretto, F. Pinna and N. Pernicone, *J Catal*, 2006, **237**, 431–434.
- 90 F. Coise Duprat, *Light-oo curve of catalytic reaction and kinetics*, 2002, vol. 57.
- 91 Y. Q. Su, Y. Y. Qin, T. Wu and D. Y. Wu, *J Catal*, 2022, **407**, 353–363.
- 92 F. M. Dautzenberg, 1989, pp. 99–119.
- 93 M. Valden, X. Lai and D. W. Goodman, *Science (1979)*, 1998, **281**, 1647–1650.
- 94 N. Ta, J. Liu, S. Chenna, P. A. Crozier, Y. Li, A. Chen and W. Shen, *J Am Chem Soc*, 2012, **134**, 20585–20588.
- 95 M. Valden, S. Pak, X. Lai and D. W. Goodman, *Structure sensitivity of CO oxidation over model Au/TiO<sub>2</sub> catalysts*, 1998, vol. 56.
- 96 P. Woźniak, P. Kraszkiewicz and M. A. Małecka, *CrystEngComm*, 2020, **22**, 5828–5840.
- 97 S. Chen, L. Luo, Z. Jiang and W. Huang, *ACS Catal*, 2015, **5**, 1653–1662.

- 98 O. H. Laguna, M. A. Centeno, F. Romero-Sarria and J. A. Odriozola, in *Catalysis Today*, 2011, vol. 172, pp. 118–123.
- 99 G. Glaspell, L. Fuoco and M. S. El-Shall, *Journal of Physical Chemistry B*, 2005, **109**, 17350–17355.
- 100 R. Zhang, K. Lu, L. Zong, S. Tong, X. Wang, J. Zhou, Z. H. Lu and G. Feng, *Molecular Catalysis*, 2017, **442**, 173–180.
- 101 O. Bezkrivnyi, P. Kraszkiewicz, I. Krivtsov, J. Quesada, S. Ordóñez and L. Kepinski, *Catal Commun.*, DOI:10.1016/j.catcom.2019.105798.
- 102 W. Y. Hernández, F. Romero-Sarria, M. A. Centeno and J. A. Odriozola, *Journal of Physical Chemistry C*, 2010, **114**, 10857–10865.
- 103 M. Gong, J. Zhang, J. L. Luo and C. A. Wang, *Int J Appl Ceram Technol*, 2017, **14**, 908–914.
- 104 P. Sudarsanam, B. Mallesham, P. S. Reddy, D. Großmann, W. Grünert and B. M. Reddy, *Appl Catal B*, 2014, **144**, 900–908.
- 105 F. Polo-Garzon, Z. Bao, X. Zhang, W. Huang and Z. Wu, *ACS Catal*, 2019, **9**, 5692–5707.
- 106 M. Haruta, *Faraday Discuss*, 2011, **152**, 11–32.
- 107 R. J. Macfarlane, *Nano Lett*, 2021, **21**.
- 108 Y.-W. Chen and N. Sasirekha, in *Heterogeneous Gold Catalysts and Catalysis*, The Royal Society of Chemistry, 2014, pp. 73–110.
- 109 Q. Li, L. Song, Z. Liang, M. Sun, T. Wu, B. Huang, F. Luo, Y. Du and C.-H. Yan, *Advanced Energy and Sustainability Research*, 2021, **2**, 2000063.
- 110 G. Xiao, S. Li, H. Li and L. Chen, *Microporous and Mesoporous Materials*, 2009, **120**, 426–431.
- 111 W. Zhu, J. Jin, X. Chen, C. Li, T. Wang, C. W. Tsang and C. Liang, *Environmental Science and Pollution Research*, 2018, **25**, 5643–5654.
- 112 L. F. Allard, A. Borisevich, W. Deng, R. Si, M. Flytzani-Stephanopoulos and S. H. Overbury, *J Electron Microsc (Tokyo)*, 2009, **58**, 199–212.
- 113 M. Wang, F. Wang, J. Ma, M. Li, Z. Zhang, Y. Wang, X. Zhang and J. Xu, *Chemical Communications*, 2014, **50**, 292–294.
- 114 C. Zhang, A. Michaelides, D. A. King and S. J. Jenkins, *Journal of Physical Chemistry C*, 2009, **113**, 6411–6417.
- 115 X. Cao, C. Zhang, Z. Wang, W. Liu and X. Sun, *RSC Adv*, 2020, **10**, 4664–4671.
- 116 J. Vecchietti, S. Collins, W. Xu, L. Barrio, D. Stacchiola, M. Calatayud, F. Tielens, J. J. Delgado and A. Bonivardi, *Journal of Physical Chemistry C*, 2013, **117**, 8822–8831.
- 117 L. Torrente-Murciano, *Journal of Nanoparticle Research*, DOI:10.1007/s11051-016-3385-2.
- 118 F. Wang and G. Lu, *Catal Letters*, 2010, **134**, 72–77.
- 119 Y. Chen, Y. Feng, L. Li, J. Liu, X. Pan, W. Liu, F. Wei, Y. Cui, B. Qiao, X. Sun, X. Li, J. Lin, S. Lin, X. Wang and T. Zhang, *ACS Catal*, 2020, **10**, 8815–8824.
- 120 P. H. Ho, D. Yao, D. Creaser and L. Olsson, *ACS Engineering Au*, 2022, **2**, 219–235.
- 121 K. Zhou, X. Wang, X. Sun, Q. Peng and Y. Li, *J Catal*, 2005, **229**, 206–212.
- 122 H. Y. Kim and G. Henkelman, *Journal of Physical Chemistry Letters*, 2013, **4**, 216–221.
- 123 S. Royer and D. Duprez, *ChemCatChem*, 2011, **3**, 24–65.
- 124 G. C. Bond, *Molecules*, 2012, **17**, 1716–1743.
- 125 L. W. Guo, P. P. Du, X. P. Fu, C. Ma, J. Zeng, R. Si, Y. Y. Huang, C. J. Jia, Y. W. Zhang and C. H. Yan, *Nat Commun.*, DOI:10.1038/ncomms13481.
- 126 S. Malola, S. Kaappa and H. Häkkinen, *Journal of Physical Chemistry C*, 2019, **123**, 20655–20663.
- 127 H. Häkkinen, *Adv Phys X*, 2016, **1**, 467–491.
- 128 S. Yamazoe, K. Koyasu and T. Tsukuda, *Acc Chem Res*, 2014, **47**, 816–824.
- 129 K. Qian, L. Luo, H. Bao, Q. Hua, Z. Jiang and W. Huang, *Catal Sci Technol*, 2013, **3**, 679–687.
- 130 A. Davó-Quiñonero, S. López-Rodríguez, C. Chaparro-Garnica, I. Martín-García, E. Bailón-García, D. Lozano-Castelló, A. Bueno-López and M. García-Melchor, *Catalysts*, DOI:10.3390/catal11121556.
- 131 M. Chen and D. W. Goodman, *Chem Soc Rev*, 2008, **37**, 1860–1870.
- 132 I. v. Yudanov, A. Genest, S. Schauermaun, H. J. Freund and N. Rösch, *Nano Lett*, 2012, **12**, 2134–2139.
- 133 B. Solsona, R. Sanchis, A. M. Dejoz, T. García, L. Ruiz-Rodríguez, J. M. López Nieto, J. A. Cecilia and E. Rodríguez-Castellón, *Catalysts*, DOI:10.3390/catal7040096.
- 134 J. Han, H. J. Kim, S. Yoon and H. Lee, *J Mol Catal A Chem*, 2011, **335**, 82–88.
- 135 K. Blick, T. D. Mitrelías, J. S. J. Hargreaves, G. J. Hutchings, R. W. Joyner, C. J. Kiely and F. E. Wagner, *Methane oxidation using Au/MgO catalysts*.
- 136 W. Wang, D. Li, H. Yu, C. Liu, C. Tang, J. Chen, J. Lu and M. Luo, *Journal of Physical Chemistry C*, 2021, **125**, 19301–19310.
- 137 B. Li and H. C. Zeng, *Advanced Materials*, DOI:10.1002/adma.201801104.
- 138 J. Xiong, X. Mei, J. Liu, Y. Wei, Z. Zhao, Z. Xie and J. Li, *Appl Catal B*, 2019, **251**, 247–260.
- 139 L. Vivier and D. Duprez, *ChemSusChem*, 2010, **3**, 654–678.
- 140 T. Ishida, T. Murayama, A. Taketoshi and M. Haruta, *Chem Rev*, 2020, **120**, 464–525.
- 141 C. Liang, J. Y. Cheong, G. Sitaru, S. Rosenfeldt, A. S. Schenk, S. Gekle, I. D. Kim and A. Greiner, *Adv Mater Interfaces*, DOI:10.1002/admi.202100867.
- 142 N. Masoud, T. Partsch, K. P. de Jong and P. E. de Jongh, *Gold Bull*, 2019, **52**, 105–114.
- 143 M. D. Argyle and C. H. Bartholomew, *Catalysts*, 2015, **5**, 145–269.
- 144 A. M. Abdel-Mageed, S. Chen, C. Fauth, T. Häring and J. Bansmann, *ChemPhysChem*, 2021, **22**, 1302–1315.
- 145 J. L. Lu, H. J. Gao, S. Shaikhutdinov and H. J. Freund, *Catal Letters*, 2007, **114**, 8–16.

- 146 S. Hu and W.-X. Li, *Sabatier principle of metal-support interaction for design of ultrastable metal nanocatalysts*, .

## Supplementary materials for

Confinement of nano-gold in 3D hierarchically structured gadolinium-doped ceria mesocrystal: synergistic effect of chemical composition and structural hierarchy in CO and propane oxidation.

**Piotr Woźniak\*<sup>a</sup>, Małgorzata A. Małecka<sup>a</sup>, Piotr Kraszkiwicz<sup>a</sup>, Włodzimierz Miśta<sup>a</sup>, Oleksii Bezkrovnyi<sup>a</sup>, Lidia Chinchilla<sup>b</sup>, Susana Trasobares<sup>b</sup>**

*<sup>a</sup>Institute of Low Temperature and Structure Research, Polish Academy of Sciences,*

*P.O. Box 1410, 50-950 Wrocław 2, Poland*

*<sup>b</sup>Departamento de Ciencia de los Materiales e Ing. Metalúrgica y Química Inorgánica, Universidad de Cádiz, Campus Universitario de Puerto Real, 11510, Cádiz - España*

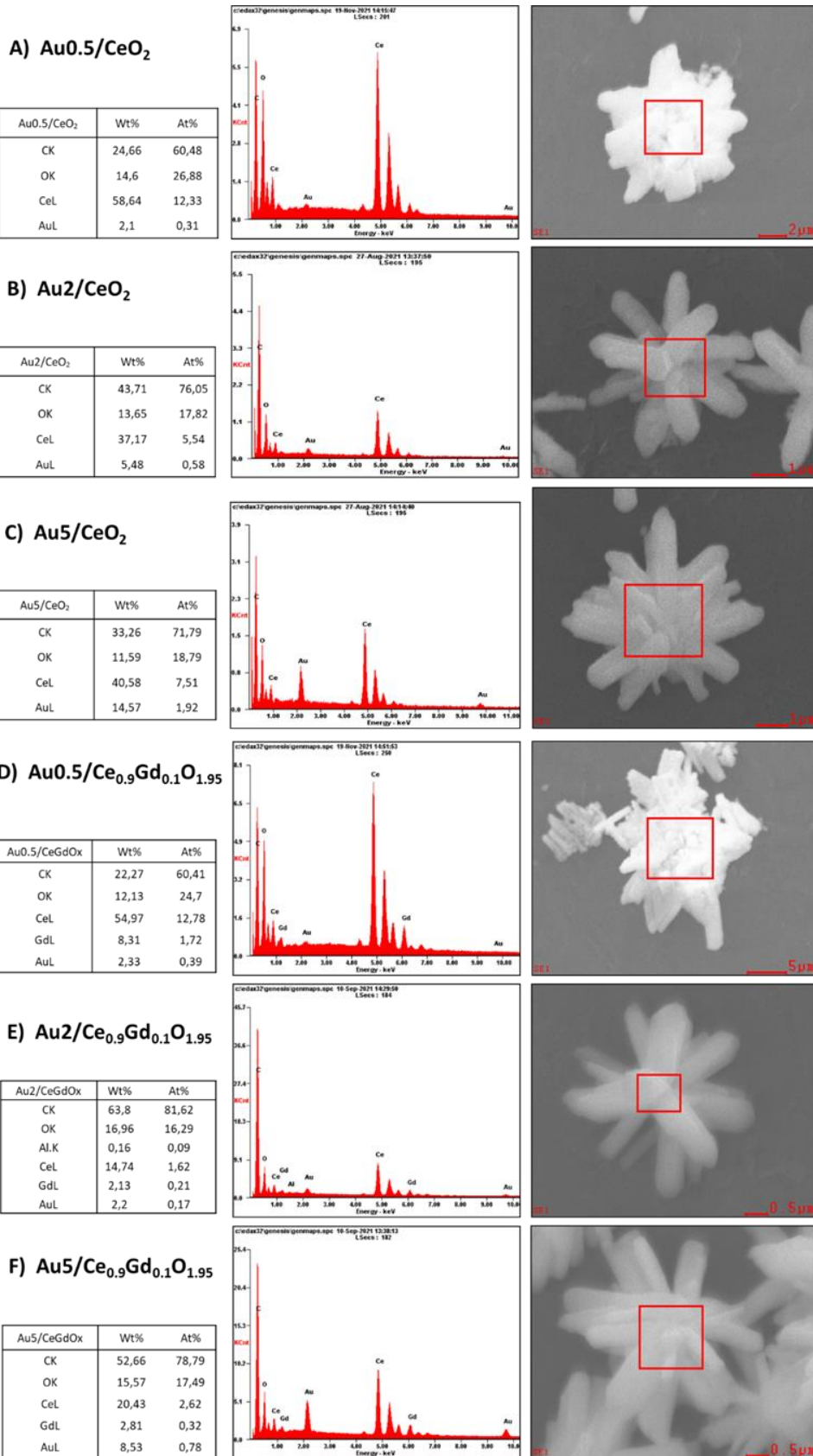
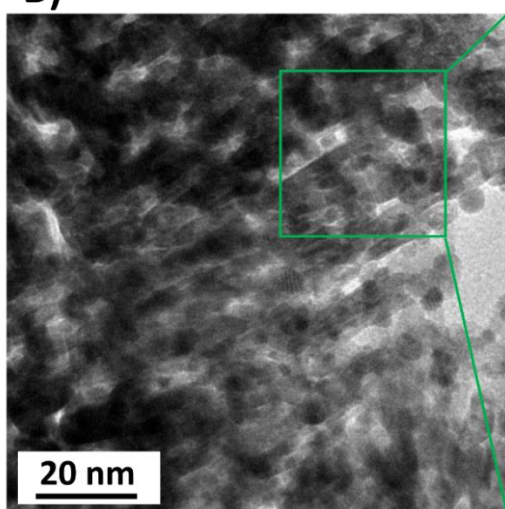


**Fig. S1** A-F) SEM-EDX elemental analysis of the hierarchically structured gold-decorated catalysts Au<sub>x</sub>/Ce<sub>1-γ</sub>Gd<sub>γ</sub>O<sub>2-γ/2</sub> (x - the surface coverage parameter value ; γ = 0 or 0.1). For each material from A to F measurements of 3-5 particles were collected and average at% and wt% values has been calculated; method of calculation and results are shown and described in Fig. 4.D.

A)

Catalyst architecture (gold loading)		
Sample	Au NPs size	
	TEM volume-weighted mean	PXRD
Au0.5/CeO <sub>2</sub>	-	-
Au2/CeO <sub>2</sub>	4.8	4.6
Au5/CeO <sub>2</sub>	4.5	3.9
Au0.5/GDC-10%	-	-
Au2/GDC-10%	4.1	3.6
Au5/GDC-10%	6.7	3.8

B)



C)

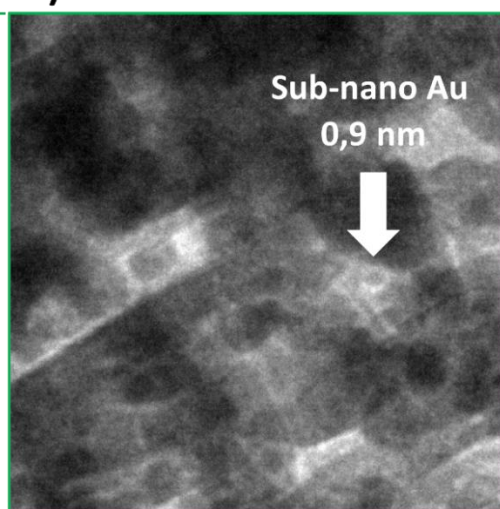


**Fig. S2** A) Volume-weighted mean size (obtained from TEM) vs mean size obtained from PXRD (Scherrer formula) of Au NPs on the Au x/HSNPs catalysts differed by gold loading (x indicate SC value = 0.5, 2 or 5) ; B) TEM image of Au5/CeO<sub>2</sub> HSNPs sample C) Magnification of the area marked in the image B showing sub-nanometer gold nanoparticle.



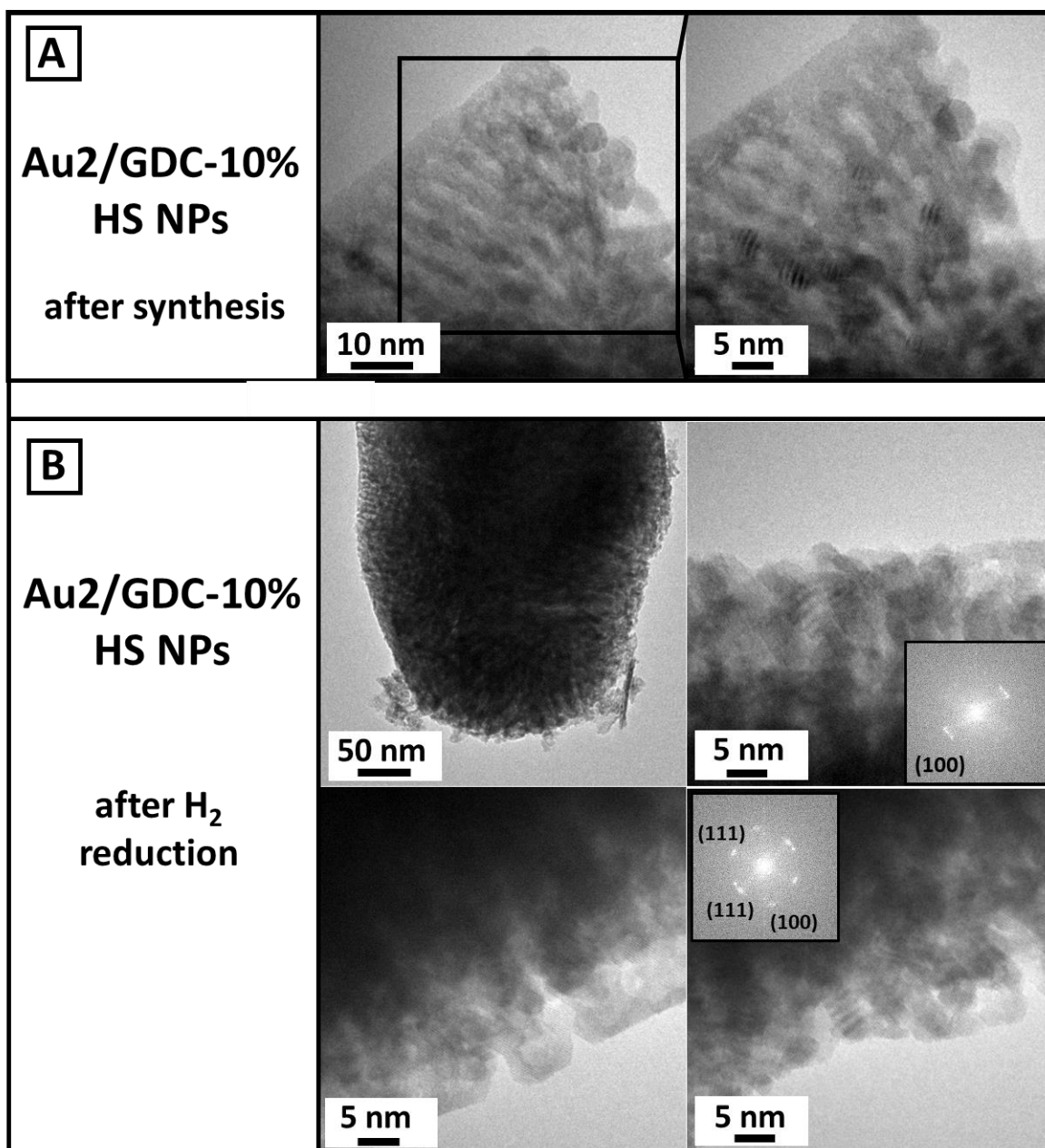


**Fig. S3.** A) Au<sub>2</sub>/GDC-10% HSNPs after synthesis. Gold NPs within hierarchical structure visible as Moiré patterns; B) Au<sub>2</sub>/GDC-10% HS NPs catalyst reduced at 400°C in H<sub>2</sub> flow for 3h. No Au NPs abundance has been observed on the external surface of the arm of star-shaped hierarchical carrier. Moiré patterns suggest occurrence of Au NPs in the sub-surface regions and inside the hierarchical structure.

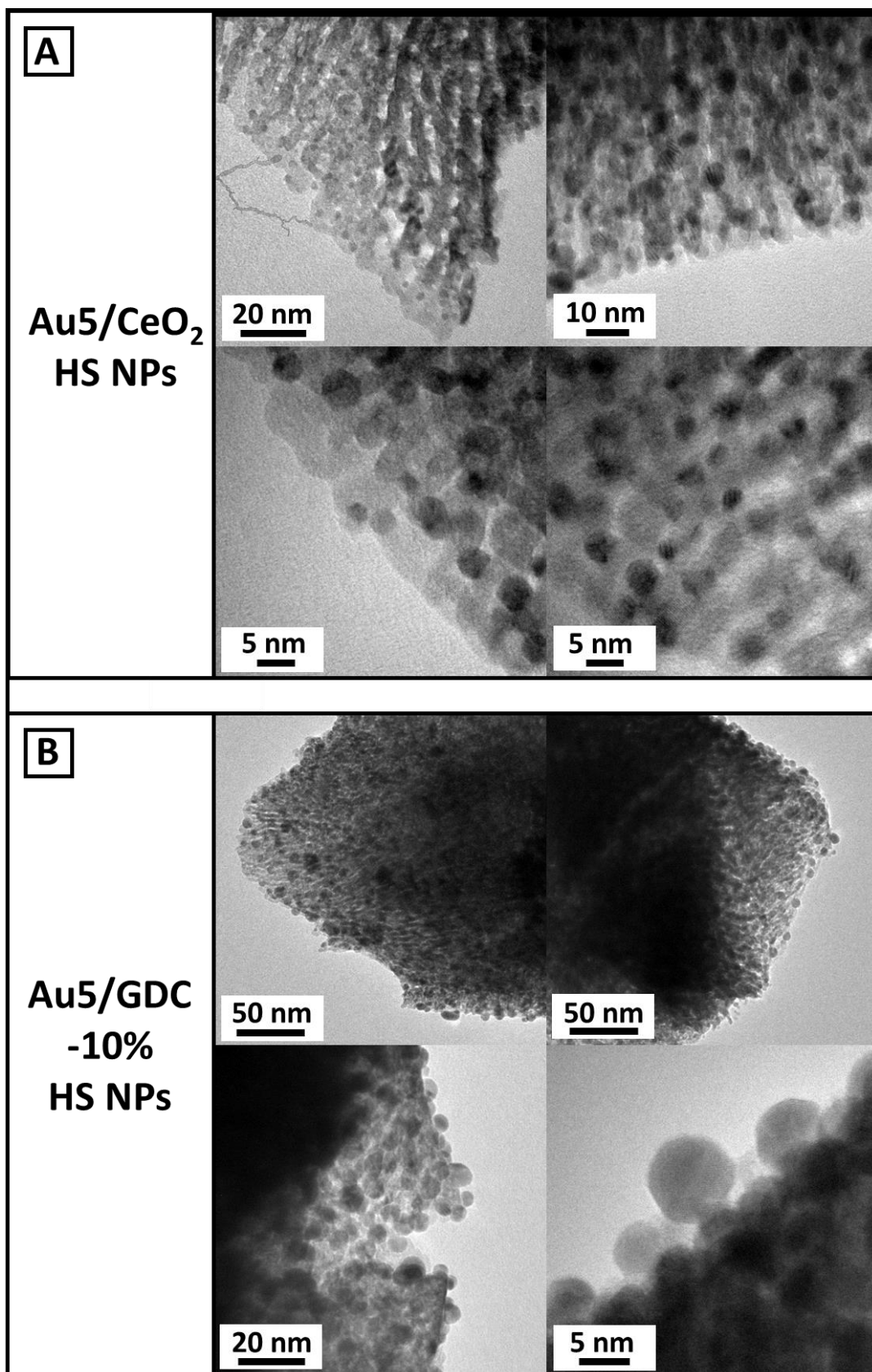


**Fig. S4.** A) TEM images of gold-decorated Au5/Ce<sub>1-x</sub>Gd<sub>x</sub>O<sub>2-x/2</sub> (x=0; 0.1) HS NPs catalysts. A) Au5/CeO<sub>2</sub> catalyst; Au NPs observed both, on the external surface of star-shaped ceria carrier and inside the pores in sub-surface (TEM-transparent) region of sample; B). Au5/GDC-10% HS NPs catalysts; Au NPs observed mostly on the external surface of star-shaped particle arms.

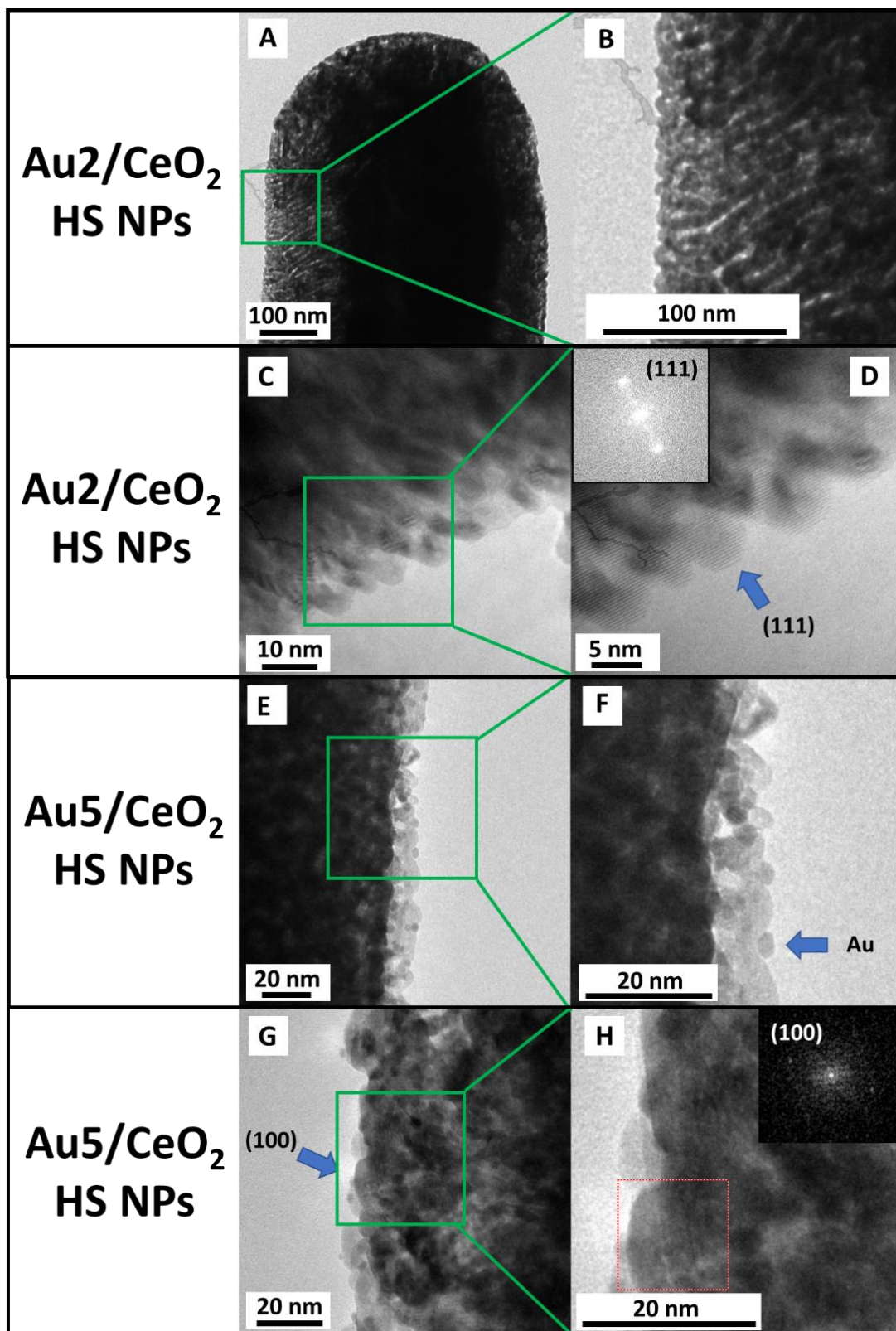


**Fig. S5.** Morphology of the external surface of the arms of star-shaped Au  $x$ /CeO<sub>2</sub> hierarchical catalyst ( $x$  denotes surface coverage parameter equal to 2 or 5). A-B) TEM images of Au<sub>2</sub>/CeO<sub>2</sub> arm showing diversified support surface morphology; C-D) TEM images of Au<sub>2</sub>/CeO<sub>2</sub> showing exposition of CeO<sub>2</sub>(111) planes; E-F) TEM images of Au<sub>5</sub>/CeO<sub>2</sub> showing Au NPs embedded between CeO<sub>2</sub> crystallites; G-H) TEM images of Au<sub>5</sub>/CeO<sub>2</sub> showing exposition of CeO<sub>2</sub>(100) planes.

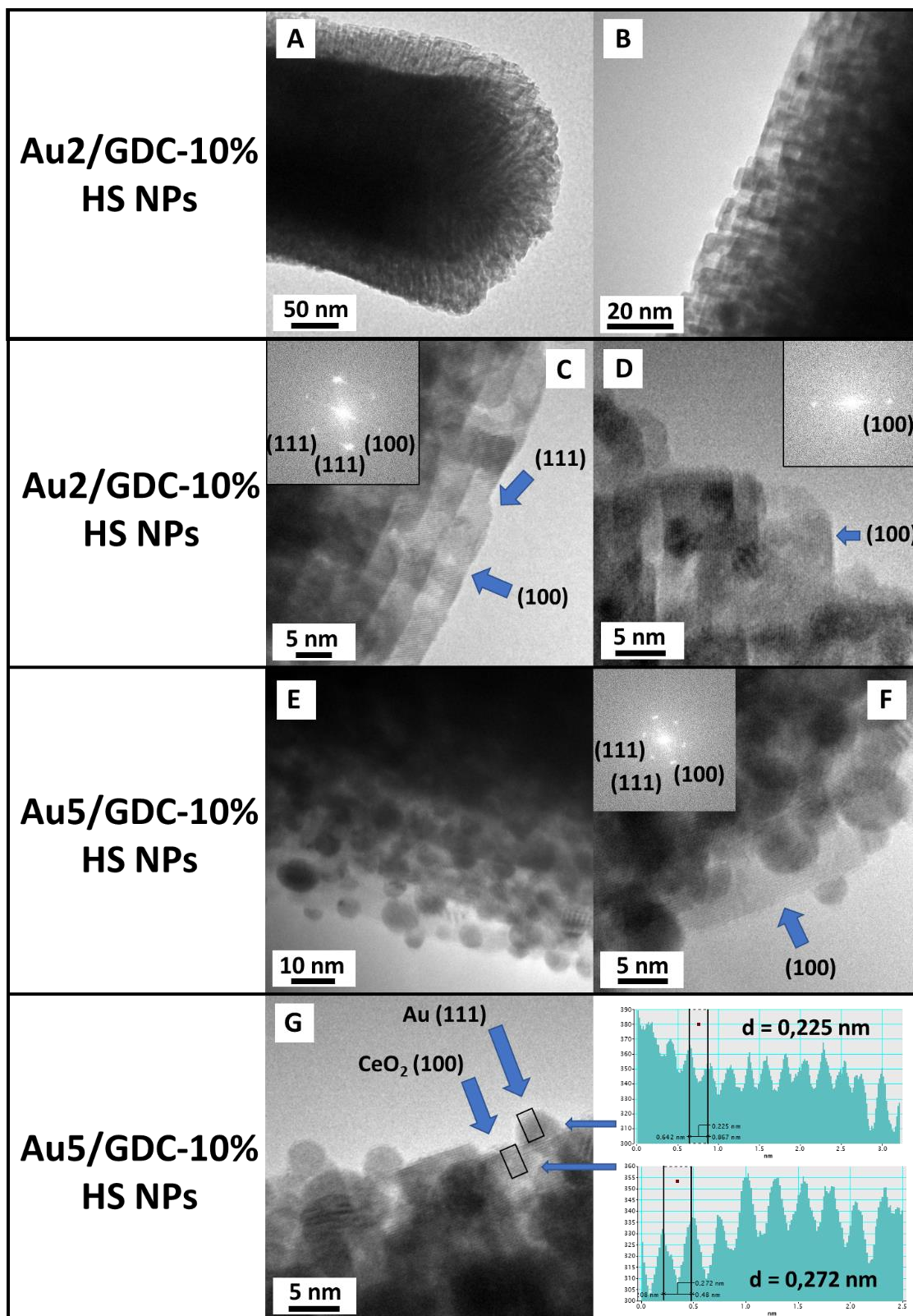
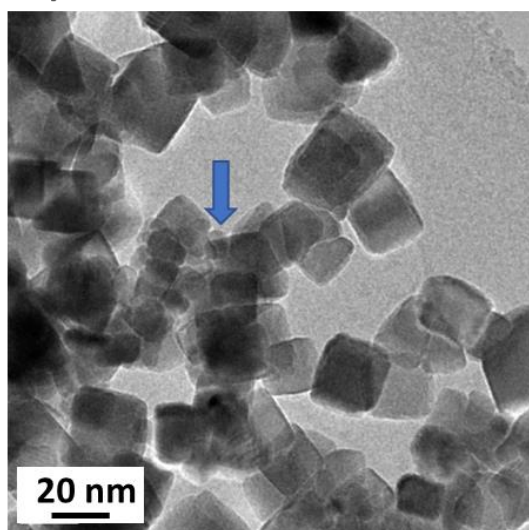


**Fig. S6.** Morphology of the external surface of the arms of star-shaped Au x/GDC-10% hierarchical catalyst (x denotes surface coverage parameter equal to 2 or 5). A-B) TEM images of Au<sub>2</sub>/GDC-10% arm showing plain support surface morphology; C-D) TEM images of Au<sub>2</sub>/CeO<sub>2</sub> showing dominant exposition of CeO<sub>2</sub>(100) planes; E-F) TEM images of Au<sub>5</sub>/GDC-10% showing Au NPs embedded on CeO<sub>2</sub>(100) planes; G-H) TEM images of Au<sub>5</sub>/GDC-10% showing Au NPs exposition of CeO<sub>2</sub>(100) planes.

A)

Sample		TEM volume weighted mean	PXRD
NPs	CeO <sub>2</sub>	8.0	7.7
	GDC-10%	6.0	6.1
Cubes	CeO <sub>2</sub>	20.8	16.1
	GDC-10%	22.2	16.5
HS NPs	CeO <sub>2</sub>	6,2	7.8
	GDC-10%	4.1	6.9

B)



C)

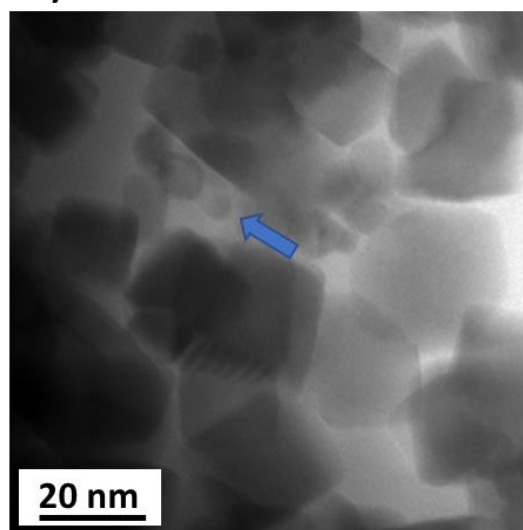


**Fig S7.** A. Volume-weighted mean size (obtained from TEM) vs mean size obtained from PXRD (Scherrer formula) of ceria particles differed by morphology; B) TEM image of CeO<sub>2</sub> cubes sample; small non-cubic (oval-shaped) crystallites marked by arrow, C) TEM image of GDC-10% cubes sample; small non-cubic (oval-shaped) crystallites marked by arrow.

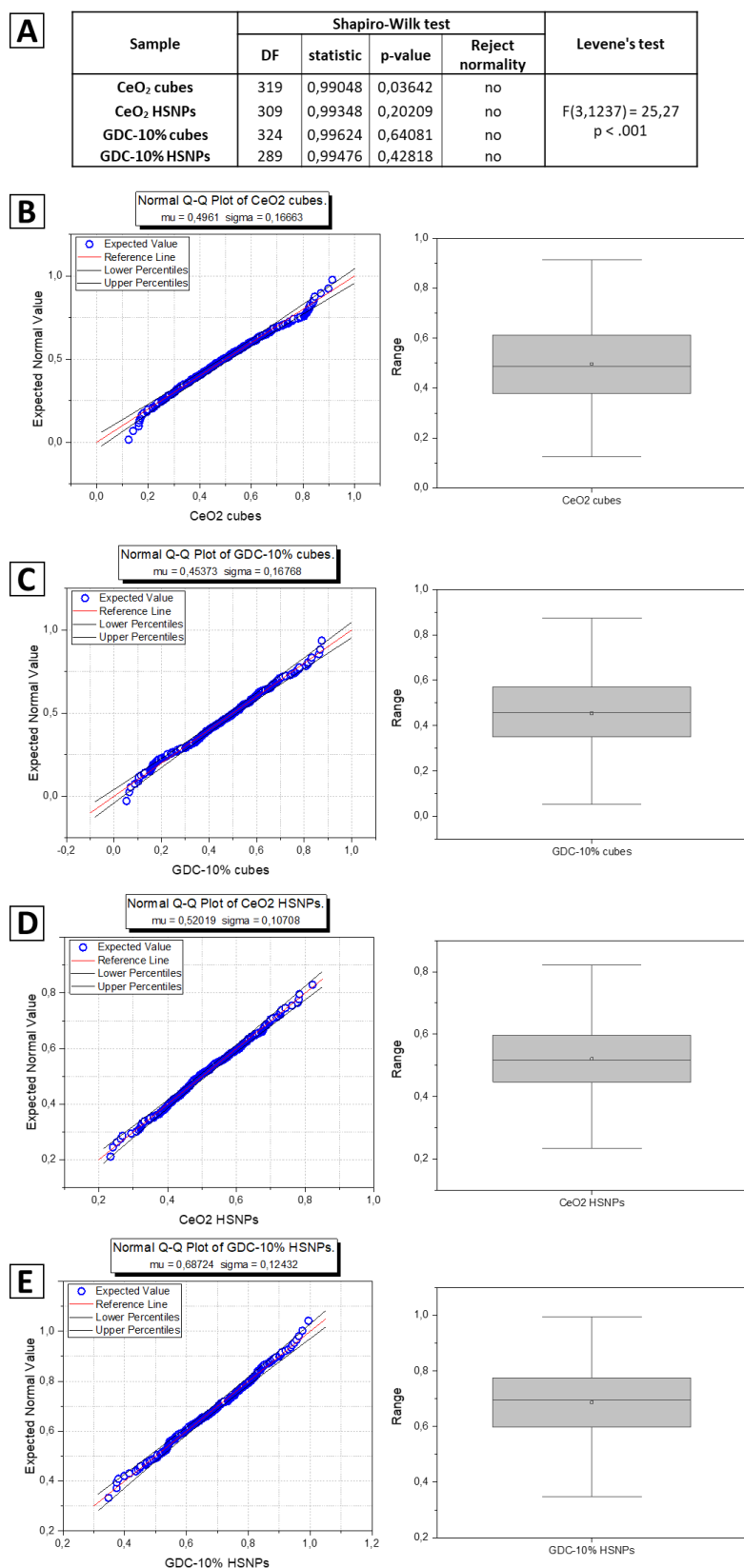


**Fig. S8.** A) Shapiro-Wilk test and Levene's test results for AuNPs size data for supports differed by architecture and doping level. Samples are before propane oxidation (size data obtained from TEM); B-E) Q-Q plots and box charts for tested samples: B) Au<sub>5</sub>/CeO<sub>2</sub> cubes C) Au<sub>5</sub>/GDC-10% cubes D) Au<sub>5</sub>/CeO<sub>2</sub> HSNPs E) Au<sub>5</sub>/GDC-10% HSNPs. All samples are normally distributed. Variances are not

equal across groups, however, samples have similar size and outliers has been eliminated for statistical analysis of variance.

## IR , TPD and iDPC-STEM results

Temperature programmed desorption (TPD) and infrared spectroscopy (IR) were conducted to investigate the surface chemical composition of hierarchical catalysts.

ATR-FTIR spectra do not show any dissimilarities between bare CeO<sub>2</sub> HSNPs support and its Au<sub>2</sub> or Au<sub>5</sub> gold-decorated counterparts (Fig. S9). All spectra show maxima characteristic to CeO<sub>2</sub> at 1550 cm<sup>-1</sup> and 1391 cm<sup>-1</sup> [1]. The maxima at 3400 cm<sup>-1</sup> and 1638 cm<sup>-1</sup> may be ascribed to water chemisorbed on the surface [2]. In line with this, increased H<sub>2</sub> release from hierarchically structured catalysts as compared to model cubic one is observed in CO-TPR experiment described in Section 3.2.2. As indicated in the literature, surface hydroxyls may play a significant role in stabilization and propagation of oxygen vacancies [3], the presence of which, in turn, is linked to facilitation of catalytic activity.

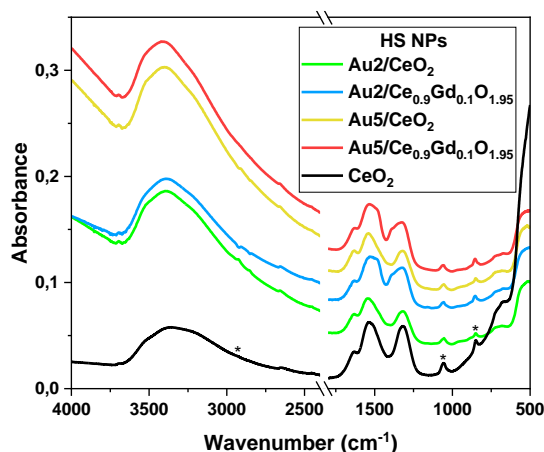


**Fig. S9.** ATR-FTIR spectra of the gold-decorated hierarchically structured catalysts. \*Maxima corresponding to alcohol that was used during measurement.

TPD results for bare CeO<sub>2</sub> HSNPs show possible contamination of the sample with carbonaceous residues that form during thermal decomposition of cerium formate (Fig. S10). In particular, the desorption of CO<sub>2</sub> and CO above 400°C indicates presence of carbon contaminants not removed during calcination that has been conducted up to 400°C. In fact, acquisition of Integrated Differential Phase Contrast (iDPC) images in STEM mode, that has been taken in order to observe oxygen vacancies at the atomic level, was not successful due the high carbon contamination induced by electron beam interaction with the sample, at the present the process of contamination growth have been mainly attributed to adsorbed hydrocarbon molecules on the sample [4]. Presence of those carbon residues is presented in iDPC-STEM images (Fig. S11).

Simultaneous desorption of CO and H<sub>2</sub> at 750°C may indicate relatively strong adsorption of formate groups on CeO<sub>2</sub> surface. Stable carbonate moieties on the real catalyst surface have been observed by many authors [5][6]. As a prevailing view today CO<sub>3</sub> residues are thought to be spectator species in CO oxidation, although it was once thought that they took an active part in the reaction mechanism [7]. Also, Davó-Quiñonero et al. have shown that CeO<sub>2</sub>(100) surface, which is the dominant surface in HSNPs studied in this research, have a strong tendency for binding of multidentate carbonates whose desorption is hampered [8]. Nevertheless, Chen et al. have observed

that the decomposition reactivity of carbonate species depends on size of AuNPs deposited on CeO<sub>2</sub> [9]. Trace NO amounts that coincide with CH<sub>4</sub> desorption may come from DMF that had been used as synthetic solvent. Also, the decent CO<sub>2</sub> maximum at 100°C indicates a large sorption capacity of the material, as this may be ascribed to CO<sub>2</sub> adsorbed from the air.

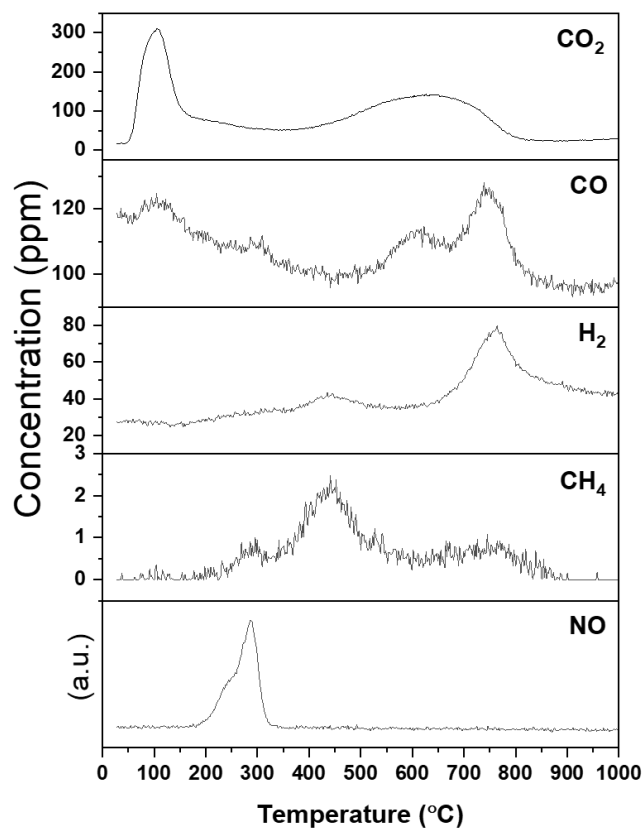


**Fig. S10.** The TPD curves obtained for bare CeO<sub>2</sub> hierarchically structured support (HSNPs).

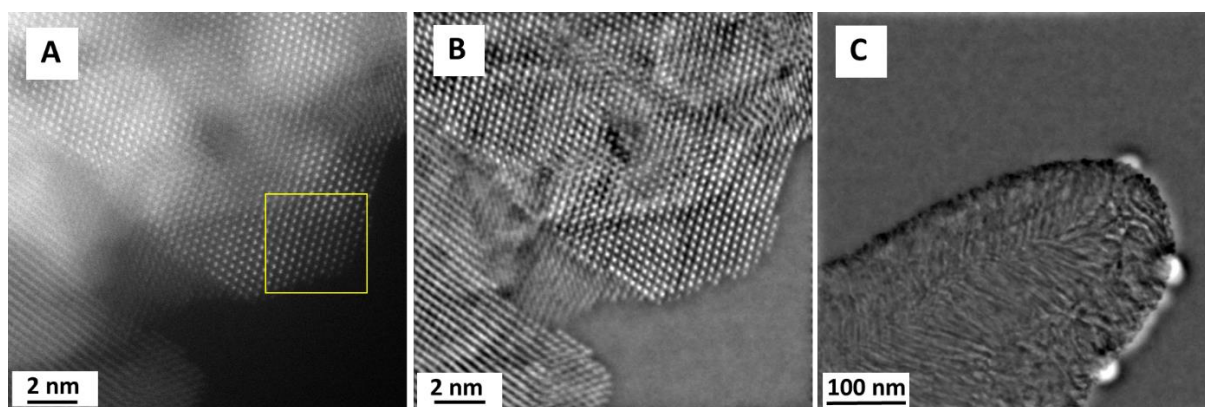


**Fig. S11.** HAADF images of GDC-10% carrier. A) High-magnification HAADF image; B) High-magnification iDPC-STEM image; C) Low-magnification iDPC-STEM image. iDPC technique is very sensitive to carbon contamination, as may be seen on low-magnification iDPC-STEM image. All zones analyzed were contaminated under image acquisition, therefore oxygen positions are not visible.



## Literature

- [1] P. Kumar, A. Kumar, C. Joshi, R. Singh, S. Saran and S. L. Jain, *RSC Advances*, 2015, **5**, 42414–42421.
- [2] J. S. Lee and S. C. Choi, *Materials Letters*, 2004, **58**, 390–393.
- [3] X. P. Wu and X. Q. Gong, *Physical Review Letters*, DOI:10.1103/PhysRevLett.116.086102.
- [4] S. Hettler, M. Dries, P. Hermann, M. Obermair, D. Gerthsen and M. Malac, *Micron*, 2017, **96**, 38–47.
- [5] H. Liu, A. I. Kozlov, A. P. Kozlova, T. Shido, K. Asakura and Y. Iwasawa, *J. Catal.* 1999, vol. 185, 252-264.
- [6] M. Maciejewski, P. Fabrizioli, J. D. Grunwaldt, O. S. Becker and A. Baiker, *Physical Chemistry Chemical Physics*, 2001, **3**, 3846–3855.
- [7] R. Meyer, C. Lemire, S. K. Shaikhutdinov and H.-J. Freund, *Surface Chemistry of Catalysis by Gold, Gold Bulletin*, 2004, **37**, 72-124.
- [8] A. Davó-Quiñonero, S. López-Rodríguez, C. Chaparro-Garnica, I. Martín-García, E. Bailón-García, D. Lozano-Castelló, A. Bueno-López and M. García-Melchor, *Catalysts*, 2021, **11**(12), 1556.
- [9] S. Chen, L. Luo, Z. Jiang and W. Huang, *ACS Catalysis*, 2015, **5**, 1653–1662.

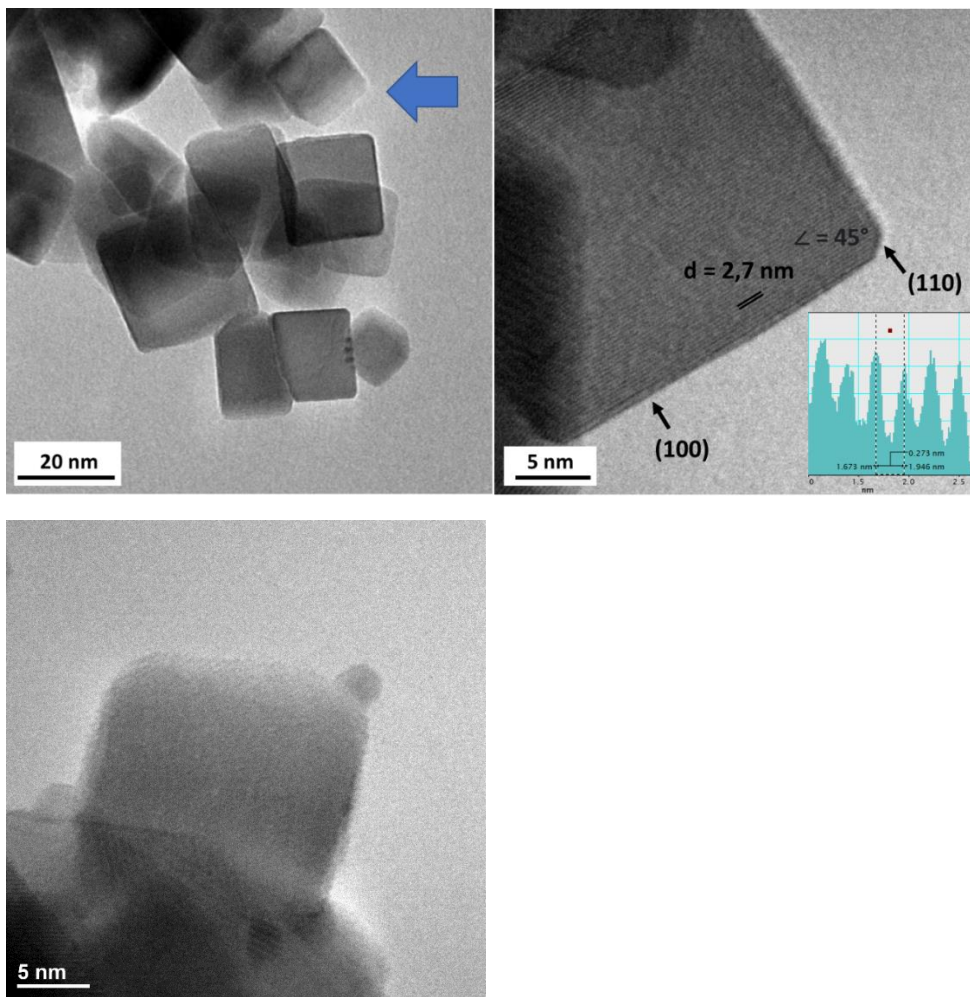
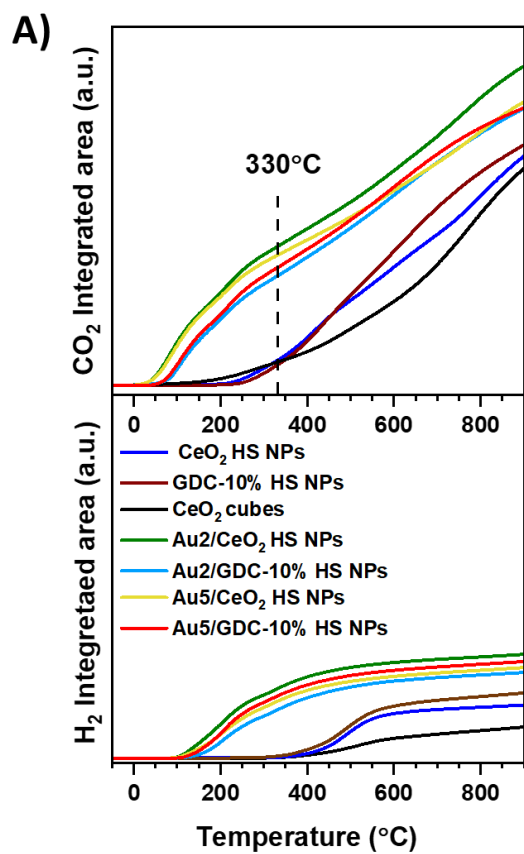


**Fig. S12.** TEM images of CeO<sub>2</sub> cubes. Deviation from regular cube morphology (edge- and corner-truncated crystallites); Au/5GDC-10% cubes (bottom image). Gold embedded on site deflected from cubic morphology.

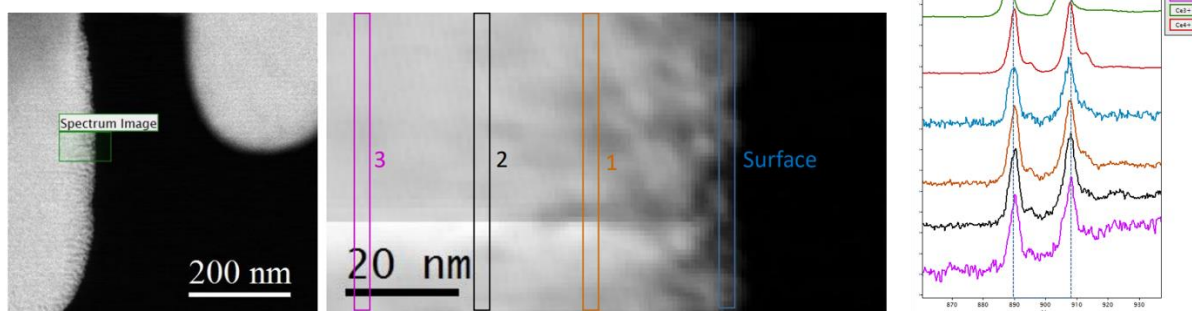


**B)**

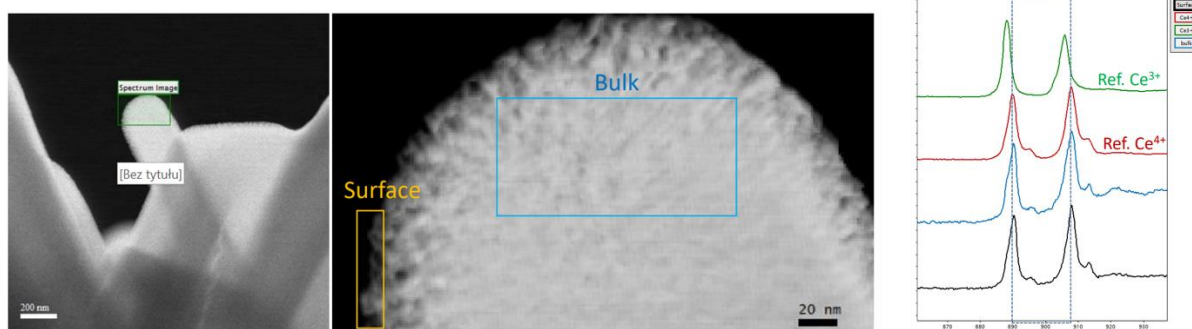
Sample	Oxygen consumption	
	surface (-25°C-500°C) (% total)	bulk (-500°C-900°C) (% total)
CeO <sub>2</sub> HS NPs	37	63
GDC-10% HS NPs	38	62
Au <sub>2</sub> /CeO <sub>2</sub> HS NPs	57	43
Au <sub>2</sub> /GDC-10% HS NPs	57	43
Au <sub>5</sub> /CeO <sub>2</sub> HS NPs	59	41
Au <sub>5</sub> /GDC-10% HS NPs	60	40

**Fig. S13.** A) Temperature dependences of the cumulative CO<sub>2</sub> and H<sub>2</sub> release during CO-TPR; B) Surface vs bulk oxygen consumption calculated from CO-TPR data.

## Surface and near-surface region



## Bulk region



## Electron beam damage

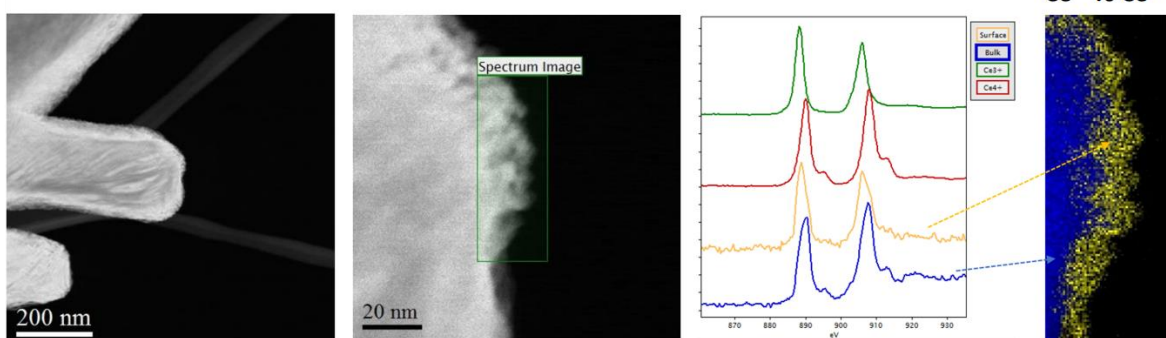
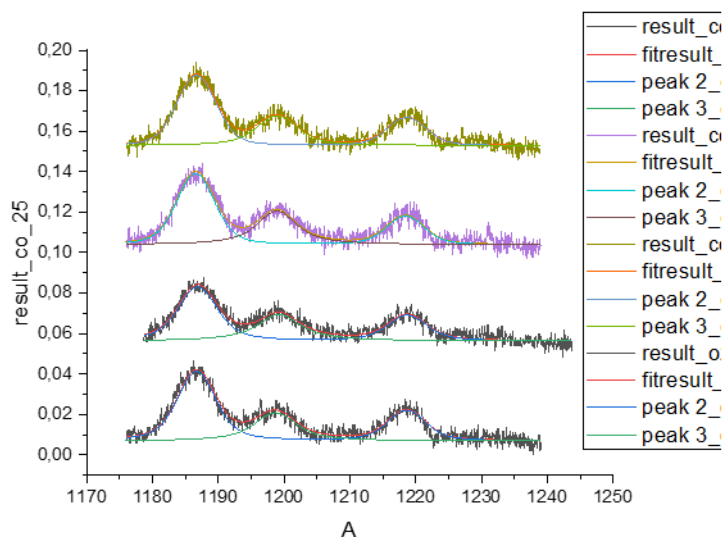


**Fig. S14.** EELS-SI analysis of the arm of star-shaped particle ( $\text{CeO}_2$  HSNPs) in the surface/near-surface region (top), and bulk region (middle). Ceria reduction induced by electron beam has been also presented (bottom).



Sample	Ce <sup>3+</sup> /Ce	Au/Ce	Gd/Ce	Au <sup>+</sup> /Au
Au/CeO <sub>2</sub> @O <sub>2</sub> @573K	0	0.21	0	0.08
Au/CeO <sub>2</sub> @CO@300K	0	0.22	0	0.05
Au/CeO <sub>2</sub> @CO@373K	0.04	0.21	0	0.03
Au/CeO <sub>2</sub> @CO@473K	0.1	0.21	0	0.02
Au/GDC-10%@O <sub>2</sub> @573K	0	0.2	0.19	0.015
Au/GDC-10%@CO@300K	0	0.21	0.18	0.016
Au/GDC-10%@CO@373K	0	0.24	0.17	0.019
Au/GDC-10%@CO@473K	0.05	0.23	0.17	0.018

**Fig S15.** NAP-XPS of Au<sub>5</sub>/GDC-10% HS NPs (top); The relative abundance of Au, Ce, Gd content and oxidation states in Au<sub>5</sub>/CeO<sub>2</sub> and Au<sub>5</sub>/GDC-10% determined using NAP-XPS (bottom). Relative contributions of the fitted components were calculated as the ratio of peak areas.

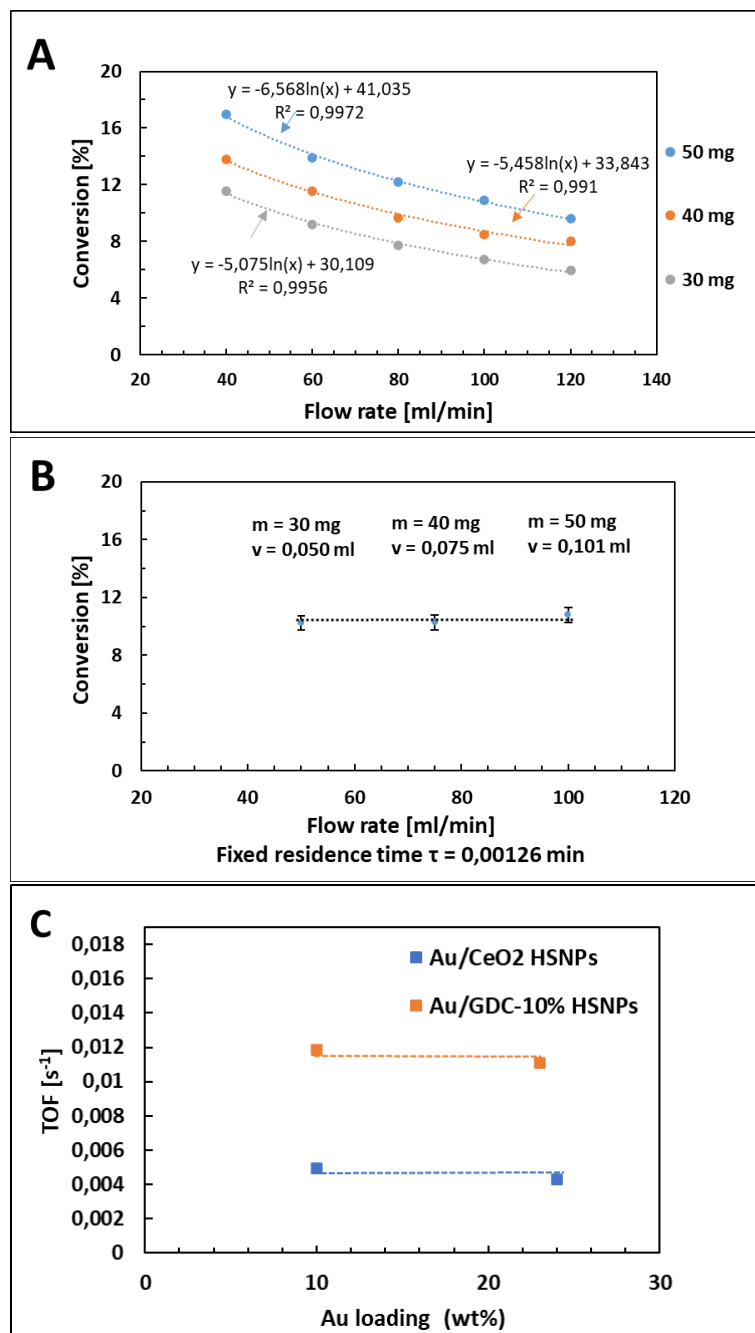


**Fig. S16.** Mass transfer limitation tests. A) Conversion as a function of flow rate for different loadings of CeO<sub>2</sub> HSNPs catalyst support in propane oxidation: 30mg, 40mg and 50mg. B) Diagnostic test for interphase transport limitation (Dautzenberg, 1989); plots of conversion versus flow rate in fixed residence time for different loadings of CeO<sub>2</sub> HSNPs support. C) The Koros-Nowak test ; plots of TOF versus Au loading at 25°C for Au/CeO<sub>2</sub> HSNPs and Au/GDC-10% HSNPs.

F. M. Dautzenberg, Ten guidelines for catalyst testing , Characterization and Catalyst Development, Chapter 11, ACS Symposium Series, Vol. 411, 1989, pp. 99–119.

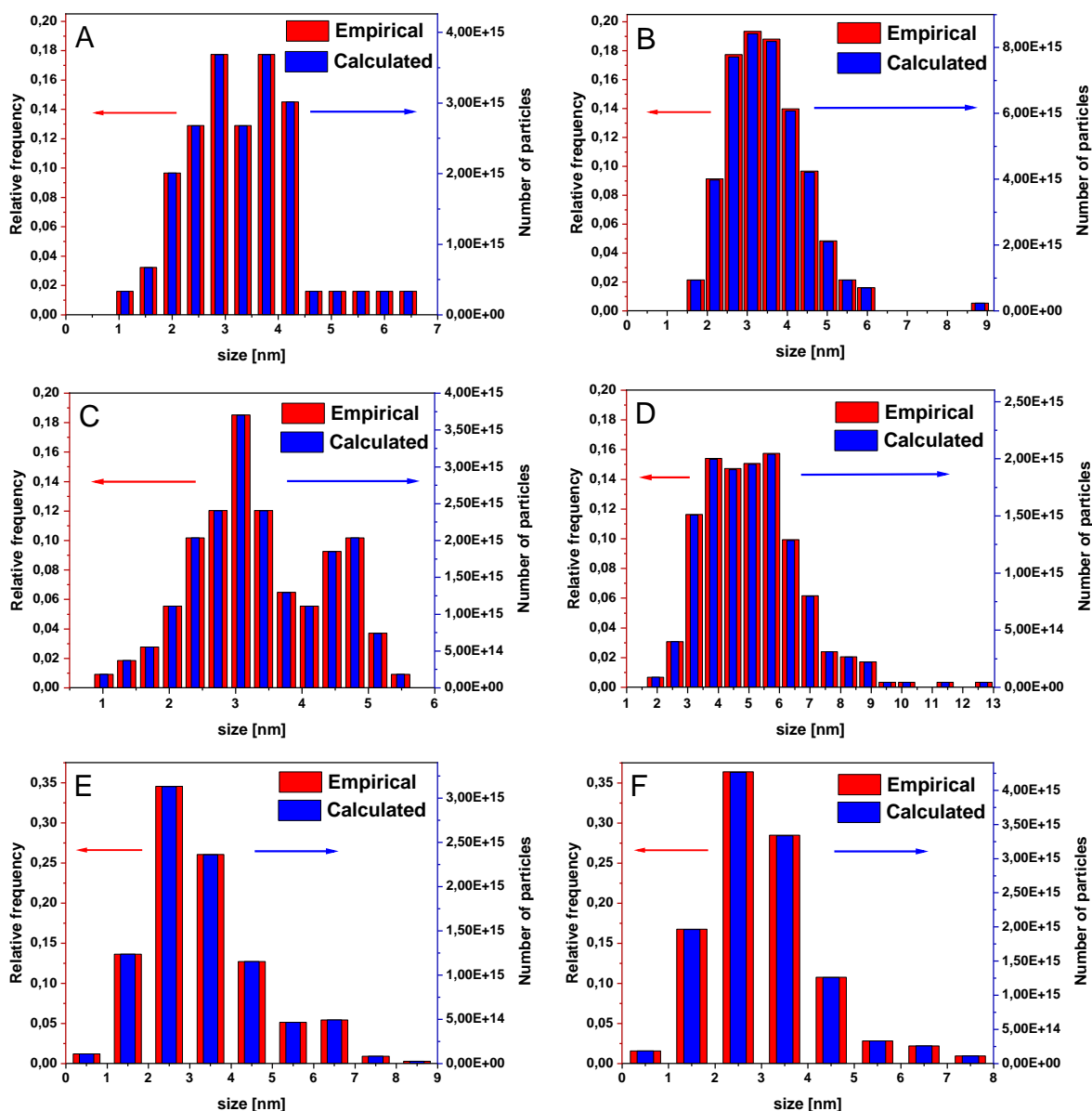
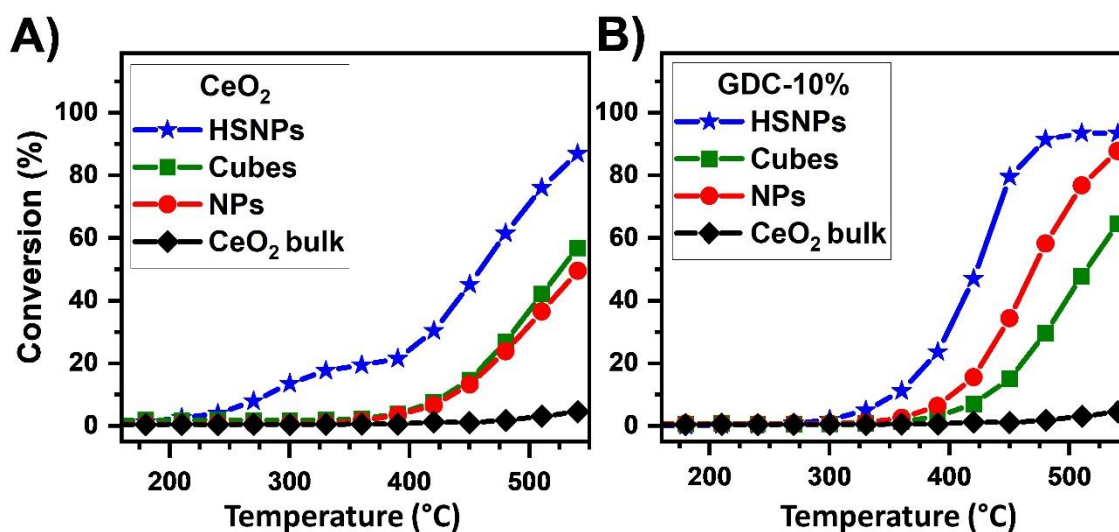


**Fig. S17.** Histograms showing empirical Au NPs size distribution determined from TEM (lefts axis) and corresponding number of Au particles (modeled as half-spheres) calculated via the use of Solver tool with restriction to total mass of active phase (Au-wt%) in 0,05g catalyst (right axis). A) Au<sub>2</sub>/CeO<sub>2</sub> HSNPs; B) Au<sub>5</sub>/CeO<sub>2</sub> HSNPs; C) Au<sub>2</sub>/GDC-10% HSNPs; D) Au<sub>5</sub>/GDC-10% HSNPs; E) Au<sub>5</sub>/CeO<sub>2</sub> cubes; F) Au<sub>5</sub>/GDC-10% cubes.

### TOF<sub>[b]</sub> calculation

TOF<sub>[b]</sub> defined as specific rate normalized to the number of active sites at the Au/ceria interface (ring around Au nanoparticle, Au NP modeled as a half-sphere) has been calculated from the following formula:  $TOF_{300^{\circ}C} [s^{-1}] = r_{300^{\circ}C} [\text{mole of propane} \cdot \text{g}^{-1} \cdot \text{s}^{-1}] / (\text{mole of Au/ceria interface active sites} [\text{mole}] / \text{mass of the Au active phase} [\text{g}])$ . The mole number of Au active sites at the Au/CeO<sub>2</sub> interface was determined from empirical histograms generated from TEM data. Firstly, Solver tool in Excel was used to determine number of particles that corresponds to empirical histograms (Fig. S13.2 A-F). The total volume that corresponds to the mass of the active phase in 0,05g catalyst has been chosen as

objective cell, while relative frequency as constraints to model the total number of the Au half-sphere nanoparticles redistributed to each bin of the histogram. The number of Au interface atoms that correspond to each size interval of the histogram has been calculated from the number of Au particles in a bin, the diameter of the Au NP and van-der-Waals radii of Au atom (166 pm).



Catalyst support	$r \times 10^6$ [mol m <sup>-2</sup> h <sup>-1</sup> ]	
	330°C	420°C
CeO <sub>2</sub> NPs	1,4	10,8
CeO <sub>2</sub> cubes	8,0	32,2
CeO <sub>2</sub> HSNPs	15,1	25,9
GDC-10% NPs	1,2	17,9
GDC-10% cubes	3,4	27,9
GDC-10% HSNPs	3,8	36,5

**Fig. S18.** Propane conversion plots of samples differing by support morphology, nanoparticles (NPs), nanocubes (cubes), hierarchically structured particles (HSNPs); A) CeO<sub>2</sub> supports, B) GDC-10% supports; C) specific rate at 330°C and 420°C.



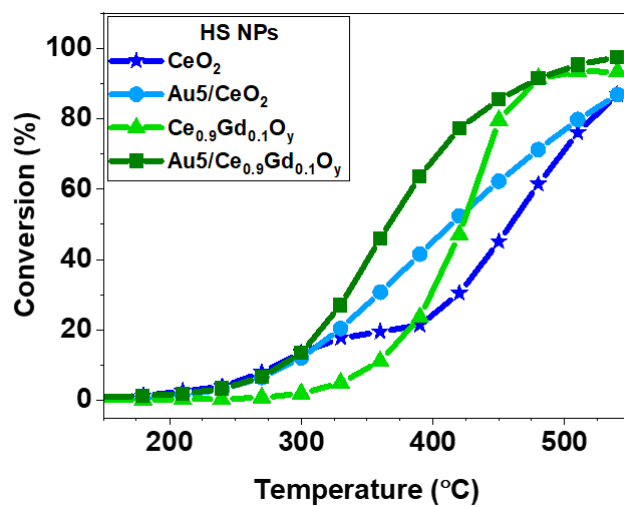


**Fig. S19.** Propane conversion of Ce<sub>0.9</sub>Gd<sub>0.1</sub>O<sub>1.95</sub> (x=0;0.1) HS NPs carrier and Au5/ Ce<sub>0.9</sub>Gd<sub>0.1</sub>O<sub>1.95</sub> (x=0;0.1) HS NPs catalyst.

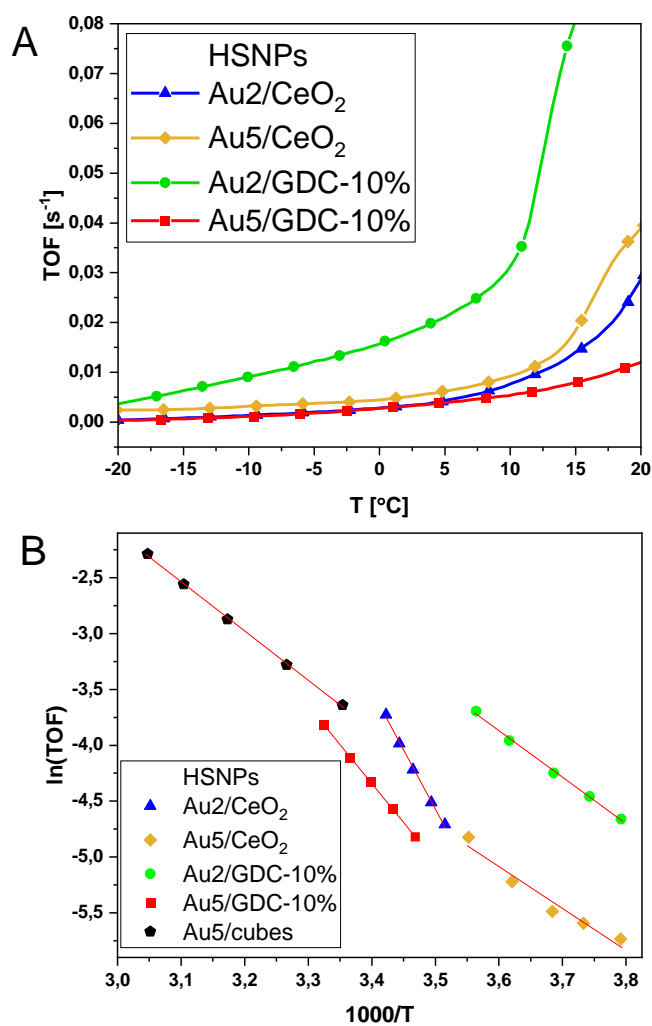


**Fig. S20.** Catalytic performance in CO oxidation. A) TOF as a function of temperature; B) corresponding Arrhenius plots.

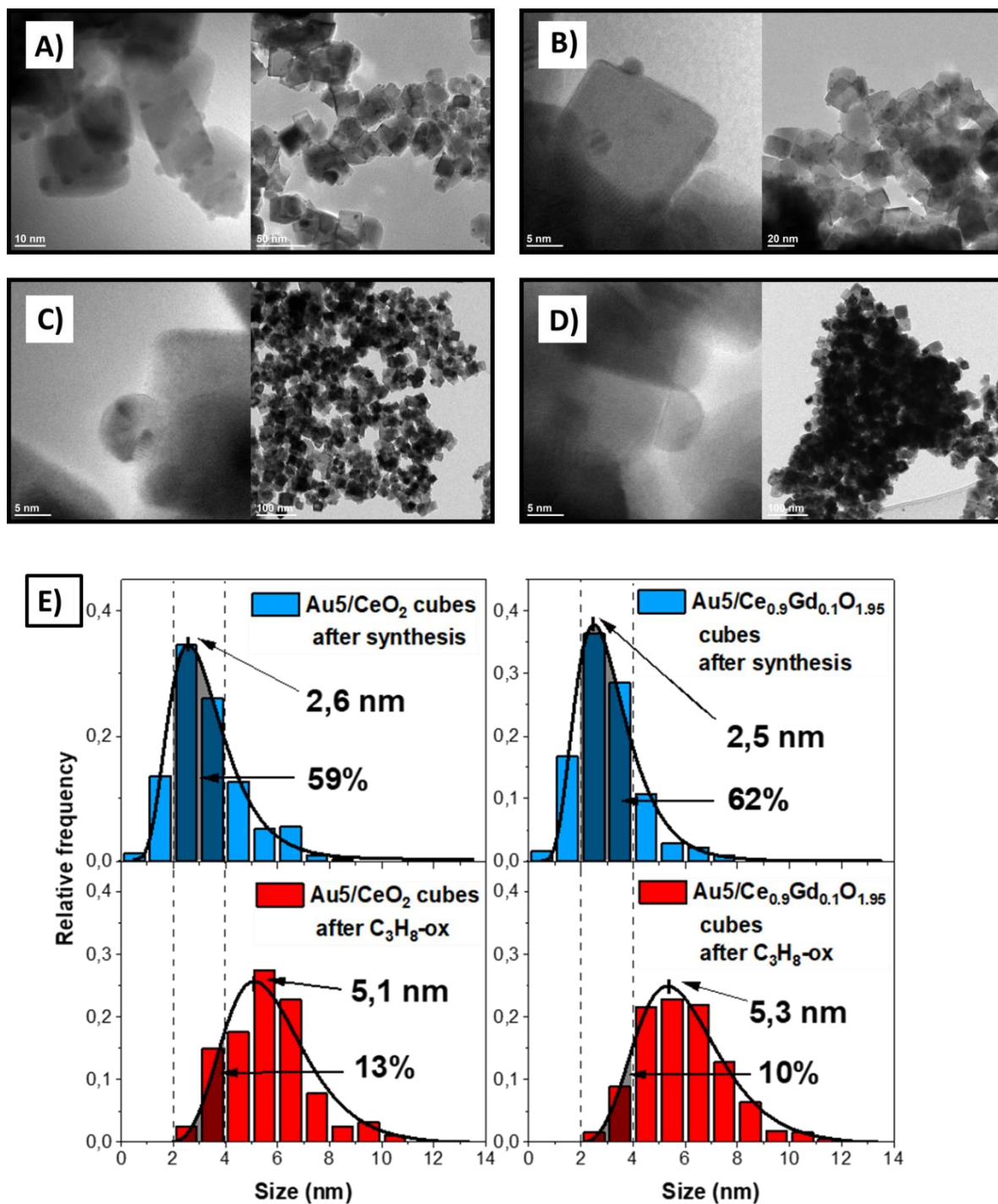


**Fig. S21.** TEM images of Ce<sub>1-x</sub>Gd<sub>x</sub>O<sub>2-x/2</sub> (x=0; 0.1) cubes before and after propane oxidation. A) Au5/CeO<sub>2</sub> cubes before oxidation; B) Au5/GDC-10% before oxidation; C) Au5/CeO<sub>2</sub> cubes after oxidation; D) Au5/GDC-10% after oxidation; E) Au NPs size distribution plots.

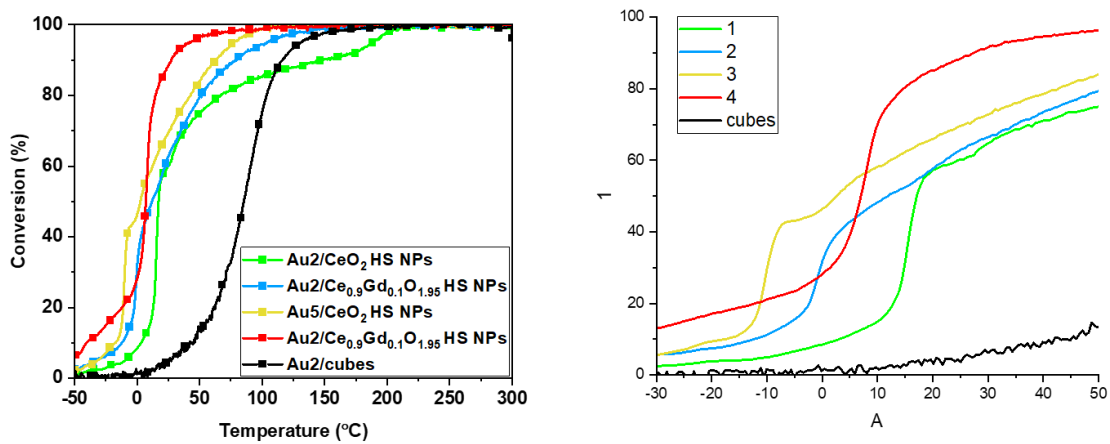
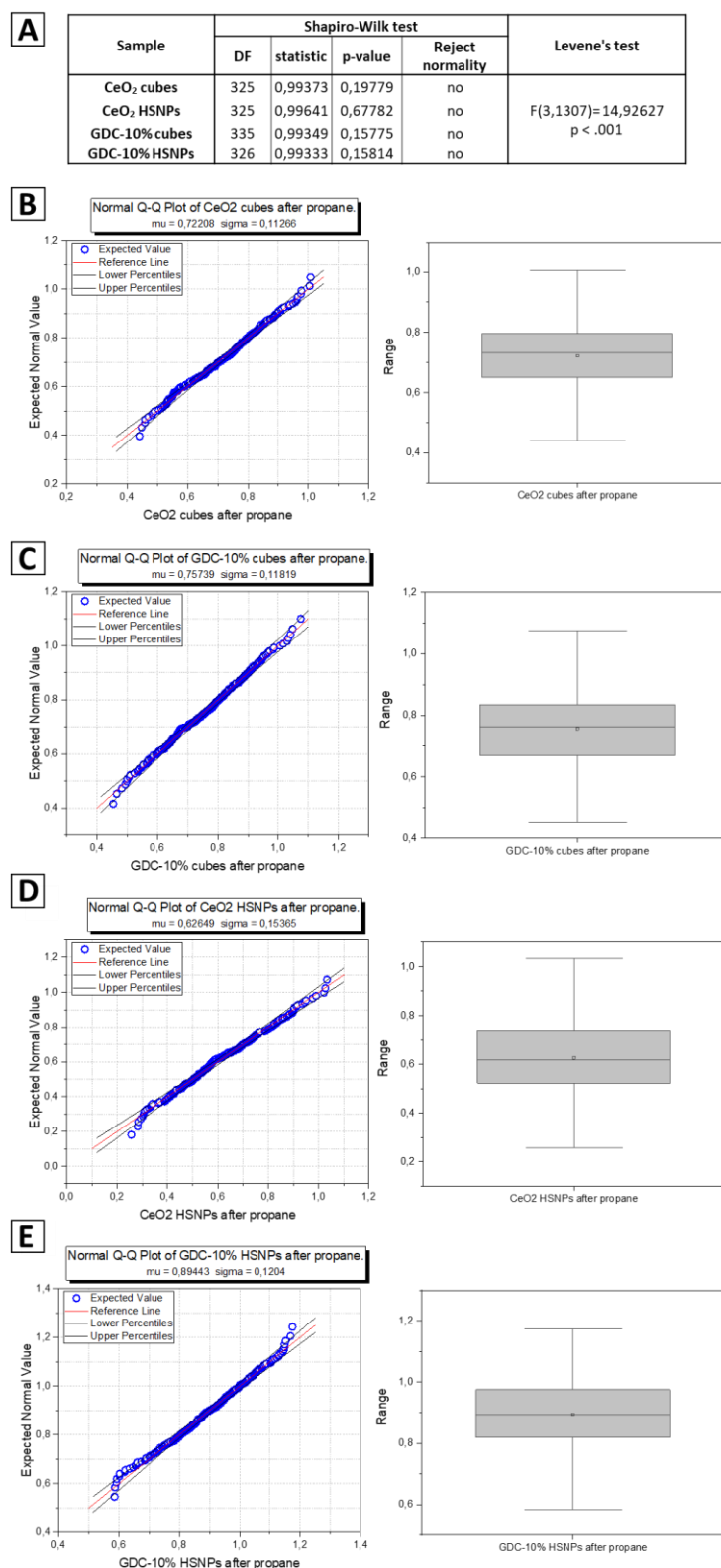


**Fig. S22.** CO conversion plot of hierarchically structured catalysts after reduction in H<sub>2</sub> flow at 400°C for 3h.



**S23.** A) Shapiro-Wilk test and Levine's test results for AuNPs size data for supports differed by architecture and doping level. Samples are after propane oxidation (size data obtained from TEM); B- E) Q-Q plots and box charts for tested samples: B) Au<sub>5</sub>/CeO<sub>2</sub> cubes C) Au<sub>5</sub>/GDC-10% cubes D) Au<sub>5</sub>/CeO<sub>2</sub> HSNPs E) GDC-10% HSNPs. All samples are normally distributed. Variances are not equal across groups, however, samples have similar size and outliers has been eliminated for statistical analysis of variance.

# Hierarchical Au/CeO<sub>2</sub> systems – influence of Ln<sup>3+</sup> dopants on the catalytic activity in the propane oxidation process.

Piotr Woźniak, Piotr Kraszkiewicz, Małgorzata A. Malecka\*

*Institute of Low Temperature and Structure Research, Polish Academy of Sciences,*

*Okólna 2, 50-422 Wrocław, Poland*

## ABSTRACT

In this paper, the information on interactions in Au/CeO<sub>2</sub> (and Au/Ce<sub>0.9</sub>Ln<sub>0.1</sub>O<sub>1.95</sub>, Ln = La, Gd and Yb) system have been presented from a novel point of view. This work focuses on showing the (nano)Au – (hierarchical/nano)CeO<sub>2</sub> interaction. Hierarchically 3D organized ceria-based mixed oxides (tube-like macroparticles) were prepared by a wet chemical method. Decoration of macroparticles was successfully carried out using the deposition–precipitation method. It was observed that the predetermined shape of the investigated macroparticles and the uniform distribution of gold nanoparticles were not dependent on the ion radius of the Ln<sup>3+</sup> dopant. It has been noted that the hierarchical materials, investigated in this work, exhibit sensational red-ox properties. It was concluded that the presence of a 3D structure of catalysts results in a strong lowering of the cerium ion reduction temperature (during H<sub>2</sub>-TPR) down to temperatures below zero (-8 °C). The materials tested in this work also turned out to be catalytically active in the propane oxidation process. The temperature of half propane oxidation (T<sub>50</sub> = 399 °C) obtained for Au/CeO<sub>2</sub> was 96 °C lower than that for the undecorated support. Moreover, introduction of the small amount of the La<sup>3+</sup> and Yb<sup>3+</sup> ions (in a 1: 1 ratio) into the ceria matrix led to further improvement of the propane oxidation performance (T<sub>50</sub> = 361 °C). What is interesting, such effect was not observed for Au/Ce<sub>0.9</sub>Gd<sub>0.1</sub>O<sub>1.95</sub> sample. This makes us believe that the catalytic activity of the decorated systems in this process depends not only on the presence of Au nanoparticles on the support surface but also on the type of deformation in the CeO<sub>2</sub> network. Unfortunately, the hierarchical Au/CeO<sub>2</sub> (and Au/Ce<sub>0.9</sub>Ln<sub>0.1</sub>O<sub>1.95</sub>) systems lost their activity very quickly due to the growth of gold nanoparticles at quite high reaction temperatures, but decorating macroparticles with gold nanoparticles significantly improves the selectivity of the propane oxidation process.

Key words: catalysis; ceria; gold; mixed oxides; hierarchical structure; TEM

\*corresponding author:

Małgorzata Alicja Malecka

P.O. Box 1410, 50-950 Wrocław, Poland,

Tel: (4871) 3954150, Fax (4871) 441029, e-mail: [M.Malecka@intibs.pl](mailto:M.Malecka@intibs.pl)

[doi.org/10.1039/D2CE00827K](https://doi.org/10.1039/D2CE00827K)

## INTRODUCTION

For hundreds of years, gold has been a symbol of durability, divinity and immortality. Large particles of gold are catalytically inactive, so until 40 years ago the idea of using a gold-based catalyst seemed ridiculous. However, in the 80's of the XX century, the works of Haruta [1;2] and Hutchings [3] showed that, the nanosized particles of gold well dispersed on oxide support have a great activity as a catalyst in the low temperature CO oxidation process. The interest of scientists in the use of gold nanoparticles as a catalyst began to grow intensively and this trend continues to this day. The highest catalytic activity (in the CO oxidation reaction) was observed for nanoparticles of gold with a size of 3-4 nm [4;5]. For Au particles having a size below this value, the catalytic activity significantly decreases. It is probably due to the impeded adsorption of CO molecule on the very small gold nanoparticle [5]. Similarly, the activity of gold-based catalysts decreases with increasing of the Au particle size to finally become an inactive material. Catalysts based on the highly dispersed gold nanoparticles on oxide support show high activity in many reactions, like CO oxidation [6;7] cyclohexane oxidation [8-10], selective hydrogenation of 1,3-butadiene [11-13], WGS reaction [14;15], hydrogenation of crotonaldehyde [16;17], complete benzene oxidation [18;19] and reduction of NO by CO [20].

Besides the active phase, also supports play the important role in catalytic act. The supports can be classified in the various ways. The first one is the division into two main classes: “active” and “nonactive” supports. “Active” supports can be described as easily reducible oxides, which take part in the catalytic act [21-23]. Whereas “nonactive” ones are hardly reducible (or nonreducible) oxides [21-23], which do not take part in the reaction but only ensure high dispersion of the active phase. Another basis for the classification of supports may be their porosity level. According to the IUPAC classification, porous materials have been divided into micro-, meso-, macro- and nonporous materials [24]. Nowadays, hierarchical materials are starting to play more and more important role in the catalysis [25;26]. Researchers around the world are studying the utility of the hierarchical materials as the catalytic supports. The definition of the hierarchical materials based on the multi-level order which may be defined as the number  $n$  of levels of scale with recognized structure [27]. Hierarchical materials may be defined in terms of structure [28] or porosity [29]. Examples of materials exhibiting structure hierarchy are 3D macrostructures built of nanoparticles in an ordered manner as star-like or tube-like ceria macroparticles [30;31]. In the literature, a lot of methods for synthesizing hierarchical materials (e.g. template methods, self-organization, post-synthetic processing or 3D printing) with at various properties and possibility application can be found [26;28;32;33]. In heterogeneous catalysis, the size

and shape of the developed surface of the catalyst which comes into contact with the reactants during the catalytic reaction are of key importance. In the literature, a series of reports regarding the possible use of hierarchical materials in the catalytic process as Fischer–Tropsch synthesis, cracking, oxidation, epoxidation and reduction [34-38] can be found.

Ceria and ceria based mixed oxides have many technological applications. For example, rare-earth mixed oxides find wide application as three-way catalysts [39] and in solid oxide fuel cell technology [40-43]. High activity of the ceria based mixed oxides as well as pure ceria as the catalysts is due to their ability to reversible change of the cerium oxidation state  $Ce^{4+} \leftrightarrow Ce^{3+}$  (or better as the conversion of cerium IV oxide to doped cerium IV oxide with cerium III ions -  $Ce^{IV}O_2 \leftrightarrow Ce^{IV}_{1-x}Ce^{III}_xO_{2-(x/2)}$ ) [44;45]. This process can be modified by partial substitution of  $Ce^{+4}$  with  $Ln^{+3}$  (Ln – trivalent lanthanide ion), which facilitates a bulk reduction of ceria [46;47]. The improved reducibility is due to the creation of extrinsic oxygen vacancies in the ceria lattice, which enhances the oxygen anion mobility [46;47]. For  $Ce_{1-x}Ln_xO_{2-x/2}$  mixed oxide, two main structure types are expected: fluorite (F-type, Fm-3m) characteristic of  $CeO_2$  and bixbyite (C-type, Ia-3) characteristic of  $Ln_2O_3$  (where Ln – heavy trivalent lanthanide ion). These two structure types are closely related. C-type unit cell could be built by the doubling F-type cell with simultaneous removing  $\frac{1}{4}$  of  $O^{2-}$ -ions (from sites 16c) [48]. Microstructure of ceria based mixed oxides has been widely studied by various research groups [49-53]. Additionally, the doping of  $CeO_2$  matrix by the lanthanide  $Ln^{3+}$  ions are known to strongly hinder crystallite growth of ceria during heating in an oxidizing atmosphere. The inhibiting effect is explained by additive segregation at the ceria grain boundaries [54;55].

Ceria-based hierarchical materials are beginning to increasingly attract the attention of scientists from around the world. In the literature, some data about the properties of hierarchically organized macro-structures composed of ceria nanoparticles are available [56;57]. In our previous paper [30], the synthesis, thermal stability and redox properties of tube-like Yb-doped ceria build from hierarchically organized nanocrystalline  $Ce_{1-x}Yb_xO_{2-(x/2)}$  had been investigated. The combination of the unique properties of oxide nanoparticles, high specific surface area and structural hierarchy with a presence of the well dispersed gold nanoparticles is a very interesting topic for catalysis and environmental protection. In this work, we will focus on the demonstration of the interactions between nanosized gold particles and ceria-based support organized in the hierarchical structure.

## EXPERIMENTAL

The tube-like, hierarchical  $CeO_2$  and  $Ce_{0.9}Ln_{0.1}O_{1.95}$  macro-particles build by the nano-sized mixed oxide crystallites were prepared by wet chemical synthesis involving several steps. First,

nanocrystalline CeO<sub>2</sub> or Ce<sub>0.9</sub>Ln<sub>0.1</sub>O<sub>1.95</sub> oxides (where Ln = La, Gd and Yb) were prepared by precipitation in microemulsion (water-in-oil, W/O) method. Additionally, double-doped Ce<sub>0.9</sub>La<sub>0.05</sub>Yb<sub>0.05</sub>O<sub>1.95</sub> oxide was prepared by the same method. Details of this technique were described in our previous paper [58]. Briefly, Triton X-100 was used as a non-ionic surfactant and cyclohexane and 1-pentanol as an organic phase. Aqueous solutions of lanthanides (as nitrates-mixed in appropriate molar ratios) and ammonia were used as a water phase. Syntheses were performed at room temperature. In the next step, the powder samples obtained by centrifugation were treated with formic acid for 5 days to obtain mixed Ce-Ln formates. Then, formates were dried in atmospheric air. Subsequently, the tube-like macroparticles were prepared by the precipitation method in the presence of CTAB as an auxiliary agent. Details of this technique were inspired by [59] and were described in [30]. Briefly, to the surfactant solution (CTAB/H<sub>2</sub>O/NH<sub>4</sub>OH in the appropriate amounts), the water-ethanol suspension of cerium (or mixed Ce-Ln) formate was added dropwise. After stirring for 1 h the precipitate was centrifuged and washed with deionized water. Finally, after drying at 60 °C in atmospheric air, the samples were heated at 400 °C for 3 h (heating rate: 1 °C/min).

The hierarchical Au/CeO<sub>2</sub> and Au/Ce<sub>0.9</sub>Ln<sub>0.1</sub>O<sub>1.95</sub> samples were prepared by the deposition-precipitation method [60]. The mixture (suspension) of ceria or mixed oxide macro-particles, HAuCl<sub>4</sub>, (NH<sub>2</sub>)<sub>2</sub>CO and H<sub>2</sub>O were stirred and kept at 80 °C in a silicone oil bath for 24 h. The amount of gold in the hierarchical Au/oxide samples was described as follows: 5 particles of the HAuCl<sub>4</sub> on 1 nm<sup>2</sup> (surface area) of the hierarchical support [61]. Then, the obtained product was washed and dried at 70 °C. The solid product was heated at 300 °C in static air by 3 h (heating rate: 5 °C/min).

The phase composition and structural parameters of the crystalline phases present in the samples were determined by XRD (X'Pert PRO PANalytical powder diffractometer, Cu K $\alpha$  radiation) with a FullProf program [62] used for the display and analysis of the diffractograms. The Scherrer formula was used to estimate crystallite mean sizes. The morphology and microstructure were investigated by TEM (Philips CM-20 SuperTwin operating at 160 kV). HRTEM images and SAED patterns were analysed with a DigitalMicrograph program. The uniformity, chemical composition and topography of the samples were checked with a FE-SEM microscope (FEI NovaNanoSEM 230) equipped with an EDS analyser (EDAX Genesis XM4). The global EDX analyses were performed from the large area (250  $\mu$ m  $\times$  200  $\mu$ m) of the samples. The powder samples were included in the carbon resin and then pressed at 180 °C and 250 bar to obtain a large, flat area. Each of the line profile EDX measurement was performed from single tube-like macroparticle of catalyst.

Before the reducibility and catalytic tests, all samples were pre-treated at 300 °C in static air for 3 h. The reducibility of the selected samples was tested by H<sub>2</sub>-TPR (temperature programmed reduction



in hydrogen). Typically, 50 mg of sample was placed in a quartz-glass microreactor (Autochem II 2920, Micromeritics) and heated with a temperature ramp of 10 °C/min up to 900 °C in a stream of 5% H<sub>2</sub> in Ar. The hydrogen consumption was monitored by a thermal conductivity detector (TCD), calibrated with CuO (99.99%) as the reference material. The catalytic activity of the samples was tested in propane oxidation process. 50 mg of catalyst was heated up to 180 °C and stabilized at this temperature for 0.5 h in the gas flow (mixture 2500 ppm of propane in the synthetic air (10% O<sub>2</sub>/N<sub>2</sub>); 100 cm<sup>3</sup>/min). The measurements were performed using Perkin-Elmer ARNEL Clarus 500 gas chromatograph equipped with a flame ionization detector and Elite Plot-Q chromatographic column. Measurements were performed at each step until the steady-state activity was obtained.

## RESULTS AND DISCUSSION

### *Supports characteristic*

The synthesis methods of hierarchical ceria-based materials are well described in the literature [63-66]. In the case of the Ce<sub>1-x</sub>Ln<sub>x</sub>O<sub>2-x/2</sub> macroparticles, literature reports are much less numerous [30;67]. In our previous paper [30], synthesis procedure and characteristic of the hierarchical, tube-like Ce<sub>1-x</sub>Yb<sub>x</sub>O<sub>2-x/2</sub> macroparticles (x = 0.1; 0.2; 0.3; 0.4 and 0.5) have been thoroughly described. In this work, a series of the hierarchical, tube-like Ce<sub>0.9</sub>Ln<sub>0.1</sub>O<sub>1.95</sub> (where Ln = La, Gd, Yb) mixed oxides were obtained. The main goal was to investigate the shape stability of macroparticles as a function of ionic radius of doping ion. The level of doping (x = 0.1) was chosen based on our previous experience, where the tube-like shape of macroparticles was achieved only for low-doped materials [30]. Additionally, to investigate the influence of the mean lanthanide ion radius on the properties of the support, double-doped Ce<sub>0.9</sub>La<sub>0.05</sub>Yb<sub>0.05</sub>O<sub>1.95</sub> oxide was prepared (where the mean radius of the lanthanide is close to that of the Ce<sub>0.9</sub>Gd<sub>0.1</sub>O<sub>1.95</sub> mixed oxide). In this case, a similar mean lanthanide ion radius, but different kind of the deformations of the ceria lattice has been observed (see Table 1). In the first step, all the samples were investigated by SEM-EDS. In Table 1, the results of the chemical composition measurements carried out both for Ln-formates (reactants) and for finished products (oxides after heating at 400 °C) were shown. As noted, the amount of incorporated Ln-ions into the ceria structure is in good agreement with the nominal one (despite the multi-step synthesis procedure described in [30]).

Table 1. Concentration of Ln<sup>3+</sup> in the formate and ceria matrix (from SEM-EDX measurement – (% at) calculated as (Ln × 100)/(Ln + Ce)). Additionally, mean lanthanide ion radiuses for oxides (coordination VIII) have been added [68].

formate	at%	oxide	at%	R(Ln) <sub>av</sub> [Å]
Ce(HCOO) <sub>3</sub>	Ce: 100	CeO <sub>2</sub>	Ce: 100	0.9700
Ce <sub>0.9</sub> La <sub>0.1</sub> (HCOO) <sub>3</sub>	Ce: 88.3 La: 11.7	Ce <sub>0.9</sub> La <sub>0.1</sub> O <sub>1.95</sub>	Ce: 88.8 La: 11.2	0.9890
Ce <sub>0.9</sub> La <sub>0.05</sub> Yb <sub>0.05</sub> (HCOO) <sub>3</sub>	Ce: 89.3 La: 6.5 Yb: 4.2	Ce <sub>0.9</sub> La <sub>0.05</sub> Yb <sub>0.05</sub> O <sub>1.95</sub>	Ce: 88.8 La: 6.5 Yb: 4.7	0.9802
Ce <sub>0.9</sub> Gd <sub>0.1</sub> (HCOO) <sub>3</sub>	Ce: 90.6 Gd: 9.4	Ce <sub>0.9</sub> Gd <sub>0.1</sub> O <sub>1.95</sub>	Ce: 87.2 Gd: 12.8	0.9783
Ce <sub>0.9</sub> Yb <sub>0.1</sub> (HCOO) <sub>3</sub>	Ce: 89.9 Yb: 10.1	Ce <sub>0.9</sub> Yb <sub>0.1</sub> O <sub>1.95</sub>	Ce: 90.7 Yb: 9.3	0.9715

In Fig. S1, TEM images of the pure and doped hierarchical, tube-like macroparticles are presented. TEM images show the tube-like, hollow inside and closed on one side macroparticles build from nanocrystalline ceria or ceria based mixed oxides. The average size of crystallites for the CeO<sub>2</sub> was determined to be 10.6 nm (from XRD data), however, a significant decrease in the mean crystallite size of about 2-3 nm was observed for the doped samples (see Table 2). As known, the addition of the trivalent lanthanide ion into the ceria matrix may lead to phase segregation into a Ce-rich and Ln-poor phase (Ce<sub>1-a</sub>Ln<sub>a</sub>O<sub>2-a/2</sub> - core) and a Ln-rich and Ce-poor phase (Ln<sub>2-b</sub>Ce<sub>b</sub>O<sub>3+b</sub> - surface) [54;69] and change of the mixed oxide structure with increasing of the defects content [69]. The above reasons may be related to the inhibition of mixed oxide crystallite growth relative to pure cerium oxide [70]. Additionally, an in-depth analysis of the TEM images shows that, despite the wide spread of the tube-like macroparticles width, the measurement results for CeO<sub>2</sub> were about two times larger than for the doped oxides. This effect has been observed on the SEM images (fig. S2), where a large population of support macroparticles is visible. It could be due to the slightly smaller crystallites of the mixed oxides making up the macroparticle (see Table 2).

As shown in the Fig. S3., all tested samples of supports have the cubic, F-type structure described Fm-3 m space group (225), characteristic for CeO<sub>2</sub> [48] and low-doped Ce<sub>1-x</sub>Ln<sub>x</sub>O<sub>2-x/2</sub> mixed oxides [53]. In the literature, a lot of papers about the solubility limits in the ceria based mixed oxides Ce<sub>1-x</sub>Ln<sub>x</sub>O<sub>2-x/2</sub> (where Ln - La [54;71], Gd [72;73], Yb [74;75]) could be found. The available data very often refer to the bulk materials prepared by high temperature thermal treatment of mixture of the single lanthanide oxides (~1400 °C, oxidizing atmosphere). The biphasic region, where phase separation into the Ce-rich and Ln-rich occurs, is usually noted over the doping value assumed by us (x

= 0.1). According to our previous reports [53], the addition of a foreign trivalent ion to the CeO<sub>2</sub> matrix causes the creation of an appropriate number of oxygen gaps and mutual shifts of the cationic and anionic sublattices. However, for different ionic radii the dopants ion shift and hence the microstructure of the oxides will be different [49;53]. The lattice parameter and unit cell volume for mixed oxides (see Table 2) increases with increasing mean lanthanide ion radius (see Table 1), which is consistent with the literature [76;77]. As noted, the increase in unit cell volume (and lattice parameter) as a function of mean lanthanide ion radius was linear. From the above considerations, it follows that doping the CeO<sub>2</sub> matrix with trivalent lanthanide ions changes not only the oxide microstructure but also influences the overall construction of tube-like macroparticles (the size, shape and mutual arrangement of the nanocrystalline ceria-based blocks). During the TEM research, it was noticed that there was no preferential orientation of CeO<sub>2</sub> and mixed oxide nanoparticles relative to the beam. Obtained SAED patterns were characteristic for polycrystalline samples (ring-type). However, Woźniak et. al. [31;67] reported that the SAED patterns and FFT images indicated almost the same orientation of the Ce<sub>1-x</sub>Ln<sub>x</sub>O<sub>2-x/2</sub> nanocrystals within a single star-like macroparticle arm (pseudo point-type; mosaic arrangement). Such difference could be due to the completely different way of synthesizing hierarchical macroparticles, in [31;67] - oxidative thermolysis of Ce- or Ce/Ln-formate and in this work – wet chemical method.

In order to analyse the porosity of the obtained supports, N<sub>2</sub> adsorption–desorption studies were performed. As known, according to IUPAC classification, the shape of the N<sub>2</sub> adsorption–desorption isotherm can be sorted into the six types from I to VI (with four hysteresis pattern types from H1 to H4) [24]. Thanks to examining the evolution of the N<sub>2</sub> isotherm run, the detailed characteristics of pores in the investigated material can be determined [78;79]. Additionally, the shape of the hysteresis loop allows to define the shape of the pores [78;80-82]. In the Fig. S4, the N<sub>2</sub> adsorption–desorption isotherms obtained for all investigated supports have been presented. Similar as in [30], the all isotherms have been assigned to a meso-macroporous material with a characteristic H3-type hysteresis loop [78]. The presence of the H3 hysteresis loop suggests the presence of slit-like pores between the oxide nanocrystallites that build the tube-like macroparticles [82-84]. The course of the isotherm for all 5 samples has the same character, but the value of the specific surface area (S<sub>BET</sub>) of the tested materials changes strongly (see Table 2). The size of the specific surface area increases with the addition of a dopant ion to the oxide structure, which was previously described in [30]. Such effect is probably due to a smaller average size of the oxide crystallites from which the macroparticles are formed (Table 2). This is in line with [85] where the strong correlation between the specific surface area and catalytic activity was observed. However, careful analysis of the results shows a linear

relationship between the mean lanthanide ion radius and the  $S_{\text{BET}}$  surface area for our sample series (Fig. S4). This observation suggests the possibility of designing the catalytic support in a wider scope (more than just the amount of dopant ion). Interestingly, the double-doped oxide  $\text{Ce}_{0.9}\text{La}_{0.05}\text{Yb}_{0.05}\text{O}_{1.95}$  (where we deal with two different dopant ions - the larger - the  $\text{La}^{3+}$  ion ( $R = 0.1160$  nm [68]) and the smaller -  $\text{Yb}^{3+}$  ion ( $R = 0.0985$  nm [68]) than  $\text{Ce}^{4+}$  ( $R = 0.0970$  nm [68])) also fits well with this trend.

Table 2. Mean size [nm], lattice parameter [nm], cell volume [ $\text{nm}^3$ ] of  $\text{Ce}_{1-x}\text{Ln}_x\text{O}_{2-x/2}$  nanocrystals calculated from XRD data and BET surface area of the investigated samples.

sample	$d_{\text{av}}$ [nm]	$a_{\text{F}}$ [nm]	$V$ [ $\text{nm}^3$ ]	$S_{\text{BET}}$ [ $\text{m}^2/\text{g}$ ]
$\text{CeO}_2$	10.6	0.5414	0.158692	55
$\text{Ce}_{0.9}\text{La}_{0.1}\text{O}_{1.95}$	7.2	0.5443	0.161256	69
$\text{Ce}_{0.9}\text{La}_{0.05}\text{Yb}_{0.05}\text{O}_{1.95}$	7.4	0.5424	0.159573	73
$\text{Ce}_{0.9}\text{Gd}_{0.1}\text{O}_{1.95}$	8.1	0.5421	0.159308	74
$\text{Ce}_{0.9}\text{Yb}_{0.1}\text{O}_{1.95}$	8.5	0.5410	0.158340	82

### *Catalysts characteristic*

The decoration process of the pure and Ln-doped hierarchical ceria tube-like macroparticles by gold nanoparticles was performed by the deposition-precipitation method [60]. As shown in the literature [86-89] and our previous experiences [61;90], the decoration method used in this work is effective in obtaining ceria (or defected ceria) with small gold nanocrystals well dispersed on the surface (with various support morphologies – cubes, octahedrons, rods, etc.). However, the above information concerns rather large  $\text{CeO}_2$  crystallites with often defined morphology (flat surfaces). In this study, the large macroparticles build by the nanoparticles of ceria-based oxides have been investigated, so the Au-support contact sites could be modified due exposition of various crystal planes by nano-sized ceria and occurrence of slit-like pores within support. Moreover, as shown in [61], a key role in the decoration process plays the ratio of the molar content of the chloroauric acid to the total surface area of the support ( $M_{\text{Au}}/S_{\text{support}}$ ). In view of the high surface area of the support  $S_{\text{BET}}$  (see Table 2), it was necessary to use a large amount of gold to obtain Au particles with a size of about 3-4 nm.

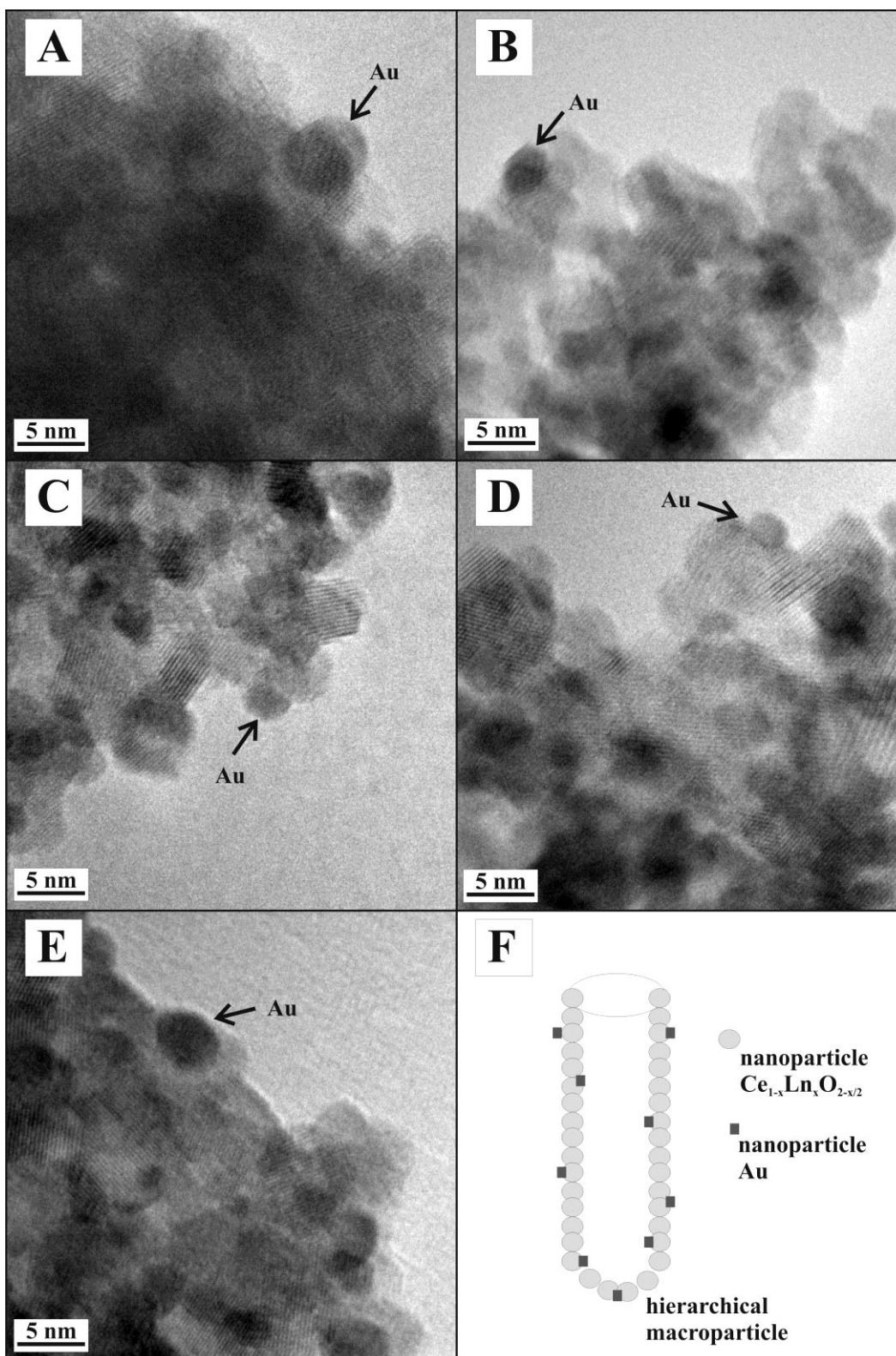


Fig. 1. HR-TEM images of hierarchical tube-like (A) Au/CeO<sub>2</sub>, (B) Au/Ce<sub>0.9</sub>La<sub>0.1</sub>O<sub>1.95</sub>, (C) Au/Ce<sub>0.9</sub>La<sub>0.05</sub>Yb<sub>0.05</sub>O<sub>1.95</sub>, (D) Au/Ce<sub>0.9</sub>Gd<sub>0.1</sub>O<sub>1.95</sub>, (E) Au/Ce<sub>0.9</sub>Yb<sub>0.1</sub>O<sub>1.95</sub>, (F) model of the decorated hierarchical tube-like macroparticle.

Table 3. Au content in the investigated samples measured by the SEM-EDX technique and calculated from the experimental data and mean size of Au nanoparticles (supported on oxides) calculated from the XRD data.

oxide	Au			d <sub>av</sub> Au [nm]
	at %	wt %	wt % (calculated from experimental data)	
Au/CeO <sub>2</sub>	2.3	6.6	8.2	4.3
Au/Ce <sub>0.9</sub> La <sub>0.1</sub> O <sub>1.95</sub>	2.8	8.5	10.2	3.5
Au/Ce <sub>0.9</sub> Gd <sub>0.1</sub> O <sub>1.95</sub>	3.1	9.0	10.8	3.8
Au/Ce <sub>0.9</sub> La <sub>0.05</sub> Yb <sub>0.05</sub> O <sub>1.95</sub>	3.9	11.1	10.4	3.5
Au/Ce <sub>0.9</sub> Yb <sub>0.1</sub> O <sub>1.95</sub>	3.7	10.6	11.7	3.7

In Fig. 1, the HRTEM images of the Au nanoparticles supported on the hierarchical, tube-like ceria and ceria-based supports. Detailed analyses of the HRTEM images show, that the observed Au nanoparticles supported on the macroparticles surface are rather sparse. It seems that the samples (regardless of the chemical composition of the support) must also contain smaller, hardly noticeable gold particles. To confirm the above thesis, a TEM test was performed again, but using the dark field technique (TEM-DF). In the DF image, a series of bright dots on the almost black tube-like surface CeO<sub>2</sub> (Fig. S5) are shown. The selected position of the aperture (between the rings CeO<sub>2</sub>200 = 0.27 and CeO<sub>2</sub>220 = 0.19 nm [PDF no 00-004-0593]) allows to obtain a bright image for appropriately oriented gold particles (Au111 = 0.23 nm [PDF no 00-004-0784]). As shown in Fig. S5, small gold particles are quite densely deposited on the support surface (although they are poorly visible in the TEM-BF images – bright field). Due to the non-planar surfaces of hierarchical macroparticles, the orientation between gold nanoparticles and CeO<sub>2</sub> (or Ce<sub>0.9</sub>Ln<sub>0.1</sub>O<sub>1.95</sub>) nanoparticles appears to be random. This observation is in contrast to the work [90], where in the case of flat surfaces of the CeO<sub>2</sub> support, the preferred orientation Au111||CeO<sub>2</sub>111 or Au111||CeO<sub>2</sub>100 was noted. However, the random orientation between Au and ceria-based oxides may be responsible for the interesting catalytic properties of our materials. As it is known, in many catalytic processes involving Au/CeO<sub>2</sub> materials, active centres located at the Au/CeO<sub>2</sub>/atmosphere interface are responsible for the catalytic activity [89;91;92]. Fig. 2 shows the XRD patterns of the decorated hierarchical, tube-like, ceria-based supports. In all presented curves, apart from the intense diffraction maxima characteristic of the fluorite structure, also very wide maxima corresponding to the structure of gold are visible. This result confirms that the gold content in the tested samples is quite high. At the same time, it confirms the hypothesis that besides the gold nanoparticles

visible in HRTEM images, the samples must also contain smaller “hidden on the rugged macroparticle surface” gold clusters.

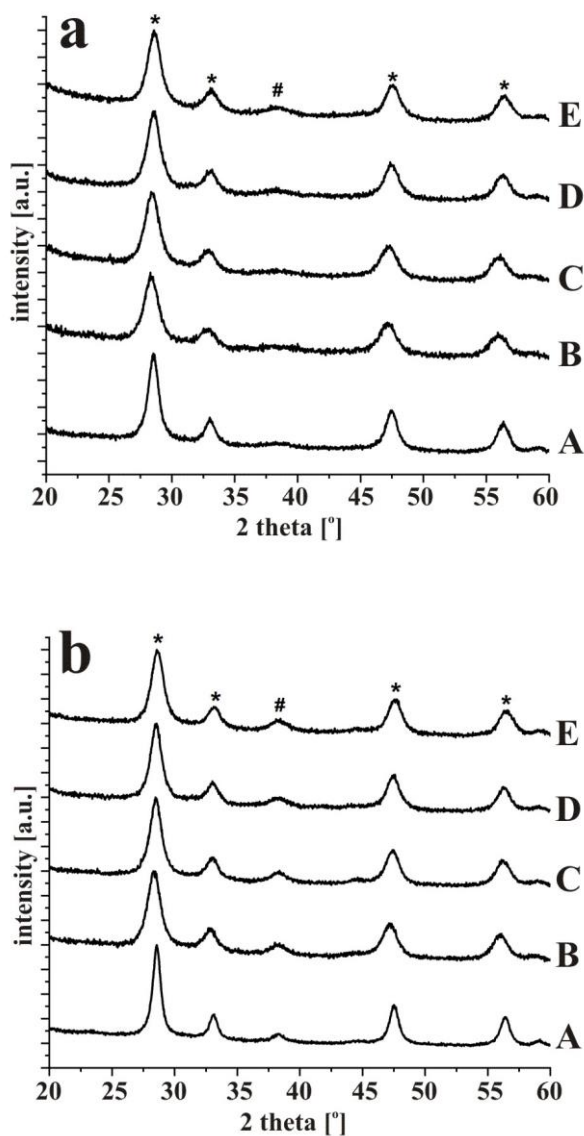


Fig. 2. XRD patterns of (A) Au/CeO<sub>2</sub>, (B) Au/Ce<sub>0.9</sub>La<sub>0.1</sub>O<sub>1.95</sub>, (C) Au/Ce<sub>0.9</sub>La<sub>0.05</sub>Yb<sub>0.05</sub>O<sub>1.95</sub>, (D) Au/Ce<sub>0.9</sub>Gd<sub>0.1</sub>O<sub>1.95</sub>, (E) Au/Ce<sub>0.9</sub>Yb<sub>0.1</sub>O<sub>1.95</sub>, (a) before and (b) after catalytic test.

To ensure that the gold nanoparticles were uniformly dispersed over the surface of the macroparticles, the line-profile SEM-EDX measurements were made (Fig. S6). As shown in Fig. S6, the EDX signal corresponding to the presence of gold in the material is visible together with the signal for cerium, lanthanides and oxygen. It proves that the gold is evenly distributed over the surface of the tube-like macroparticle. It is in line with our previous experiences with Au/CeO<sub>2</sub> [61;90] systems. As

shown in Table 3, it seems that gold nanoparticles deposited on Ln-doped supports are slightly smaller than those dispersed on pure CeO<sub>2</sub>. It could be due to better anchoring of gold nanoparticles on defective fluorite type structures (F#-type, Ce<sub>0.9</sub>Ln<sub>0.1</sub>O<sub>1.95</sub>) than on CeO<sub>2</sub> [86;90]. Additionally, one may expect that the presence of oxygen vacancies in the Ln<sup>3+</sup>-doped Au/Ce<sub>0.9</sub>Ln<sub>0.1</sub>O<sub>1.95</sub> hierarchical systems will be responsible for the increased catalytic activity in relation to Au/CeO<sub>2</sub> [53;93;94]. At this point, it is appropriate to ask the question about the influence of the size of the doping ion (and therefore the type of lattice deformation) on the catalytic activity of Au/Ce<sub>0.9</sub>Ln<sub>0.1</sub>O<sub>1.95</sub> systems.

### ***Reducibility and catalytic tests***

As in our previous research into decorated systems [90], before the reducibility and catalytic tests, all Au/Ce<sub>0.9</sub>Ln<sub>0.1</sub>O<sub>1.95</sub> samples were pre-treated at 300 °C in static air for 3 h. The activation of the investigated materials by the heat treatment at 300 °C was aimed at the oxygenation of the support (Ce<sup>IV</sup>O<sub>2</sub> ↔ Ce<sup>IV</sup><sub>1-x</sub>Ce<sup>III</sup><sub>x</sub>O<sub>2-x/2</sub>) [45] and generation of the Au<sup>δ+</sup> species in the gold nanoparticles [95]. As shown in the literature, increase of the value of the lattice oxygen and the presence of a certain amount of the Au<sup>δ+</sup> species increases the catalytic activity of the Au/Ce<sub>0.9</sub>Ln<sub>0.1</sub>O<sub>1.95</sub> systems [95]. In addition, we believe that heating at 300 °C allowed the Au crystallites to grow to the desired size of 3-4 nm (as shown in [90]). According to the literature [4;5], the nanoparticles of gold deposited on the support show the highest activity in the low temperature catalytic reactions for particle sizes of about 3 nm. For Au particles having a size below or above this value, the catalytic activity significantly decreases [5].

In Fig. 3, the H<sub>2</sub>-TPR curves obtained for hierarchical, tube-like Au/Ce<sub>0.9</sub>Ln<sub>0.1</sub>O<sub>1.95</sub> (Ln = La, Gd and Yb) and Au/Ce<sub>0.9</sub>La<sub>0.05</sub>Yb<sub>0.05</sub>O<sub>1.95</sub> systems are presented. In our previous paper [30], a thorough analysis of the H<sub>2</sub>-TPR results obtained for hierarchical, tube-like CeO<sub>2</sub> and Ce<sub>0.9</sub>Yb<sub>0.1</sub>O<sub>1.95</sub> was carried out. Similar to Au-decorated cube-like and octahedron-like ceria-based oxides [90], the strong shift has been noted for the low temperature peaks of H<sub>2</sub> uptake (surface reduction peaks) for the decorated samples. As noted, two ranges can be distinguished on all H<sub>2</sub>-TPR curves: low-temperature (-50 – 200 °C) and high-temperature (200 – 900 °C) regions. According to literature [90;96;97], the band observed in the low-temperature region are responsible for surface reduction and ones from high temperature region for bulk reduction of Ce-ions. It was found that the presence of the Ln<sup>3+</sup> dopant in the ceria matrix causes a shift of the high-temperature band to slightly lower temperatures, what is in good agreement with literature [98;99.] and our previous data [30;100]. It is probably related to the



formation of chains of oxygen vacancies in the structure of mixed oxides [50;51] which facilitates oxygen transport from bulk to surface [101]. On the other hand, according to Burbano et. al. [102] analysis the oxygen conductivity is determined by the local lattice strain generated by the single defect rather than by synergistic effects between different dopants [103]. Interestingly, the dependence of the temperature of the high-temperature reduction maximum on the average lanthanide ion creates a linear relationship, for the single-doped samples (Au/Ce<sub>0.9</sub>Ln<sub>0.1</sub>O<sub>1.95</sub>). It seems that with the increase of the ionic radius of the doping ion, and thus with the size of the lattice deformation, the ionic conductivity of oxygen in these materials increases (see Fig. 3.). A similar relationship was previously noted for Ce<sub>1-x</sub>Ln<sub>x</sub>O<sub>2-x/2</sub> nanopowders (x = ~0.17; Ln = Pr, Tb, Lu) [77;104]. However, this rule does not work for the Au/Ce<sub>0.9</sub>La<sub>0.05</sub>Yb<sub>0.05</sub>O<sub>1.95</sub> sample. It could be due to the introduction of two types of local deformation of the crystal lattice (smaller Yb<sup>3+</sup> ion and larger La<sup>3+</sup> ion than Ce<sup>4+</sup> ion [68]), which may impede the transport of network oxygen.

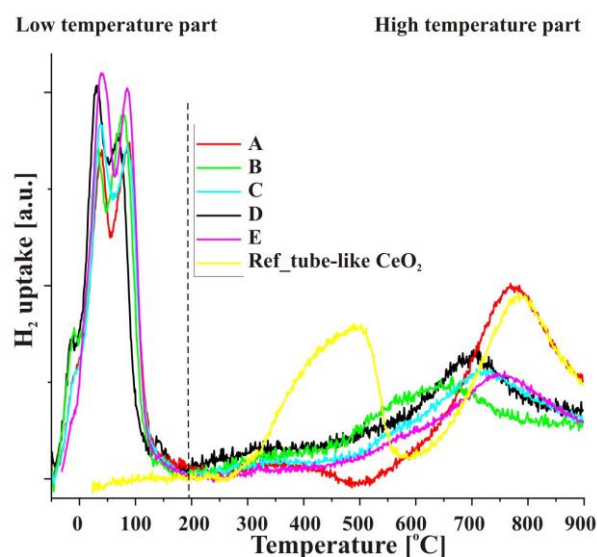


Fig. 3. H<sub>2</sub>-TPR curves obtained for (A) Au/CeO<sub>2</sub>, (B) Au/Ce<sub>0.9</sub>La<sub>0.1</sub>O<sub>1.95</sub>, (C) Au/Ce<sub>0.9</sub>La<sub>0.05</sub>Yb<sub>0.05</sub>O<sub>1.95</sub>, (D) Au/Ce<sub>0.9</sub>Gd<sub>0.1</sub>O<sub>1.95</sub>, (E) Au/Ce<sub>0.9</sub>Yb<sub>0.1</sub>O<sub>1.95</sub>. Additionally, reference data have been added: Ref – hierarchical tube-like CeO<sub>2</sub>.

Whereas, a thorough analysis of the low-temperature part of the H<sub>2</sub>-TPR curves indicates a very good reducibility of all tested samples (Fig. 3.). It is noted that the low temperature band is tripled with a first maximum at ~-8 °C. Such a low temperature of the cerium ions reduction has not been observed by us before for Au/CeO<sub>2</sub> (Au/Ce<sub>1-x</sub>Ln<sub>x</sub>O<sub>2-x/2</sub>) systems [90]. Our previous research conducted on model Au-decorated ceria-based supports with a given morphology (cubs, octahedrons) also showed very

good redox properties, but the reduction temperatures of  $\text{Ce}^{4+}$  ions were significantly higher [90]. In the literature [105-108], the temperature of the low-temperature reduction of cerium ions in Au/CeO<sub>2</sub> systems is noted in the range of 50-200 °C. Literature reports on Au/CeO<sub>2</sub> systems with DOM3 type structure show that low-temperature bands on the H<sub>2</sub>-TPR curve are located at temperatures of 80 - 90 °C [109]. However, in [109] the average particle size of gold is visibly larger than in our work, which is probably responsible for weaker redox result.

Table 4. H<sub>2</sub> uptake during H<sub>2</sub>-TPR for the investigated Au/Ce<sub>1-x</sub>Ln<sub>x</sub>O<sub>2-x/2</sub> materials.

sample	H <sub>2</sub> uptake [ $\mu\text{mol}$ ]/50mg of sample			H <sub>2</sub> uptake [mmol]/g of ceria
	Low temp	High temp	Total	Total
Au/CeO <sub>2</sub>	24.7 (45.6%)	29.5 (54.5%)	54.2	1.16
Au/Ce <sub>0.9</sub> La <sub>0.1</sub> O <sub>1.95</sub>	25.5 (49.6%)	25.9 (50.4%)	51.4	1.26
Au/Ce <sub>0.9</sub> Gd <sub>0.1</sub> O <sub>1.95</sub>	25.9 (46.0%)	30.4 (54.0%)	56.3	1.37
Au/Ce <sub>0.9</sub> La <sub>0.05</sub> Yb <sub>0.05</sub> O <sub>1.95</sub>	25.0 (50.3%)	24.7 (49.7%)	49.7	1.25
Au/Ce <sub>0.9</sub> Yb <sub>0.1</sub> O <sub>1.95</sub>	27.2 (55.4%)	21.9 (44.6%)	49.1	1.22
CeO <sub>2</sub> *	19.9 (44.9%)	24.4 (55.1%)	44.3	0.89
Ce <sub>0.9</sub> Yb <sub>0.1</sub> O <sub>1.95</sub> *	26.5 (52.5%)	24.0 (47.5%)	50.5	1.12

\* - data from [30]; low temp range = 100-600 °C, high temp range = 600-900 °C

As already mentioned, for all tested profiles, the low-temperature hydrogen uptake band on the H<sub>2</sub>-TPR curve consists of three maxima. In [110], the dependence of the H<sub>2</sub> uptake band position on the Au clusters size (individual atom, monolayer, multilayer and nanoparticle) deposited on cube-like CeO<sub>2</sub> has been described. Wang et. al. [110], postulate that the analysis of H<sub>2</sub>-TPR profiles allows to estimate the qualitative dispersion of gold on CeO<sub>2</sub> support. The presented studies indicate that the lowest reduction temperature (73 °C) was obtained for the Au/CeO<sub>2</sub> sample where the gold particles had an average size of 2-5 nm, and the highest (329 °C) for the sample where individual gold atoms were present on the support. It should be taken into consideration that the research described in [110]

concerned ceria support with a cube-like morphology, where almost only  $\langle 100 \rangle$  walls are exposed [111]. In our case, the occurrence of the interaction of nanocrystalline Au with  $\text{CeO}_2$  nanocrystallites, where different walls are exposed and the Au/ $\text{CeO}_2$  contact surface can have very complicated characteristics. Therefore, we believe that the triple bands visible on the  $\text{H}_2$ -TPR profiles for our samples are associated with a series of nanoAu-nano $\text{CeO}_2$  (or  $\text{Ce}_{0.9}\text{Ln}_{0.1}\text{O}_{1.95}$ ) interactions. Although the differences observed in the positions of the maximums in the low-temperature hydrogen uptake band do not form a linear dependence on the radius of the doping ion (as in the case of the high-temperature band), but they are arranged in a somewhat organized manner (see Fig. 3.). It was noted that the temperatures of all three low temperature reduction peaks were the lowest for the Au/ $\text{Ce}_{0.9}\text{Gd}_{0.1}\text{O}_{1.95}$  sample and increased slightly with the increase and decrease of the dopant ion radius (in relation to  $\text{Gd}^{3+}$ ). This proves that the type and size of deformation in the ceria-based oxide lattice is important for its possible use as a catalytic support.

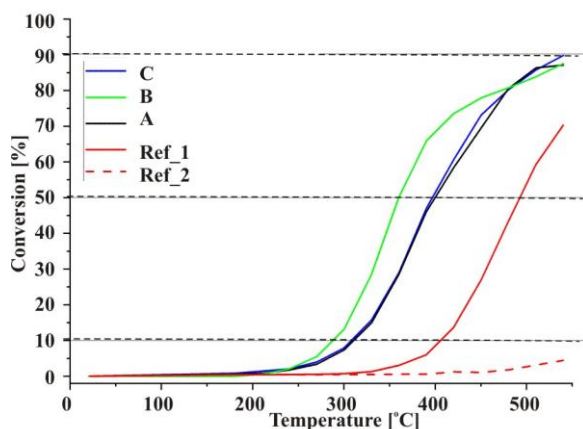


Fig. 4.  $\text{C}_3\text{H}_8$  oxidation activity of (A) Au/ $\text{CeO}_2$ , (B) Au/ $\text{Ce}_{0.9}\text{La}_{0.05}\text{Yb}_{0.05}\text{O}_{1.95}$ , (C) Au/ $\text{Ce}_{0.9}\text{Gd}_{0.1}\text{O}_{1.95}$ . Additionally, reference data have been added: Ref\_1 – hierarchical tube-like  $\text{CeO}_2$ ; Ref\_2 – commercial  $\text{CeO}_2$ .

As shown in table 4, hydrogen uptake calculated per 1 g of ceria increases in doped samples (Au/ $\text{Ce}_{0.9}\text{Ln}_{0.1}\text{O}_{1.95}$ ) by about 5-15% in relation to Au/ $\text{CeO}_2$ . Decorating the supports with gold nanoparticles significantly increases the total reducibility of ceria-based oxides. As noted, the ratio of hydrogen uptake for low- to high-temperature parts is similar for “oxide - decorated oxide” pairs of samples. However, for each pair of “oxide – decorated oxide”, the strong shift has been noted for the low temperature peaks of  $\text{H}_2$  uptake (surface reduction peaks) for the decorated samples. Such effect is mainly attributed to the reduction of  $\text{CeO}_2$  strongly bound with the gold species [112]. The above effect

has already been widely discussed in the literature [90;106]. Additionally, as mentioned in [103], isothermal ionic conductivity increases with  $x$  ( $x = \text{Ln}/\text{Ln}+\text{Ce}$ ) only for light Ln-dopants. For heavier lanthanides ionic conductivity decreases above a critical concentration of  $\text{Ln}^{3+}$  in the ceria matrix. The critical concentrations reported in the literature are estimated in the range 0.06-0.2, depending on  $\text{Ln}^{3+}$  [113]. Moreover, the ionic conductivity has also changed by moving across the lanthanide series. According to [114-116] the highest ionic conductivity is observed for Gd and Sm, while it reduces for lighter and heavier  $\text{Ln}^{3+}$  elements [103]. The above reports are consistent with our experiments (see table 4), where the highest  $\text{H}_2$  uptake (during TPR measurement) was noticed for  $\text{Au}/\text{Ce}_{0.9}\text{Gd}_{0.1}\text{O}_{1.95}$  sample.

The next step to obtain the fullest possible characterization of the tested materials was to carry out catalytic tests in the propane oxidation reaction. Although the propane oxidation reaction is not a model catalytic process for  $\text{Au}/\text{CeO}_2$  systems, it is a very important reaction from the point of view of environmental and human health protection [117-119]. Propane along with methane, benzene, xylene and butane is a component of VOCs gases (volatile organic compounds). In Fig. 8, the results of the propane oxidation tests for  $\text{Au}/\text{CeO}_2$ ,  $\text{Au}/\text{Ce}_{0.9}\text{Gd}_{0.1}\text{O}_{1.95}$  and  $\text{Au}/\text{Ce}_{0.9}\text{La}_{0.05}\text{Yb}_{0.05}\text{O}_{1.95}$  samples are presented. The above samples were selected for further testing for the following reasons: for the  $\text{Au}/\text{Ce}_{0.9}\text{Gd}_{0.1}\text{O}_{1.95}$  sample, the highest hydrogen uptake per 1g ceria was observed, double-doped  $\text{Au}/\text{Ce}_{0.9}\text{La}_{0.05}\text{Yb}_{0.05}\text{O}_{1.95}$  sample – as comparative catalyst (where the mean radius of the lanthanide is close to that of the  $\text{Au}/\text{Ce}_{0.9}\text{Gd}_{0.1}\text{O}_{1.95}$ , but different kind of the deformations of the ceria lattice has been observed in the support structure) and  $\text{Au}/\text{CeO}_2$  – as a reference sample (blank). As shown in our previous work [30], the organization of the nanoparticles into the hierarchical tube-like macroparticles decreases the half-oxidation temperature of the propane from 550 to 495 °C. Additionally, the presence of the trivalent lanthanide ions in the ceria matrix lowers the  $T_{50}$  temperature by another 40 °C. Moreover, the incorporation of the  $\text{Ln}^{3+}$ -ions into  $\text{CeO}_2$  structure increases the maximum conversion (at 550 °C) from 70 to 90 %. As shown in table 5., decoration of the tube-like ceria based macroparticles by the gold nanoparticles causes a further  $T_{50}$  temperature reduction down to 399 °C. Interestingly, as in the case of  $\text{Au}/\text{CeO}_2$  and  $\text{Au}/\text{Ce}_{0.9}\text{Yb}_{0.1}\text{O}_{1.95}$  materials with a cube-like and octahedron-like support morphology [90], the catalytic activity of single-doped material ( $\text{Au}/\text{Ce}_{0.9}\text{Gd}_{0.1}\text{O}_{1.95}$  – from this work) depends mainly on the presence of gold nanoparticles on the support (while the presence of an admixture in the  $\text{CeO}_2$  matrix are of little importance). Whereas, catalytic activity of the double doped sample ( $\text{Au}/\text{Ce}_{0.9}\text{La}_{0.05}\text{Yb}_{0.05}\text{O}_{1.95}$ ) turned out to be significantly higher (half oxidation temperature reduction by ~40 °C) than in the case of  $\text{Au}/\text{CeO}_2$  and  $\text{Au}/\text{Ce}_{0.9}\text{Gd}_{0.1}\text{O}_{1.95}$  (see Table 5). The above

observations show that it is not the mere presence of deformations (defects) in the support crystal lattice that matters, but its type. Moreover, an important observation is that the maximum conversion in all cases reaches about 90%.

Table 5. Performances of the investigated  $Ce_{1-x}Ln_xO_{2-x/2}$  and  $Au/Ce_{1-x}Ln_xO_{2-x/2}$  materials:  $C_3H_8$  oxidation reaction

Sample	Catalytic tests propane oxidation	
	$T_{50}$ [°C]	$C_{MAX}$ [%]
Au/CeO <sub>2</sub>	399	87
Au/Ce <sub>0.9</sub> Gd <sub>0.1</sub> O <sub>1.95</sub>	397	90
Au/Ce <sub>0.9</sub> La <sub>0.05</sub> Yb <sub>0.05</sub> O <sub>1.95</sub>	361	87
Au/CeO <sub>2</sub> _II	494	75
Au/Ce <sub>0.9</sub> La <sub>0.05</sub> Yb <sub>0.05</sub> O <sub>1.95</sub> _II	450	84
CeO <sub>2</sub>	495	70
Ce <sub>0.9</sub> La <sub>0.05</sub> Yb <sub>0.05</sub> O <sub>1.95</sub>	473	86

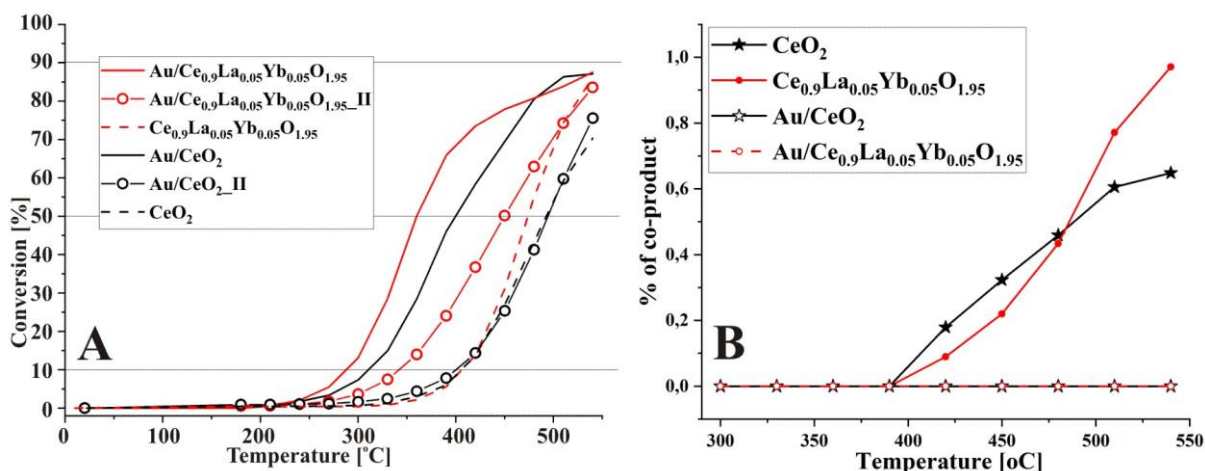


Fig. 5. A)  $C_3H_8$  oxidation activity of investigated samples – first and second run of reaction, B) selectivity of investigated samples – the percentage of the co-product in the final reaction product.

As shown, the hierarchical materials investigated in this work show quite good catalytic activity in the propane oxidation process in comparison to pure support, nanopowder or bulk ceria (see Fig. 4). The design of the  $Au/Ce_{1-x}Ln_xO_{2-x/2}$  catalyst in the form of hierarchical ceria-based tubes decorated by the gold is a very promising idea. It has been proven that the organization of the nanocrystalline ceria (or ceria-based mixed oxides) into the 3D structure with the simultaneous decoration by the nanosized noble metal has a significant (positive) influence on the catalytic properties of  $Au/Ce_{1-x}Ln_xO_{2-x/2}$  materials in the oxidation processes. It should also be noted that the exposure of the nanocrystalline

gold surface is a key parameter for the catalytic activity of the systems studied here. As shown in [120], Au@CeO<sub>2</sub> particles supported on the CeO<sub>2</sub> nanotubes show rather poor activity in the CO oxidation process (T<sub>50</sub> = ~170 °C) in comparison to Au/CeO<sub>2</sub> cube-like (T<sub>50</sub> = ~85 °C) or Au/CeO<sub>2</sub> octahedron-like (T<sub>50</sub> = ~75 °C) [90].

Unfortunately, the results obtained in the second run of the catalytic reaction were disappointing. Propane conversion curves obtained in the second reaction cycle are presented in Fig. 5A. The analysis of the obtained results indicates a significant deactivation of the catalysts (see Table 5). In the case of Au/CeO<sub>2</sub> sample (second run), the T<sub>50</sub> decreased by 96 °C, and the conversion curve almost coincides with that of undecorated hierarchical tube-like support [30] (see Fig. 5A). The situation is slightly different in the case of Au/Ce<sub>0.9</sub>La<sub>0.05</sub>Yb<sub>0.05</sub>O<sub>1.95</sub> sample. In this case, an increase in the T<sub>50</sub> temperature by about 89 °C was also observed, but the active phase has not been completely deactivated (the conversion curves for the second run of Au/Ce<sub>0.9</sub>La<sub>0.05</sub>Yb<sub>0.05</sub>O<sub>1.95</sub> and the undecorated support do not match, ΔT<sub>50</sub> = 23 °C). The strong decrease in the activity of Au/CeO<sub>2</sub> and Au/Ce<sub>0.9</sub>La<sub>0.05</sub>Yb<sub>0.05</sub>O<sub>1.95</sub> materials, in the second reaction cycle, is caused by the intense growth of gold crystallites (an increase of about 50-70%), which has been confirmed by TEM and XRD (Table 6, Fig. 6) techniques. However, as shown in Table 6, the average size of Au nanocrystallites (calculated for samples after the catalytic test) deposited on the doped support is significantly smaller than on pure CeO<sub>2</sub>. It may be related to the slightly better stability of Au/Ce<sub>0.9</sub>La<sub>0.05</sub>Yb<sub>0.05</sub>O<sub>1.95</sub> than Au/CeO<sub>2</sub> sample under reaction conditions. The differences in the growth of gold nanoparticles deposited on Ln-doped and pure ceria supports is probably related to the anchoring of nanosized gold on oxygen vacancies, what was described by Bezkrovnyi et. al [86]. Moreover, a strong decrease in the activity of the tested catalysts may be related to the formation of various organic impurities during the reaction [121;122] and / or a change in the degree of oxidation of cerium ions in the crystallites of the support (reduction of network oxygen mobility by partial support reduction) [123;124]. The second catalytic cycle was run immediately after the first one and the catalyst was not regenerated (re-oxidated) after the first cycle. Such conditions could favor the catalyst deactivation due to both the formation of organic impurities and the reduction of oxygen mobility in CeO<sub>2</sub> (and doped-CeO<sub>2</sub>). In addition to the above options, observed fast deactivation could be due to the consumption of OH species [125]. As noted by Zhao et. al. [125], in the case of the oxidation of CO, a small addition of water (steam) to the reaction mixture greatly improves the stability of the Au/CeO<sub>2</sub> catalyst. The authors postulate that the presence of OH/H<sub>2</sub>O plays a key role in controlling the activity of CO oxidation on the Au/CeO<sub>2</sub>.

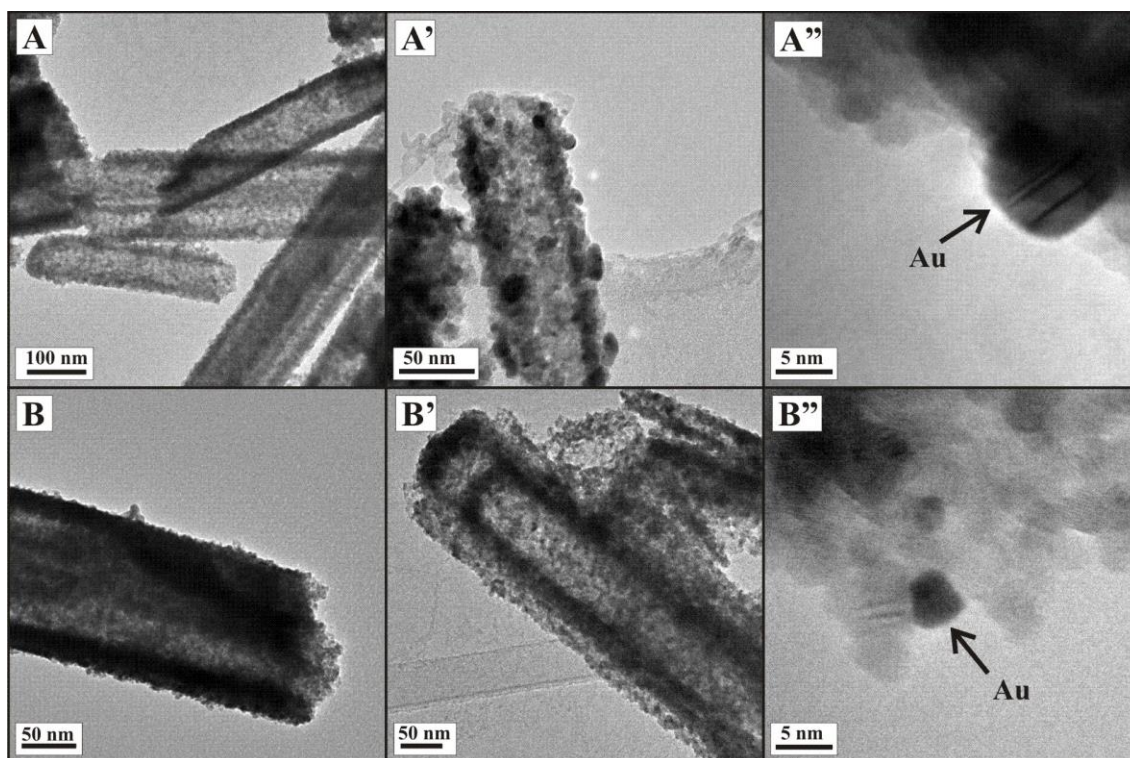


Fig. 6. TEM images of hierarchical tube-like Au/CeO<sub>2</sub> (A) before and (A') after catalytic test; Au/Ce<sub>0.9</sub>La<sub>0.05</sub>Yb<sub>0.05</sub>O<sub>1.95</sub> (B) before and (B') after catalytic test; HR-TEM images of gold nanoparticles supported on the hierarchical tube-like CeO<sub>2</sub> (A'') and (B'') Ce<sub>0.9</sub>La<sub>0.05</sub>Yb<sub>0.05</sub>O<sub>1.95</sub> after catalytic test.

Table 6. Mean size [nm] of Ce<sub>1-x</sub>Ln<sub>x</sub>O<sub>2-x/2</sub> and Au nanocrystals calculated from XRD after propane oxidation test.

sample	d <sub>av</sub> oxide [nm]	d <sub>av</sub> Au [nm]
Au/CeO <sub>2</sub>	20.8	7.3
Au/Ce <sub>0.9</sub> La <sub>0.05</sub> Yb <sub>0.05</sub> O <sub>1.95</sub>	10.5	5.8
Au/Ce <sub>0.9</sub> Gd <sub>0.1</sub> O <sub>1.95</sub>	10.0	5.7

On the other hand, decorating macroparticles with gold nanoparticles significantly improves the selectivity of the propane oxidation process. In our case, the process of propane oxidation should lead to obtaining only CO<sub>2</sub> and H<sub>2</sub>O. However, according to Maillet et al. [126] there are two possible ways for partial oxidation of propane. The first of them takes place at temperatures below 400 °C, and the reaction products are our desired CO<sub>2</sub> and H<sub>2</sub>O (complete oxidation). On the other hand, at temperatures above 400 °C, the reaction of incomplete propane oxidation takes place, which results in the presence of CO in the final gas mixture. The presence of CO in the reaction product is very unfavorable due to the highly poisonous nature of carbon monoxide [127;128]. As shown in Fig 5B, during the oxidation of propane on undecorated hierarchical oxides (CeO<sub>2</sub> and Ce<sub>0.9</sub>La<sub>0.05</sub>Yb<sub>0.05</sub>O<sub>1.95</sub>) at

temperatures above 390 °C, a small amount (up to 1% vol) of unwanted co-product is formed. As noted, the percentage of unwanted co-product in the final gas mixture increases with increasing temperature. A similar result was obtained by Woźniak et. al [67] for hierarchical, star-like (macroparticles) ceria-base catalysts. This observation is consistent with the data presented in [126]. Probably the additional co-product that we are observing is a hydrocarbon (with similar weight of propane), that is formed during incomplete combustion of propane. However, decorating the hierarchical ceria-base macroparticles with nanosize gold resulted in an improvement in the selectivity of propane oxidation up to 100% (no apparent co-products). During the analysis of the catalytic results, it was noticed that the signal related to the presence of unwanted co-product does not appear at all even at high temperatures. This may indicate a different mechanism of the propane oxidation reaction taking place on the decorated and non-decorated samples. Probably, for pure oxides, the mechanism associated with the use of network oxygen is the dominant one [129], while for the decorated ones, the process most likely goes according to Langmuir–Hinshelwood mechanism with adsorption of propane and oxygen on different types of sites [130].

## CONCLUSIONS

Summarizing, hierarchical, tube-like  $\text{Ce}_{0.9}\text{Ln}_{0.1}\text{O}_{1.95}$  mixed oxides where  $\text{Ln} = \text{La}, \text{Gd}, \text{Yb}$  and  $\text{Ce}_{0.9}\text{La}_{0.05}\text{Yb}_{0.05}\text{O}_{1.95}$  were synthesized using a simple wet chemical method. Moreover, the deposition-precipitation method [60] is appropriate for the decoration of the ceria-based hierarchical materials by the gold nanoparticles. It has been observed that the hierarchical materials investigated in this work exhibit sensational red-ox properties. It is noted that the low temperature  $\text{H}_2$  uptake on the  $\text{H}_2$ -TPR curve is tripled with a first maximum at  $\sim -8$  °C. Such a low temperature of the cerium ions reduction has been observed for the first time. Additionally, hierarchical, tube-like  $\text{Au}/\text{Ce}_{0.9}\text{Ln}_{0.1}\text{O}_{1.95}$  materials turned out to be active catalysts in the oxidation reactions. The decoration of the hierarchical support with gold nanoparticles significantly decreased the temperature of the catalytic oxidation of propane compared to the process carried out on an undecorated support. Unfortunately, the systems described in this paper lost their activity very quickly due to the rather high temperature at which the catalytic reaction takes place. For this reason, we believe that hierarchical  $\text{Au}/\text{ceria}$ -based systems can be excellent catalysts for low-temperature reactions, such as CO oxidation. On the other hand, the use of a different type of active phase (less sensitive to temperature) may prove to be a solution to the problem of the stability of such materials in reactions which proceed at higher temperatures. What is very interesting decorating macroparticles with gold nanoparticles significantly improves the selectivity of



the propane oxidation process.

## ACKNOWLEDGMENTS

The author thanks Prof. Leszek Kępiński for inestimable help with discussion of experimental results and unshakable belief in author's capacity, Mrs. Zofia Mazurkiewicz for valuable help with preparation of the samples and Mrs. Ewa Bukowska for XRD measurements.

## REFERENCES

- [1] M. Haruta, N. Yamada, T. Kobayashi and S. Iijima, *J. Catal.*, 1989, **115**, 301
- [2] M. Haruta, S. Tsubota, T. Kobayashi, H. Kageyama, M.J. Genet and B. Delmon, *J. Catal.*, 1993, **144**, 175
- [3] G.J. Hutchings, M.R.H. Siddiqui, A. Burrows, C.J. Kiely and R. Whyman, *J. Chem. Soc. Faraday Trans.*, 1997, **93**, 187
- [4] M. Valden, X. Lai and D. W. Goodman, *Science*, 1998, **281**, 1647
- [5] M. Chen and D. W. Goodman, *Chem. Soc. Rev.*, 2008, **37**, 1860
- [6] M. A. Centeno, T. R. Reina, S. Ivanova, O. H. Laguna and J. A. Odriozola, *Catalysts*, 2016, **6**, 158
- [7] O. H. Laguna, A. Pérez, M. A. Centeno and J. A. Odriozola, *Appl. Catal. B*, 2015, **176–177**, 385
- [8] R. Zhao, D. Ji, G. Lv, G. Qian, L. Yan, X. Wang and J. Suo, *Chem. Commun.*, 2004, **7**, 904
- [9] G. Lu, R. Zhao, G. Qian, Y. Qi, X. Wang and J. Suo, *Catal. Lett.*, 2004, **97**, 115
- [10] G. Lu, D. Ji, G. Qian, Y. Qi, X. Wang and J. Suo, *Appl. Catal. A*, 2005, **280**, 175
- [11] A. Hugon, L. Delannoy and C. Louis, *Gold Bull.*, 2008, **41**, 127
- [12] X. Zhang, H. Shi and B. Q. Xu, *Angew. Chem. Int. Ed.*, 2005, **44**, 7132
- [13] X. Zhang, H. Shi and B. Q. Xu, *Catal. Tod.*, 2007, **122**, 330
- [14] D. Andreeva, I. Ivanov, J. W. Sobczak, W. Lisowski, P. Petrova, M.V. Abrashev and L. Ilieva, *Curr. Top. Catal.*, 2008, **7**, 33
- [15] D. Andreeva, I. Ivanova, L. Ilieva, J. W. Sobczak, G. Avdeev and T. Tabakova, *Appl. Catal. A*, 2007, **333**, 153
- [16] J. E. Bailie and G. J. Hutchings, *Chem. Commun.*, 1999, **21**, 2151
- [17] R. Zanella, C. Louis, S. Giorgio and R. Touroude, *J. Catal.*, 2004, **223**, 328
- [18] L. Ilieva, P. Petrova, L. F. Liotta, J. W. Sobczak, W. Lisowski, Z. Kaszkur, G. Munteanu and T. Tabakova, *Catalysts*, 2016, **6**, 99
- [19] D. Andreeva, P. Petrova, J. W. Sobczak, L. Ilieva and M. Abrashev, *Appl. Catal. B*, 2006, **67**, 237
- [20] L. Ilieva, G. Pantaleo, J. W. Sobczak, I. Ivanov, A. M. Venezia and D. Andreeva, *Appl. Catal. B*, 2007, **76**, 107
- [21] B. Grzybowska-Świerkosz, *Catal. Tod.*, 2006, **112**, 3
- [22] M. M. Schubert, S. Hackenberg, A. C. van Veen, M. Muhler, V. Plzak and R. J. Behm, *J. Catal.*, 2001, **197**, 113
- [23] M. Gąsior, B. Grzybowska, K. Samson, M. Ruszel and J. Haber, *Catal. Tod.*, 2004, **91–92**, 131
- [24] K. Sing, D. Everett, R. Haul, L. Moscou, R. Pierotti, J. Rouquérol and T. Siemienińska, *Pure Appl. Chem.*, 1985, **57**, 603
- [25] R.-P. Ye, J. Ding, W. Gong, M.D. Argyle, Q. Zhong, Y. Wang, C.K. Russell, Z. Xu, A.G. Russell, Q. Li, M. Fan and Y.-G. Yao, *Nat. Commun.*, 2019, **10**, 5698
- [26] C. Zhu, Z. Qi, V. A. Beck, M. Luneau, J. Lattimer, W. Chen, M. A. Worsley, J. Ye, E. B. Duoss, C. M. Spadaccini, C. M. Friend and J. Biener, *Sci. Adv.*, 2018, **4**, 9459
- [27] R. Lakes, *Nature*, 1993, **36**, 511
- [28] J. Wei, Z. Yang, H. Yang, T. Sun and Y. Yang, *CrystEngComm*, 2011, **13**, 4950
- [29] F. Kurosaki, H. Koyanaka, M. Tsujimoto and Y. Imamura, *Carbon*, 2008, **46**, 850
- [30] M.A. Małecka and P. Woźniak, *CrystEngComm*, 2021, **23**, 6743
- [31] P. Woźniak, W. Miśta and M.A. Małecka, *CrystEngComm*, 2020, **22**, 5914
- [32] I. Y. Kaplin, E. S. Lokteva, E. V. Golubina and V. V. Lunin, *Molecules*, 2020, **25**, 4242
- [33] L. S. Zhong, J. S. Hu, H. P. Liang, A. M. Cao, W. G. Song and L. J. Wan, *Adv. Mater.*, 2006, **18**, 2426
- [34] C.M.A. Parlett, K. Wilson and A.F. Lee, *Chem. Soc. Rev.*, 2013, **42**, 3876
- [35] J. Liu, G. Jiang, Y. Liu, J. Di, Y. Wang, Z. Zhao, Q. Sun, C. Xu, J. Gao, A. Duan, J. Liu, Y. Wei, Y. Zhao and L. Jiang, *Sci. Rep.*, 2014, **4**, 7276

- [36] N.V. Zaletova, A.O. Turakulova and V.V. Lunin, *Stud. Surf. Sci. Catal.*, 2010, **175**, 305
- [37] K. Lin, O.I. Lebedev, G. Van Tendeloo, P.A. Jacobs and P.P. Pescarmona, *Chem. Eur. J.*, 2010, **16**, 13509
- [38] C. Hiragond, S. Ali, S. Sorcar and S.-I. In, *Catalysts*, 2019, **9**, 370
- [39] S. Bernal, G. Blanco, M. A. Cauqui, P. Corchado, J. M. Pintado and J. M. Rodriguez-Izquierdo, *Chem. Commun.*, 1997, **16**, 1545
- [40] N. Laosiripojana and S. Assabumrungrat, *Appl. Catal. B*, 2006, **66**, 29
- [41] T. Mori, R. Buchanan, D. R. Ou, F. Ye, T. Kobayashi, J. D. Kim, J. Zou and J. Drennan, *J. Solid State Electrochem.*, 2008, **12**, 841
- [42] E. P. Murray, T. Tsai and S. A. Barnett, *Nature*, 1999, **400**, 649
- [43] B. C. H. Steele and A. Heinzel, *Nature*, 2001, **414**, 345
- [44] E. Aneggi, C. de Leitenburg, G. Dolcetti and A. Trovarelli, *Catal. Tod.*, 2006, **114**, 40
- [45] S. Rossignol, F. Gérard, D. Mesnard, C. Kappenstein and D. Duprez, *J. Mater. Chem.*, 2003, **13**, 3017
- [46] S. Bernal, G. Blanco, G. Cifredo, J.A. Perez-Omil, J.M. Pintado and J.M. Rodriguez-Izquierdo, *J. Alloys Compd.*, 1997, **250**, 449
- [47] G. Vlaic, P. Fornasiero, S. Geremia, J. Kaspar and M. Graziani, *J. Catal.*, 1997, **168**, 386
- [48] G. Adachi, and N. Imanaka, *Chem. Rev.*, 1998, **98**, 1479
- [49] D. Ou, T. Mori, F. Ye, J. Zou, G. Auchterlonie and J. Drennan, *Phys. Rev. B*, 2008, **77**, 024108
- [50] F. Ye, T. Mori, D. R. Ou, A. N. Cormack, R. J. Lewis and J. Drennan, *Solid State Ionics*, 2008, **179**, 1962
- [51] F. Ye, T. Mori, D. R. Ou, J. Zou and J. Drennan, *Solid State Ionics*, 2009, **180**, 1414
- [52] V. Grover, S. N. Achary and A. K. Tyagi, *J. Appl. Crystallogr.*, 2003, **36**, 1082
- [53] M. A. Małecka, J. J. Delgado, L. Kepiński, J. J. Calvino, S. Bernal, G. Blanco and X. Chen, *Catal. Tod.*, 2012, **187**, 56
- [54] V. Belliere, G. Joorst, O. Stephan, F. de Groot and B. Weckhuysen, *J. Phys. Chem. B*, 2006, **110**, 9984
- [55] M. Luo, Z. Yan, L. Jin and M. He, *J. Phys. Chem. B*, 2006, **110**, 13068
- [56] Q. Wang, Y. Zhang, Y. Zhou, Z. Zhang, J. Xue, Y. Xu, C. Zhang, X. Sheng and N. Kui, *RSC Adv.*, 2016, **6**, 730
- [57] F. Sakina, J.M. Muñoz-Ocaña, A. Bouziane, M. Lopez-Haro and R.T. Baker, *Nanoscale Adv.*, 2019, **1**, 4772
- [58] M. A. Małecka and L. Kepiński, *J. Alloys Compd.*, 2007, **430**, 282
- [59] M. Grun, K. Unger, A. Matsumoto and K. Tsutsumi, *Microporous Mesoporous Mater.*, 1999, **27**, 207
- [60] Y. Lin, Z. Wu, J. Wen, K. Ding, X. Yang, K. R. Poepplmeier and L. D. Marks, *Nano Lett.*, 2015, **15**, 5375
- [61] M.A. Małecka, K. Matus and P. Woźniak, *ChemistrySelect*, 2020, **5**, 2871
- [62] J. Rodríguez-Carvajal, *Phys. B*, 1993, **192**, 55
- [63] V. Alcalde-Santiago, E. Bailón-García, A. Davó-Quiñonero, D. Lozano-Castelló and A. Bueno-López, *Appl. Catal. B: Environmental*, 2019, **248**, 567
- [64] K. Pugazhendhi, V. Bharathi Lenin, D. J. Sharmila, J. Kethzy Agnes, B. Praveen and J. Merline Shyla, *AIP Conf. Proc.*, 2019, **2115**, 030606
- [65] G. Shen, M. Liu, Z. Wang and Q. Wang, *Nanomaterials*, 2018, **8**, 773
- [66] J. Wei, Z. Yang and Y. Yang, *CrystEngComm*, 2011, **13**, 2418
- [67] P. Woźniak, M.A. Małecka, L. Chinchilla and S. Trasobares, *Mater. Res. Bull.*, 2022, **151**, 111816
- [68] R. D. Shannon, *Acta Crystallographica*, 1976, **A32**, 751
- [69] X. Wang, J. Hanson, G. Liu, J. Rodriguez, A. Iglesias-Juez and M. Fernandez-Garcya, *J. Chem. Phys.*, 2004, **121**, 5434
- [70] A. Bueno-Lopez, K. Krishna, M. Makkee and J. Moulijn, *J. Catal.*, 2005, **230**, 237
- [71] S. Dikmen, P. Shuk and M. Greenblatt, *Solid State Ion.*, 1999, **126**, 89
- [72] V. Grover and A. Tyagi, *Mater. Res. Bull.*, 2004, **39**, 859
- [73] V. Grover and A. Tyagi, *J. Solid State Chem.*, 2004, **177**, 4197
- [74] B. Mandal, V. Grover, M. Roy and A. Tyagi, *J. Am. Ceram. Soc.*, 2007, **90**, 2961
- [75] S. Chavan and A. Tyagi, *Mater. Sci. Eng. A*, 2005, **404**, 57
- [76] Sk. Anirbanab, T. Paula and A. Dutta, *RSC Adv.*, 2015, **5**, 50186
- [77] M.A. Małecka, L. Kepiński, W. Mišta, *Appl. Catal. B: Environmental*, 2007, **74**, 290
- [78] L. M. Anovitz and D. R. Cole, *Rev. Mineral. Geochem.*, 2015, **80**, 61
- [79] M. Naderi, *Prog. Filtr. Sep.*, 2015, 585
- [80] S. Yang, G. Chen, C. Lv, C. Li, N. Yin, F. Yang and L. Xue, *Energy Explor. Exploit.*, 2018, **36**, 265
- [81] M. Abunowara, M. A. Bustam, S. Sufian, M. Babar, U. Eldemerdash, H. Suleman, R. Bencini and S. Ullah, *J. Environ. Eng.*, 2020, **146**, 04020087
- [82] Z. Wang, X. Jiang, M. Pan and Y. Shi, *Minerals*, 2020, **10**, 377
- [83] M. Thommes, K. Kaneko, A. V. Neimark, J. P. Olivier, F. Rodriguez-Reinoso, J. Rouquerol and K. S. W. Sing, *Pure Appl. Chem.*, 2015, **87**, 1051
- [84] D. S. Ivanova, J. K. Angarska and E. D. Manev, *Bulg. Chem. Commun.*, 2016, **48**, 101

- [85] H.J. Kim, M.G. Jang, D. Shin, J.W. Han, *ChemCatChem*, 2020, **12**, 11
- [86] O. Bezkrovnyi, P. Kraszkiewicz, I. Krivtsov, J. Quesada, S. Ordóñez and L. Kępiński, *Catal. Commun.*, 2019, **131**, 105798
- [87] A. Trovarelli and J. Llorca, *ACS Catal.*, 2017, **7**, 4716
- [88] S. Fernández-García, S. E. Collins, M. Tinoco, A. B. Hungria, J. J. Calvino, M. A. Cauqui and X. Chen, *Catal. Tod.*, 2019, **336**, 90
- [89] O. S. Bezkrovnyi, D. Blaumeiser, M. Vorokhta, P. Kraszkiewicz, M. Pawlyta, T. Bauer, J. Libuda and L. Kępiński, *J. Phys. Chem. C*, 2020, **124**, 5647
- [90] P. Woźniak, P. Kraszkiewicz and M.A. Małecka, *CrystEngComm*, 2020, **22**, 5828
- [91] T. Fujitani and I. Nakamura, *Angew. Chem., Int. Ed.*, 2011, **50**, 10144
- [92] N. Ta, J. Liu, S. Chenna, P. A. Crozier, Y. Li, Chen and A. Shen, *J. Am. Chem. Soc.*, 2012, **134**, 20585
- [93] H. Vidal, J. Kaspar, M. Pijolat, G. Colon, S. Bernal, A. Cordon, V. Perrichon and F. Fally, *Appl. Catal. B*, 2000, **27**, 49
- [94] B.M. Reddy, G. Thrimurthulu and L. Katta, *Catal. Lett.*, 2011, **141**, 572
- [95] A. Nozaki, T. Yasuoka, Y. Kuwahara, T. Ohmichi, K. Mori, T. Nagase, H. Y. Yasuda and H. Yamashita, *Ind. Eng. Chem. Res.*, 2018, **57**, 5599
- [96] R. Long, J. Luo, M. Chen and H. Wan, *Appl. Catal. A*, 1997, **159**, 171
- [97] A. Trovarelli, *Catal. Rev.: Sci. Eng.*, 1996, **38**, 439
- [98] G.L. Markaryan, L.N. Ikryanikova, G.P. Muravieva, A.O. Turakulova, B.G. Kostyuk, E.V. Lunina, V.V. Lunin, E. Zhilinskaya and A. Aboukais, *Coll. Surf. A: Physicochemical and Engineering Aspects*, 1999, **151**, 435
- [99] W. Y. Hernandez, F. Romero-Sarria, M. A. Centeno and J. A. Odriozola, *J. Phys. Chem. C*, 2010, **114**, 10857
- [100] M.A. Małecka, P. Kraszkiewicz and O. Bezkrovnyi, *Mater. Characterization*, 2019, **155**, 109796
- [101] X. Liu, K. Zhou, L. Wang, B. Wang, and Yadong Li, *J. Am. Chem. Soc.*, 2009, **131**, 3140
- [102] M. Burbano, S. Nadin, D. Marrocchelli, M. Salannec and G.W. Watson, *Phys. Chem. Chem. Phys.*, 2014, **16**, 8320
- [103] M. Coduri, S. Checchia, M. Longhi, D. Ceresoli and M. Scavini, *Front. Chem.*, 2018, **6**, 526
- [104] M.A. Małecka, L. Kępiński and W. Miśta, *J. Alloys Compd.*, 2008, 451, 567
- [105] Y. Zhang, Y. Zhao, H. Zhang, L. Zhang, H. Ma, P. Dong, D. Li, J. Yu and G. Cao, *RSC Adv.*, 2016, **6**, 70653
- [106] G. Yi, Z. Xu, G. Guo, K. Tanaka and Y. Yuan, *Chem. Phys. Lett.*, 2009, **479**, 128
- [107] O. S. Bezkrovnyi, P. Kraszkiewicz, W. Miśta and L. Kępiński, *Catal. Lett.*, 2021, **151**, 1080
- [108] Y. Bu, Y. Chen, G. Jiang, X. Hou, S. Li and Z. Zhang, *Appl. Catal. B: Environmental*, 2020, **260**, 118138
- [109] Y. Liu, B. Liu, Q. Wang, Y. Liu, C. Li, W. Hu, Peng .Jing, W. Zhao and J. Zhang, *RSC Adv.*, 2014, **4**, 5975
- [110] J. Wang, H. Tan, S. Yu, and K. Zhou, *ACS Catal.*, 2015, **5**, 2873
- [111] R. Si, M. Flytzani-Stephanopoulos, *Angew.Chem.Int.Ed.*, 2008, **47**, 2884
- [112] S. Li, H. Zhu, Z. Qin, Y. Zhang, G. Wang, Z. Wu, W. Fan and J. Wang, *Catalysts*, 2018, **8**, 469
- [113] J. Koettgen, S. Grieshammer, P. Hein, B.O.H. Grope, M. Nakayama and M. Martin, *Phys. Chem. Chem. Phys.*, 2018, **20**, 14291
- [114] K. Eguchi, T. Setoguchi, T. Inoue and H. Arai, *Solid State Ionics*, 1992, **52**, 165
- [115] S. Omar, E.D. Wachsman and J.C. Nino, *Solid State Ionics*, 2006, **177**, 3199
- [116] W. Zając and J. Molenda, *Solid State Ionics*, 2008, **179**, 154
- [117] X. Zhang, R. You, D. Li, T. Cao and W. Huang, *ACS Appl. Mater. Interfaces*, 2017, **9**, 35897
- [118] O. Demoulin, B. Le Clef, M. Navez and P. Ruiz, *Appl. Catal. A*, 2008, **344**, 1
- [119] C. He, X. Liu, J. Shi, C. Ma, H. Pan and G. Li, *J. Colloid Interface Sci.*, 2015, **454**, 216
- [120] F. Zhu, G. Chen, S. Suna and X. Sun, *J. Mater. Chem. A*, 2013, **1**, 288
- [121] P. Oelker, A. Bernier, P. Ruiz, B. Delmon and P. Isnard, *Stud. Surf. Sci.Catal.*, 1997, **111**, 267
- [122] N.C. Nelson, J.S. Manzano and I.I. Slowing, *J. Phys. Chem. C*, 2016, **120**, 28067
- [123] A.A. El-Moemen, A.M. Abdel-Mageed, J. Bansmann, M. Parlinska-Wojtan, R.J. Behm and G. Kučerová, *J. Catal.*, 2016, **341**, 160
- [124] J. Gaálová and P. Topka, *Catalysts*, 2021, **11**, 789
- [125] S. Zhao, F. Chen, S. Duan, B. Shao, T. Li, H. Tang, Q. Lin, J. Zhang, L. Li, J. Huang, N. Bion, W. Liu, H. Sun, A.-Q. Wang, M. Haruta, B. Qiao, J. Li, J. Liu and T. Zhang, *Nature Comm.*, 2019, **10**, 3824
- [126] T. Maillot, J. Barbier Jr. and D. Duprez, *Appl. Catal. B*, 1996, **9**, 251
- [127] K. Sobieraj, S. Stegenta-Dąbrowska, G. Luo, J.A. Koziel and A. Białowiec, *Front. Environ. Sci.* 2022, **10**, 822463
- [128] A. Ernst, J.D. Zibrak, *N Engl J Med*, 1998, **339**, 1603
- [129] M.D. Krcha, M.J. Janik, *Surf. Sci.*, 2015, **640**, 119
- [130] R. Velinova, S. Todorova, G. Ivanov, D. Kovacheva, H. Kolev and A. Naydenov, *Int. J. Chem. React. Eng.*, 2020, **18**, 20200017

## Supplementary materials for

Hierarchical Au/CeO<sub>2</sub> systems – influence of Ln<sup>3+</sup> dopants on the catalytic activity in the propane oxidation process.

Piotr Woźniak, Piotr Kraszkiewicz, Małgorzata A. Malecka\*

*Institute of Low Temperature and Structure Research, Polish Academy of Sciences,*

*P.O. Box 1410, 50-950 Wrocław 2, Poland*

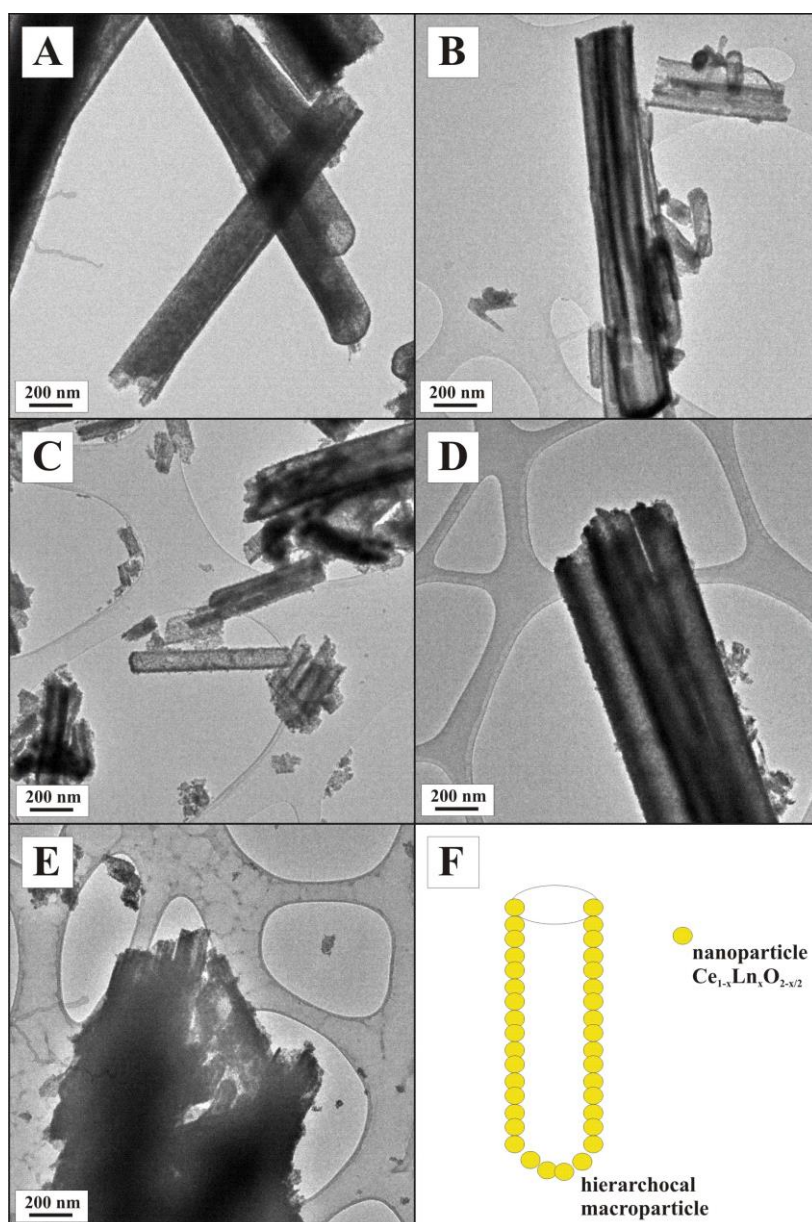


Fig.S1 TEM images of hierarchical tube-like (A) CeO<sub>2</sub>, (B) Ce<sub>0.9</sub>La<sub>0.1</sub>O<sub>1.95</sub>, (C) Ce<sub>0.9</sub>La<sub>0.05</sub>Yb<sub>0.05</sub>O<sub>1.95</sub>, (D) Ce<sub>0.9</sub>Gd<sub>0.1</sub>O<sub>1.95</sub>, (E) Ce<sub>0.9</sub>Yb<sub>0.1</sub>O<sub>1.95</sub>, (F) model of the hierarchical tube-like macroparticle.

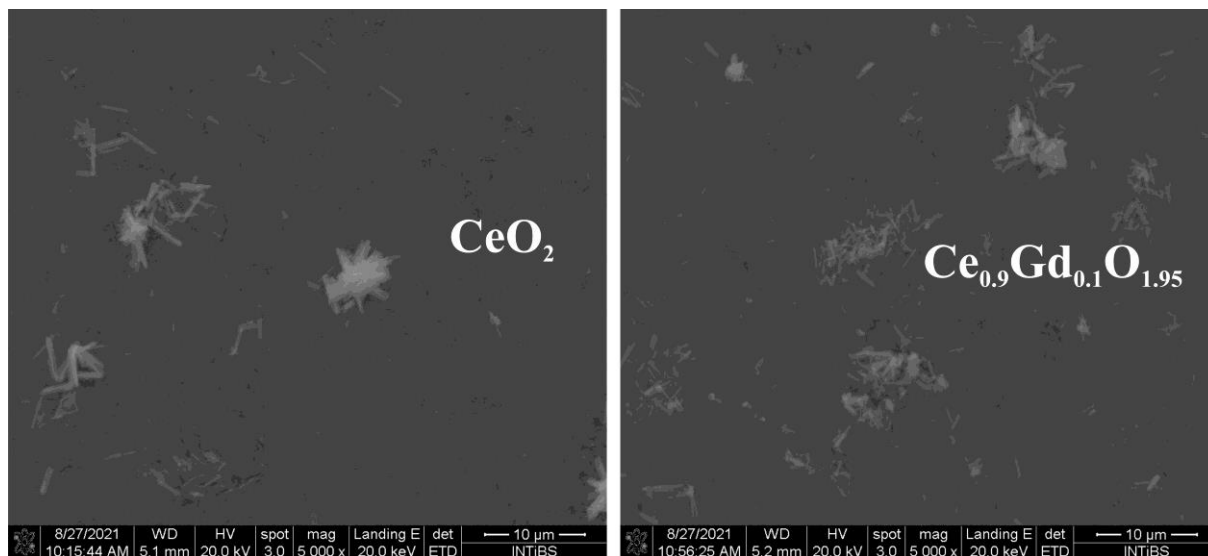


Fig.S2 SEM images of hierarchical tube-like  $\text{CeO}_2$  and  $\text{Ce}_{0.9}\text{Gd}_{0.1}\text{O}_{1.95}$

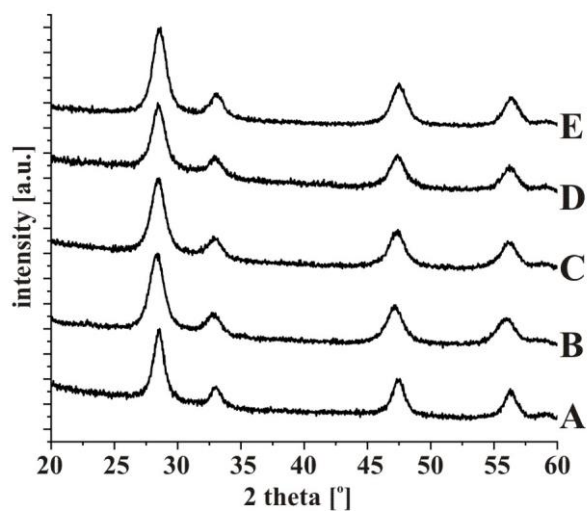


Fig.S3 XRD patterns of (A)  $\text{CeO}_2$ , (B)  $\text{Ce}_{0.9}\text{La}_{0.1}\text{O}_{1.95}$ , (C)  $\text{Ce}_{0.9}\text{La}_{0.05}\text{Yb}_{0.05}\text{O}_{1.95}$ , (D)  $\text{Ce}_{0.9}\text{Gd}_{0.1}\text{O}_{1.95}$ , (E)  $\text{Ce}_{0.9}\text{Yb}_{0.1}\text{O}_{1.95}$ .

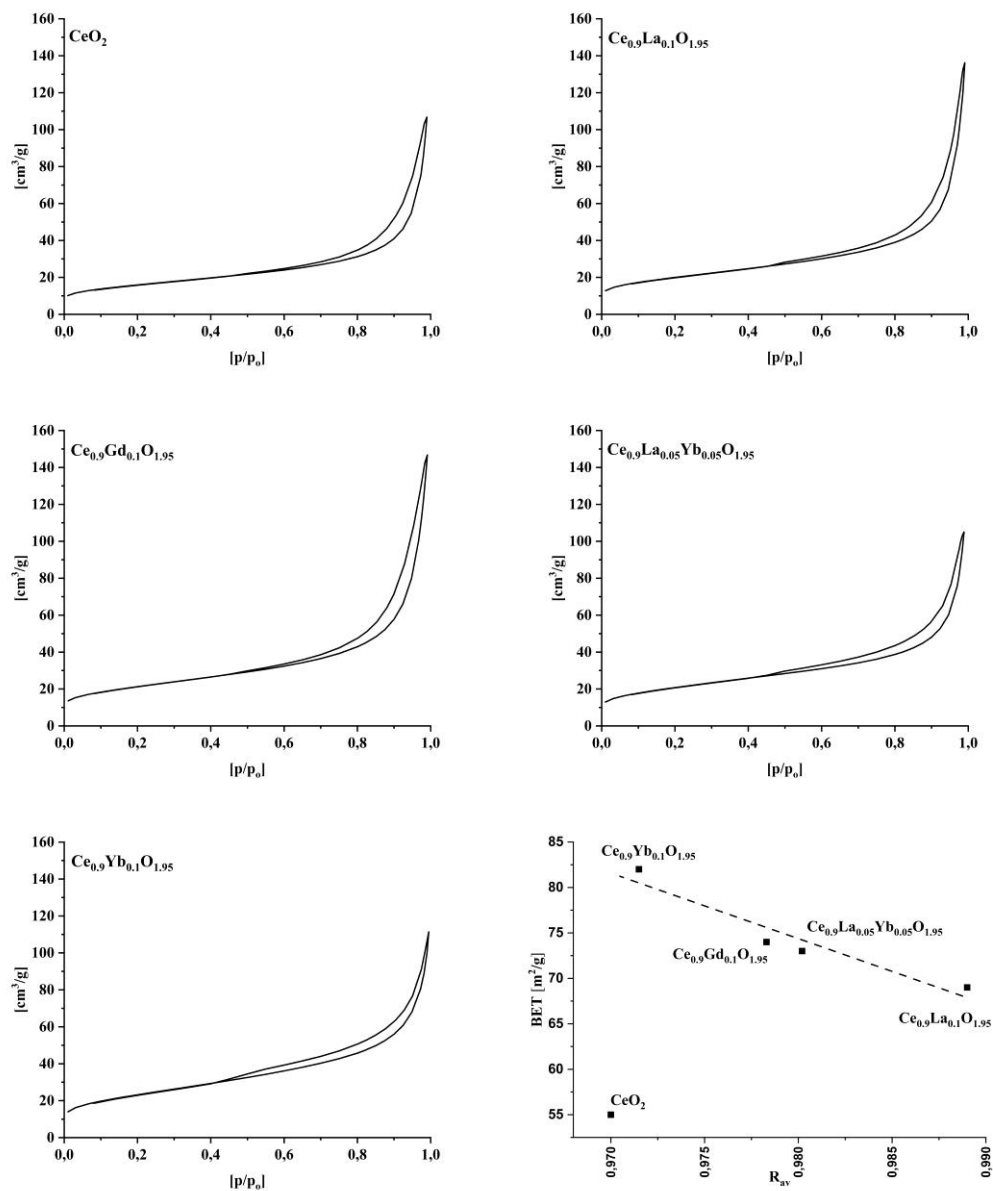


Fig.S4 Nitrogen adsorption–desorption isotherm of investigated hierarchical supports and a linear relationship between the mean lanthanide ion radius and the  $S_{\text{BET}}$  surface area for our sample series.

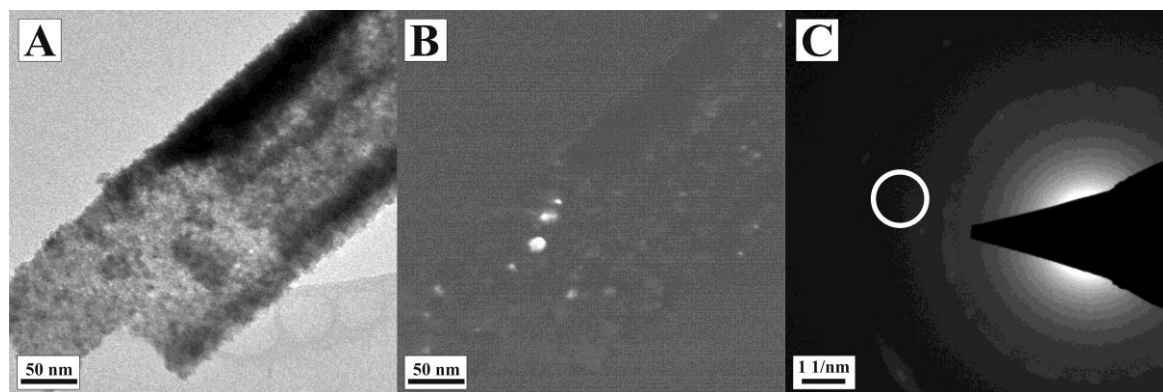


Fig.S5 (A) TEM-BF and (B) TEM-DF images of hierarchical tube-like  $\text{CeO}_2$  and (C) SAED pattern with position of the aperture (between the rings  $\text{CeO}_2(200)$  and  $\text{CeO}_2(220)$ ).

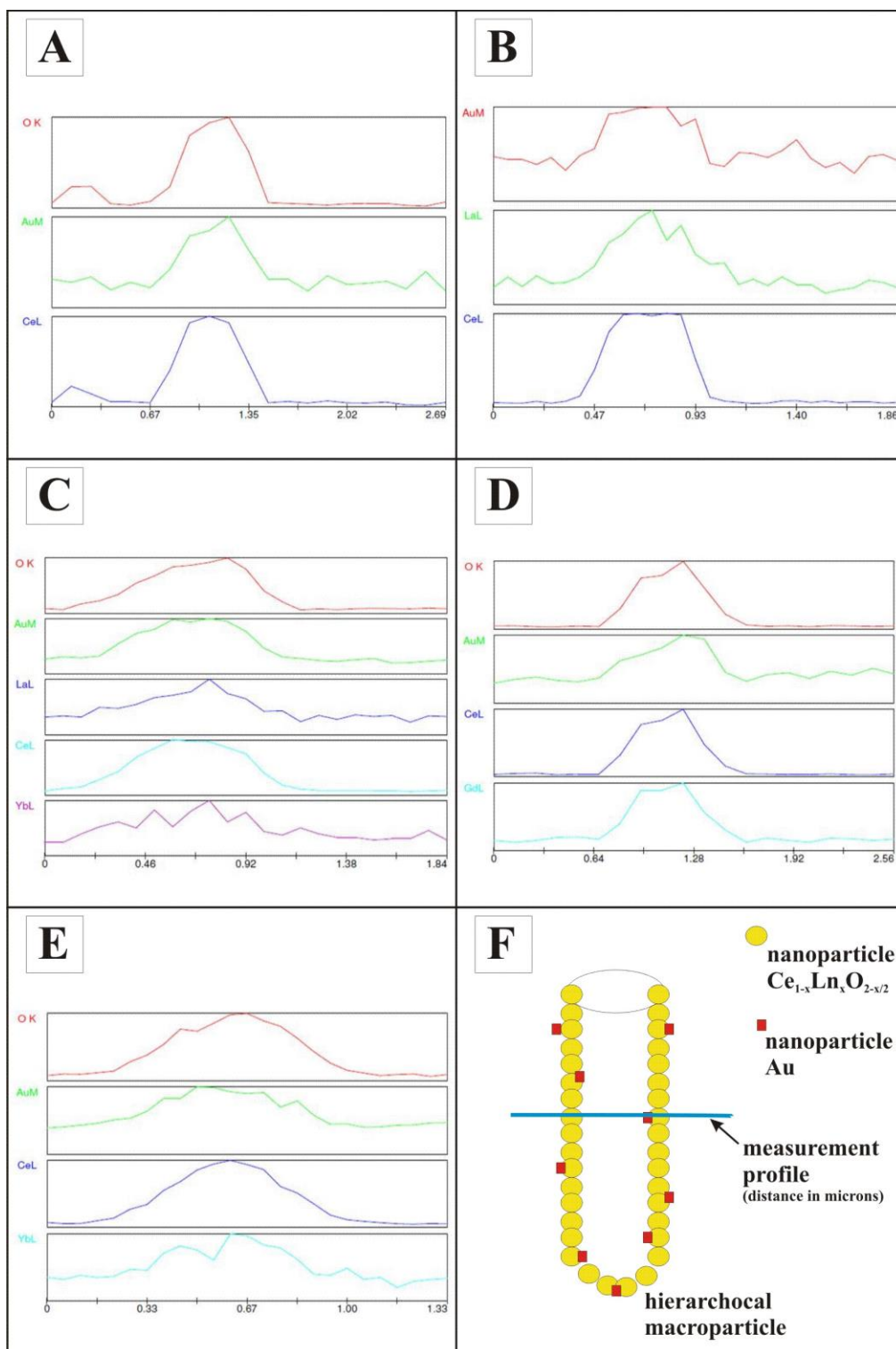


Fig.S6 Line profile of SEM-EDX of hierarchical tube-like (A) Au/CeO<sub>2</sub>, (B) Au/Ce<sub>0.9</sub>La<sub>0.1</sub>O<sub>1.95</sub>, (C) Au/Ce<sub>0.9</sub>La<sub>0.05</sub>Yb<sub>0.05</sub>O<sub>1.95</sub>, (D) Au/Ce<sub>0.9</sub>Gd<sub>0.1</sub>O<sub>1.95</sub>, (E) Au/Ce<sub>0.9</sub>Yb<sub>0.1</sub>O<sub>1.95</sub>, (F) model of measurement.

Dr. hab. Małgorzata Małecka  
Instytut Niskich Temperatur i Badań Strukturalnych  
Im. Włodzimierza Trzebiatowskiego  
Polskiej Akademii Nauk  
Ul. Okólna 2, 50-422 Wrocław

Wrocław 24.10.2022

## OŚWIADCZENIE

Oświadczam, że mój udział jako współautora w następujących publikacjach:

- 1) **“Function of various levels of hierarchical organization of porous Ce<sub>0.9</sub>REE<sub>0.1</sub>O<sub>1.95</sub> mixed oxides in catalytic activity.”** Woźniak Piotr, Miśta Włodzimierz, Małecka Małgorzata, CrystEngComm, 2020, vol. 22, nr 35, s.5914-5930. DOI:10.1039/d0ce00883d
- 2) **“Decoration of Cube-Like Ceria Crystals by Well-Dispersed Au Nanoparticles: Surface Influence.”** Małecka Małgorzata, Matus Krzysztof, Woźniak Piotr, ChemistrySelect, 2020, vol. 5, nr 10, s.2871-2877. DOI:10.1002/slct.202000098
- 3) **“Hierarchical macroparticles of ceria with tube-like shape – synthesis and properties.”** Małecka Małgorzata, Woźniak Piotr, CrystEngComm, 2021, vol. 23, nr 38, s.6743-6754. DOI:10.1039/d1ce00755f
- 4) **“Hierarchical Au/CeO<sub>2</sub> systems – influence of Ln<sup>3+</sup> dopants on the catalytic activity in the propane oxidation proces.”** Woźniak Piotr, Kraszkiewicz Piotr, Małecka Małgorzata, CrystEngComm, 2022, vol. 24, nr 36, s.6408-6420. DOI:10.1039/d2ce00827k
- 5) **“3D hierarchically structured Ce<sub>1-x</sub>Gd<sub>x</sub>O<sub>2-x/2</sub> mixed oxide particles: the role of microstructure, porosity and multi-level architecture stability in soot and propane oxidation.”** Woźniak Piotr, Małecka Małgorzata, Chinchilla Lidia, Trasobares Susana, Materials Research Bulletin, 2022, vol. 151, Numer artykułu:111816. DOI:10.1016/j.materresbull.2022.111816
- 6) **“Confinement of nano-gold in 3D hierarchically structured gadolinium-doped ceria mesocrystal: synergic effect of chemical composition and structural hierarchy in CO and propane oxidation.”** Woźniak Piotr, Małecka Małgorzata, Kraszkiewicz Piotr, Miśta Włodzimierz, Bezkravnyi Oleksii, Chinchilla Lidia, Trasobares Susana, Catalysis Science & Technology, DOI: 10.1039/D2CY01214F

polegał na uczestnictwie w planowaniu eksperymentów, dyskusji wyników oraz końcowej edycji manuskryptów.

Oświadczam ponadto że, wkład pracy Pana Piotra Woźniaka w powstanie każdej z powyższych prac był dominujący.

*Małgorzata  
Małecka*



Dr Lidia Chinchilla

October, 28 th, 2022

Departamento de Ciencia de los Materiales  
e Ing. Metalúrgica y Química Inorganica  
Universidad de Cadiz  
Campus Universitario de Puerto Real  
11510, Cadiz, Espana

To Whom It May concern,

I declare that my contribution to the publication “Piotr Woźniak, Małgorzata A. Małecka, Lidia Chinchilla, Susana Trasobares, **3D hierarchically structured  $Ce_{1-x}Gd_xO_{2-x/2}$  mixed oxide particles: the role of microstructure, porosity and multi-level architecture stability in soot and propane oxidation.**, Materials Research Bulletin, 151, 2022, 111816.” was to perform the measurements using double aberration-corrected FEI Titan3 Themis 60-300 microscope and analyze the data obtained.

I also declare that the principal role in the elaboration of the mentioned work as well as in the preparation of the manuscript belonged to Mr. Piotr Woźniak.

I declare that my contribution to the publication “Piotr Woźniak, Małgorzata A. Małecka , Piotr Kraszkievicz, Włodzimierz Miśta, Oleksii Bezkrovnyi, Lidia Chinchilla, Susana Trasobares, **Confinement of nano-gold in 3D hierarchically structured gadolinium-doped ceria mesocrystal: synergistic effect of chemical composition and structural hierarchy in CO and propane oxidation**, Catalysis Science & Technology, DOI: 10.1039/D2CY01214F” was to perform the measurements using double aberration-corrected FEI Titan3 Themis 60-300 microscope and analyze the data obtained.

I also declare that the principal role in the elaboration of the mentioned work as well as in the preparation of the manuscript belonged to Mr. Piotr Woźniak.

Sincerely yours,



Lidia F. Chinchilla

Prof. Susana Trasobares

06<sup>th</sup> November 2022

Departamento de Ciencia de los Materiales  
e Ing. Metalúrgica y Química Inorgánica  
Universidad de Cádiz  
Campus Universitario de Puerto Real  
11510, Cadiz, Spain

To Whom It May concern,

I declare that my contribution to the publication “Piotr Woźniak, Małgorzata A. Małecka, Lidia Chinchilla, Susana Trasobares, **3D hierarchically structured Ce<sub>1-x</sub>Gd<sub>x</sub>O<sub>2-x/2</sub> mixed oxide particles: the role of microstructure, porosity and multi-level architecture stability in soot and propane oxidation.**, Materials Research Bulletin, 151, 2022, 111816.” was investigation and formal analysis.

I also declare that the principal role in the elaboration of the mentioned work as well as in the preparation of the manuscript belonged to Mr. Piotr Woźniak.

Sincerely yours,

CSV (Código de Verificación Segura)	IV7A2PPZN7ZCRRE6435BAEBTEE	Fecha	06/11/2022 19:29:05
Normativa	Este documento incorpora firma electrónica reconocida de acuerdo a la ley 6/2020, de 11 de noviembre, reguladora de determinados aspectos de los servicios electrónicos de confianza	Validez del documento	Original
Firmado por	SUSANA TRASOBARES SUSANA		
Url de verificación	<a href="https://sede.uca.es/verifirma/code/IV7A2PPZN7ZCRRE6435BAEBTEE">https://sede.uca.es/verifirma/code/IV7A2PPZN7ZCRRE6435BAEBTEE</a>	Página	1/1



Prof. Susana Trasobares

06<sup>th</sup> November 2022

Departamento de Ciencia de los Materiales  
e Ing. Metalúrgica y Química Inorgánica  
Universidad de Cádiz  
Campus Universitario de Puerto Real  
11510, Cádiz, España


To Whom It May concern,

I declare that my contribution to the publication “Piotr Woźniak, Małgorzata A. Małecka , Piotr Kraszkiewicz, Włodzimierz Miśta, Oleksii Bezkrovnyi, Lidia Chinchilla, Susana Trasobares, **Confinement of nano-gold in 3D hierarchically structured gadolinium-doped ceria mesocrystal: synergistic effect of chemical composition and structural hierarchy in CO and propane oxidation**, Catalysis Science & Technology, DOI: 10.1039/D2CY01214F” was investigation and formal analysis

I also declare that the principal role in the elaboration of the mentioned work as well as in the preparation of the manuscript belonged to Mr. Piotr Woźniak.

Sincerely yours,

CSV (Código de Verificación Segura)	IV7A3SJZJZPIJ6RZRQYMKZYR4Q	Fecha	07/11/2022 11:01:55
Normativa	Este documento incorpora firma electrónica reconocida de acuerdo a la ley 6/2020, de 11 de noviembre, reguladora de determinados aspectos de los servicios electrónicos de confianza	Validez del documento	Original
Firmado por	SUSANA TRASOBARES SUSANA		
Url de verificación	<a href="https://sede.uca.es/verifirma/code/IV7A3SJZJZPIJ6RZRQYMKZYR4Q">https://sede.uca.es/verifirma/code/IV7A3SJZJZPIJ6RZRQYMKZYR4Q</a>	Página	1/1



Dr Piotr Kraszkiewicz  
Instytut Niskich Temperatur i Badań Strukturalnych  
Im. Włodzimierza Trzebiatowskiego  
Polskiej Akademii Nauk  
Ul. Okólna 2, 50-422 Wrocław

Wrocław, 07.11.2022r.

### Oświadczenie

Oświadczam, że mój udział jako współautora w publikacji: **„Hierarchical Au/CeO<sub>2</sub> systems – influence of Ln<sup>3+</sup> dopants on the catalytic activity in the propane oxidation proces.”** **Woźniak Piotr, Kraszkiewicz Piotr, Małecka Małgorzata, CrystEngComm, 2022, vol. 24, nr 36, s.6408-6420. DOI:10.1039/d2ce00827k** polegał na wykonaniu pomiarów H<sub>2</sub>-TPR, opracowaniu otrzymanych wyników H<sub>2</sub>-TPR oraz recenzji i poprawieniu manuskryptu.

Oświadczam ponadto że, wkład pracy Pana Piotra Woźniaka w powstanie tej pracy był dominujący.

Oświadczam, że mój udział jako współautora w publikacji: **„Confinement of nano-gold in 3D hierarchically structured gadolinium-doped ceria mesocrystal: synergic effect of chemical composition and structural hierarchy in CO and propane oxidation.”** **Piotr Woźniak, Małgorzata A. Małecka, Piotr Kraszkiewicz, Włodzimierz Miśta, Oleksii Bezkravnyi, Lidia Chinchilla, Susana Trasobares, Catalysis Science & Technology, DOI: 10.1039/D2CY01214F** polegał na wykonaniu pomiarów H<sub>2</sub>-TPR, opracowaniu otrzymanych wyników H<sub>2</sub>-TPR oraz recenzji i poprawieniu manuskryptu.

Oświadczam ponadto że, wkład pracy Pana Piotra Woźniaka w powstanie tej pracy był dominujący.

Piotr Kraszkiewicz

mgr inż. Krzysztof Matus  
Laboratorium Badania Materiałów  
Wydział Mechaniczny Technologiczny  
Politechnika Śląska  
ul. Konarskiego 18a, 44-100 Gliwice, Polska

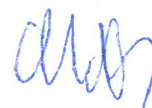
Gliwice, 26.10.2022

### Oświadczenie

Oświadczam, że mój udział jako współautora w publikacji: „**Decoration of Cube-Like Ceria Crystals by Well-Dispersed Au Nanoparticles: Surface Influence**” **Małecka Małgorzata, Matus Krzysztof, Woźniak Piotr, ChemistrySelect, 2020, vol. 5, nr 10, s.2871-2877. DOI:10.1002/slct.202000098** polegał na charakteryzacji próbek z wykorzystaniem transmisyjnej mikroskopii elektronowej w tym HRTEM, HAADF wraz z analizami spektroskopowymi EDS oraz dyskusji wyników.

Oświadczam ponadto że, wkład pracy Pana Piotra Woźniaka w powstanie tej pracy był dominujący.

Krzysztof Matus



Dr Oleksii Bezkravnyi  
Instytut Niskich Temperatur i Badań Strukturalnych  
Im. Włodzimierza Trzebiatowskiego  
Polskiej Akademii Nauk  
Ul. Okólna 2, 50-422 Wrocław

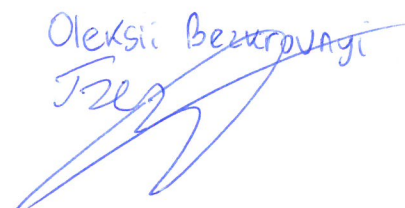
Wrocław, 2.11.2022

### Oświadczenie

Oświadczam, że mój udział jako współautora w publikacji: „**Confinement of nano-gold in 3D hierarchically structured gadolinium-doped ceria mesocrystal: synergic effect of chemical composition and structural hierarchy in CO and propane oxidation.**” Piotr Woźniak, Małgorzata A. Małecka, Piotr Kraszkievicz, Włodzimierz Miśta, Oleksii Bezkravnyi, Lidia Chinchilla, Susana Trasobares, Catalysis Science & Technology, DOI: 10.1039/D2CY01214F polegał na dokonaniu pomiaru NAP-XPS oraz opracowaniu i dyskusji uzyskanych wyników.

Oświadczam ponadto że, wkład pracy Pana Piotra Woźniaka w powstanie tej pracy był dominujący.

Oleksii Bezkravnyi  
F.22



Dr. Włodzimierz Miśta  
Instytut Niskich Temperatur i Badań Strukturalnych  
Im. Włodzimierza Trzebiatowskiego  
Polskiej Akademii Nauk  
Ul. Okólna 2, 50-422 Wrocław

Wrocław, 10.11.2022

### Oświadczenie

Oświadczam, że mój udział jako współautora w publikacji: **“Function of various levels of hierarchical organization of porous  $Ce_{0.9}RE_{0.1}O_{1.95}$  mixed oxides in catalytic activity”** **Woźniak Piotr, Miśta Włodzimierz, Małecka Małgorzata, CrystEngComm, 2020, vol. 22, nr 35, s.5914-5930. DOI:10.1039/d0ce00883d** polegał na wykonaniu pomiarów utleniania CO oraz analizie i dyskusji otrzymanych wyników.

Oświadczam ponadto że, wkład pracy Pana Piotra Woźniaka w powstanie tej pracy był dominujący.

Oświadczam, że mój udział jako współautora w publikacji: **„Confinement of nano-gold in 3D hierarchically structured gadolinium-doped ceria mesocrystal: synergic effect of chemical composition and structural hierarchy in CO and propane oxidation.”** **Piotr Woźniak, Małgorzata A. Małecka, Piotr Kraszkiewicz, Włodzimierz Miśta, Oleksii Bezkravnyi, Lidia Chinchilla, Susana Trasobares, Catalysis Science & Technology, DOI: 10.1039/D2CY01214F** polegał na wykonaniu pomiarów TPD-MS i utleniania CO oraz analizie i dyskusji otrzymanych wyników.

Oświadczam ponadto że, wkład pracy Pana Piotra Woźniaka w powstanie tej pracy był dominujący.

*W. Miśta*

### Oświadczenie

Oświadczam, że mój udział jako współautora w publikacji: „**Woźniak P., Mišta W., Malecka M.A., Function of various levels of hierarchical organization of porous  $Ce_{0.9}REE_{0.1}O_{1.95}$  mixed oxides in catalytic activity, CrystEngComm, 2020, 22, 5914–5930.**” polegał na:

- udziale w konceptualizacji badań.
- syntezie serii mieszanych mrowczanów  $Ce_{0.9}REE_{0.1}O_{1.95}$  (REE= Sc, Y, La, Pr, Nd, Sm, Eu, Gd, Tb, Dy, Ho, Er, Tm, Yb, Lu, Sc, Y) o morfologii gwiazd.
- optymalizacji warunków termolizy celem uzyskania cerowych materiałów hierarchicznych.
- dokonaniu charakterystyki strukturalnej i morfologicznej próbek przy pomocy TEM, SAED, SEM, EDX oraz opracowaniu i interpretacji wyników.
- zmierzeniu profili TG wybranych próbek oraz opracowaniu i interpretacji wyników.
- opracowaniu i interpretacji wyników PXRD oraz spektroskopii Ramana.
- zbadaniu reaktywności i stabilności morfologicznej materiałów w reakcji utleniania sadzy.
- opracowaniu wyników utleniania CO.
- wykonaniu przeglądu literaturowego.
- zintegrowaniu i interpretacji wyników charakteryzacji fizykochemicznej materiałów.
- napisaniu manuskryptu oraz wykonaniu finalnego opracowania graficznego wyników.

Oświadczam, że mój udział jako współautora w publikacji: „**Woźniak, P., Malecka, M.A., Chinchilla, L., Trasobares, S., 3D hierarchically structured  $Ce_{1-x}Gd_xO_{2-x/2}$  mixed oxide particles: the role of microstructure, porosity and multi-level architecture stability in soot and propane oxidation, Mater. Res. Bull. 151 (2022) 111816.**” polegał na:

- udziale w konceptualizacji badań.
- syntezie serii mieszanych hierarchicznych tlenków  $Ce_{1-x}Gd_xO_{2-x/2}$  ( $x=0; 0.1; 0.3; 0.5; 0.7; 0.9; 1$ ) o morfologii gwiazd.
- charakteryzacji materiałów za pomocą technik TEM, HRTEM, SAED, SEM-EDX oraz opracowaniu i interpretacji wyników.
- wykonaniu pomiarów  $H_2$ -TPR i opracowaniu wyników.
- wykonaniu pomiarów fizysorpcji  $N_2$  oraz opracowaniu i interpretacji wyników.
- opracowaniu i interpretacji wyników PXRD, w tym dokonanie analizy mikrostruktury materiałów przy pomocy udokładniania Rietvelda.
- zbadaniu stabilności architektury próbek, w tym opracowaniu temperaturowo zależnych profili PXRD.
- pomiarze i opracowaniu wyników aktywności katalitycznej, selektywności oraz stabilności materiałów w reakcjach utleniania propanu oraz aktywności katalitycznej i stabilności w reakcji utleniania sadzy.
- zintegrowaniu i interpretacji wyników charakteryzacji fizykochemicznej oraz aktywności katalitycznej materiałów.
- wykonaniu przeglądu literaturowego.
- napisaniu manuskryptu oraz wykonaniu finalnego opracowania graficznego wyników.

Piotr Woźniak



Oświadczam, że mój udział jako współautora w publikacji „**Malecka, M.A. Woźniak, P., Hierarchical macroparticles of ceria with tube-like shape – synthesis and properties, CrystEngComm, 2021, 23, 6743-6754.**” polegał na:

- dyskusji nad metodą syntezy materiałów cerowych o morfologii słomek.
- wykonaniu pomiarów H<sub>2</sub>-TPR serii próbek Ce<sub>1-x</sub>Yb<sub>x</sub>O<sub>2-x/2</sub> (x= 0-0.5) o morfologii słomek i opracowaniu wyników.
- wykonaniu pomiarów fizysorpcji N<sub>2</sub> i opracowaniu wyników.
- wykonaniu pomiarów TG w reakcji utleniania sadzy i opracowaniu wyników.
- wykonaniu pomiarów aktywności i selektywności materiałów w utlenianiu propanu oraz opracowaniu wyników.
- dyskusji nad zintegrowanymi wynikami charakteryzacji fizykochemicznej materiałów.
- edycji manuskryptu.

Oświadczam, że mój udział jako współautora w publikacji: „**Malecka M.A., Matus K., Woźniak P., Decoration of Cube-Like Ceria Crystals by Well-Dispersed Au Nanoparticles: Surface Influence, ChemistrySelect 2020, 5, 2871 –2877.**” polegał na:

- udziale w konceptualizacji badań.
- syntezie nanocząstek CeO<sub>2</sub> o morfologii kostek, identyfikacji czynników wpływających na rozmiary cząstek i optymalizacji warunków syntezy.
- optymalizacji procesu osadzania nanocząstek Au na nanokostkach CeO<sub>2</sub> oraz identyfikacji istotnych parametrów warunkujących formowanie nanocząstek Au.
- charakteryzacji materiałów za pomocą technik TEM, HRTEM.
- dyskusji nad zintegrowanymi wynikami charakteryzacji fizykochemicznej materiałów.
- edycji manuskryptu.

Oświadczam, że mój udział jako współautora w publikacji: „**Woźniak, P. , Malecka, M.A., , Kraszkiewicz, P. , Miśta, W. , Bezkrvnyi, O. , Chinchilla, L. , Trasobares, S., Confinement of nano-gold in 3D hierarchically structured gadolinium-doped ceria mesocrystal: synergic effect of chemical composition and structural hierarchy in CO and propane oxidation. Catal. Sci. Technol. DOI: 10.1039/d2cy01214f.**” polegał na:

- udziale w konceptualizacji badań.
- syntezie hierarchicznych materiałów Ce<sub>1-x</sub>Gd<sub>x</sub>O<sub>2-x/2</sub> (x= 0; 0.1) o morfologii gwiazd oraz Ce<sub>1-x</sub>Gd<sub>x</sub>O<sub>2-x/2</sub> (x=0; 0.1) o morfologii nanokostek.
- optymalizacji metody osadzania nanocząstek Au na nośnikach katalitycznych (materiały hierarchiczne, nanokostki, nanocząstki).
- dokonaniu charakterystyki strukturalnej i morfologicznej próbek przy pomocy TEM i HRTEM (CM Philips), SAED, SEM, SEM-EDX oraz analizie statystycznej, opracowaniu i interpretacji wyników.
- opracowaniu i interpretacji wyników PXRD.
- wykonaniu pomiarów fizysorpcji N<sub>2</sub>, opracowaniu i interpretacji wyników.
- pomiarze aktywności, selektywności oraz stabilności materiałów w reakcjach katalitycznego utleniania propanu, opracowaniu i interpretacji wyników.
- zintegrowaniu i interpretacji wyników charakteryzacji fizykochemicznej oraz aktywności katalitycznej materiałów.
- wykonaniu przeglądu literaturowego.
- napisaniu manuskryptu oraz wykonaniu finalnego opracowania graficznego wyników.

Piotr Woźniak

Oświadczam, że mój udział jako współautora w publikacji: „**Woźniak, P., Kraszkiewicz, P., Malecka, M.A., Hierarchical Au/CeO<sub>2</sub> systems – influence of Ln<sup>3+</sup> dopants on the catalytic activity in the propane oxidation process, CrystEngComm, 2022, 24, 6408.**” polegał na:

- udziale w konceptualizacji badań.
- pomiarach fizysoorpcji N<sub>2</sub> nośników katalitycznych Ce<sub>0.9</sub>REE<sub>A</sub>REE<sub>B</sub>O<sub>1.95</sub> (A = 0 or 0.05, B = 0.05 or 0.1, REE = La, Yb, Gd) o morfologii słomek oraz opracowaniu i interpretacji wyników.
- osadzaniu nanocząstek Au na serii nośników katalitycznych o morfologii słomek.
- pomiarze aktywności katalitycznej, selektywności oraz stabilności katalizatorów w reakcji utleniania propanu.
- dyskusji nad zintegrowanymi wynikami właściwości katalitycznych materiałów.
- edycji manuskryptu.

Piotr Woźniak